ERCI/HSV-TR01-01

Final Report

SRM Internal Flow Tests and Computational Fluid Dynamic Analysis

Volume II
CFD RSRM Full-Scale Analyses

30 October 2001

Prepared for:
George C. Marshall Space Flight Center
National Aeronautics and Space Administration
Marshall Space Flight Center, AL 35812

Contract NAS8-40347

Prepared by:
ERC, Incorporated
555 Sparkman Drive, Suite 1622
Huntsville, AL 35816

PREFACE

This report was prepared by the Huntsville Operation of ERC, Incorporated for the Fluid Dynamics Division of the Science and Engineering Directorate, George C. Marshall Space Flight Center, National Aeronautics and Space Administration. This effort was performed under Contract NAS8-40347 with Andrew Schorr, MP51, serving as the Contracting Officer's Technical Representative. Jack Hengel, ED34, served as the initial COTR for the program.

The ERC, Incorporated Program Manager and Project Engineer is R. Harold Whitesides. The Computational Fluid Dynamics Task Analyst is William A. Mahaffey. A majority of the CFD analysis was performed by Richard A. Dill, the former Computational Fluid Dynamics Task Leader. Cold flow model design analyses and computational engineering support were provided by David C. Purinton.

TABLE OF CONTENTS

Volume I

1.0 RSRM FULL SCALE ANALYSES

1.38 RSRM 11-Mesh Sandwich Screen Evaluation
1.39 RSRM External Nozzle Surface Pressure Data
1.40 ESD Assessment for RSRM Asbestos-Free Insulations
1.41 RSRM OPT CDR
1.42 RSRM Nozzle Adhesive Replacement TIM
1.43 RSRM Carbon Fiber EPDM Discriminator Test
1.44 RSRM Propellant Structural Technology TIM
1.45 RSRM Nozzle
1.46 RSRM Propellant
1.47 RSRM Steel Cell Plating
1.48 RSRM Silica Fiber EPDM
1.49 RSRM Work Center Reviews
1.50 RSRM Enhanced Sustaining Engineering Review
1.51 BSM/CSD NASA Independent Review Team
1.52 RSRM Propellant Geometry Upgrade PRR
1.53 RSRM Chief Engineer's Review Board
1.54 RSRM Igniter Booster Basket Grease Contamination
1.55 Shuttle Booster Upgrades
1.56 RSRM Propellant Grain Modification
1.57 RSRM Nozzle Joint 5 PD TIM
1.58 RSRM Primer/Degreaser TIM
1.59 RSRM Carbon Fiber Rope Joint #2 TIM
1.60 RSRM Independent Audit Assessment
1.61 FSM-9 Nozzle Pocketing/Flight Implications

2.0 SUBSCALE MOTOR ANALYSES

2.1 RSRM Subscale Spin Motor Slag Tests
2.2 24-Inch Hybrid Motor Simulation Testing of J-Leg/PSA
2.3 11-Inch Hybrid Motor Asbestos-Free Materials Testing
2.4 24-Inch Solid Propellant Test Motor
2.5 24-Inch Solid Rocket Propellant Test Motor (SRTM)
2.6 SRTM-IC (24-Inch Solid Rocket Test Motor, Insulation Configuration)
2.7 RSRM MNASA-11, 12, 13, & 14
2.8 RSRM ETM-2
2.9 RSRM ETM-3

3.0 COLD FLOW ANALYSES

3.1 RSRM Inhibitor Dynamics Model
3.2 RSRM 10% Scale Cold Flow Model

Appendix A: RSRM Project Documentation and Review Planning
Appendix B: RSRM Project Test Planning and Management

Volume II

4.0 CFD RSRM FULL-SCALE ANALYSES

Volume III

5.0 CFD SUBSCALE ANALYSES

4.0 CFD RSRM FULL-SCALE ANALYSES

4.1 Full Scale RSRM, 20 second Burn Time

During the May 2000 time period, questions arose about the extent of slag impact and accumulation within the submerged cavity of the full scale RSRM due to the presence of propellant in the submerged region. ERC attempted to answer this question by developing a CFD model for this burn time as a part of ongoing modeling efforts of the full scale RSRM. ERC has developed models for 33 second, 50 second, 65 second, 67 second, 80 second, and 110 second burn times at various times in the past, and this model joined that series. These models used the best available propellant properties and most recent combustion models, as validated in previous model scale and full scale simulations.

The propellant mix used in this analysis represents a propellant with a nominal or "as-received" mixture of aluminum and AP particles. The constituent particle sizes represent an in-specification production propellant mix. This propellant mix and the descriptive properties of the mix were obtained from the analysis of the Thiokol 1997 5-Inch spin motor tests and quench bomb data. The nominal propellant characteristics were constructed by averaging test mixes 209-97-84 and 209-97-85 from this data. The mix represents the best available description of a nominal production propellant mix. This propellant was compared to an earlier representative nominal production propellant mix and was found to have very similar properties and slag retention characteristics. Figure 1 shows the discrete phase particle size distribution for this nominal propellant mix.

Average ballistic data and properties obtained from Thiokol motor design charts were used to compute the thermophysical characteristics of the gas phase. The thermophysical properties were computed at an average chamber pressure of 850 psia using the nominal RSRM propellant ingredients to drive the equilibrium-chemistry CET86 thermophysical properties code. This motor pressure along with the thermophysical properties of the gas phase was used to compute a propellant surface thermal boundary condition. The propellant thermal boundary condition at the appropriate partially combusted propellant conditions was 5906 degrees Rankine. The discrete phase particles released at the propellant surface contain 11.1% unburned aluminum and the caps fraction used in the analysis was 34.67%. In order to compute the mass flow rate for the motor, the mass flow of each segment was evaluated. The forward segment was analyzed as 2 segments, since at this burn time the "star" part of the forward segment is still burning. Thus the forward segment was analyzed as the star-section, and the cylindrical section. The mass flow for the star section was evaluated by using mass flow information from ballistics calculations along with the surface area of the 2-dimensional representation of the star segment as calculated by the CELMINT CFD code used for this analysis. This yields a surface mass flux of 7.389 lbm/sq.ft./s in the star section and 3.271 lbm/sq.ft./s in the cylindrical part. The mass flux is higher in the star section because the extra surface area of the star cross section

is not directly modeled in the 2-D CFD model, but accounted for by the increased mass flux over the smaller area of the 2-D model. The mass fluxes for the other 3 segments were evaluated using already available geometry data for these segments directly. The mass fluxes and mass flow rates for all segments in the motor are tabulated in Table 4.1.1. The total mass flow for the motor at this burn time was 12380 lbm/s.

Table 4.1.1 20 Second RSRM Motor Operating Conditions for Nominal Propellant

	Surface Mass Flux	Mass Flow Rate
Star Section	7.389 lbm/sq.ft./s	4448 lbm/s
Fwd Section	3.271 lbm/sq.ft./s	1035 lbm/s
Fwd-Ctr Segment	3.244 lbm/sq.ft./s	2135 lbm/s
Aft-Ctr Segment	3.218 lbm/sq.ft./s	2113 lbm/s
Aft Segment	3.217 lbm/sq.ft./s	2649 lbm/s

Figures 2-10 show the grid used in this analysis. The degree of grid resolution is higher than in earlier models for 2 reasons. First, ERC now has available larger, faster computers than were available in the mid 1990's when the earlier models were developed. Thus more resolution could be used without creating unreasonably long run times and memory usage. Second, ERC did some grid resolution studies as part of the MNASA-11 work reported in the Jan-Feb 2000. These studies assessed the degree of resolution required to resolve the gas phase flows in the region of the nozzle nose to an apparently grid independent level. This level of resolution was used in the 24" SRTM-IC models developed last reporting period and in the current full scale RSRM model. The total resolution of this model is 610 grid points axially and 110 grid points radially. Figure 2 shows the grid in the star-portion of the forward segment. The outline is the contour of the "base" of this segment. Figure 3 shows the grid for the entire forward segment, i.e. the star portion and the cylindrical part. Figure 4 shows a zoomed-in look at the grid in the region between the forward and forward-center segments. Figure 5 shows the grid between the 2nd and 3rd (forward-center and aft-center) segments. Figure 6 shows the grid between the 3rd and 4th (aft-center and aft) segments. Figure 7 shows the grid at the aft end of the aft segment, which also shows the nozzle entrance area. Figure 8 shows the grid through the nozzle to the exit plane. Figure 9 shows the grid in the boot region, and Figure 10 show the grid in the submerged area near the nozzle nose. Figure 11 shows the gas phase velocity field in the forward segment. Figure 12 shows the gas phase vectors at the 1st joint (between forward and forward-center segments). Figure 13 shows the gas phase vectors in the region of the 2nd joint, Figure 14 shows the 3rd joint, and Figure 15 shows the aft end of the 4th segment. Figure 16 shows the gas phase vectors in the nozzle nose region. Figure 16 clearly shows the gases from the propellant underneath the nozzle exiting the submerged region in a fairly orderly fashion. Slag particles from the lower 1/3 of the submerged volume are seen to impact on the submerged nozzle surface and in the fixed-housing region, but the rest appear to exit with the gas flow. Figures 17 through 19 show discrete phase

particle trajectories in the submerged region for 100 micron, 200 micron and 400 micron particles. The Mass Mean Diameter of the discrete phase for this propellant is about 105 microns, but it is known empirically that the larger particles are often present in much higher proportions in deposits recovered after firing, so these trajectories are shown also. These trajectories show that most of the particle phase slag also exits this region without impacting. These figures almost single-handedly answer the motivating question for this simulation, namely "what is the impact of the underneath-nozzle propellant on slag impact early in the motor burn?". The answer appears to be that the effect is surprisingly minor.

It is important to note that these results are moderately sensitive to the turbulence fields within the submerged region. To that end, a small parametric study was also carried out to assess the degree of variation of these results with varying turbulence fields. This study involved varying one of the empirical constants in the epsilon equation of the 2-equation k-epsilon turbulence model. The constant was varied systematically over a range of values deemed reasonable by literature review. The suitability of each value was assessed by looking at the resulting gas vectors and particle trajectories in the submerged region. This study also showed some variation of the pressure drop down the bore of the motor with different constants, and this is documented as well. The results presented above, and regarded as "standard", use a value of 1.64 for the "C2" constant in the epsilon equation. The "box-stock" value of this constant is 1.92, and a value of 1.78 was used in the 24" SRTM-IC work last reporting period. The 1.92 value was used in the past full scale RSRM models. The 1.78 value was arrived at empirically by matching predicted pressure drops in the 24" SRTM-IC CFD model with those pressure drops from ballistics calculations for that motor. The 1.64 value was arrived at by comparing CFD pressure drops in the 20 second full scale RSRM motor with ballistics runs for that motor and burn time. All 3 of these values were run for the 20 second RSRM and the comparative results are presented. The comparative results will consist of gas phase vectors and 100 micron particle trajectories within the submerged region for the 3 different C2 values, as well as pressure drop data down the motor for all 3 values. The pressure results are tabulated in Table 4.1.2 below and discussed briefly.

Table 4.1.2 Pressure at various motor stations, 20 Second RSRM, PSIA

Motor Station	Ballistics	C2 = 1.92	C2 = 1.78	C2 = 1.64
Head end	875.6	938.3	907.2	874.7
Aft end, Star Seg.	867.6	930.1	899.2	856.9
1st Joint	861.3	917.9	887.4	854.7
2nd Joint	841.4	893.3	865.1	835.5
3rd Joint	829.8	857.6	834.5	808.7
Aft end, Aft Seg.	825.1	836.2	817.4	793.7

It is seen that the C2 value of 1.64 gives good agreement for the predicted head-end pressure level, as well as good agreement of the pressure drop in the 1st 2 segments. Thus this value was settled on as the best value to use for these calculations. Figures 20-25 show gas phase vectors and 100 micron discrete-phase particle trajectories for the 3 different "C2" cases. The 2 figures for the 1.64 are presented earlier and are repeated for convenience of presentation. Figures 20 and 21 show gas phase vectors and discrete phase trajectories for the "box-stock", C2 = 1.64, case. Figures 22 and 23 show vectors and trajectories for the C2 = 1.78 case, and Figures 24 and 25 show the 1.92 case. Figure 24 shows a small gas phase recirculation bubble on the nose of the nozzle. The particles are deflected around this flow feature on the way out of the submerged region. Figure 22 shows very little flow disturbance at the nose and very little particle deflection is observed in Figure 23. Figure 20 shows very smooth gas flow past the nose out of the submerged region, and Figure 21 shows smooth particle trajectories as well.

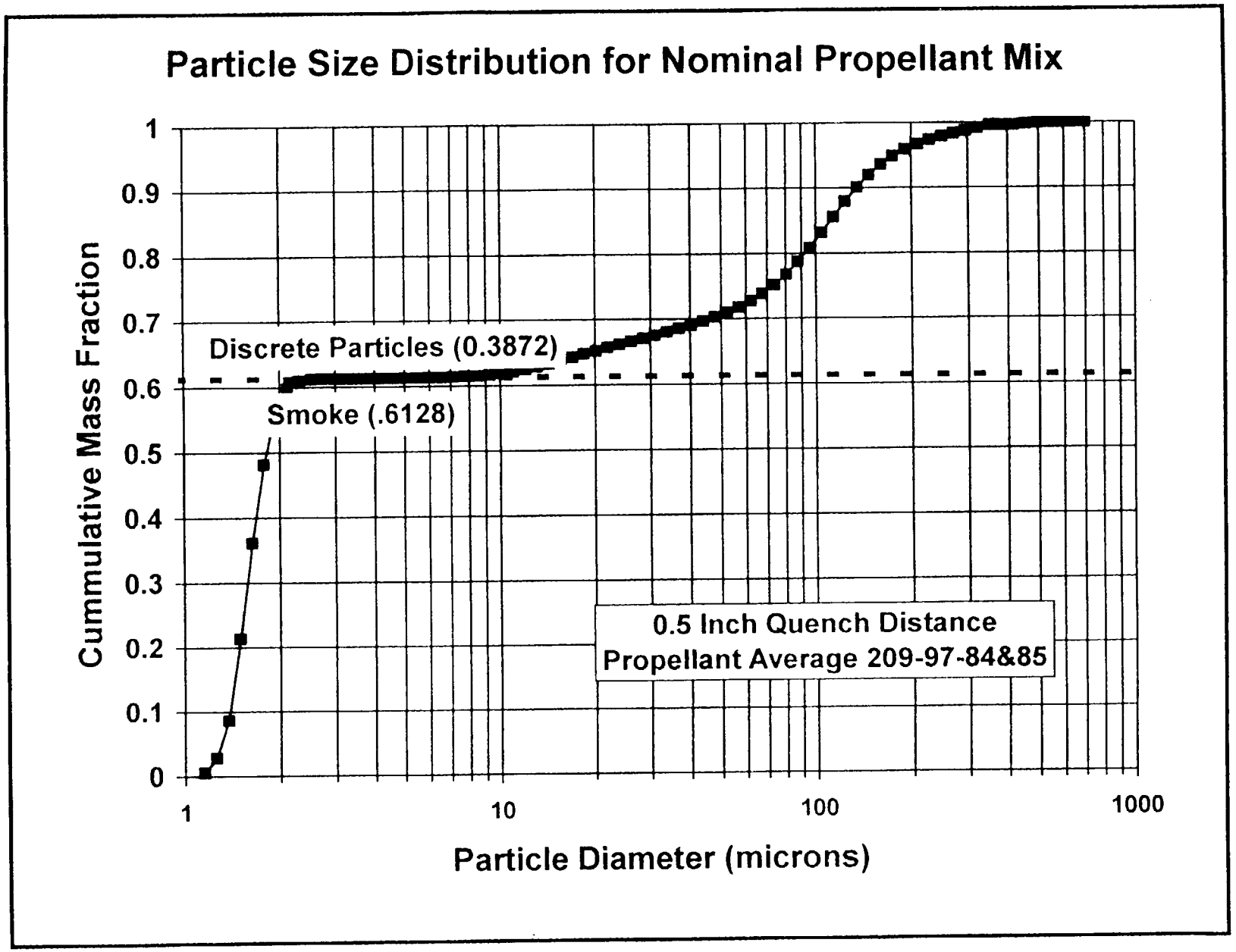

Figure 1.

ERC Inc. 6/20/00

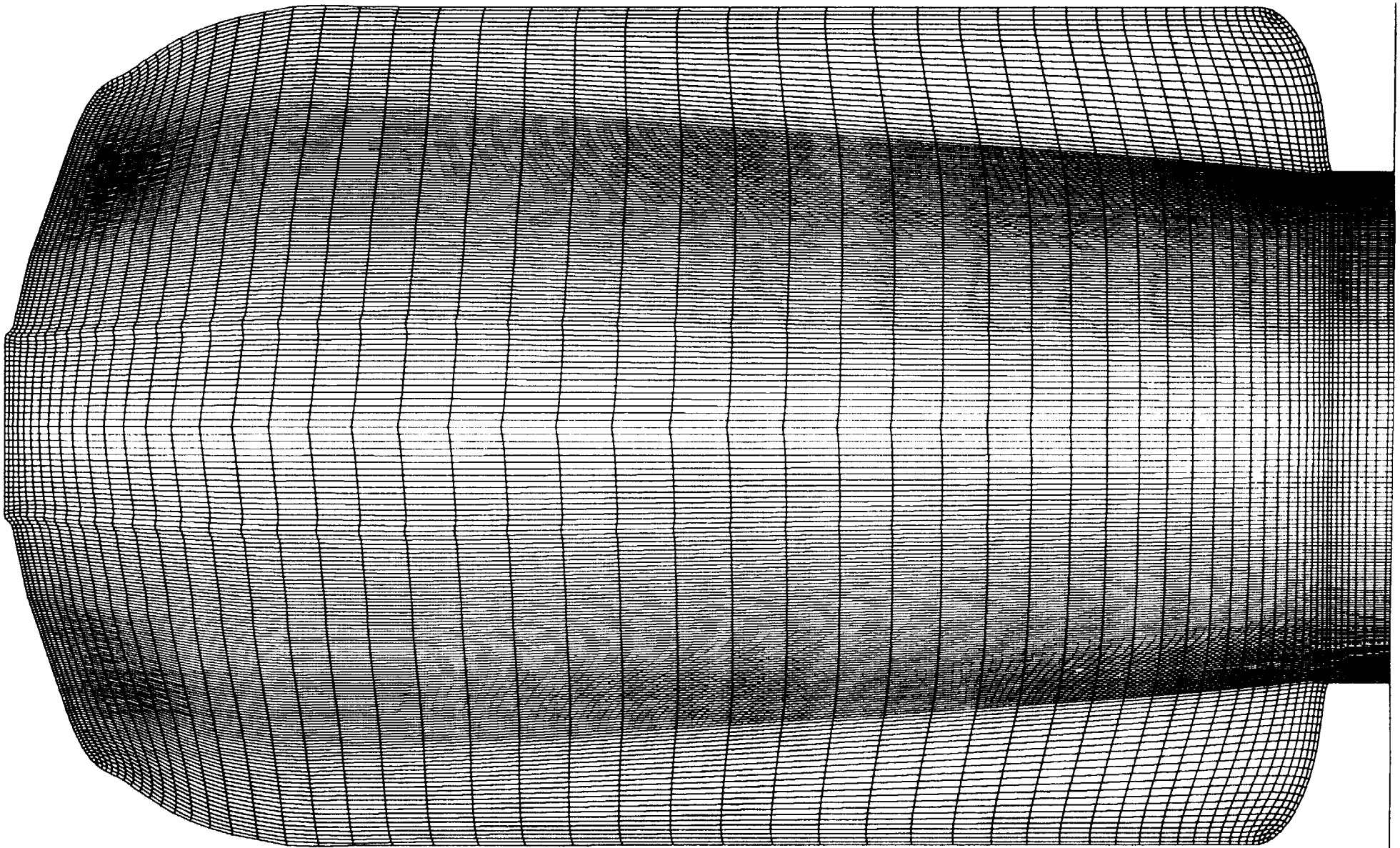

Figure 2. Full Scale RSRM, 20 Second Burn Time Grid, "Star" portion of first propellant segment

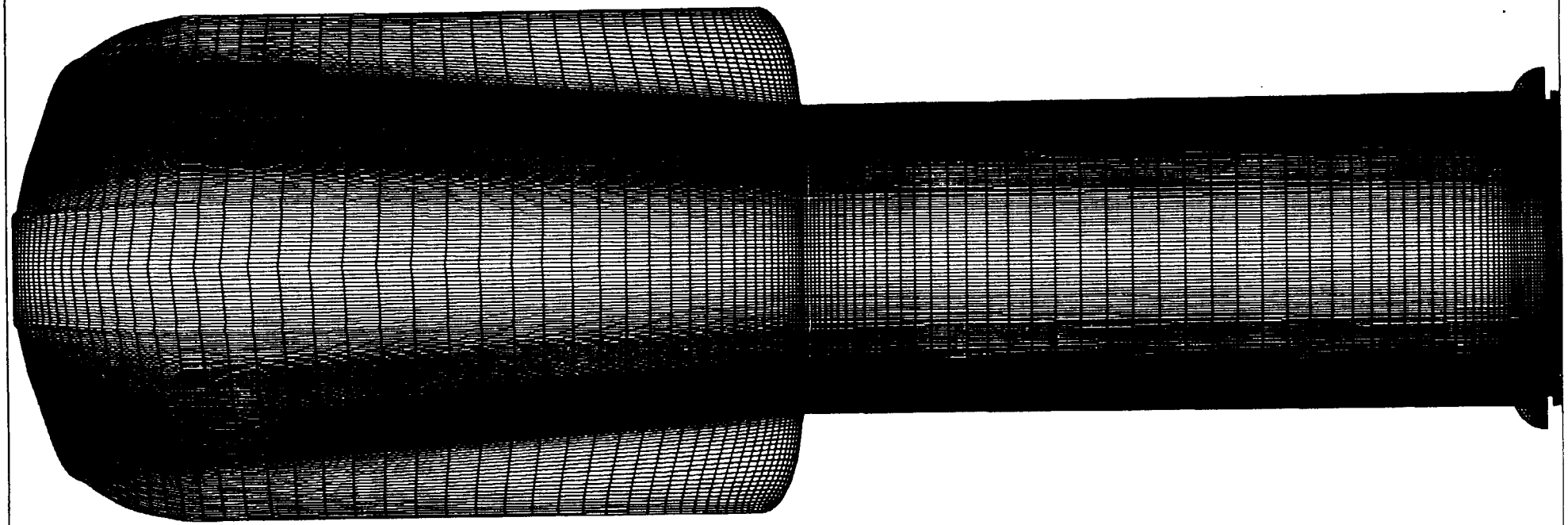

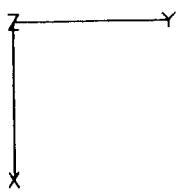

Figure 3.
Full Scale RSRM, 20 Second Burn Time Grid, entire 1st (forward) segment

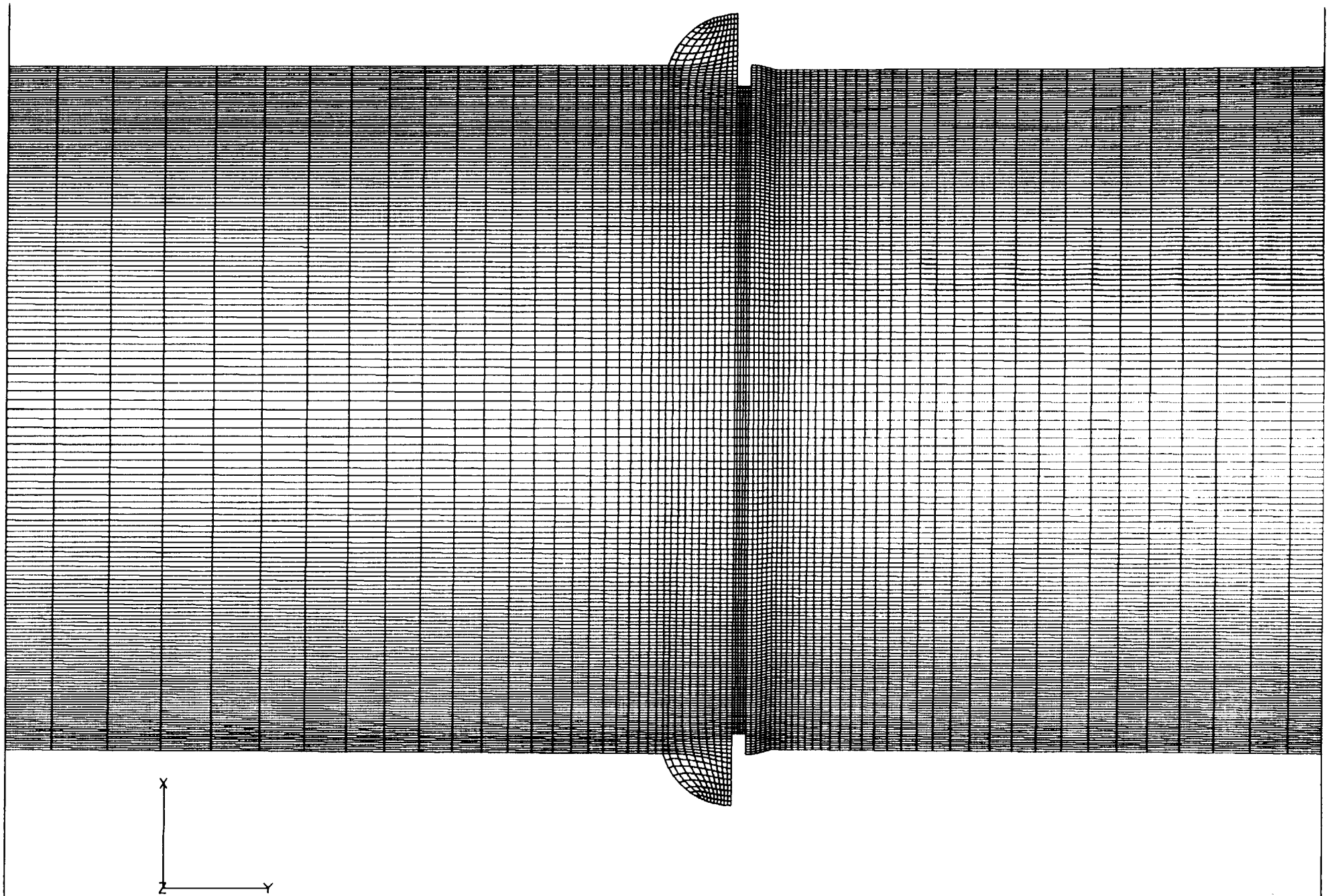

Figure 4. Full Scale RSRM, 20 Second Burn Time Grid, aft end of first propellant segment

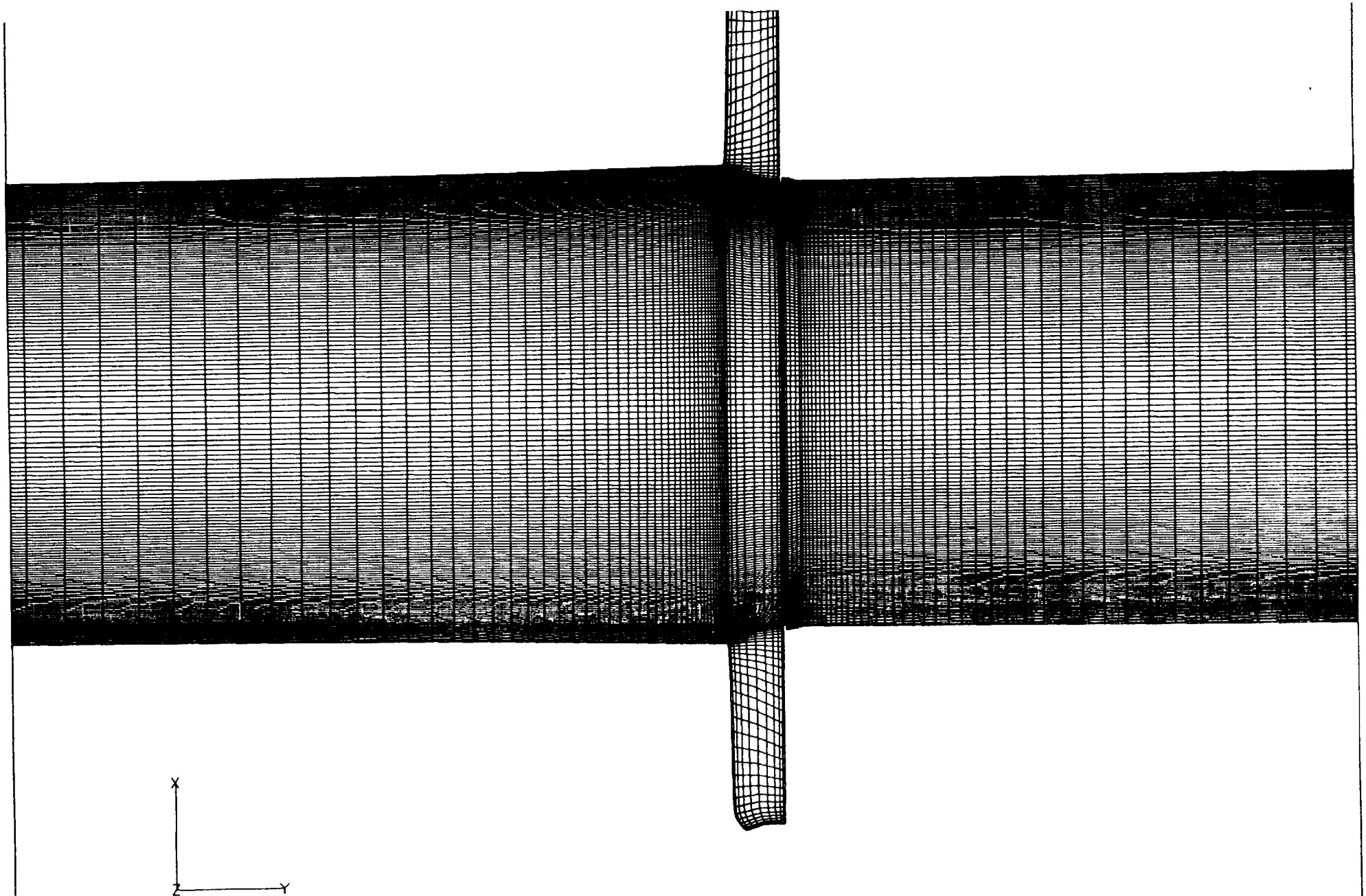

Figure 5. Full Scale RSRM, 20 Second Burn Time Grid, aft end of second propellant segment

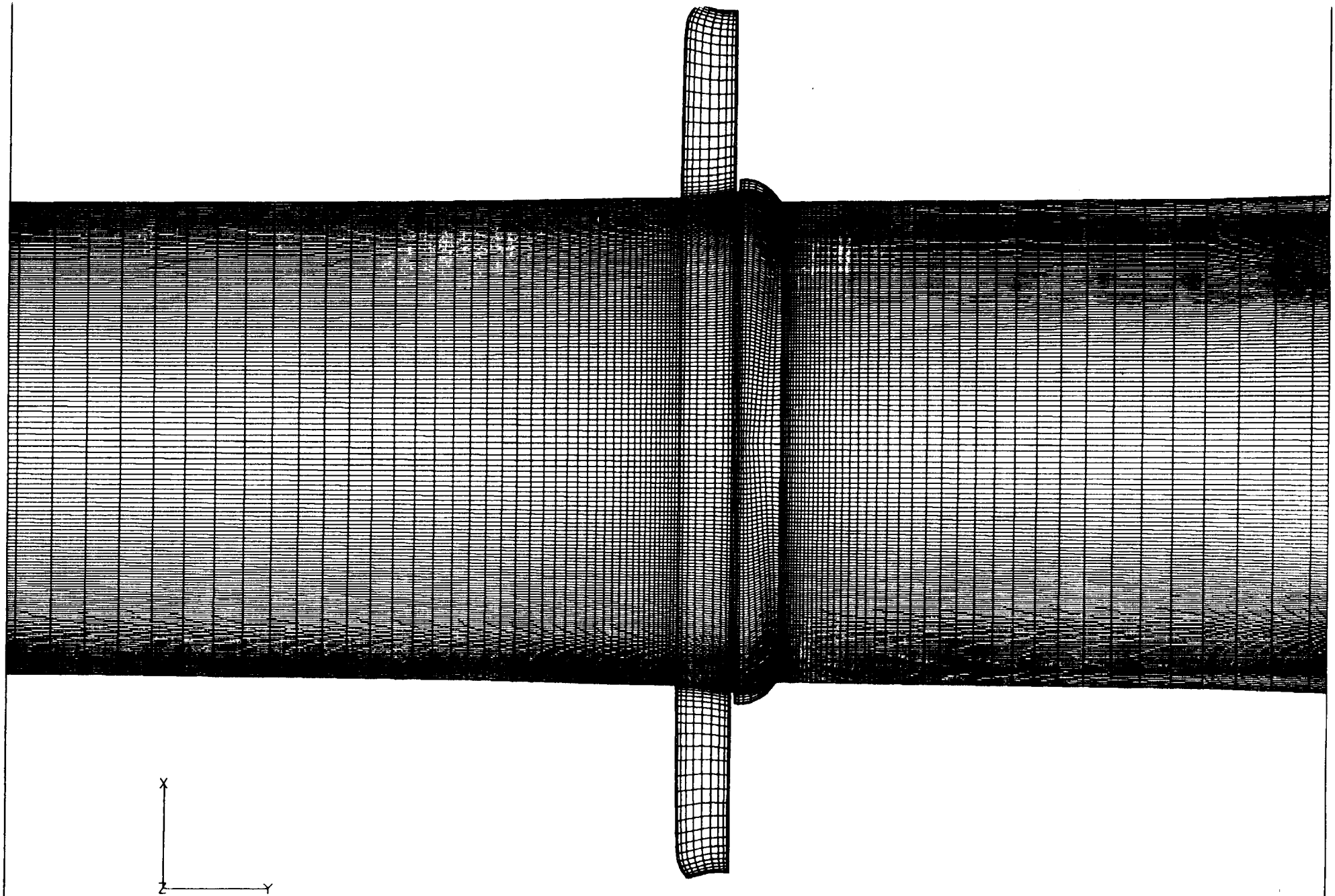

Figure 6. Full Scale RSRM, 20 Second Burn Time Grid, aft end of third propellant segment

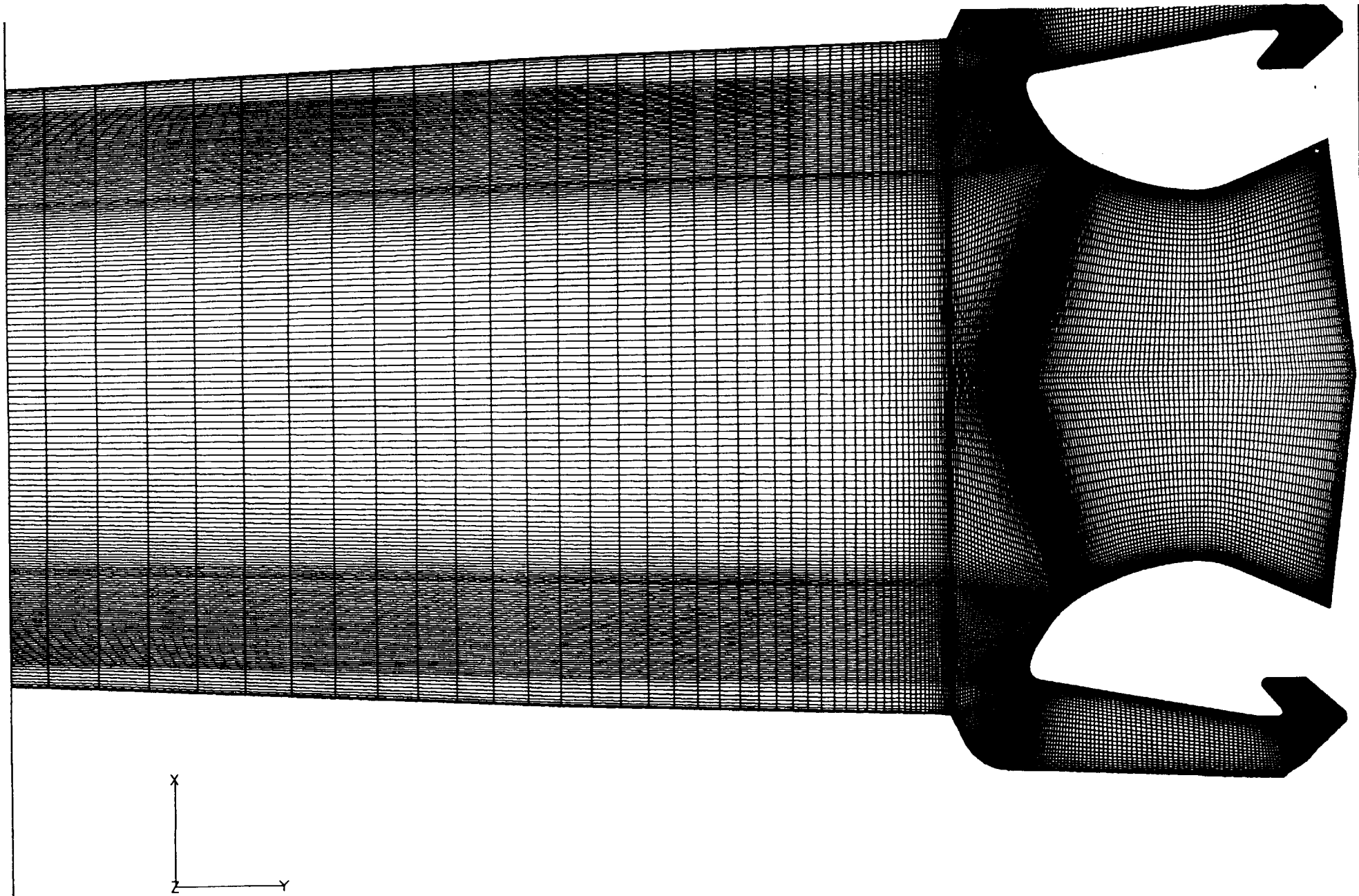

Figure 7. Full Scale RSRM, 20 Second Burn Time Grid, aft end of fourth propellant segment

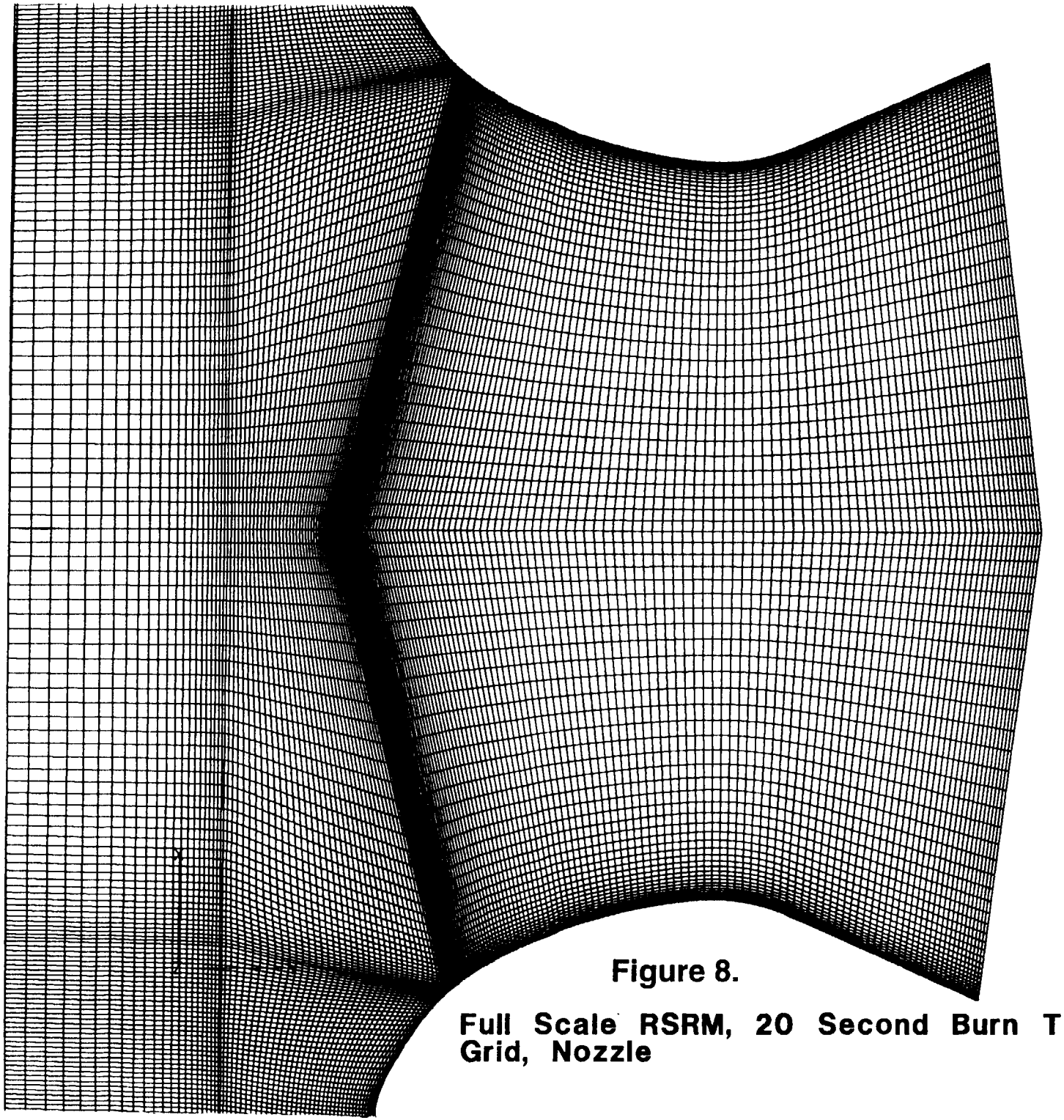

Figure 8.

Full Scale RSRM, 20 Second Burn Time Grid, Nozzle

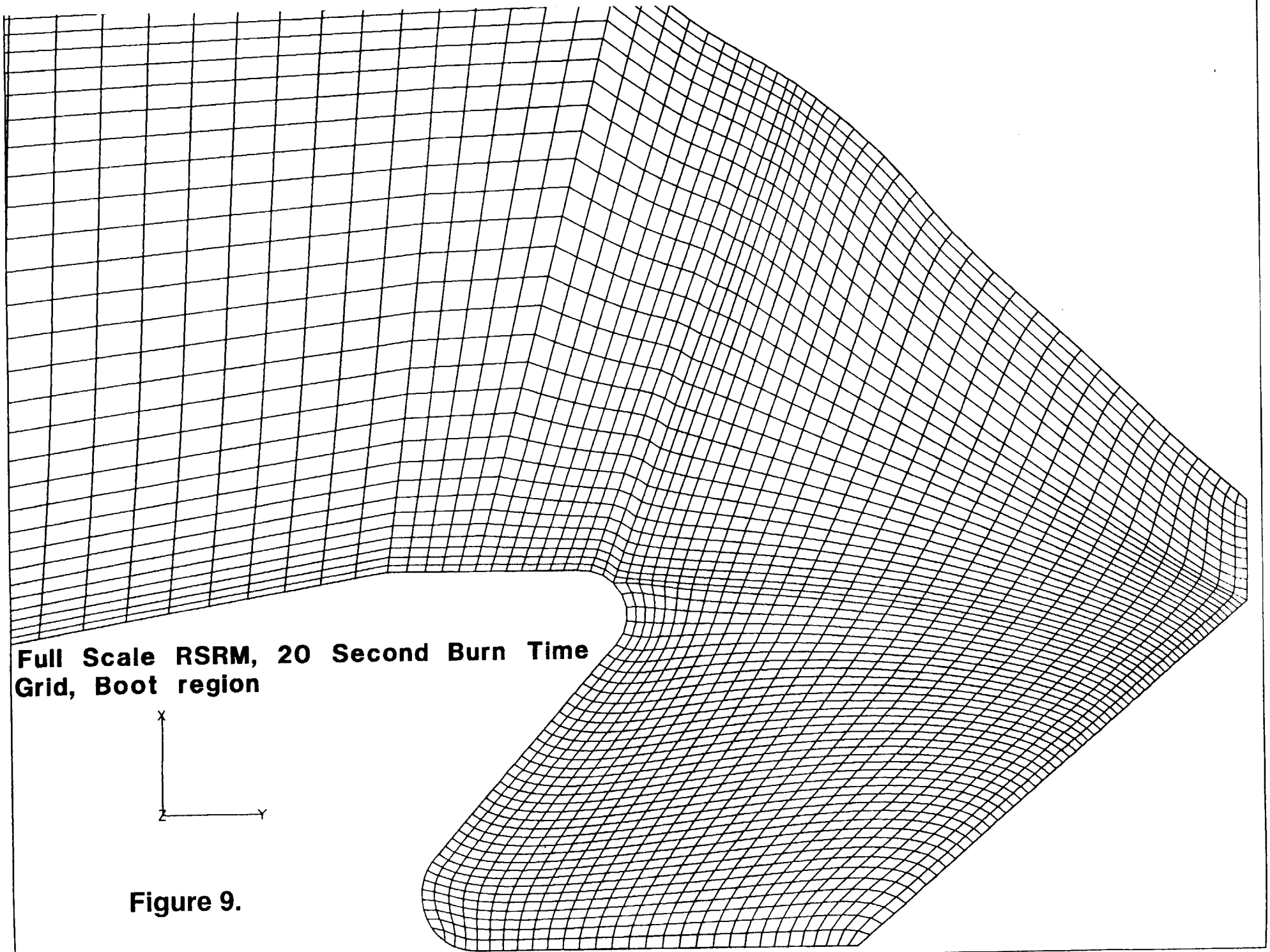

Figure 9.

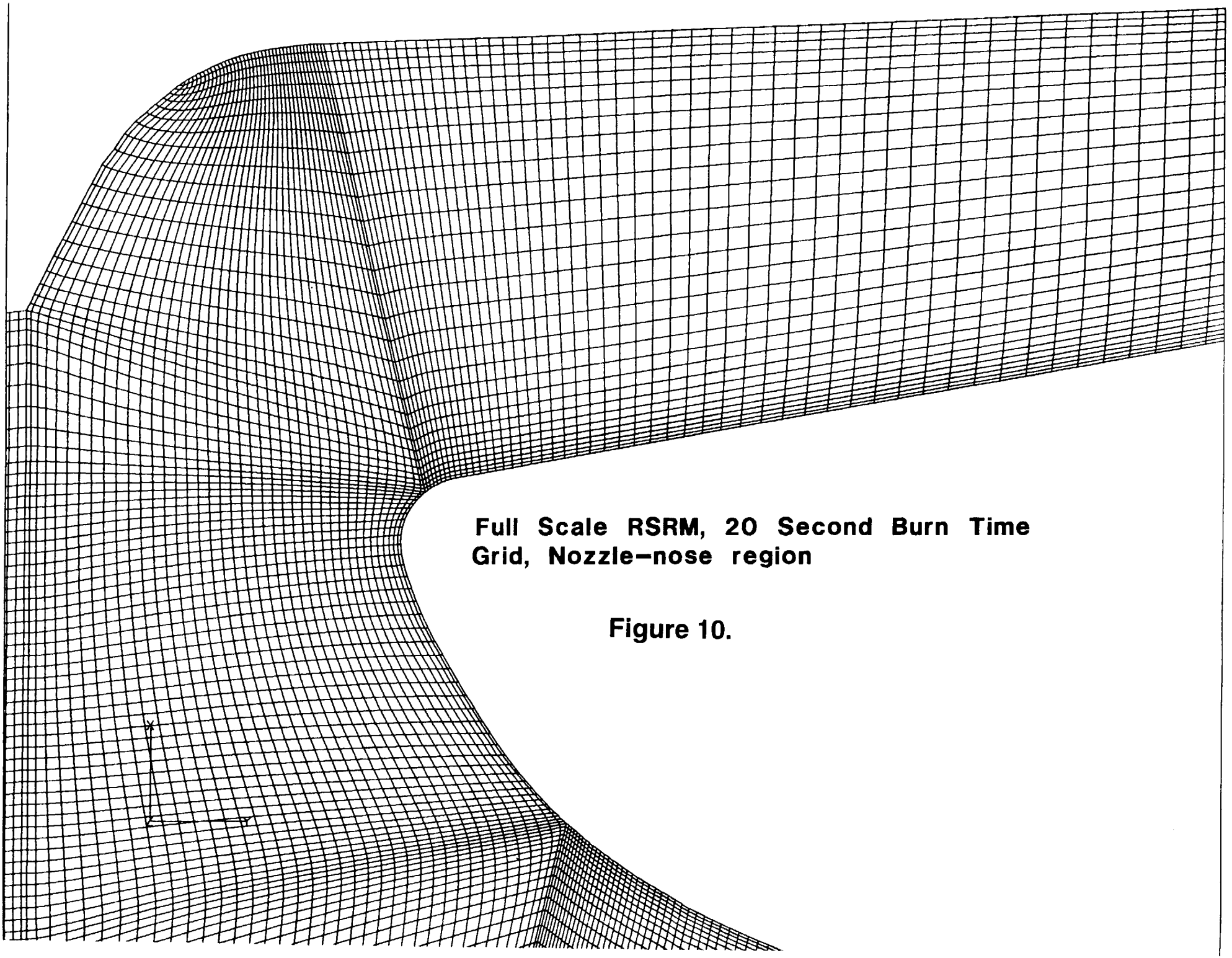

Full Scale RSRM, 20 Second Burn Time Grid, Nozzle–nose region

Figure 10.

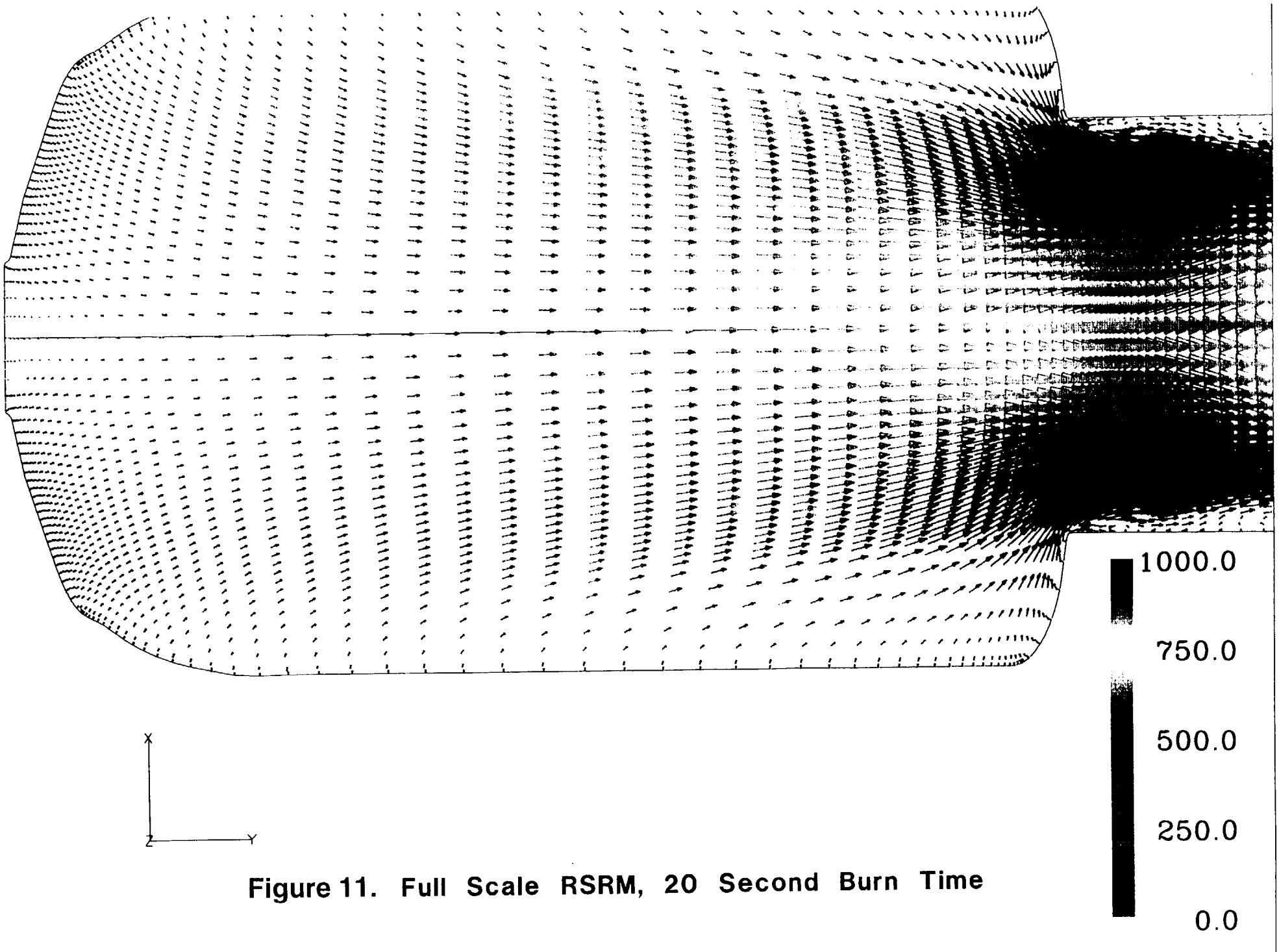

Figure 11. Full Scale RSRM, 20 Second Burn Time

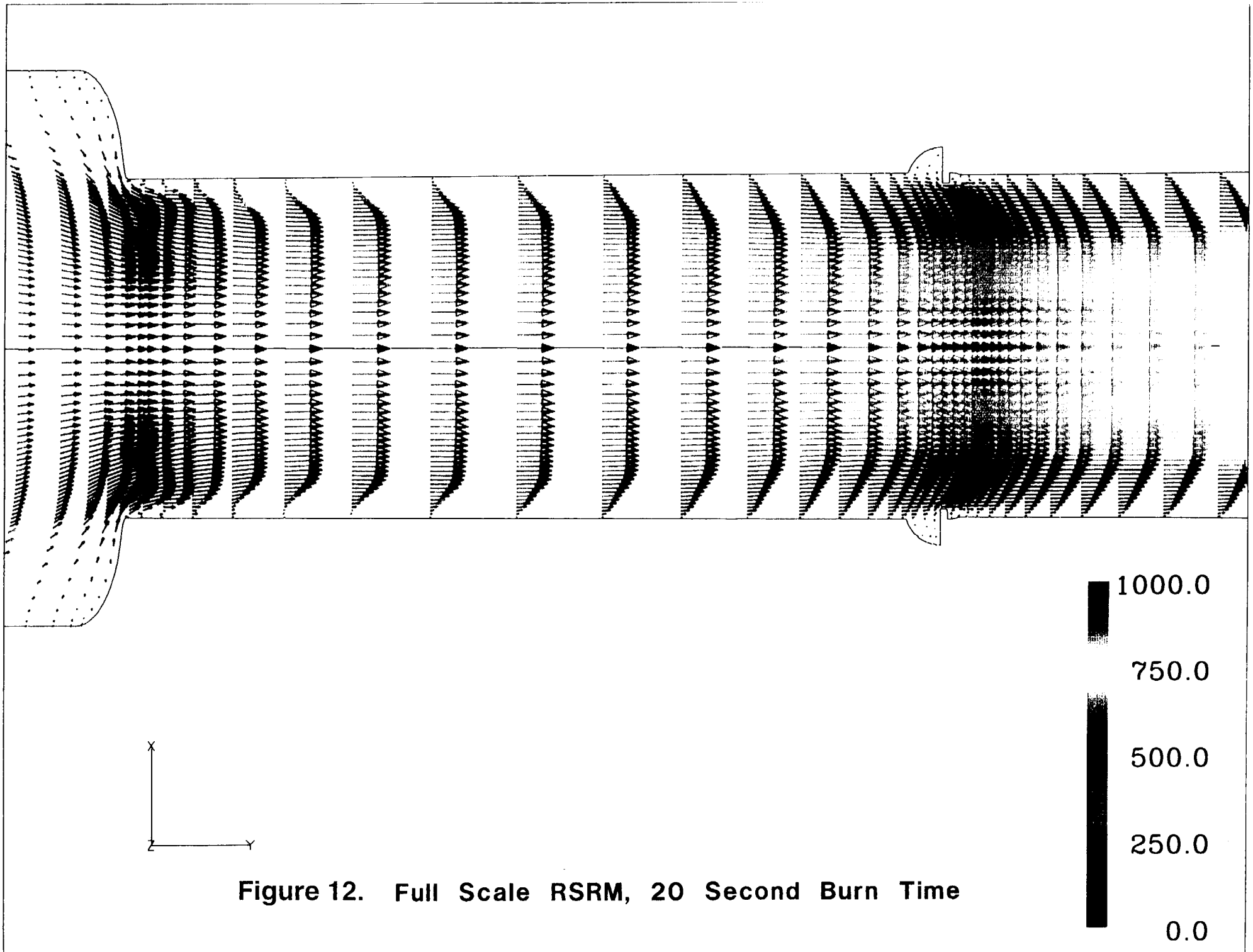

Figure 12. Full Scale RSRM, 20 Second Burn Time

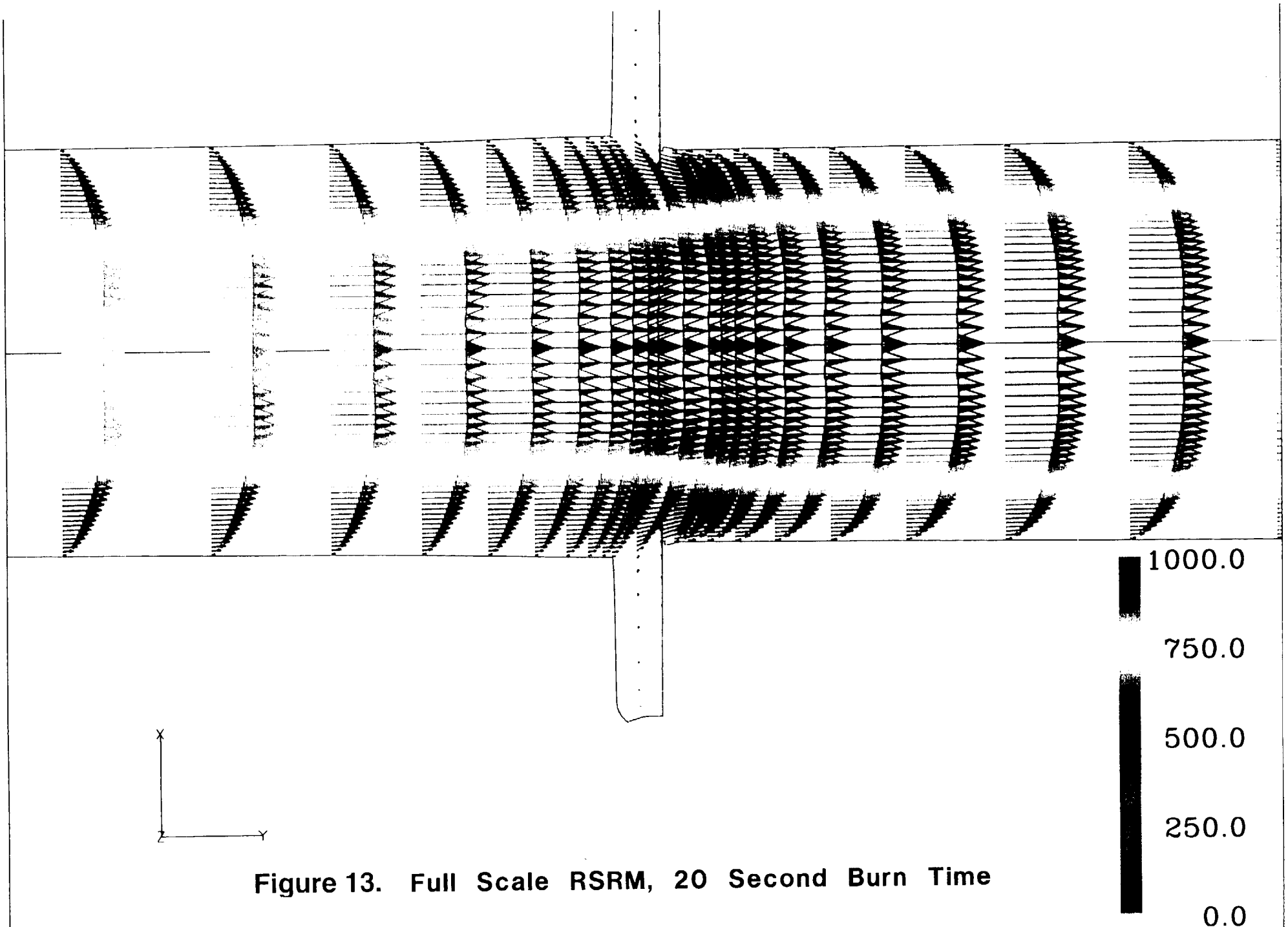

Figure 13. Full Scale RSRM, 20 Second Burn Time

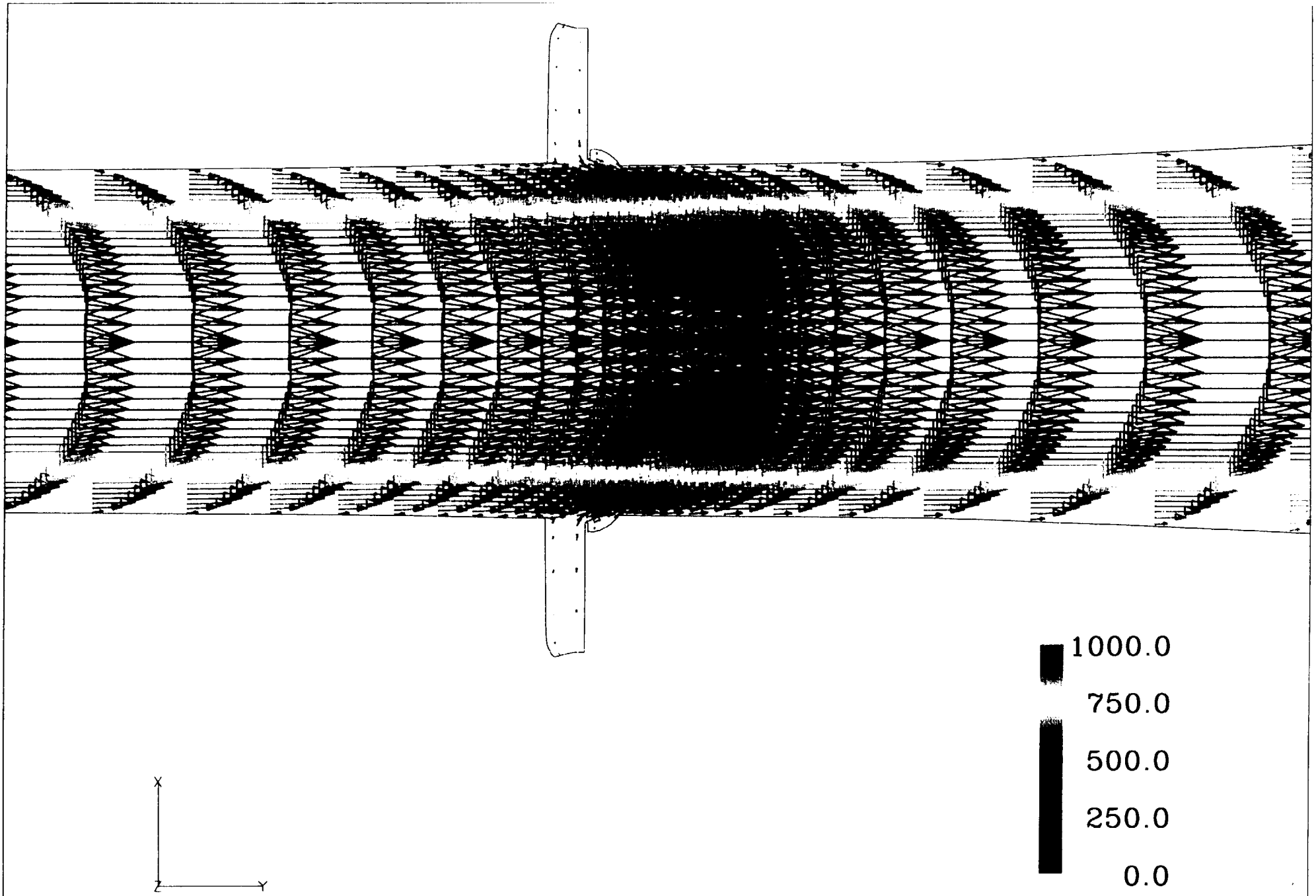

Figure 14. Full Scale RSRM, 20 Second Burn Time

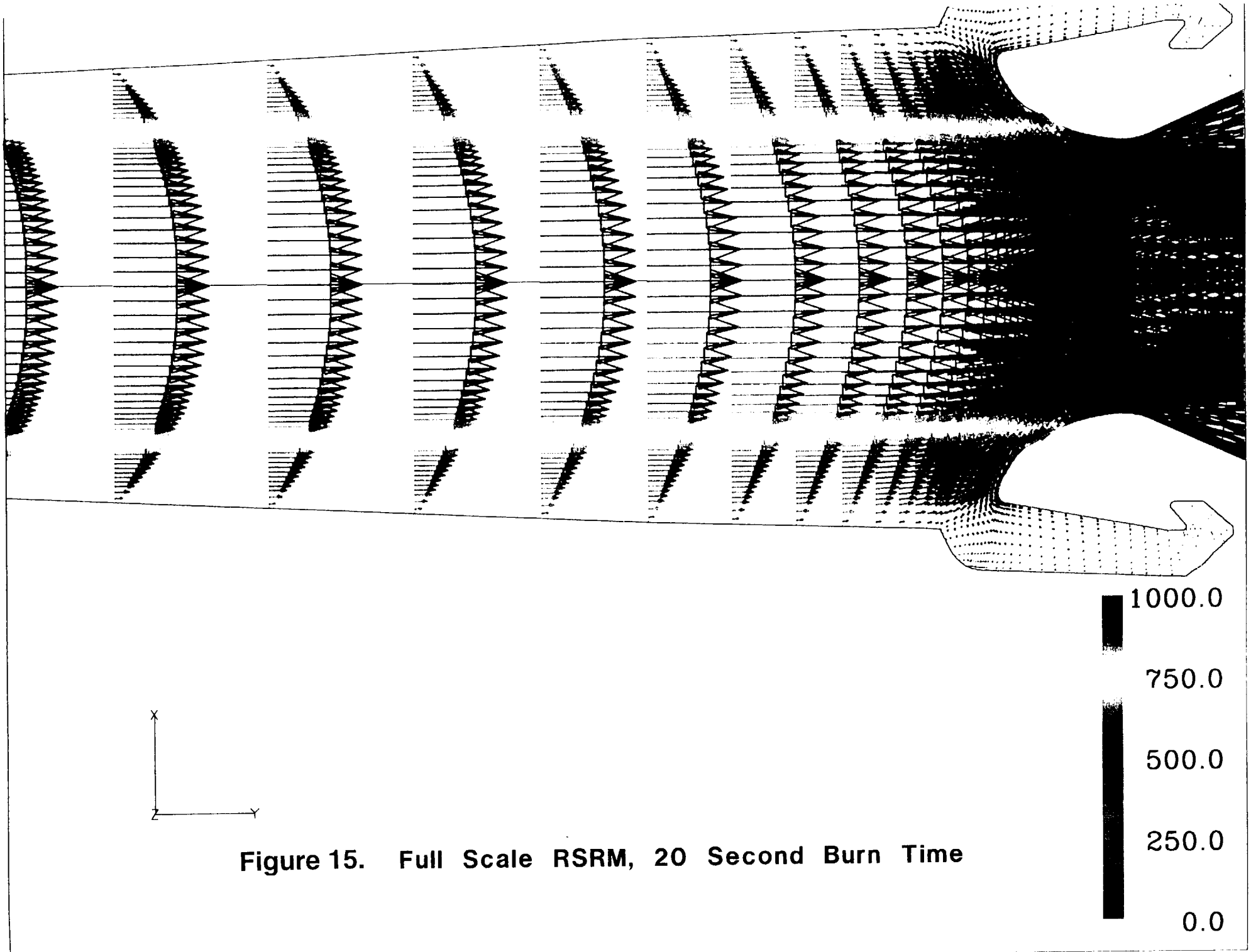

Figure 15. Full Scale RSRM, 20 Second Burn Time

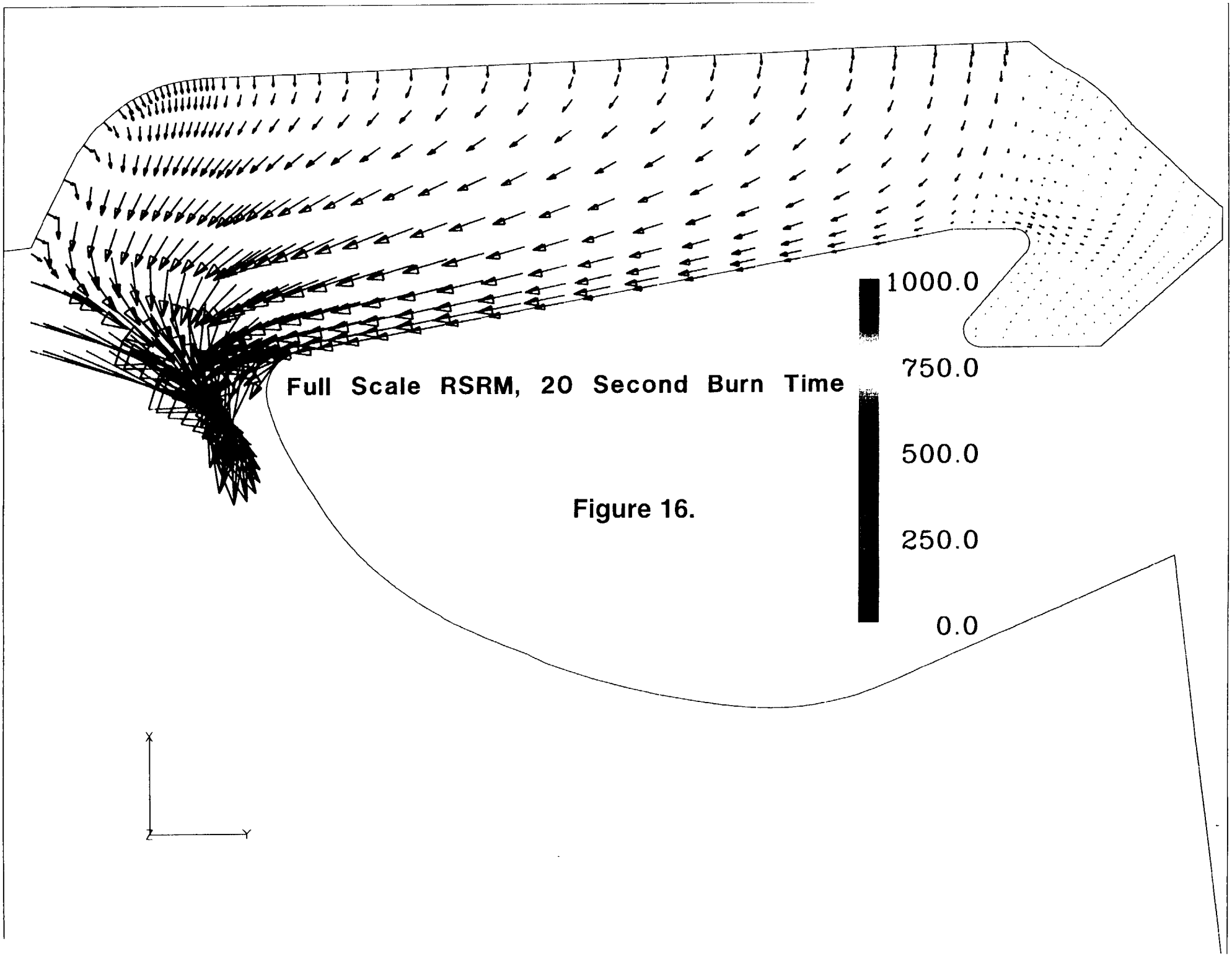
1000.0
750.0
500.0
250.0
0.0
Full Scale RSRM, 20 Second Burn Time
X
Z
Y

Figure 16.

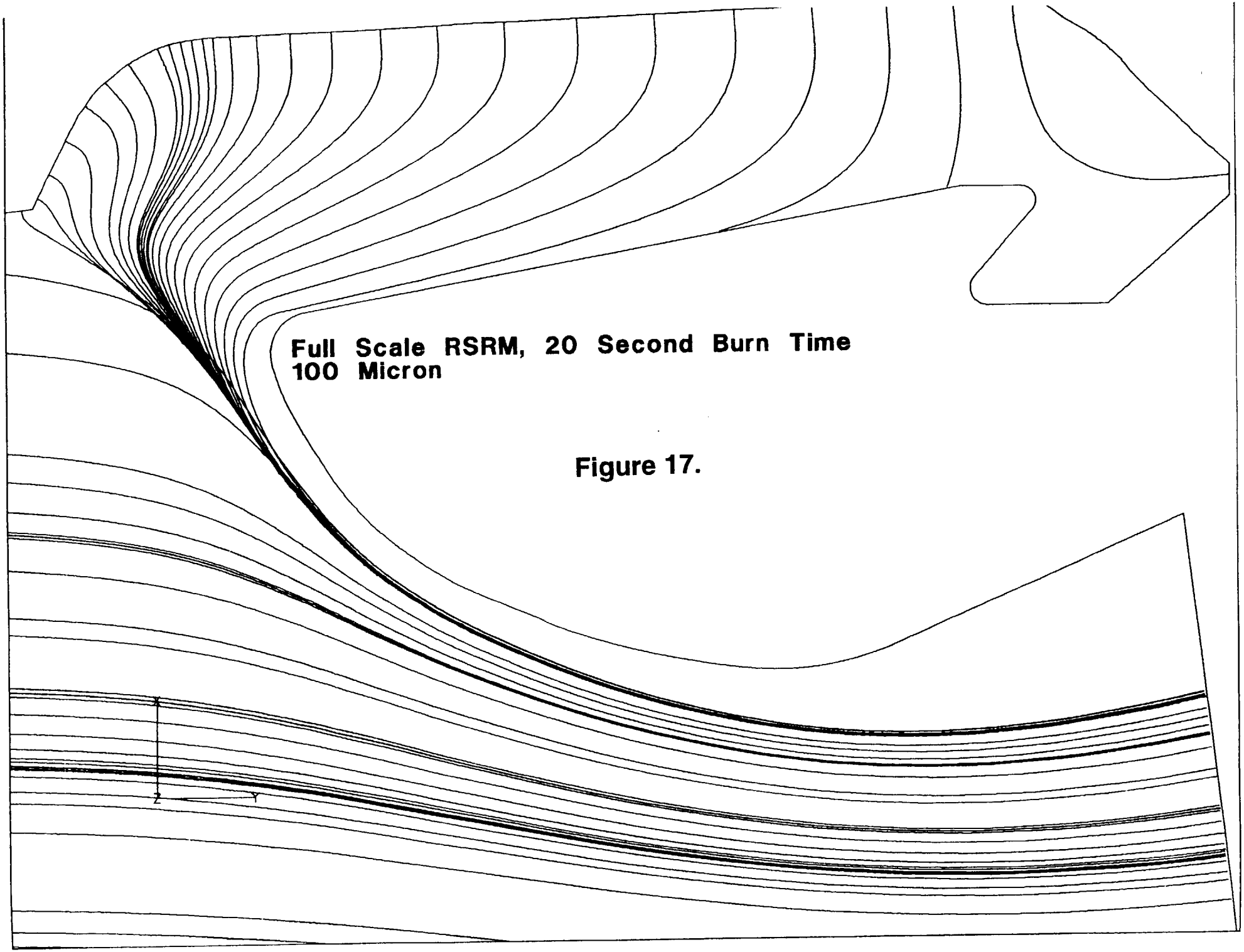

Figure 17.

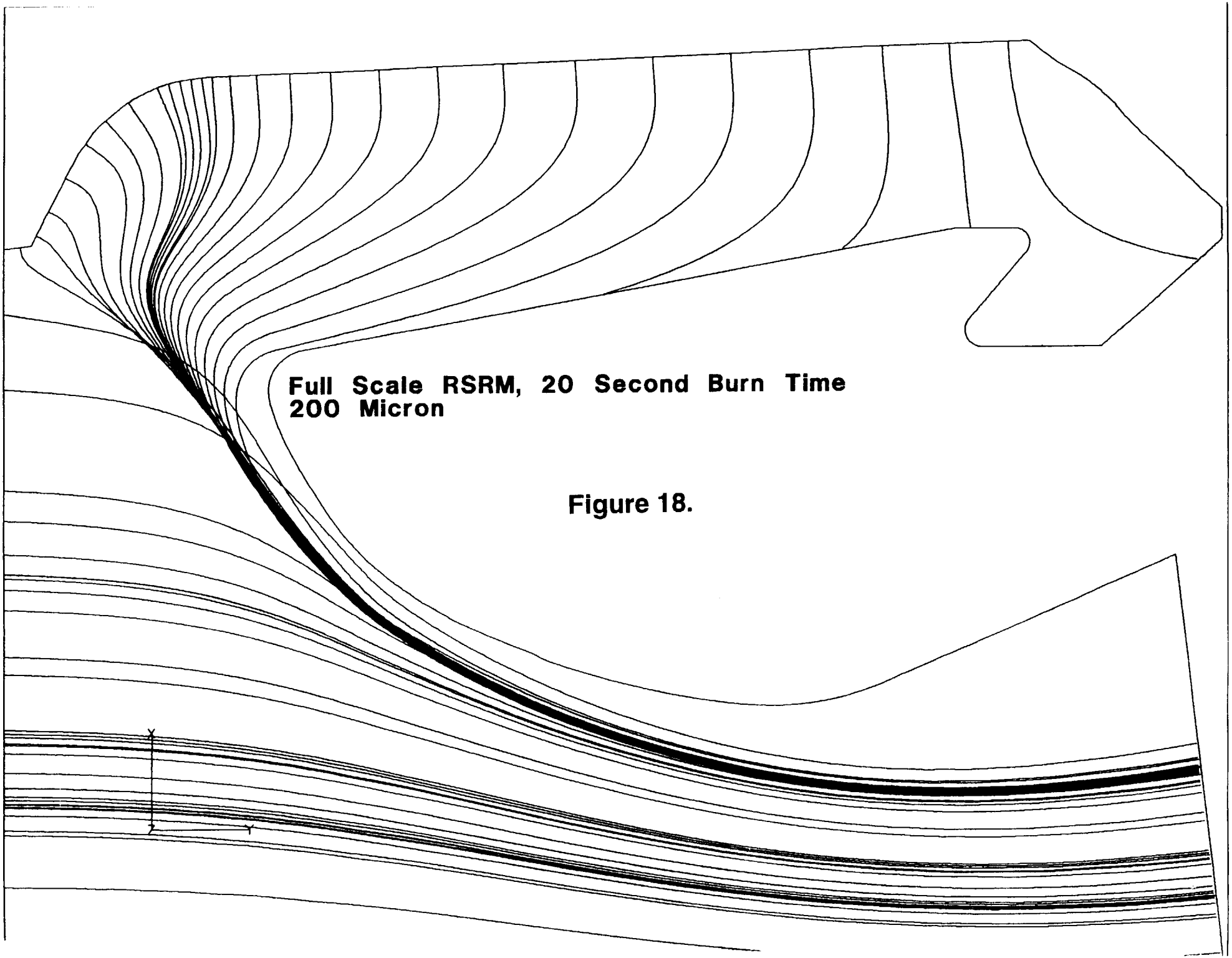

Figure 18.

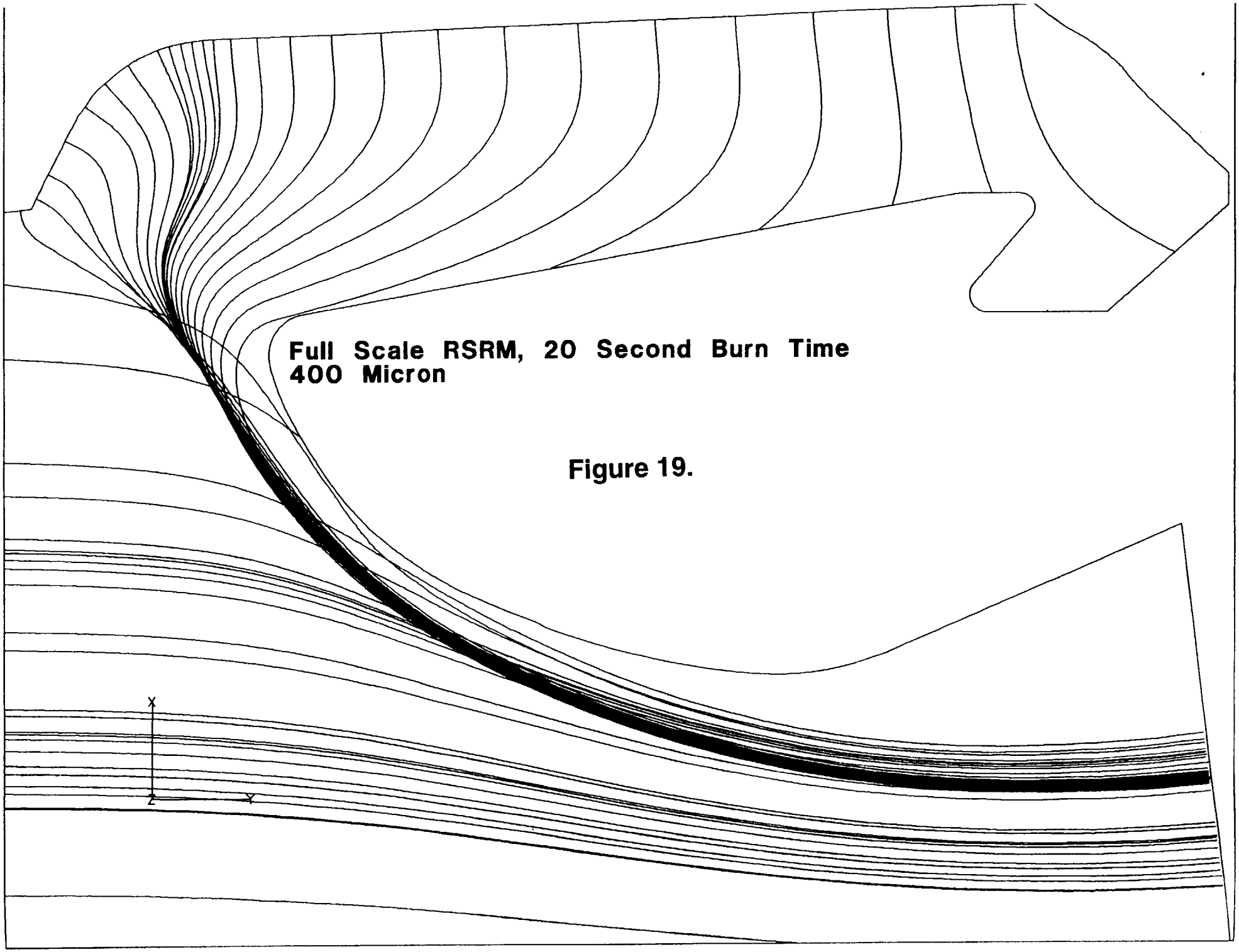

Figure 19.

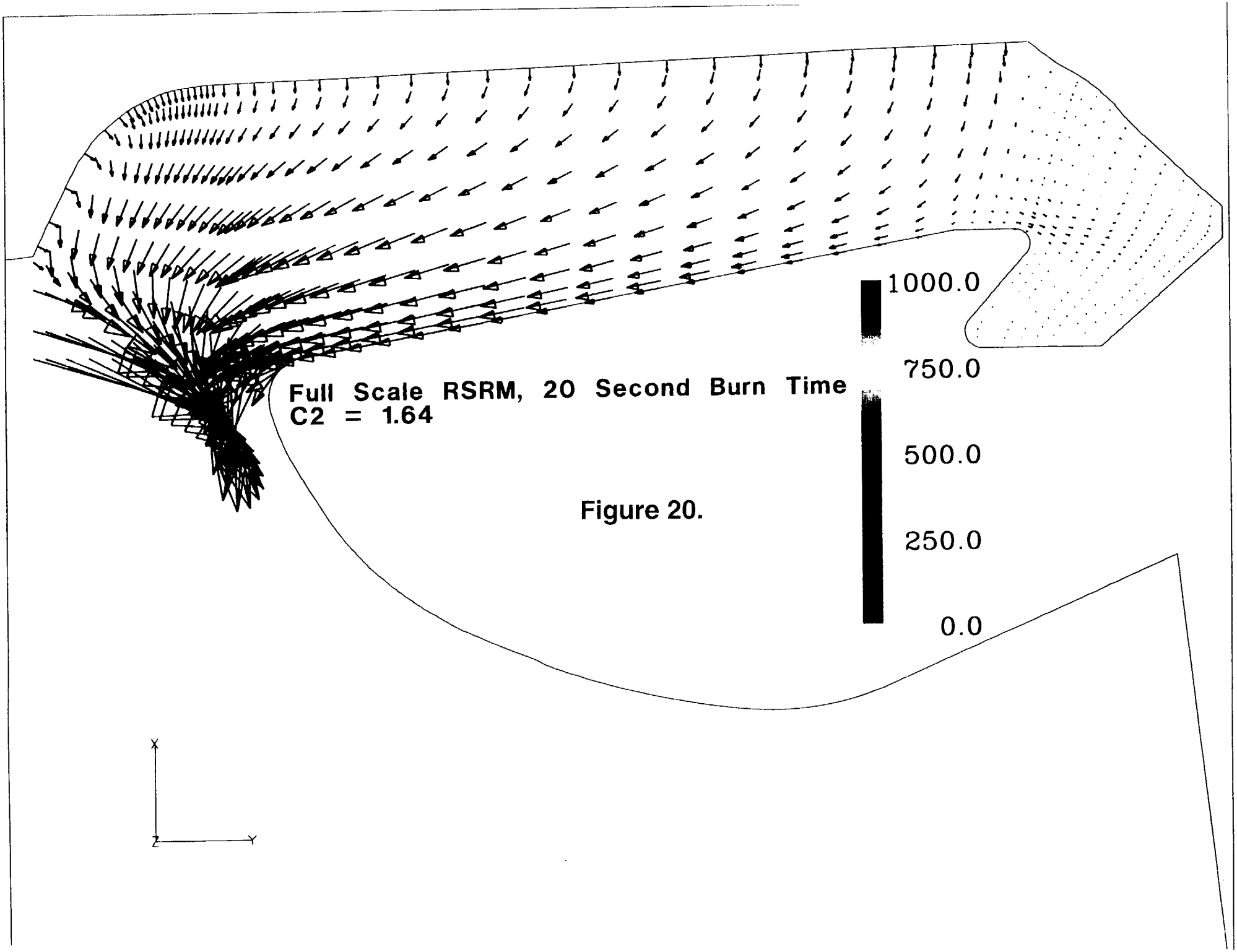
1000.0
750.0
500.0
250.0
0.0
Full Scale RSRM, 20 Second Burn Time
C2 = 1.64
X
Z
Y

Figure 20.

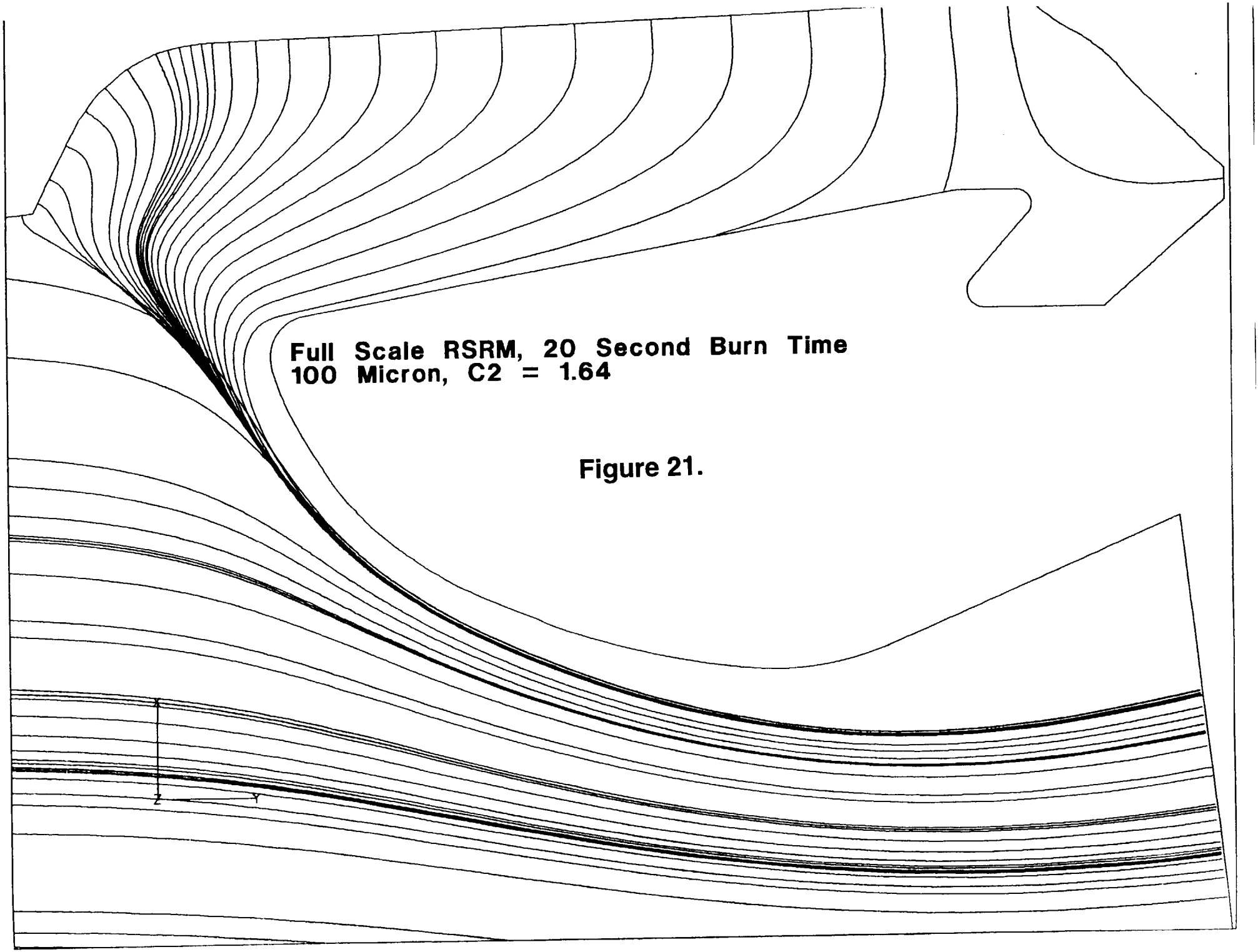

Figure 21.

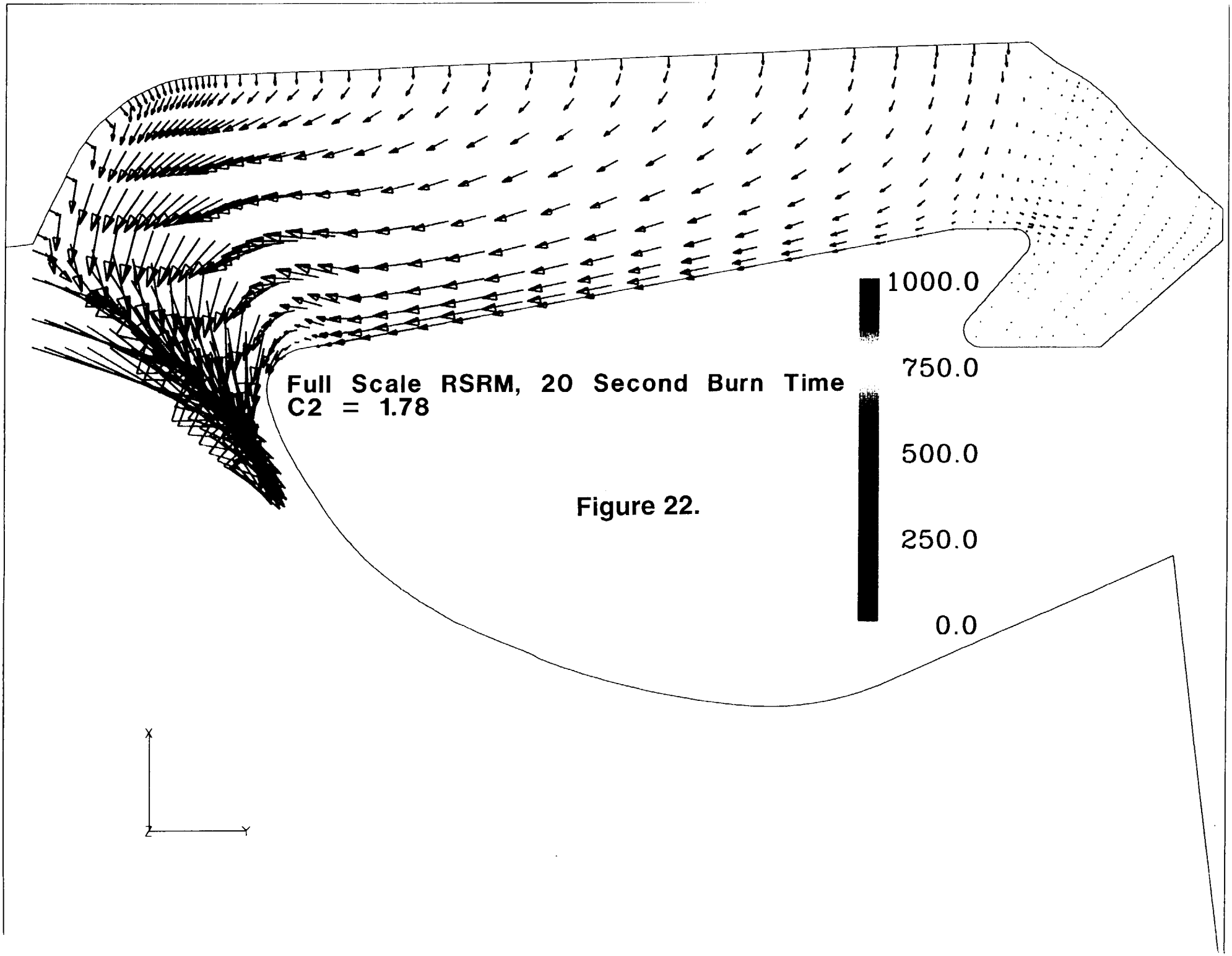
1000.0
750.0
500.0
250.0
0.0
Full Scale RSRM, 20 Second Burn Time
C2 = 1.78
X
Z
Y

Figure 22.

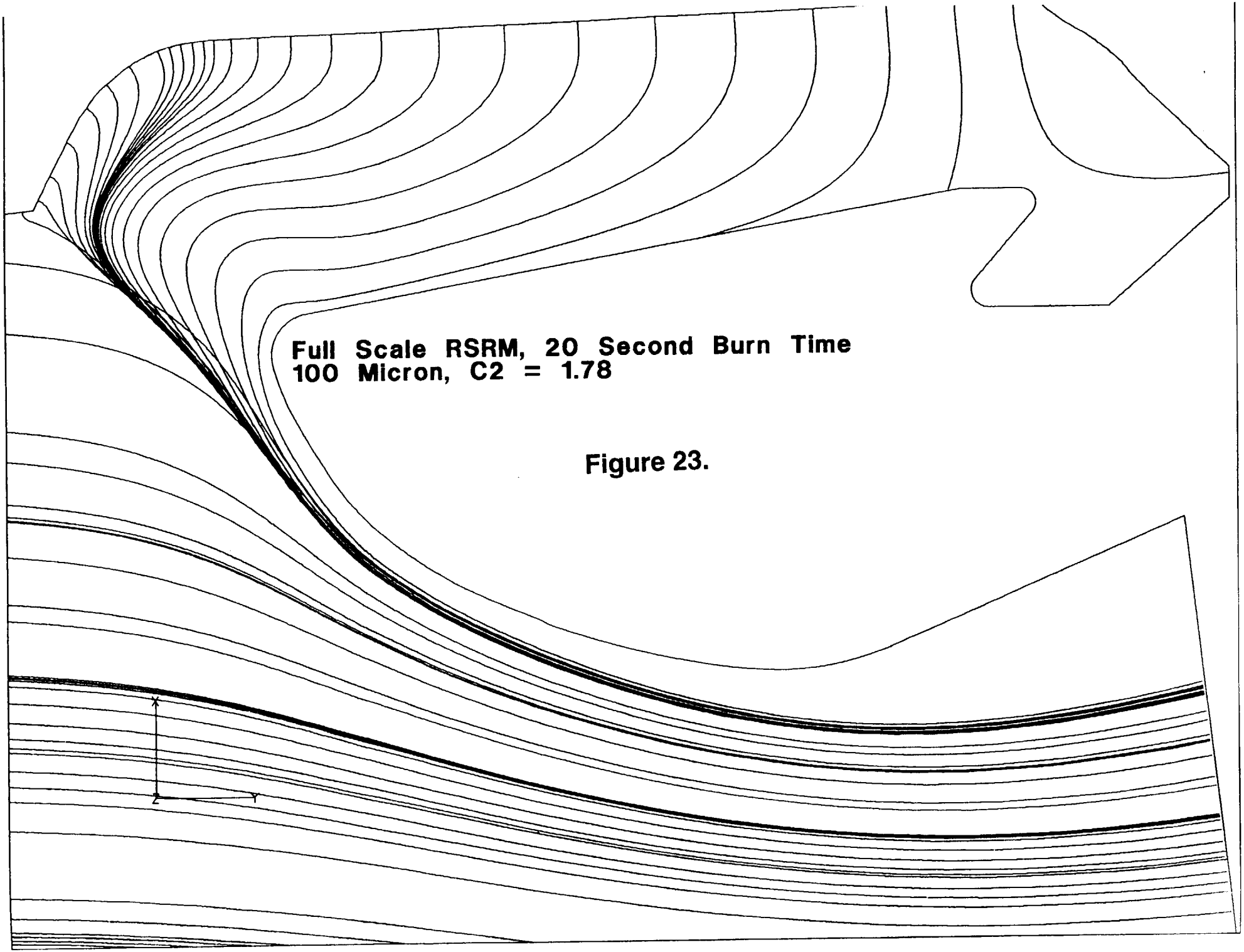

Figure 23.

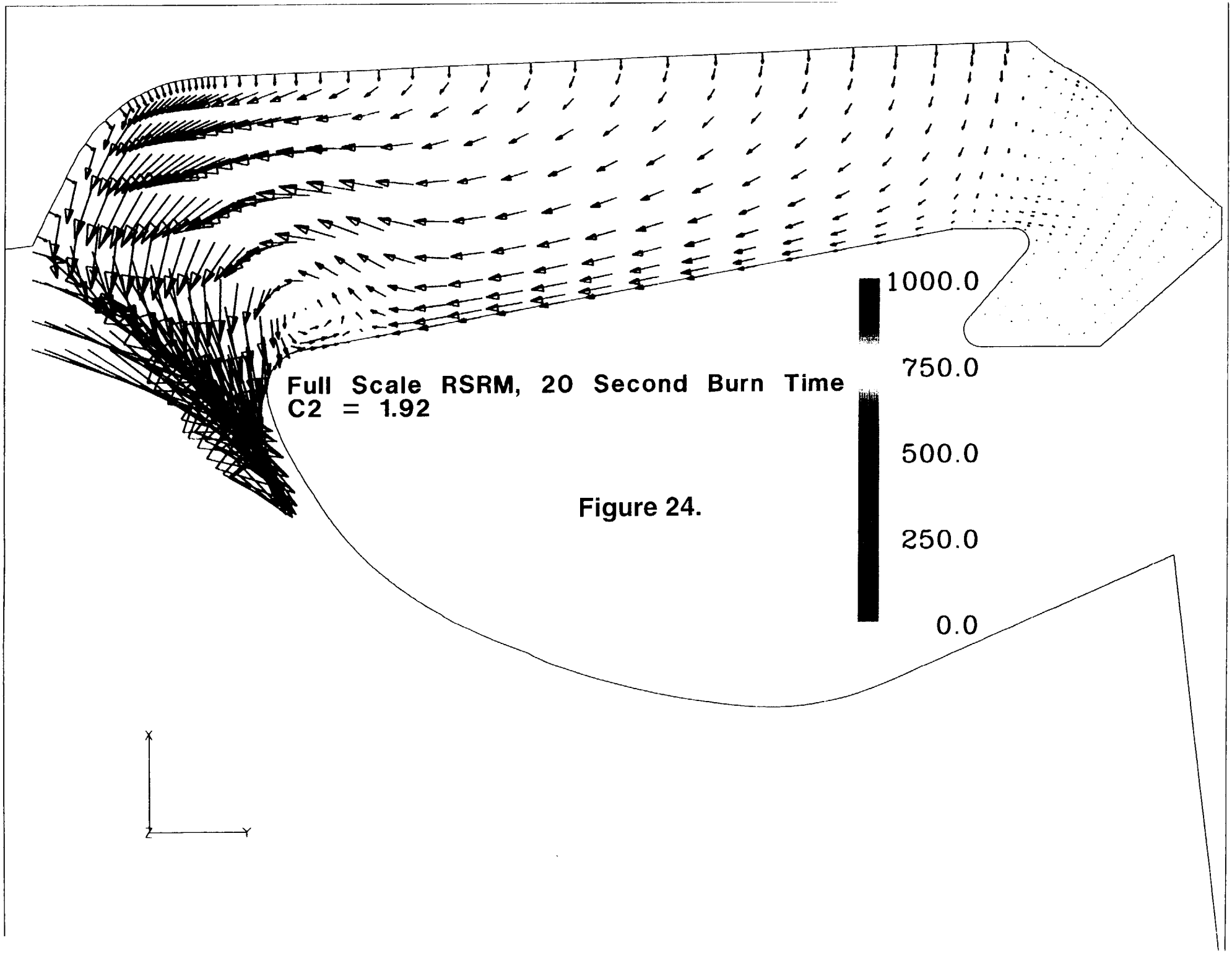
1000.0
750.0
500.0
250.0
0.0
Full Scale RSRM, 20 Second Burn Time
C2 = 1.92
X
Z
Y

Figure 24.

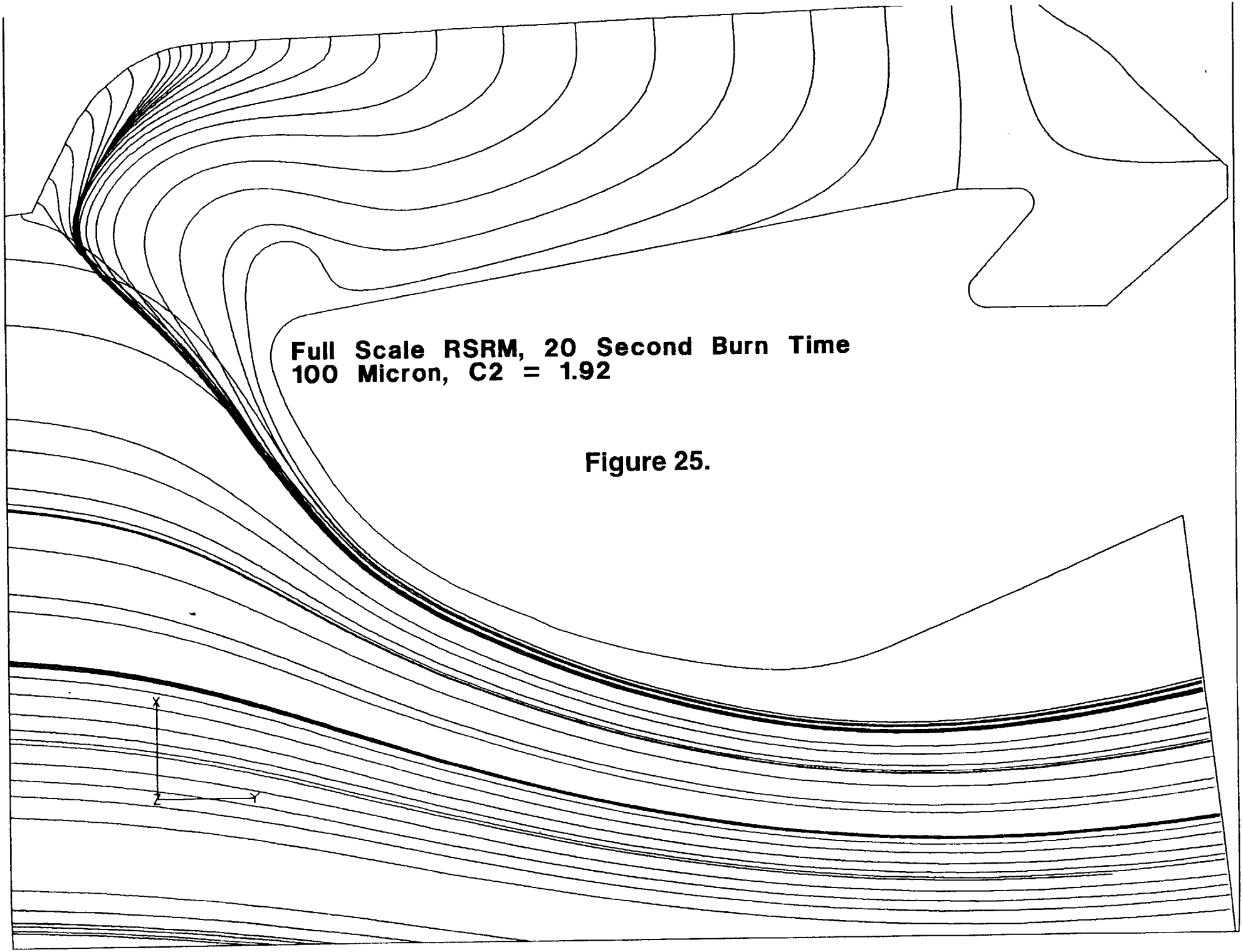

Figure 25.

4.2 RSRM Embedded Inclusion Analysis

Some form of non-propellant inclusion was found embedded in the forward segment of the RSRM-72B. ERC, Inc. performed fluid dynamic and trajectory analyses in support of the overall inclusion investigation performed by Thiokol and NASA. As with most anomaly investigations, this analysis was an evolving one in terms of the information available and the scenarios to be investigated. As more information was determined about the location, size, shape and consistency of the inclusion, the analysis was updated.

The investigation of inclusion trajectories requires the use of a full motor flow field solution. The inclusion is buried in the head end propellant and is exposed and released into the motor when the propellant burns back to the location of the inclusion. At the time the inclusion trajectory analysis was initiated, it was only known that the inclusion exposure time was somewhere between 20 and 30 seconds into motor burn. A flow field solution was available for the 33 second motor burn time. It was decided that this solution was close enough to the time of the exposure of the inclusion to provide conservative answers to the question of whether the inclusion impacts the nozzle. The answers were considered to be conservative from a motor geometry standpoint because the propellant is radially more outboard at this time than at earlier times. This would allow the inclusion to travel at a more radially outboard position which would increase the chances of impacting the nozzle.

Figure 1A shows a schematic of the 33 second burn time internal motor geometry. The inhibitors for this geometry were analyzed in the undeformed position (the normal motor fluid dynamic loads created by the motor flow field tend to bend the inhibitors in the downstream direction). The original location of the inclusion used for the initial analyses is also shown in Figure 1A. This location corresponds to a radial location from the motor centerline of 42.3 inches. The actual radial location of the inclusion was not available at the time this analysis was performed and this was a convenient location to use from an analysis standpoint because in corresponds to the end of a slither of propellant in the head end region. The forward segment fins have burned out at this time and this location corresponds to the remaining propellant left under the position where the fin originally protruded into the motor cavity. This location was also chosen because it was known to be located further radially outboard than the actual inclusion location. This more outboard radial location again supports a more conservative answer as to whether the inclusion impacts the nozzle because the inclusion is initially closer to the nozzle radial location.

The flow field solution represents a distributed combustion solution in which the aluminum particulate from the propellant is burned after being released into the motor port. The thermochemical properties at any point in the motor will therefore depend on the extent of combustion at that point. Table 4.2.1 shows the fully combusted

thermochemical properties of the propellant used for the 33 second geometry/33 second motor burn time solution.

Table 4.2.1 33 Second Geometry/33 Second Burn Time Thermochemical Properties

Thermochemical Properties	Value
Chamber Pressure (psia)	721
Flame Temperature (R)	3195
Dynamic Viscosity (lbm/ft-s)	7.4533×10^{-5}

Table 4.2.2 shows the motor flow boundary conditions used for the 33 second geometry/33 second motor burn time solution.

Table 4.2.2 33 Second Geometry/33 Second Burn Time Mass Flow Rates

Propellant Segment	Mass Flow Rate
Forward Segment (lbm/sec)	3328
Forward Center Segment (lbm/sec)	2233
Aft Center Segment (lbm/sec)	2219
Aft Segment (lbm/sec)	2760
Total Flow (lbm/sec)	10540

At the time of the earliest analysis many of the properties describing the inclusion were not known. Estimates of these properties were obtained from various sources and used in this initial analysis. The candidate composition materials considered for the inclusion were aluminum and RTV. The densities used for these materials were:

$$\rho_{RTV} = 66.80 \text{ lbm/ft}^3$$
$$\rho_{Aluminum} = 175.0 \text{ lbm/ft}^3$$

A spherical particle was initially used to model the inclusion. The drag force on the inclusion was evaluated via the commonly used empirical correlation:

$$F_p = (1/8)C_D\rho\pi D_p^2|V_R| V_R$$

Where D_p is the effective spherical diameter of the inclusion and ρ is the gas density. The drag coefficient C_D is given by

$$C_D = (24/Re_p)\{1 + 0.15\, Re_p^{0.687}\} \qquad \text{for } Re_p < 1000$$

$$C_D = 0.438 \qquad \text{for } Re_p < 1000$$

Here the spherical particle Reynolds number Re_p is given by

$$Re_p = \rho|V_R|D_p/\mu$$

and the relative velocity between the inclusion and the combustion gas, V_R, is given by

$$V_R = |V_g - V_p|$$

with, V_p, the inclusion velocity and, V_g, the gas velocity. The dynamic viscosity in the particle Reynolds number is μ.

Spherical diameters of 0.5 and 1.0 inches were considered. No lateral or axial g-force was applied to the inclusion. The effects of two different initial velocities were considered. These initial velocities were either $1.0*V_{gas}$ (Where V_{gas} is the propellant gas injection velocity in the head end) or $0.2*V_{gas}$. The results of this initial analysis showed that under these conditions the inclusion did not collide with either the propellant grain or the nozzle.

Trajectories were then computed for the inclusion under the same conditions as discussed in the previous paragraph but with 1.0 g's of lateral acceleration applied to the inclusion. This analysis showed that for all the parameters considered, the inclusion collided with the nozzle or collided with the propellant grain in the head end. This analysis showed that a more precise estimate of the lateral and axial g-forces was required to properly access the disposition of the inclusion.

In this phase of the analysis, the flight accelerations at a motor burn time of 20 seconds were applied to the inclusion. These were 1.925 g's in the axial direction and 0.194 g's in the lateral direction. The initial inclusion velocity was taken as $0.2*V_{gas}$. In addition, steel was added to the list of possible inclusion materials. The inclusion was analyzed as a spherical particle and Table 4.2.3 shows the inclusion material density and effective spherical diameter as supplied by Thiokol and used in the analysis.

Table 4.2.3 Thiokol Supplied Effective Inclusion Diameter and Density

Material	Diameter, in.	Density, lbm/ft^3
Steel	0.466	488.8
Aluminum	0.634	168.4
RTV Rubber	0.857	64.83

This portion of the inclusion trajectory analysis showed that the inclusion (whether composed of RTV, steel or aluminum) did not collide with the nozzle under the conditions tested. Figure 2A shows the RTV inclusion trajectory. Figure 3A shows the

aluminum inclusion trajectory, which passes slightly closer to the nozzle than the RTV inclusion and Figure 4A shows the steel inclusion trajectory which passes closest to the nozzle of the three inclusion materials. Table 4.2.4 shows a summary of the trajectory analysis. This information was supplied to NASA and Thiokol to be used in further analysis related to the impact energy released if the inclusion collides with the nozzle.

Table 4.2.4 Summary of 33 Sec. Geometry/33 Sec. Burn Time Trajectory Analysis

		Materials	
Parameter	Steel	Aluminum	RTV Rubber
Velocity at Nozzle Nose (ft/s)	410.8	527.5	626.3
Relative Velocity @ Nose (ft/s)	905.4	907.8	845.7
Time to Nose Tip (sec)	1.20	1.10	1.03

The next phase of the analysis updated several of the original approximations used in the trajectory analysis. It was determined that the time at which the inclusion was exposed and released from the propellant grain was 20 seconds into motor burn. In order to conserve the analysis time required to create a 20 second motor burn time computational grid, the original 33 second burn time computational grid was used along with the motor flow rate boundary conditions at the 20 second motor burn time. This methodology allows a solution to be obtained for the higher flow rates occurring at the 20 second burn time in the most time efficient manner. The trajectory analysis is still conservative because the 33 second burn time geometry propellant surfaces are further outboard radially than the 20 second geometry. The new mass flow rate boundary conditions at the propellant surface are given in Table 4.2.5.

Table 4.2.5 33 Second Geometry/20 Second Burn Time Mass Flow Rates

Propellant Segment	Mass Flow Rate
Forward Dome (lbm/sec)	4380.0
Forward CP (lbm/sec)	1044.0
Forward Center Segment (lbm/sec)	2149.0
Aft Center Segment (lbm/sec)	2127.2
Aft Segment (lbm/sec)	2670.0
Total Flow (lbm/sec)	12370.2

Figure 5A shows the velocity field in the head end dome region of the motor computed for the 20 second burn time flow rate/33 second burn time geometry configuration. The end of the propellant is visible in the head end of the motor by observing the locations that have a velocity component normal to the surface. There is a small recirculation region near the motor head end centerline created by the absence of propellant in the forward end of the dome. The major direction of motion of the propellant gases is

toward the motor port at the far right end of the figure. Figure 6A shows a color raster plot of the velocity field in the motor. The maximum velocity is 8373 ft/sec at the nozzle exit but this figure has a maximum total velocity scale of 1100 ft/sec in order to better show the increase in velocity in the motor port. The figure shows that the velocity increases rapidly as the propellant gases pass from the dome region to the smaller diameter motor port where the forward grain is located. The figure also shows that the velocity continues to increase as flow moves toward the motor nozzle with the exception that there is a region along the aft grain where there is a decrease in velocity near the propellant surface due to the outboard flare in the geometry of the aft grain. The strong radial gradient in the port is also visible in the nozzle region shown in the figure. This radial gradient is created by the geometry of the submerged cavity behind the nozzle and the smaller diameter nozzle, which accelerates the axial flow. Figure 7A shows the velocity field in the submerged nozzle region. The port flow is rapidly turned toward the motor centerline as flow moves toward the nozzle nose. The flow in the submerged cavity is stagnant in comparison to the flow velocities near the mouth of the cavity.

The flight accelerations used are the same as used in the previous analysis (1.925 g's axial and 0.194 g's lateral). The initial velocity of the inclusion is also the same as previously used (0.2 x normal gas injection velocity previously computed, 1.9 ft/sec.). The radial location of the inclusion was updated for this and the remainder of the analyses presented in this monthly report. The updated radial location of 24.8 inches outboard of the motor centerline was used. This was obtained from Thiokol.

Trajectory analyses for a spherical steel, aluminum and RTV inclusion were performed using the Thiokol supplied effective diameter and density for the inclusions as given in Table 4.2.6. Trajectory analyses for rectangular steel, aluminum and RTV inclusions were also performed. For the rectangular inclusion calculations it was assumed that the inclusion frontal area was the average of the area of the largest and smallest sides of the rectangle. This is an approximation to the average frontal area of a tumbling rectangular inclusion. The Thiokol supplied height, width and thickness for the inclusions were used as given in Table 4.2.6.

Table 4.2.6 Thiokol Supplied Height, Width and Thickness of Inclusions

Material	Height, in.	Width, in.	Thickness, in.
Steel	2.25	0.523	0.045
Aluminum	2.25	0.523	0.113
RTV Rubber	1.00	0.523	0.280

A C_D = 1.18 was used for the drag coefficient of the rectangular inclusion. This was determined from the reference book, "Fluid-Dynamic Drag" by Sighard F. Hoerner. This value was validated by comparison to several other sources and experimental data. Given this drag coefficient, the equivalent spherical diameter for the inclusion that must

be used in the CFD code can be computed by making the frontal areas for the rectangle and the equivalent sphere the same. In this way the drag coefficient will be used correctly to compute the drag force for the inclusion. The effective spherical diameter of the inclusions computed in this way is shown in Table 4.2.7.

Table 4.2.7 Thiokol Supplied Height, Width and Thickness of Inclusions

Material	Diameter, in.	Density, lbm/ft^3
Steel	1.224	26.958
Aluminum	1.224	23.322
RTV Rubber	0.816	33.371

The equivalent density for the Thiokol prescribed weight of the inclusion must also be computed by computing the volume of the rectangular inclusion and using the Thiokol prescribed weight of the inclusion to compute the density. Table 4.2.7 also shows the value of the equivalent density for the inclusions.

The spherical steel inclusion passes to within 11.5 inches of the nozzle while the rectangular steel inclusion passes to within 25.5 inches of the nozzle. The rectangular steel inclusion remains much closer to the motor centerline. This result is due to the fact that the larger drag of the rectangular inclusion causes it to accelerate much faster and achieve a larger axial velocity. The larger axial acceleration means that the flight time of the rectangular inclusion is smaller and thus there is less time for the radial velocity component to act on the inclusion and push it toward the nozzle. The ratio of the axial-to-radial velocity component for the rectangular inclusion is greater than for the spherical inclusion. This means that the rectangular inclusion axial velocity component dominates the determination of the trajectory of the inclusion, which also translates to less movement away from the motor centerline. The spherical aluminum inclusion passes to within 17.1 inches of the nozzle while the rectangular aluminum inclusion passes to within 26.2 inches of the nozzle. The aluminum inclusions remain closer to the centerline than the steel inclusions because of their smaller mass. The flight time of the aluminum inclusion is slightly less than the steel inclusion and the maximum axial velocity of the aluminum inclusion greater. The RTV inclusion trajectory remains closest to the motor centerline of all the inclusions and has the greatest axial velocity at the nozzle nose. The spherical RTV inclusion passes to within 20.6 inches of the nozzle while the rectangular RTV inclusion passes to within 26.2 inches of the nozzle. Table 4.2.8 summarizes several important quantities of the spherical inclusions at the axial station corresponding to the nozzle nose. Table 4.2.9 summarizes these same quantities for the rectangular inclusions at the axial station corresponding to the nozzle nose.

Table 4.2.8 Summary of Spherical Inclusion Trajectory Analysis

		Materials	
Parameter	**Steel**	**Aluminum**	**RTV Rubber**
Velocity at Nozzle Nose (ft/s)	469.1	585.1	677.7
Relative Velocity @ Nose (ft/s)	935.0	878.2	806.1
Time to Nose Tip (sec)	1.082	0.987	0.919

Table 4.2.9 Summary of Rectangular Inclusion Trajectory Analysis

		Materials	
Parameter	**Steel**	**Aluminum**	**RTV Rubber**
Velocity at Nozzle Nose (ft/s)	847.3	860.6	864.6
Relative Velocity @ Nose (ft/s)	659.9	650.4	646.5
Time to Nose Tip (sec)	0.804	0.797	0.795

None of the inclusions, whether spherical or rectangular, collided with the nozzle under the conditions analyzed.

An analysis was performed to examine whether an aluminum inclusion would completely burn during its flight time prior to reaching the nozzle nose. It was conjectured that the thickness of aluminum burned on a spherical particle might remain approximately constant regardless of the particle diameter. A preliminary analysis was performed which confirmed this conjecture. Spherical particles ranging in diameter from 1000 to 16000 μm were flown down the motor port and burned. The volume of the particles was fixed by the diameter of the particle and the formula for the volume of a sphere. The mass of the particle was computed from a common density for all the particles. The particles were then flown down the motor and allowed to burn. The final mass of unburned aluminum in each particle was used to compute the final diameter of the aluminum in the particle and the initial and final diameters were subtracted and divided by two to obtain the thickness of the aluminum burned. The thickness of aluminum burned remained constant for all the particles of different diameter within a few percent. Since this result is true, even though the code burns a spherical particle, it can be used to compute a thickness of aluminum that would be burned over the flight of a rectangular inclusion. Trajectories for the burning aluminum inclusion with both a spherical and rectangular drag coefficient were considered.

A package of plots describing the analysis of the burning spherical inclusion along with summary Table 4.2.10 was given to NASA and Thiokol. The package of figures contained the trace of the inclusion trajectory and several properties of the inclusion as a function of flight time including: the axial velocity of the inclusion, the relative velocity

of the inclusion, the percentage of aluminum burned, the diameter of the inclusion, the axial position of the inclusion and the total mass of the inclusion. Figure 8A shows the trajectory of the burning spherical inclusion. The trajectory differs only slightly compared to the non-burning trajectory. Figure 9A, the axial velocity of the inclusion, shows that most of the flight time of the inclusion is spent in the head end of the motor. The inclusion remains in the forward segment region for 0.65 seconds of the total flight time of 0.98 seconds. This is more than half of the total inclusion flight time. The axial velocity increases linearly until the inclusion reaches the forward grain port region. It is in this region that the axial velocity begins to rapidly due to the larger axial velocities in the motor port. By the time the inclusion reaches the forward inhibitor, about 0.77 seconds of the total flight time of has elapsed. The increasing axial velocity in relation to the lower radial velocity of the inclusion causes the inclusion to have a shorter residence time in motor from the forward inhibitor to the nozzle throat. Therefore, it is seen that the rapidly increasing axial velocity of the inclusion is the most important factor in keeping the inclusion from colliding with the nozzle. Figure 10A shows the progression of how much aluminum is burned in the inclusion from the head end to the throat. The diameter of the inclusion does not change much due to the characteristics of the burning aluminum. The initial inclusion diameter was 0.634 inches and the final inclusion diameter was 0.623 inches. The burning aluminum in the inclusion produces aluminum oxide which has a lower density than the original aluminum due to the fact that there is much more air space in the aluminum oxide than the original aluminum. According to the burning characteristics observed for aluminum burning in an experimental quench bomb, 28.3% of the aluminum that burns remains on the inclusion as aluminum oxide. Additional mass is also picked up from the combustion gases in the motor by the inclusion in the form of the oxygen in the aluminum oxide. These combined effects produce the observed inclusion diameter. There is some loss of mass in the inclusion as it burns. The analysis showed that 53.2% of the aluminum in the inclusion burned.

Table 4.2.10 Burning of the Spherical Aluminum Inclusion (0.634 in. Diameter)

Property	Initial Value	Final Value
Inclusion Mass (lbm.)	1.130×10^{-2}	9.757×10^{-3}
Inclusion Diameter (in.)	0.634	0.623
Aluminum Mass (lbm.)	1.130×10^{-2}	6.069×10^{-3}
Aluminum Oxide Mass (lbm.)	0.0	3.688×10^{-3}
Percent Aluminum Burned	0.0 %	53.2 %
Aluminum Thickness Burned (in.)	0.0	0.071

* The initial value of the properties summarized in the table is the properties of the inclusion at the release location and the final value of the properties correspond to the values for the inclusion at the nozzle throat.

Information from the analysis can also be used to derive the thickness of burned aluminum, which was 0.071 inches. This means that for a rectangular inclusion of the shape considered in this analysis (2.25 x 0.523 x 0.113) which burns from both the front

and back sides, an inclusion of a thickness of 0.142 inches would burn completely. Since the inclusion considered here is only 0.113 inches thick, the analysis suggests that the aluminum inclusion would be completely burned. The final mass computed in this analysis for the spherical inclusion is 86.3% of the original mass. Since it was shown that the rectangular inclusion would completely burn, the mass of the fully burned rectangular inclusion can be computed as 46.5% of the original inclusion mass. This can be done by multiplying the original mass of the inclusion by 0.283 (the amount of burned aluminum remaining on the inclusion) and by 1.884 (the factor accounting for the mass of oxygen picked of by the inclusion in the combustion process). This analysis shows that even though the aluminum inclusion burns completely, a significant mass of aluminum oxides remains if the inclusion should impact the nozzle.

An analysis was also performed for a burning inclusion using a drag coefficient for a rectangular shape. The higher drag coefficient reduces the flight time of the inclusion and thus changes the results of the analysis. A package of plots for this analysis was given to NASA and Thiokol. A summary of the results is shown in Table 4.2.11.

Table 4.2.11 Burning of the Rectangular Aluminum Inclusion (2.25 in. x 0.523 in.)

Property	Initial Value	Final Value
Inclusion Mass (lbm.)	1.130×10^{-2}	1.084×10^{-2}
Inclusion Diameter (in.)	0.634	0.627
Aluminum Mass (lbm.)	1.130×10^{-2}	8.401×10^{-3}
Aluminum Oxide Mass (lbm.)	0.0	2.439×10^{-3}
Percent Aluminum Burned	0.0 %	35.2 %
Aluminum Thickness Burned (in.)	0.0	0.043

* The initial value of the properties summarized in the table is the properties of the inclusion at the release location and the final value of the properties correspond to the values for the inclusion at the nozzle throat.

The trajectory describing the flight path of the inclusion is shown in Figure 11A. Figure 12A shows the axial velocity of the inclusion as a function of flight time. Figure 13A shows how much aluminum is burned as a function of the flight time. The total flight time of the inclusion flown with a rectangular drag coefficient was 0.83 seconds or 13.3% less than for the inclusion flown with a spherical drag coefficient. A total of 35.2% of the aluminum is burned. This is less than computed for the spherical inclusion due to the shorter total flight time of the inclusion. The final mass of the inclusion is 95.5% of the original mass. As seen for the spherical inclusion, the diameter of the inclusion does not change much due to the addition of aluminum oxide to the inclusion. For this analysis, the thickness of aluminum burned can be computed as 0.043 inches. If the inclusion burns from both sides as with a rectangular inclusion, 0.086 inches of inclusion would burn which is not the full thickness of the rectangular inclusion, 0.113 inches.

The next analysis performed in support of the inclusion anomaly investigation involved examining the trajectory of an inclusion that collides with the nozzle nose. This analysis examines the post-collision trajectory of the inclusion in the nozzle region from the nozzle nose to the nozzle exit. The previous solution for the 33 second geometry/20 second burn time configuration was calculated to a point just past the nozzle throat. In order to calculate the trajectory of an inclusion to the nozzle exit, the original solution domain had to be extended to the nozzle exit. In order to accomplish this in the most expedient manner, the computational grid used for the 33 second geometry/20 second burn time configuration was modified to obtain a new grid which extended from the motor head end to the nozzle exit plane. The axial grid resolution in the motor port was not modified but both the axial and radial grid resolutions in the nozzle region were modified in order to provide a better trajectory estimate in the region of concern. The same thermochemistry and boundary conditions were used for the supersonic region extended grid as were used to compute the original the 33 second geometry/20 second burn time solution.

It was assumed for the purpose of this analysis that the inclusion impacted at two locations. The post-collision trajectory of the inclusion was tracked from these two locations. The first location was the nozzle throat. The second location was along the nozzle entrance ramp at the mid-way point (in the axial direction) between the nozzle nose and throat. The two impact locations are shown in Table 4.2.12. In order to track the post-impact trajectory of the inclusion in the supersonic nozzle exit region, a supersonic drag coefficient was required. This supersonic drag coefficient was obtained from the reference book, "Fluid-Dynamic Drag" by Sighard F. Hoerner. The drag coefficient of a spherical object is approximately 1.0 for the flow Mach number of interest.

Table 4.2.12 Inclusion Impact Location Along the Nozzle Surface

Location	Axial Position	Radial Position
Nozzle Throat	1845.846	27.276
Nozzle Entrance Ramp	1833.587	30.066

The post-collision trajectory of the inclusion was analyzed as an unburned spherical object of effective diameter equal to 0.634 inches. Two different post-collision velocities for the inclusion, which impacted the nozzle throat, were considered. The first assumed an elastic collision at the nozzle throat in which the axial velocity of the inclusion at the nozzle nose was conserved. The axial velocity of inclusion as it leaves the throat location was 615 ft/sec. The radial velocity of the inclusion in this case was assumed to be 0.0 ft/sec. Figure 14A shows the trajectory of the inclusion under these initial post-impact conditions. The inclusion does not impact the nozzle wall after leaving the throat location. A second set of inclusion velocity boundary conditions were also analyzed at the throat. A totally non-elastic collision at the nozzle throat in which the initial post-impact velocity of the inclusion was 0.0 ft/sec was considered for both the

axial and radial velocity components. Figure 15A shows this trajectory. In this case, the inclusion does impact the nozzle exit cone. The initial axial velocity (with 0.0 radial velocity) required to cause this inclusion to miss the nozzle exit cone was also computed. The value of the axial velocity required was found to be 130 ft/sec. The inclusion just misses the nozzle exit cone at the nozzle exit plane.

The second nozzle impact location was along the nozzle entrance ramp. Figure 16A shows the trajectory of the inclusion assuming a completely non-elastic collision with zero initial velocity of the inclusion. The trajectory shows that the inclusion does not impact the nozzle exit cone. If it is assumed that a completely elastic collision occurs in which the angle of incidence and the angle of deflection of the inclusion are equal, the initial axial velocity of the inclusion is 555 ft/sec and Figure 17A shows the trajectory for these conditions. The inclusion under these conditions does not impact the nozzle exit cone.

An impact problem with the nozzle exit cone was only observed for one particular set of boundary conditions. After a collision with the throat, when the initial velocity leaving the throat is zero in both the axial and radial directions, the inclusion impacts the nozzle exit cone. Fortunately this is not a very probable event. A glancing impact near the throat would only be required to have an axial velocity of more than 130 ft/sec to clear the nozzle exit cone.

This phase of the overall analysis involves the investigation of the lateral lift forces associated with a tumbling non-spherical inclusion. For a spherical object or a flat plate, which is parallel to the freestream velocity, the shear forces act only in a direction which is parallel to the freestream direction. This creates only a drag force and no lift component normal to the freestream direction. If the flat plate is assumed normal to the freestream direction, the drag force is greatly increased but there is still no lift force. When the flat plate or rectangular object is turned at an angle of attack to the freestream direction a component of lift is created which tends to push the object normal to the freestream direction. In this analysis, a rectangular object is being considered which tumbles as it traverses the motor port. The lift force would vary over the course of the flight of this tumbling rectangular object and an average lift force over the course of the flight of the object could be calculated. This analysis does not attempt to compute what the actual lift force on the tumbling object but seeks to compute the lift force which would be required to cause the tumbling object to impact the nozzle wall.

In order to perform this analysis, a specific set of initial conditions was utilized to make this analysis work and remain consistent with the characteristics of the actual inclusion trajectory in the motor. In order to compute the lateral force required to make an object impact the nozzle, large lateral accelerations must be applied to the objects. If these large lateral accelerations are applied to a very low speed object, which is directed initially toward the motor centerline, the object will collide with the head end walls. This describes the normal conditions in the head end of the motor. Two conditions were changed to remedy this situation. First, the inclusion was released from the head end

at the motor centerline and secondly, a larger initial velocity was applied to the objects in this analysis than previously used. The inclusions in this analysis were released with an initial axial velocity of 100 ft/sec. These conditions are sufficient for this analysis since the inclusion trajectories analyzed in the previous analyses cross the motor centerline somewhere between the start of the forward grain c.p. and the forward inhibitor. The velocities of the inclusions at this location are between 100 and 200 ft/sec, axial velocity. These conditions remain satisfied in this analysis. Also, the lateral lift forces acting to move the inclusion radial in the head end region would be much smaller since the relative velocities between the inclusion and the flow are also small in the head end.

There is an additional item that must be considered in this analysis. The character of the internal flow field of the motor is such that there is a radial inward component of velocity created by the blowing propellant surface. This is not a lift force but is a drag force directed in such a way as to move the inclusion radially. In order to demonstrate the effect of this lateral drag force, inclusion trajectories were computed with and without drag included. The specified flight accelerations forces remained the same as in previous analyses. Figure 18A shows the trajectory of the inclusion with drag. The axial forces (flight acceleration and drag) cause the inclusion to move rapidly down the motor centerline. The flight time for this inclusion to the nozzle nose is 0.441 seconds. The flight time for the case without drag is 0.878 seconds, approximately a factor of two more. This shows that the drag acceleration in the axial direction is very important. The trajectory without drag is shown in Figure 19A. This trajectory also illustrates that without the lateral drag force, which pushes the inclusion toward the motor centerline, the 0.194 lateral g's of acceleration causes the inclusion to impact the nozzle. These figures illustrate the importance of the lateral drag force in preventing the inclusion from impacting the nozzle.

Next, the CFD code was used to calculate the approximate lateral g-force required to cause the inclusion to impact the nozzle. The analysis was performed using drag coefficients for both a non-burning spherical and rectangular aluminum inclusion. A lateral acceleration was applied to the inclusion in addition to the normal flight lateral acceleration until the inclusion just impacted the nozzle. Figure 20A shows the trajectory of the inclusion using a spherical drag coefficient. A total of 1.6 g's is required to cause the inclusion to impact the nozzle. The g's required to cause an inclusion to impact the nozzle using a rectangular drag coefficient was also computed. Figure 21A shows the trajectory of the inclusion in this case. A total of 6.3 g's of lateral acceleration were required in this case. More lateral acceleration had to be applied to the inclusion in this case because of the shorter flight time of the inclusion due to the increased drag of the rectangular shaped inclusion.

The lift coefficient required to cause the inclusion to impact the nozzle can now be computed from the analysis results. The lift coefficient is:

$$C_L = L/(0.5\rho V^2 F_A)$$

where the lift force, L, is calculated as the product of the inclusion mass and the lateral acceleration. F_A is the frontal area of the inclusion, which is just the frontal area for the spherical inclusion and is taken to be the frontal projected area of a flat plate at a 45 degree angle for the rectangular inclusion. The approximate average gas density, ρ, and inclusion axial velocity, V, were used in the above computation for the lift coefficient. Table 4.2.13 shows a summary of the calculations performed.

Table 4.2.13 Summary of Lift Coefficient Required to Cause the Nozzle Impact of the Inclusion

Inclusion Geometry	Critical Lateral g's	Required Lift Coeff.	Flat Plate Attack Angle
Sphere	1.6	0.09	2.0 degrees
Rectangular	6.3	0.18	3.0 degrees

The last column of the table shows that only a small average angle of attack is required to achieve the lift coefficient required for nozzle impact.

Figure 1A. RSRM 33 Second Burn Time/33 Second Geometry

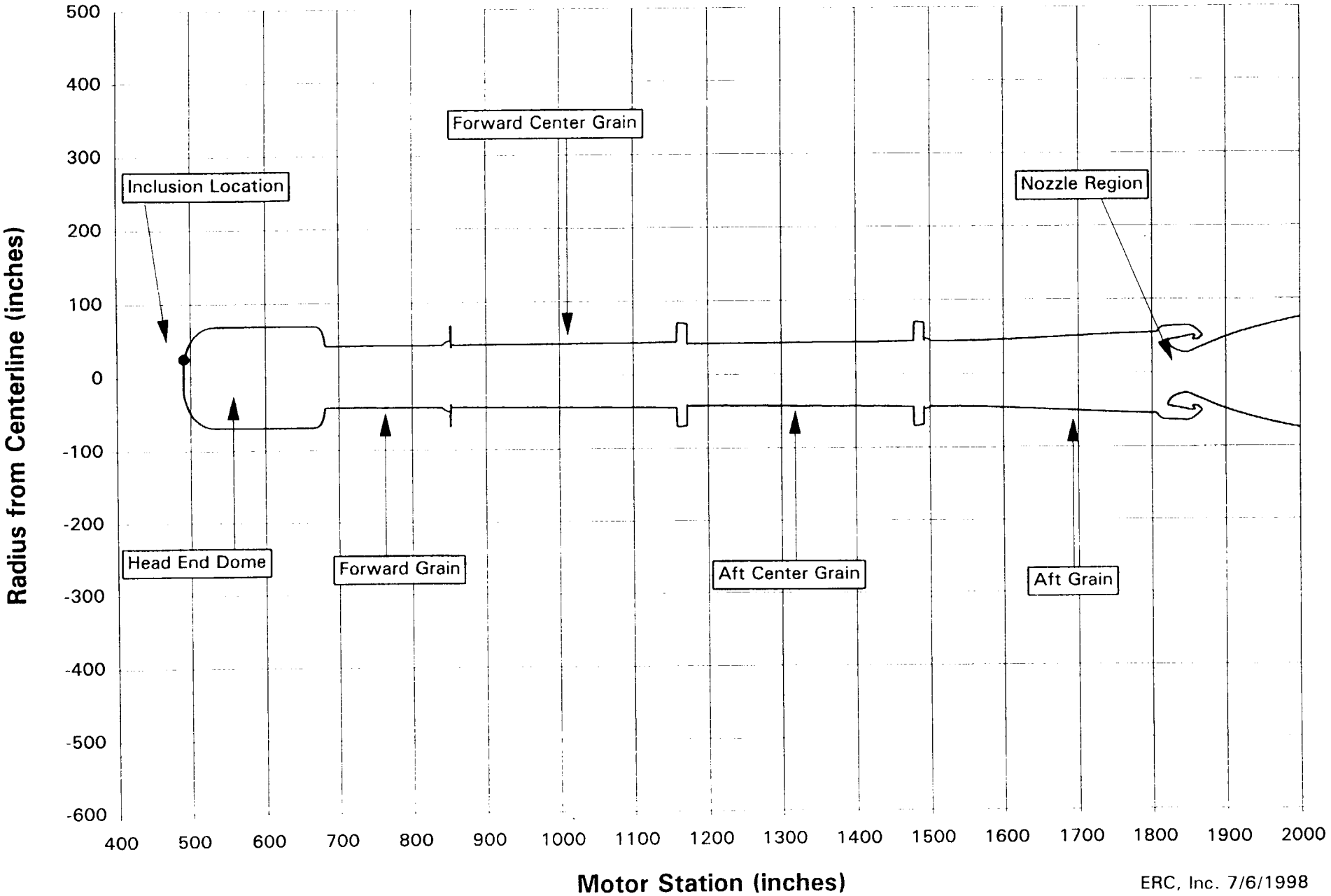

Figure 2A. RSRM 33 Second Burn Time/33 Second Geometry
Trajectory of RTV Inclusion

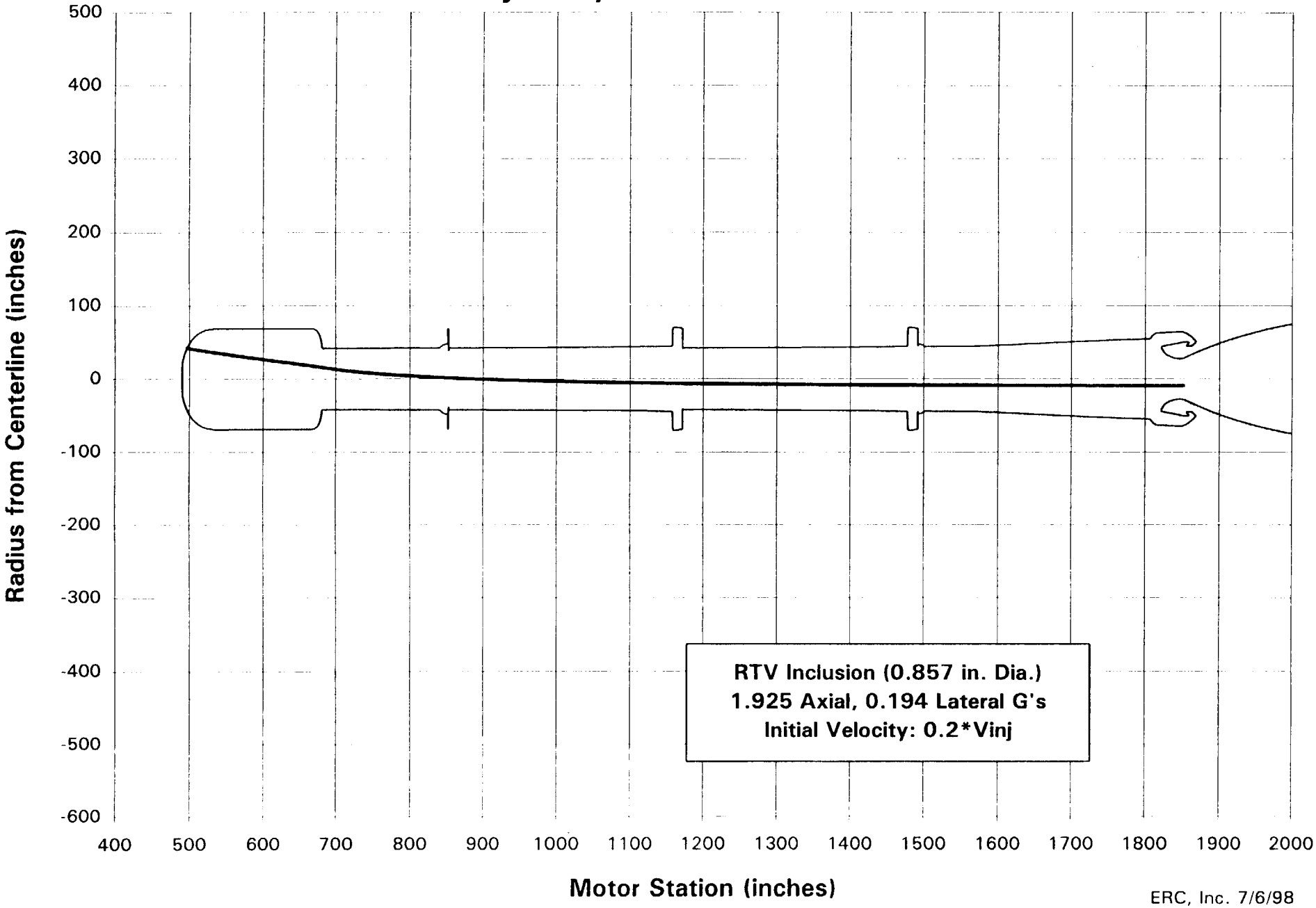

ERC, Inc. 7/6/98

Figure 3A. RSRM 33 Second Burn Time/33 Second Geometry
Trajectory of Aluminum Inclusion

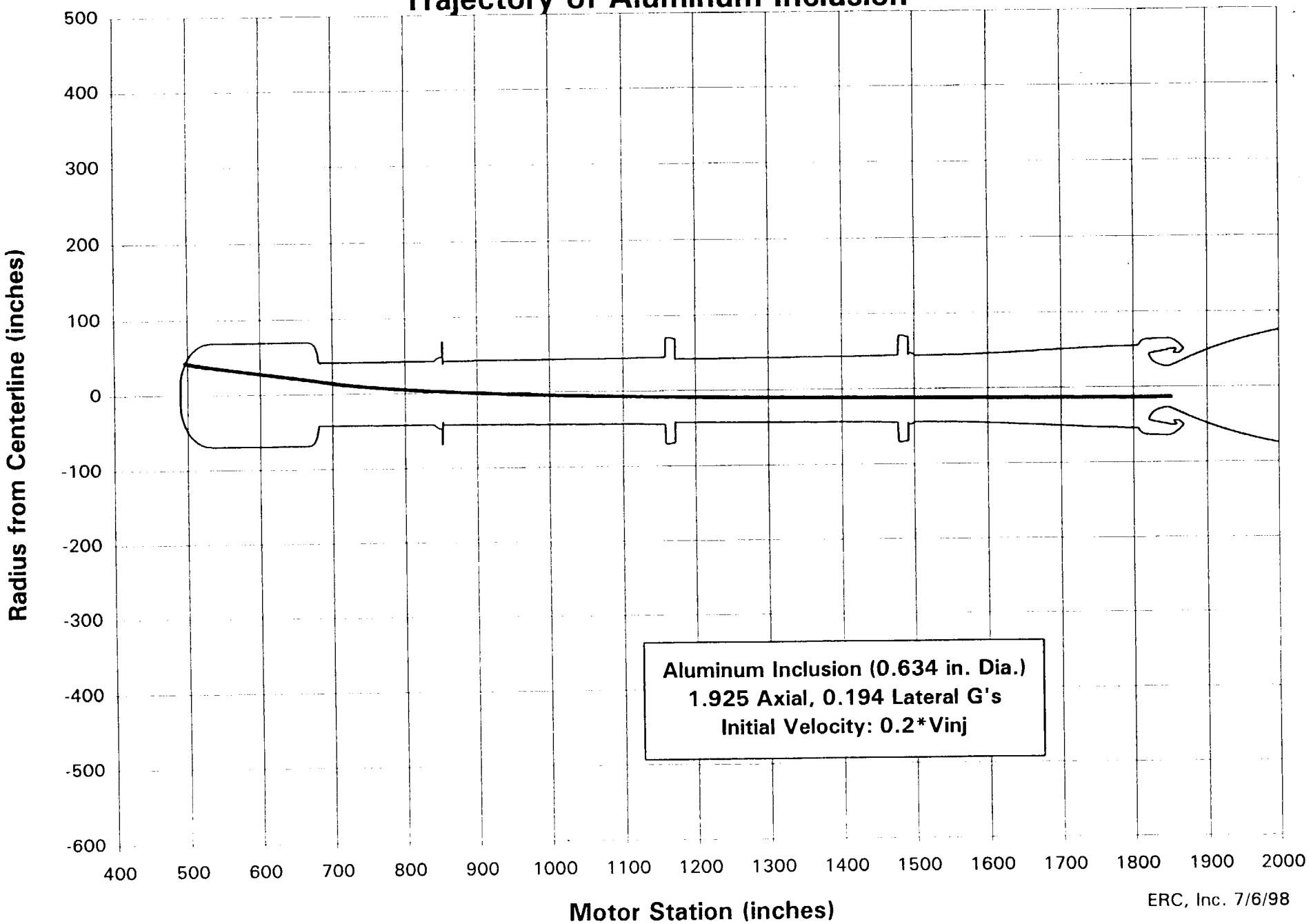

Figure 4A. RSRM 33 Second Burn Time/33 Second Geometry Trajectory of Steel Inclusion

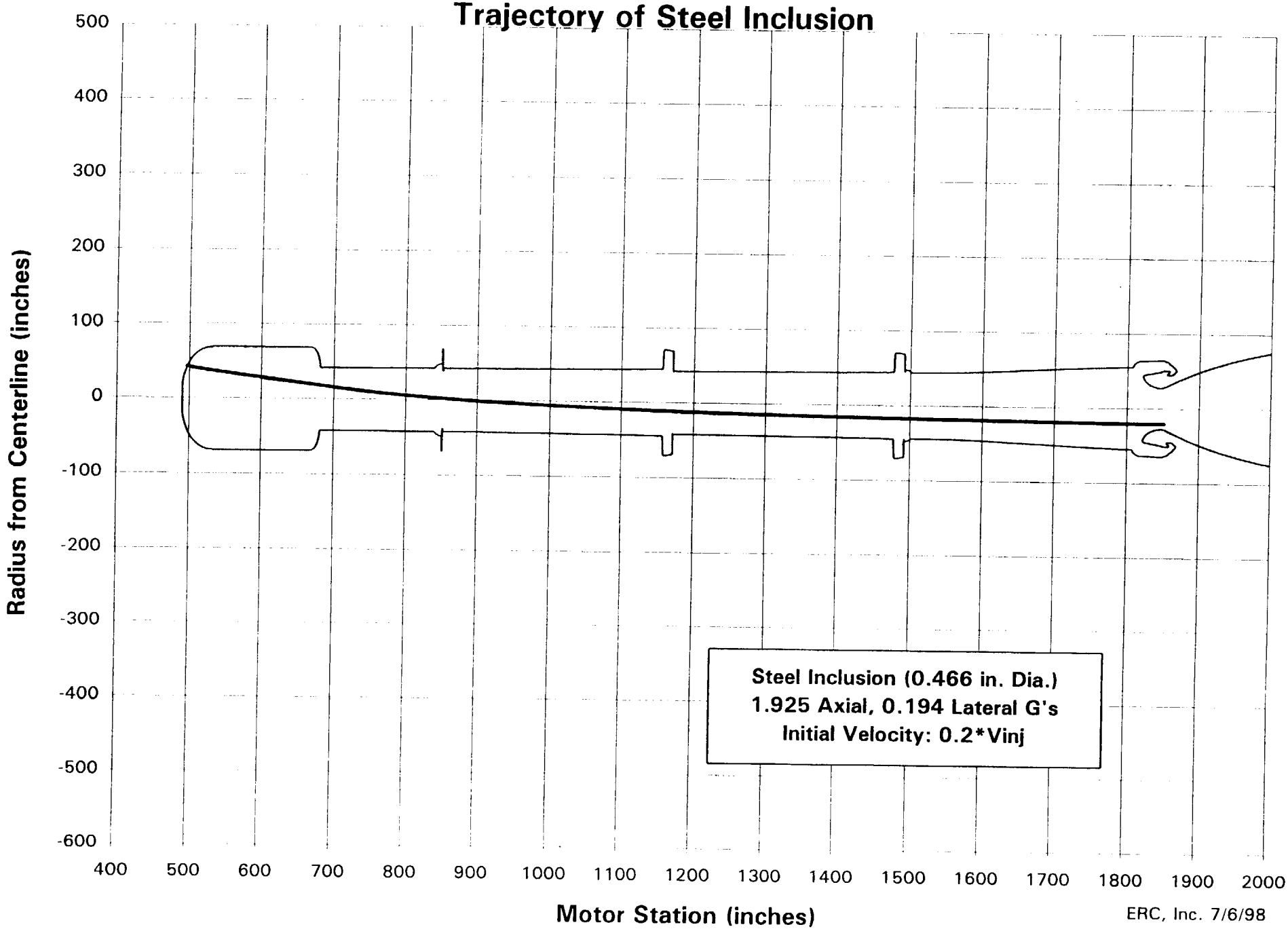

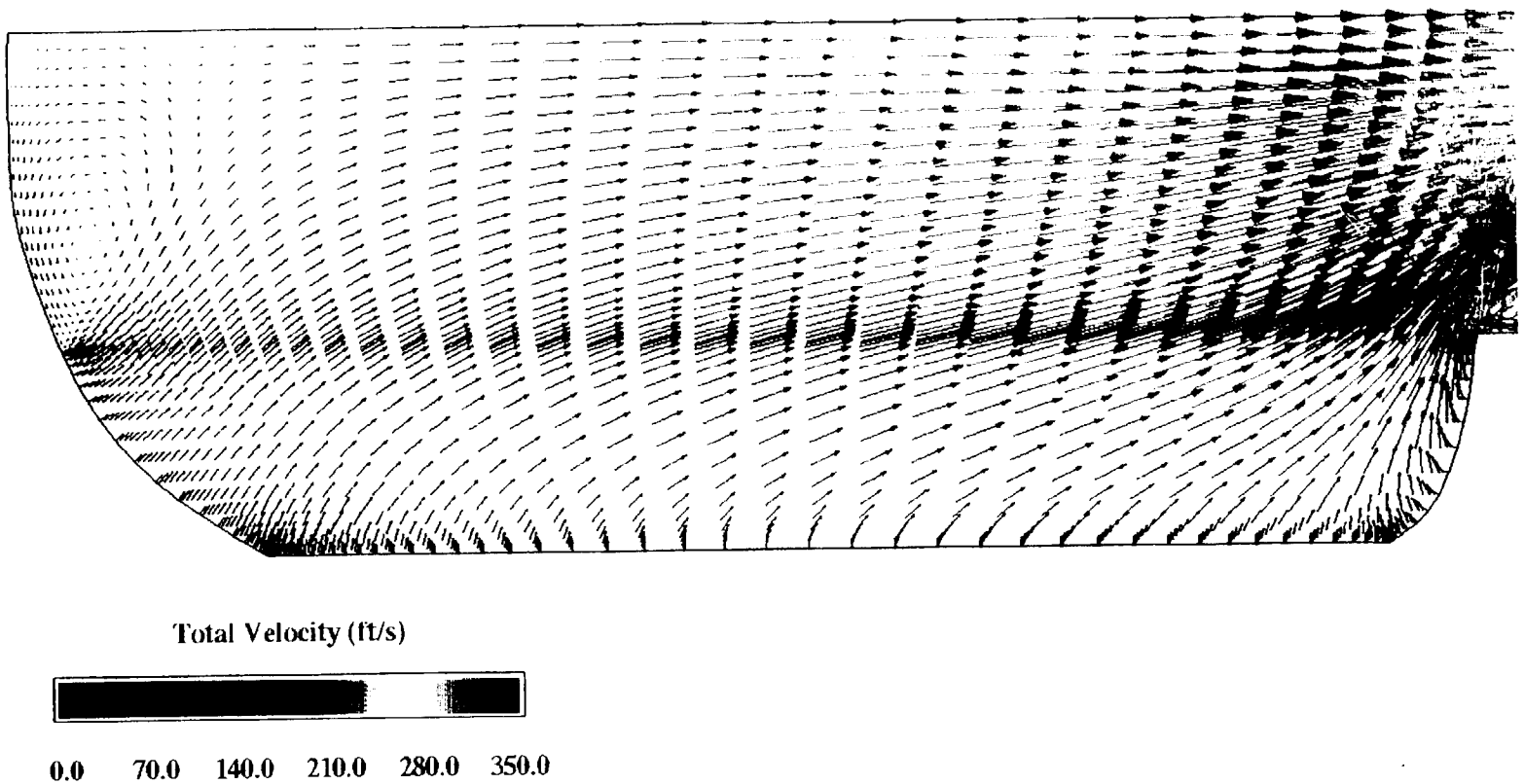

Figure 5A. Velocity Vector Field in the Motor Head End Dome Region. 33 Second Geometry/20 Second Flow Rate Motor Configuration

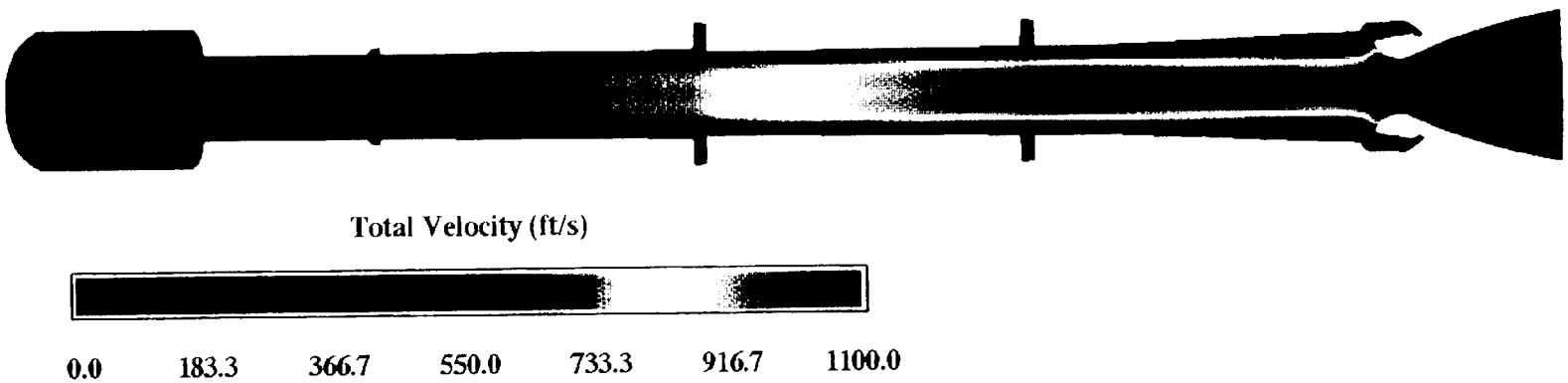

Figure 6A. Velocity Field in the RSRM Motor.
33 Second Geometry/20 Second Flow Rate Motor Configuration

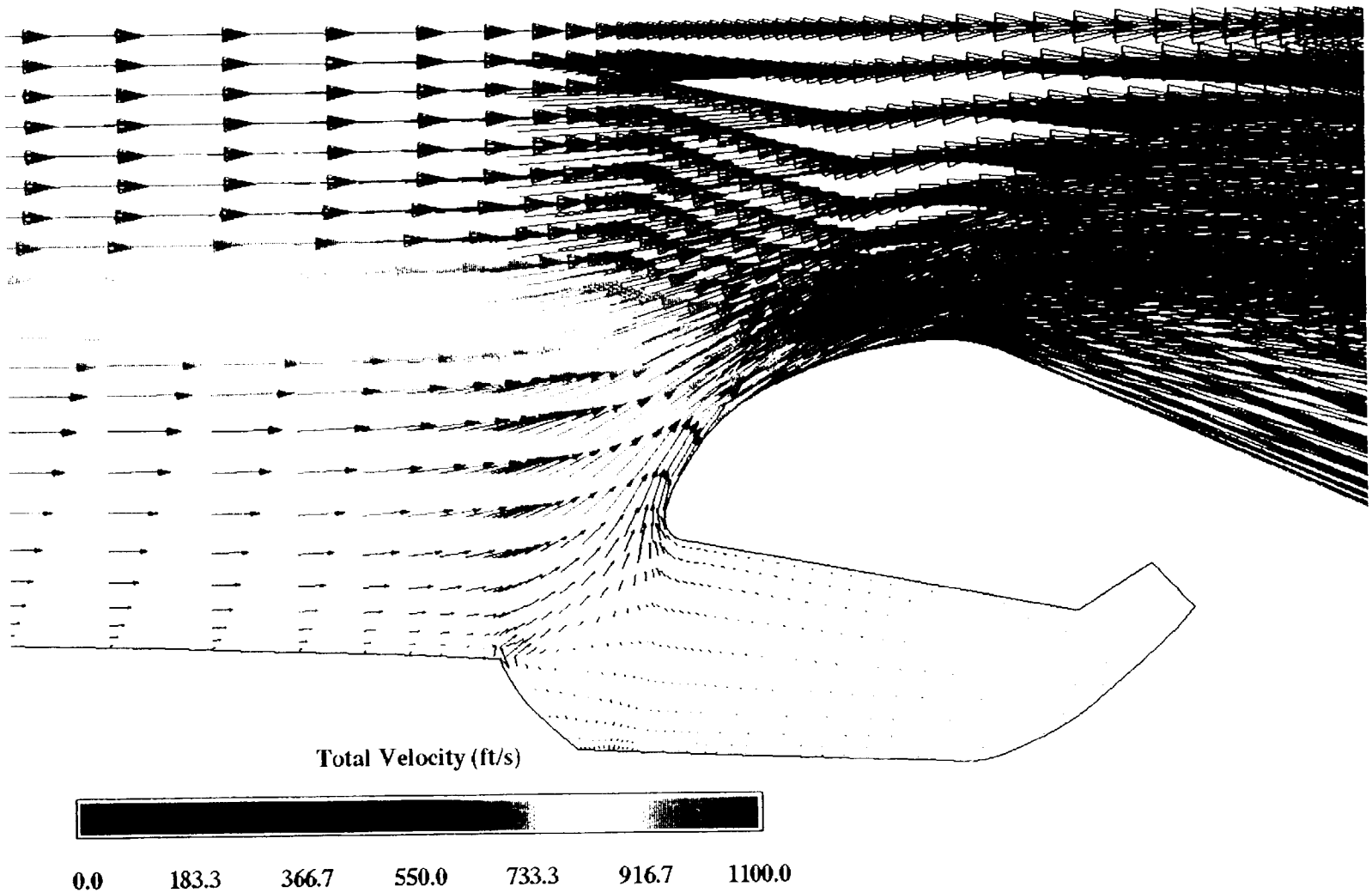

Figure 7A. Velocity Vector Field in the Motor Submerged Nozzle Region. 33 Second Geometry/20 Second Flow Rate Motor Configuration

Figure 8A. RSRM 33 Second Burn Time/20 Second Geometry
Trajectory of Burning Aluminum Inclusion

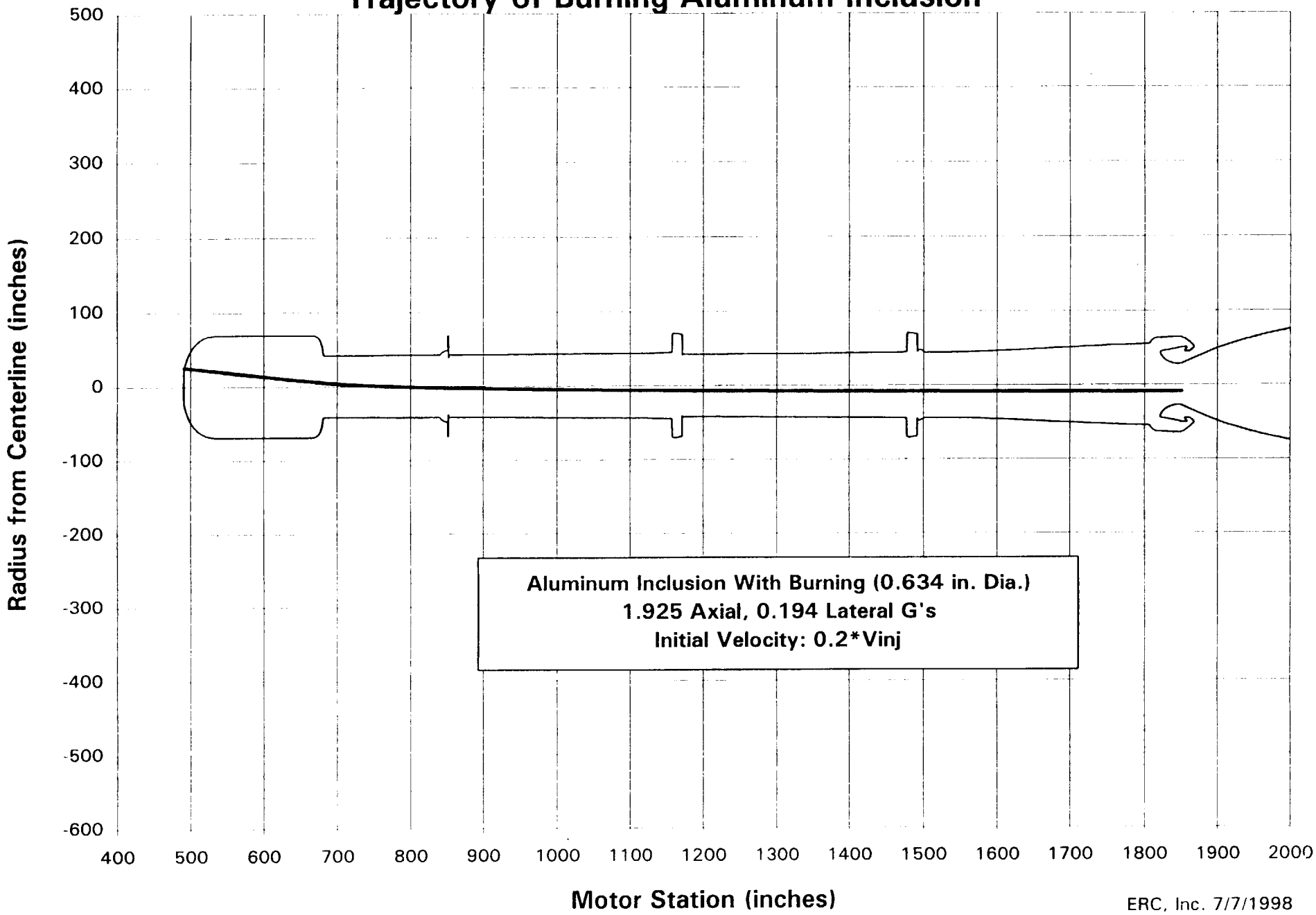

ERC, Inc. 7/7/1998

Figure 9A. RSRM 33 Second Burn Time/20 Second Geometry Inclusion Axial Velocity

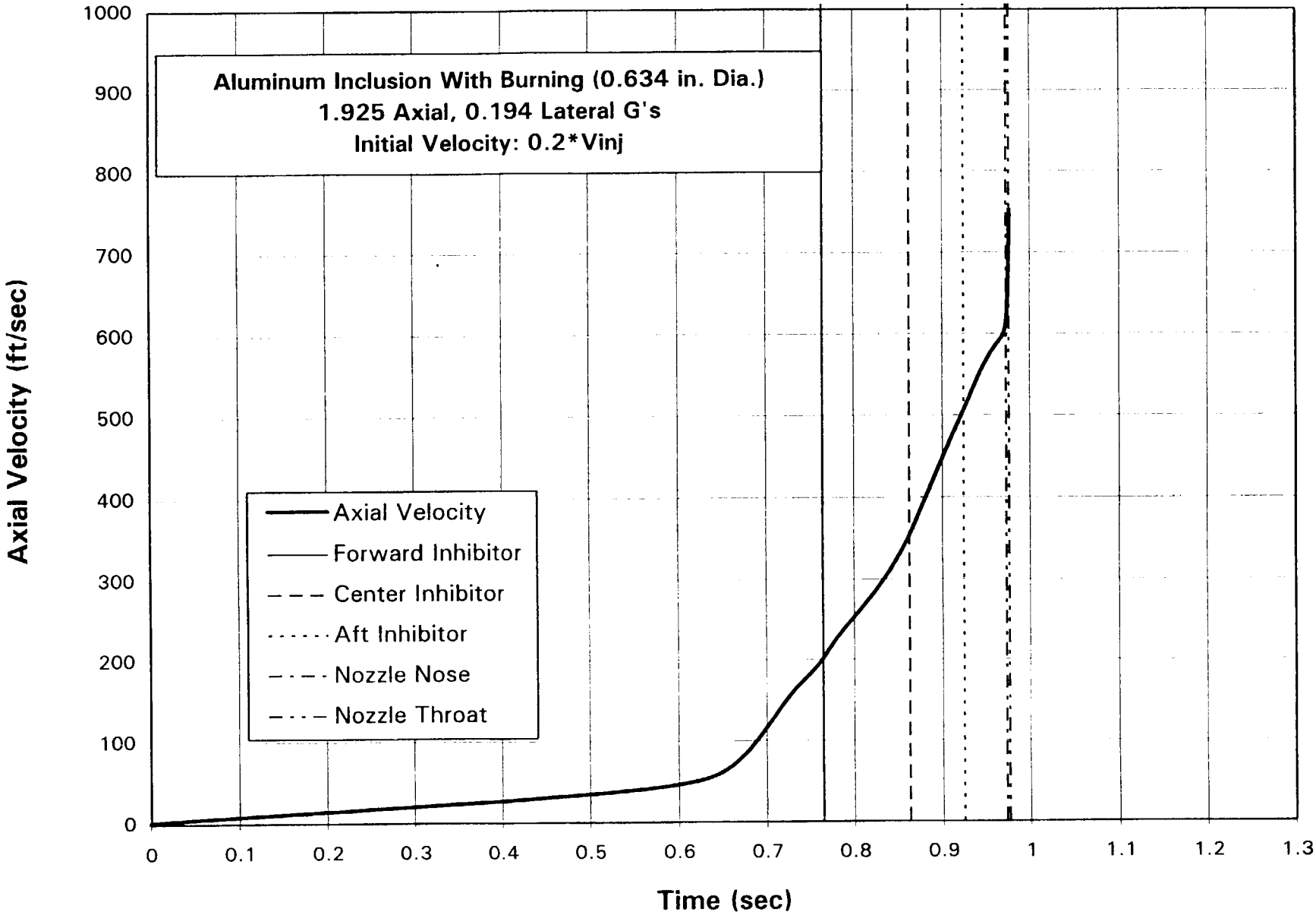

ERC, Inc. 7/7/1998

Figure 10A. RSRM 33 Second Burn Time/20 Second Geometry

Percentage of Aluminum Burned

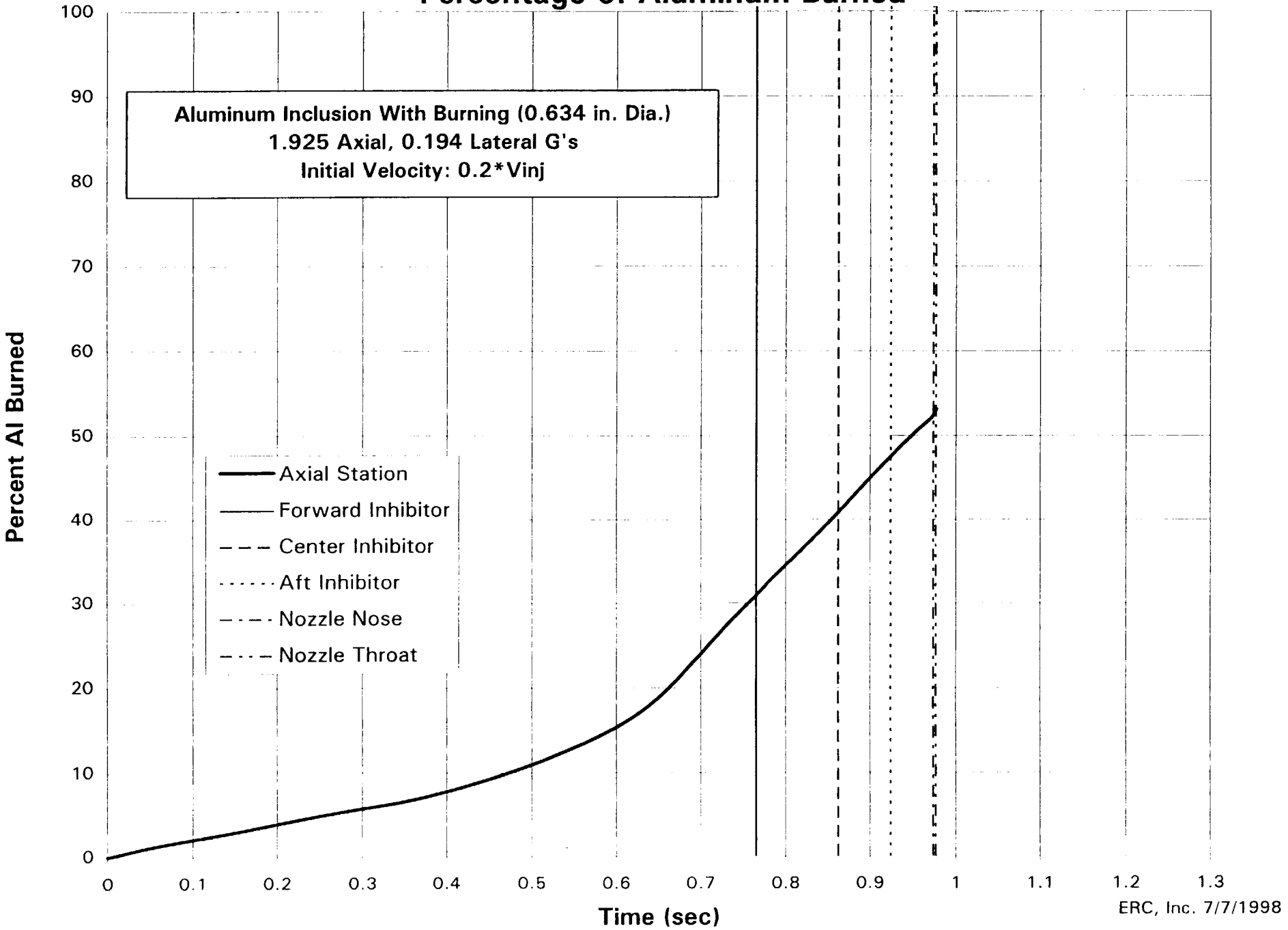

Figure 11A. RSRM 33 Second Burn Time/20 Second Geometry
Trajectory of Burning Rectangular Aluminum Inclusion

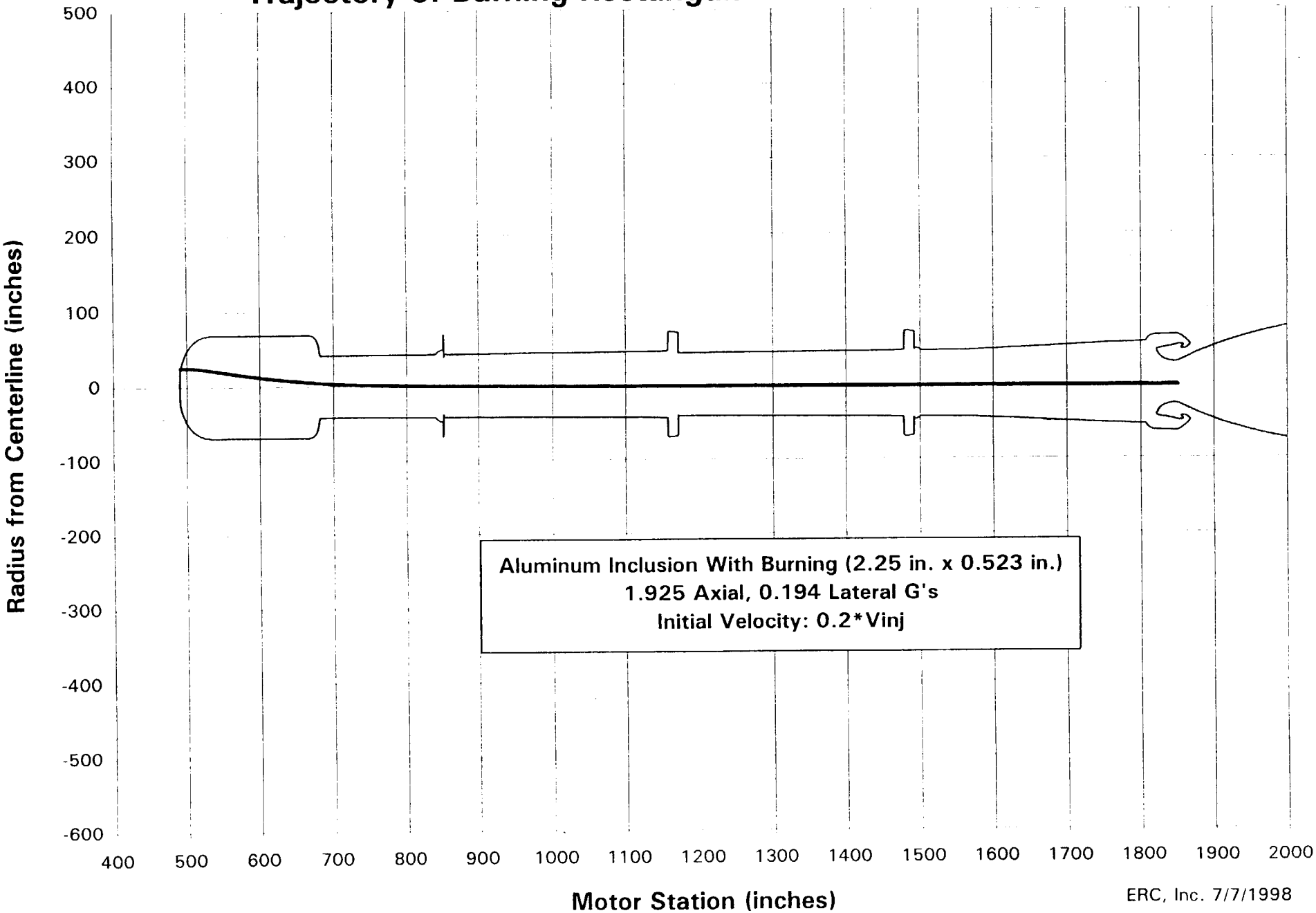

Figure 12A. RSRM 33 Second Burn Time/20 Second Geometry Inclusion Axial Velocity

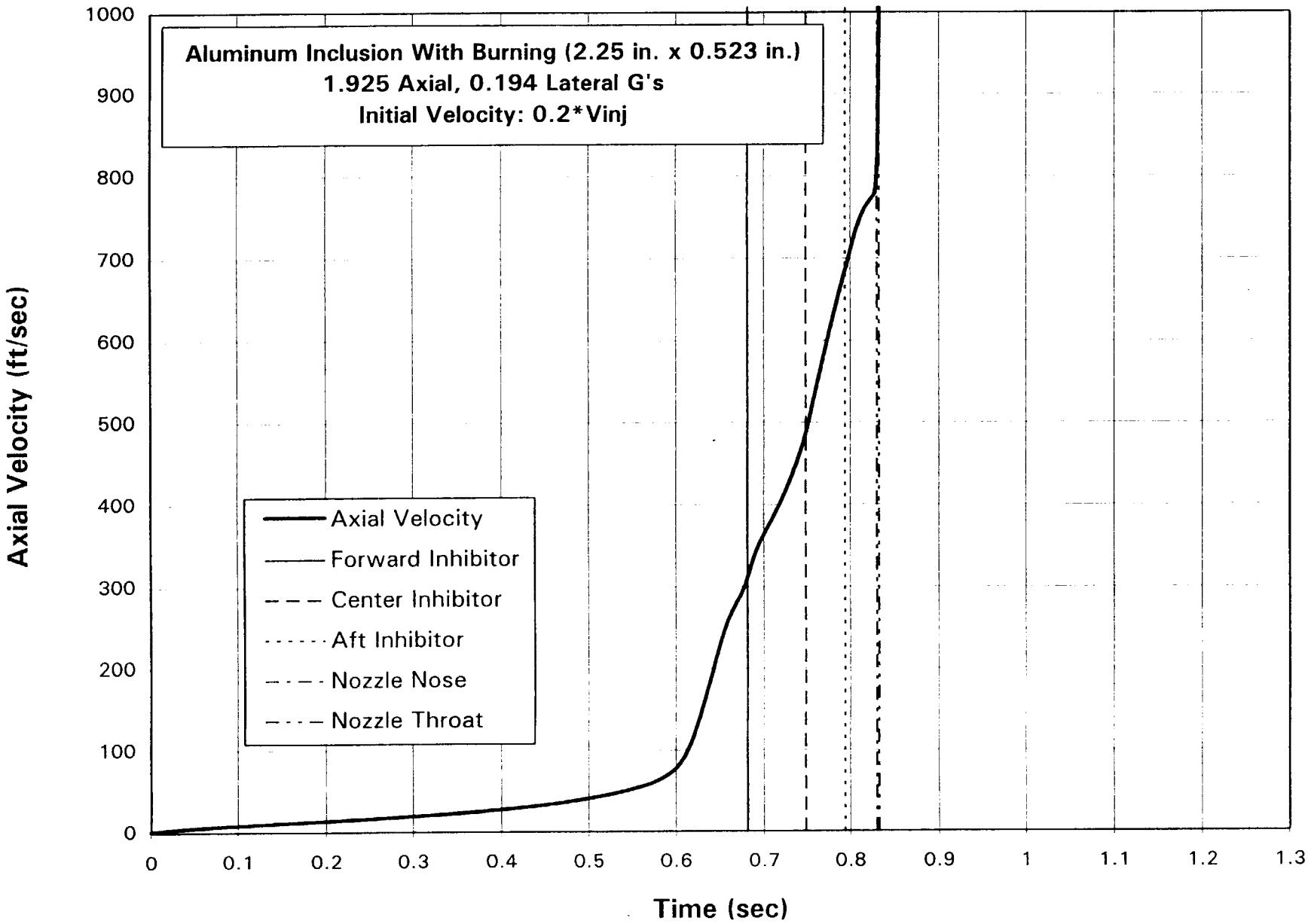

ERC, Inc. 7/7/1998

Figure 13A. RSRM 33 Second Burn Time/20 Second Geometry
Percentage of Aluminum Burned

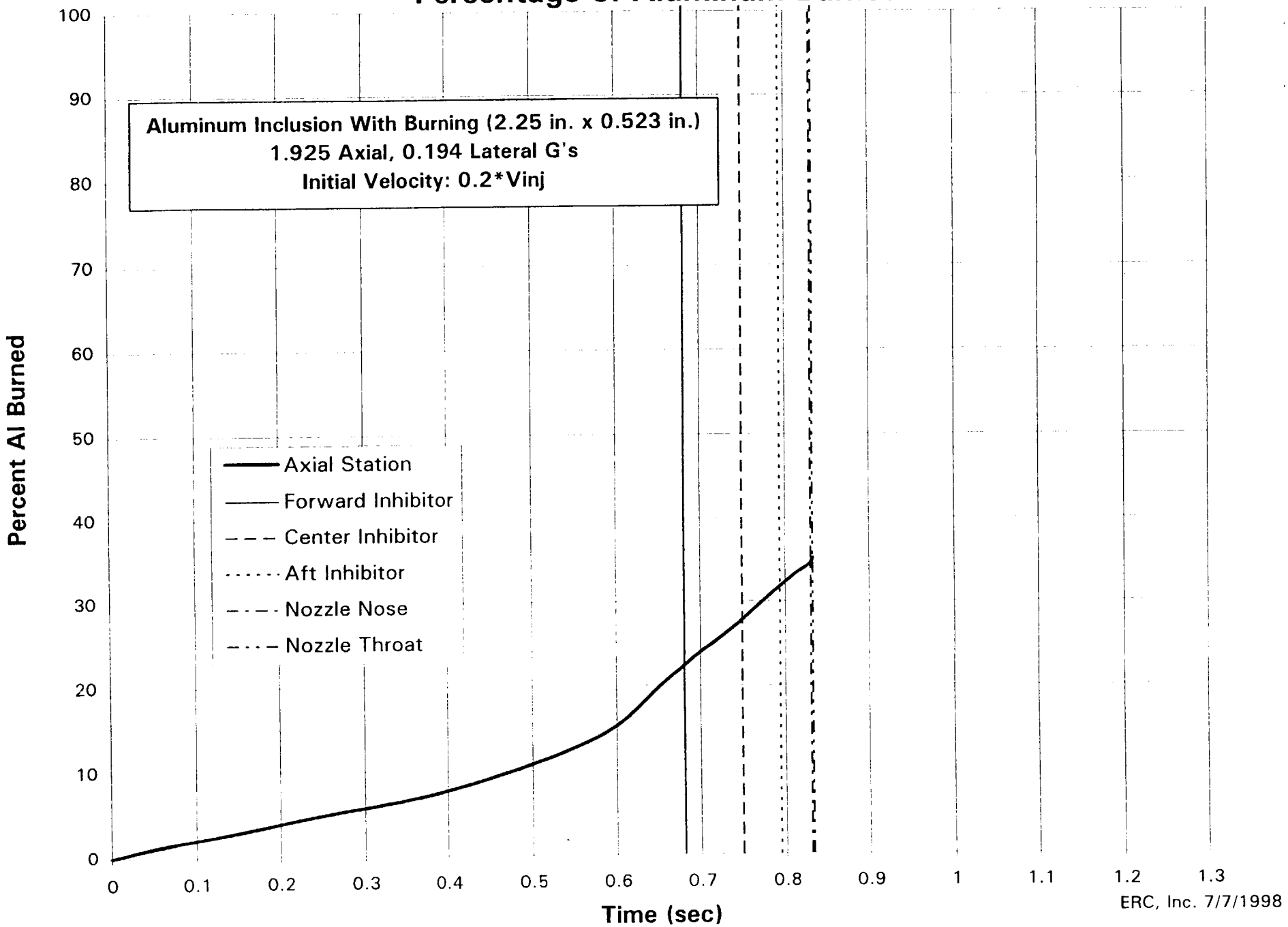

Figure 14A. RSRM 33 Second Burn Time/20 Second Geometry Trajectory After Nozzle Throat Near Miss

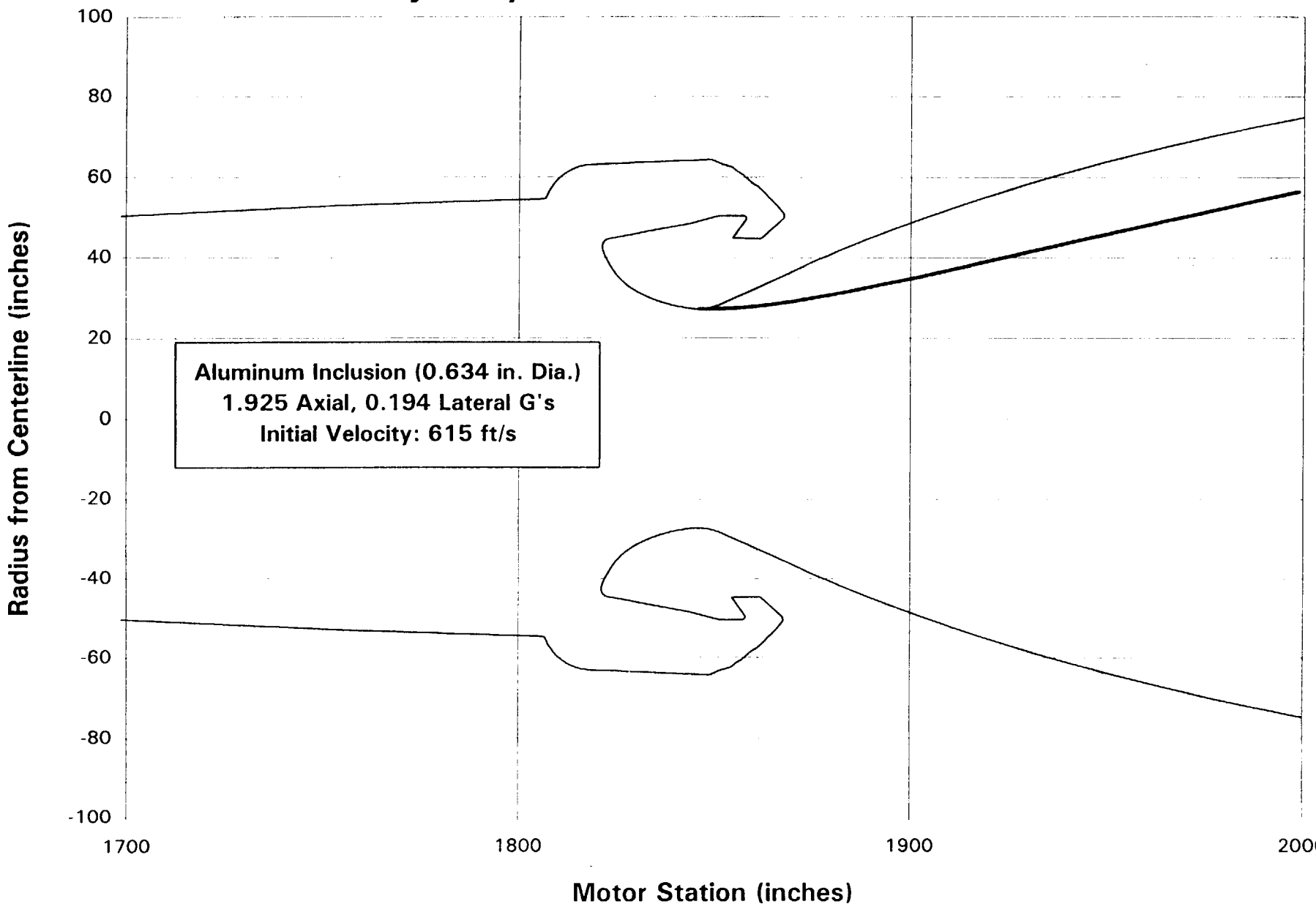

ERC, Inc. 7/19/1998

Figure 15A. RSRM 33 Second Burn Time/20 Second Geometry
Trajectory After Nozzle Throat Near Miss

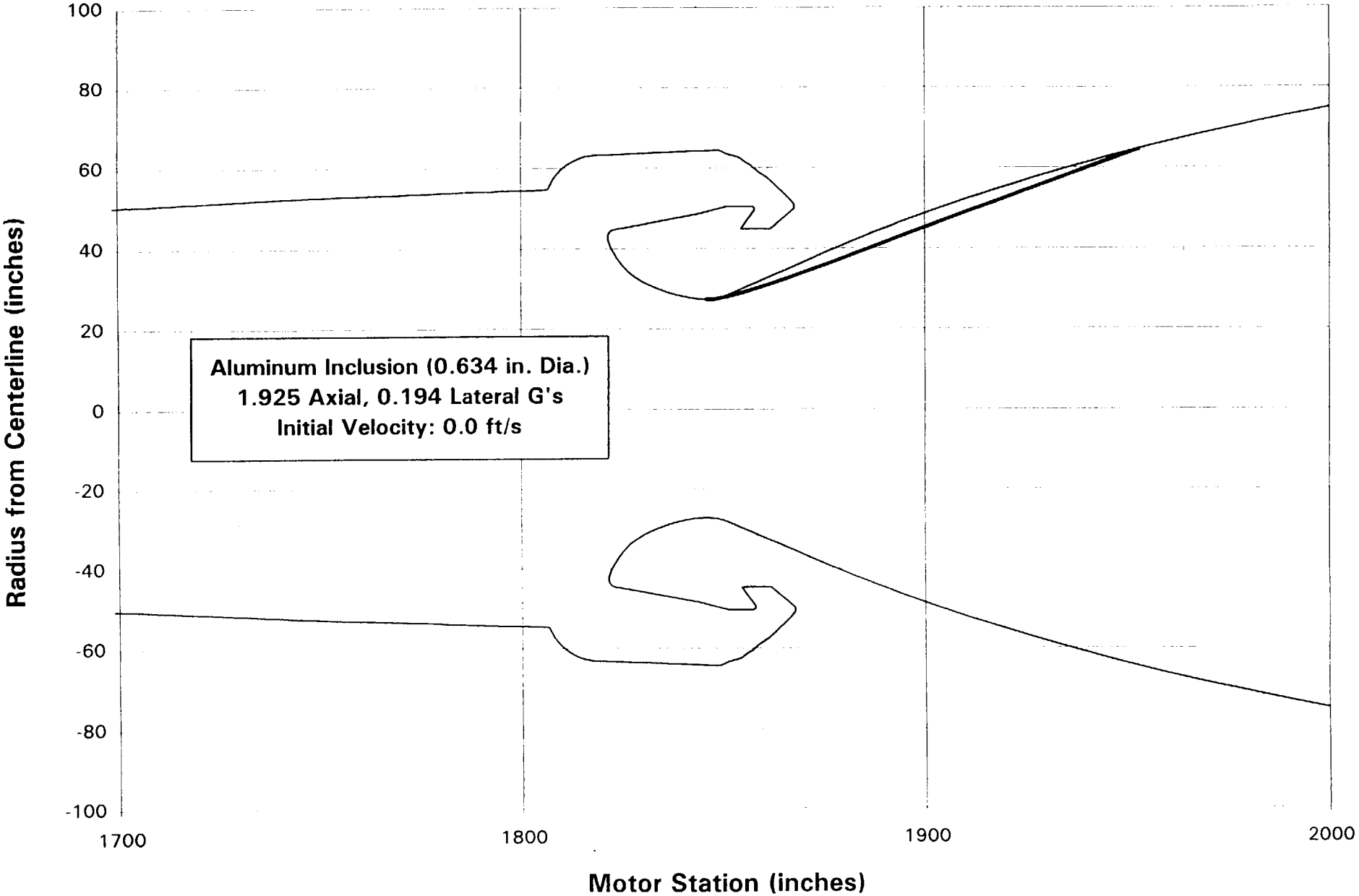

ERC, Inc. 7/19/1998

Figure 16A. RSRM 33 Second Burn Time/20 Second Geometry Trajectory After Nozzle Entrance Ramp Impact

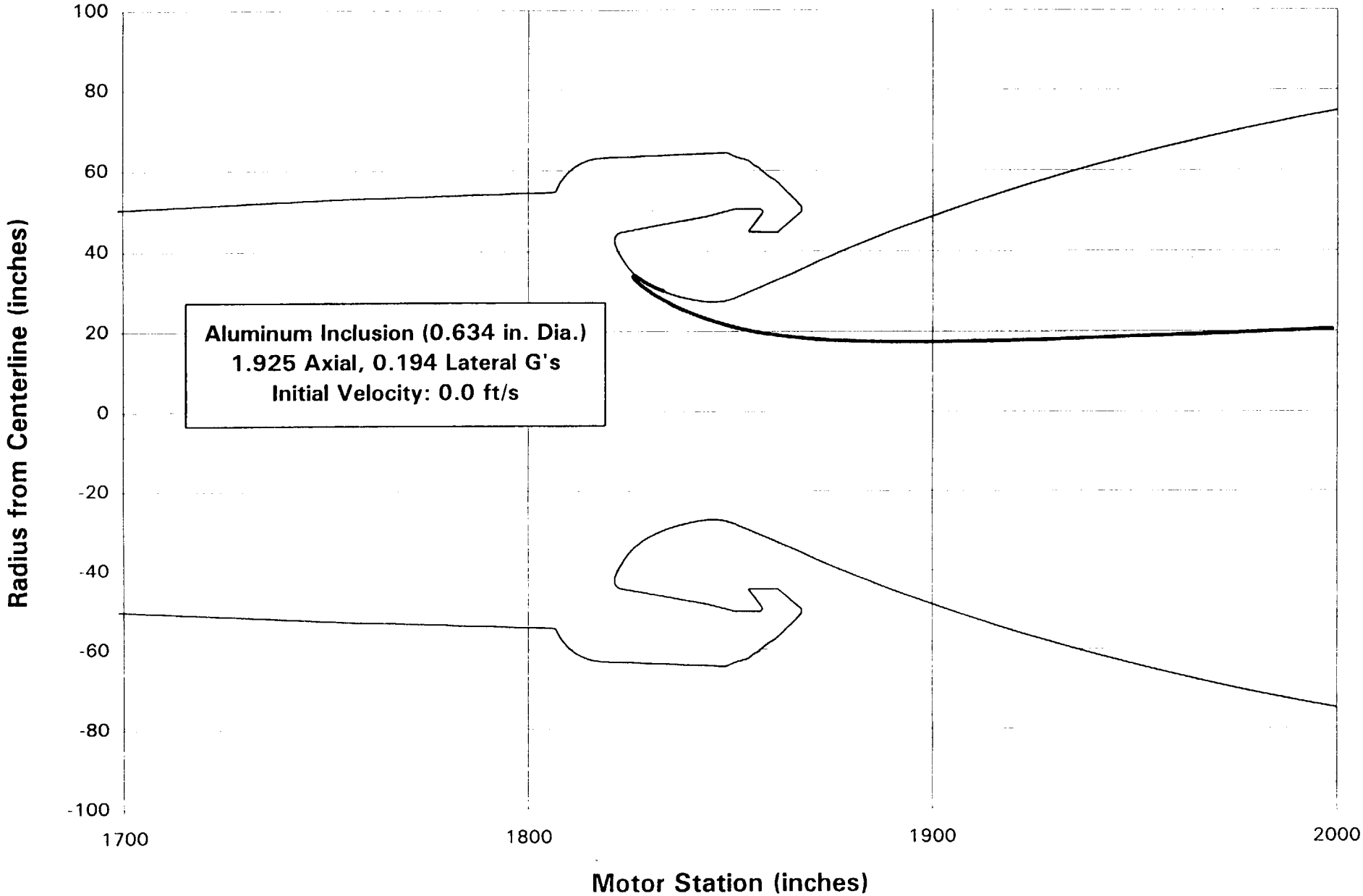

ERC, Inc. 7/7/1998

Figure 17A. RSRM 33 Second Burn Time/20 Second Geometry Trajectory After Nozzle Entrance Ramp Impact

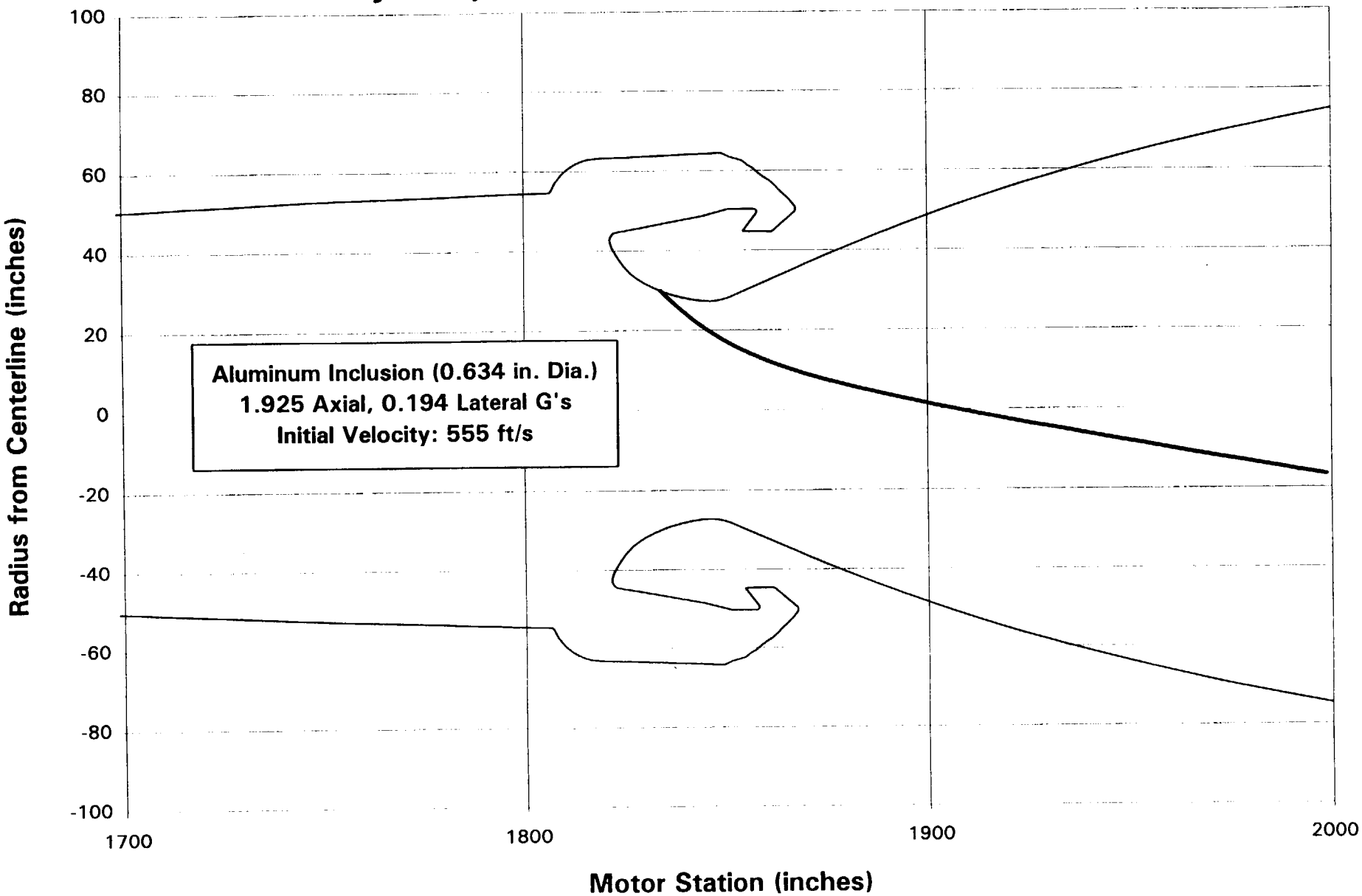

ERC, Inc. 7/7/1998

Figure 18A. RSRM 33 Second Burn Time/20 Second Geometry
Trajectory of Inclusion with Drag

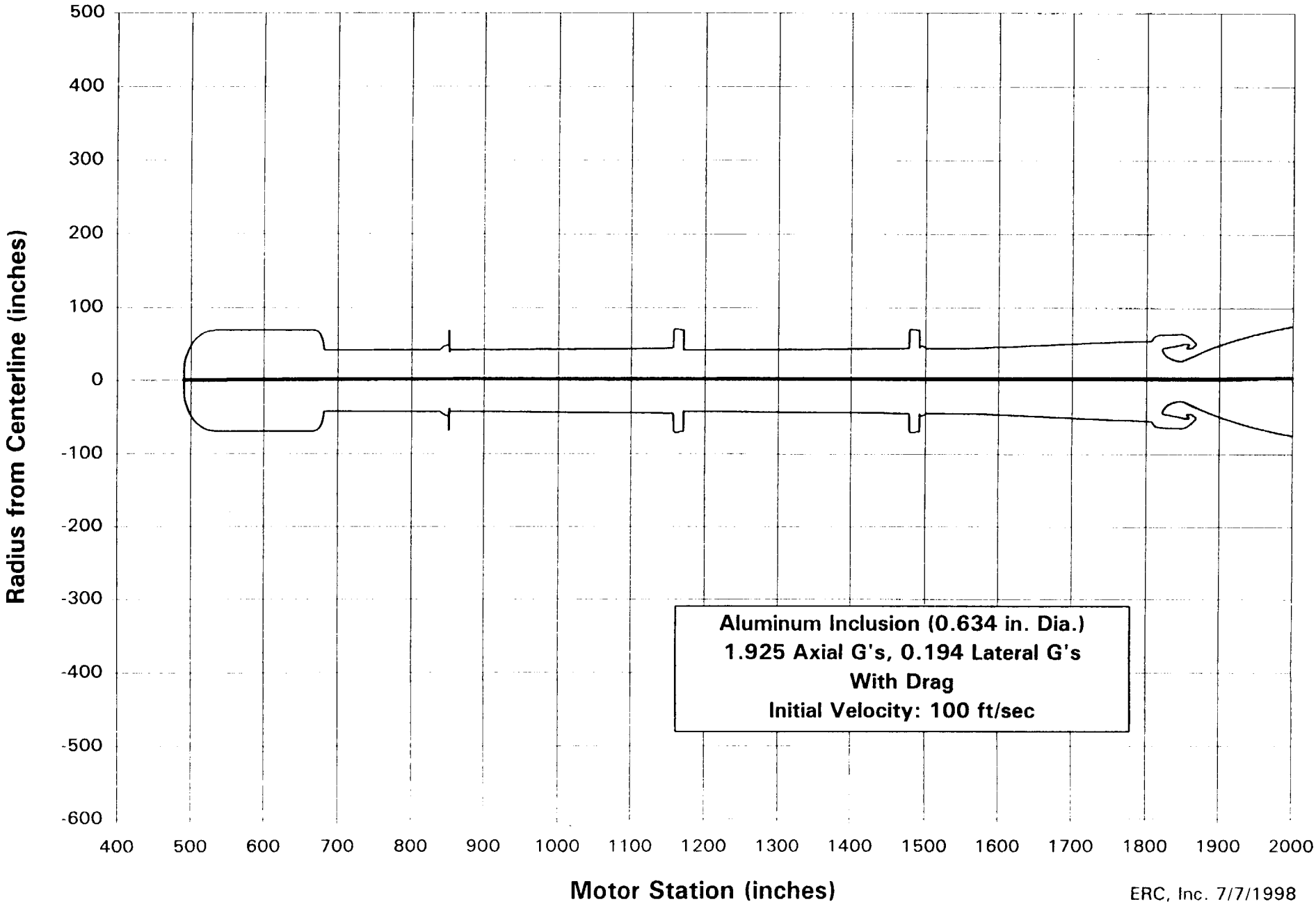

Figure 19A. RSRM 33 Second Burn Time/20 Second Geometry
Trajectory of Inclusion without Drag

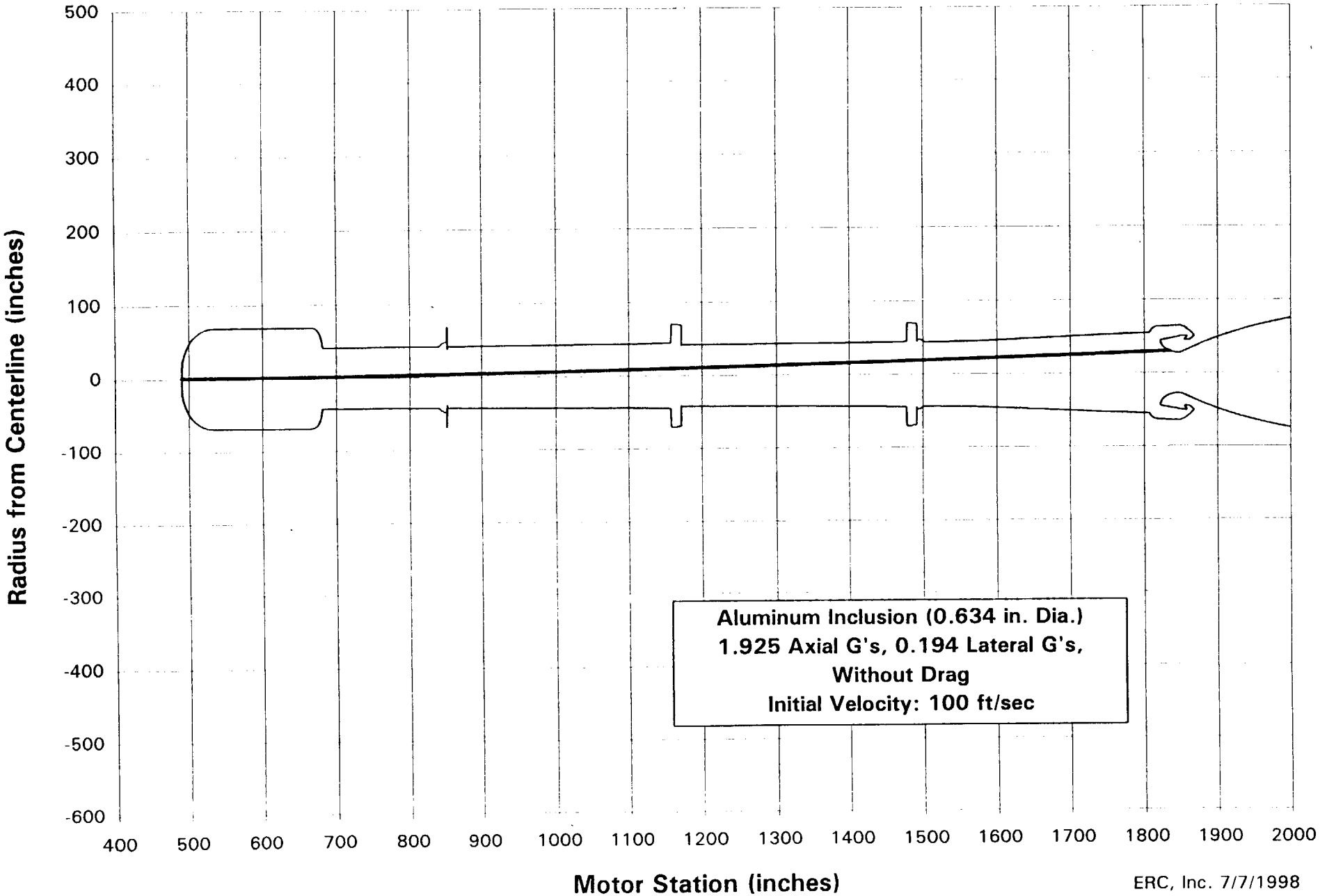

Figure 20A. RSRM 33 Second Burn Time/20 Second Geometry
Trajectory of Spherical Inclusion

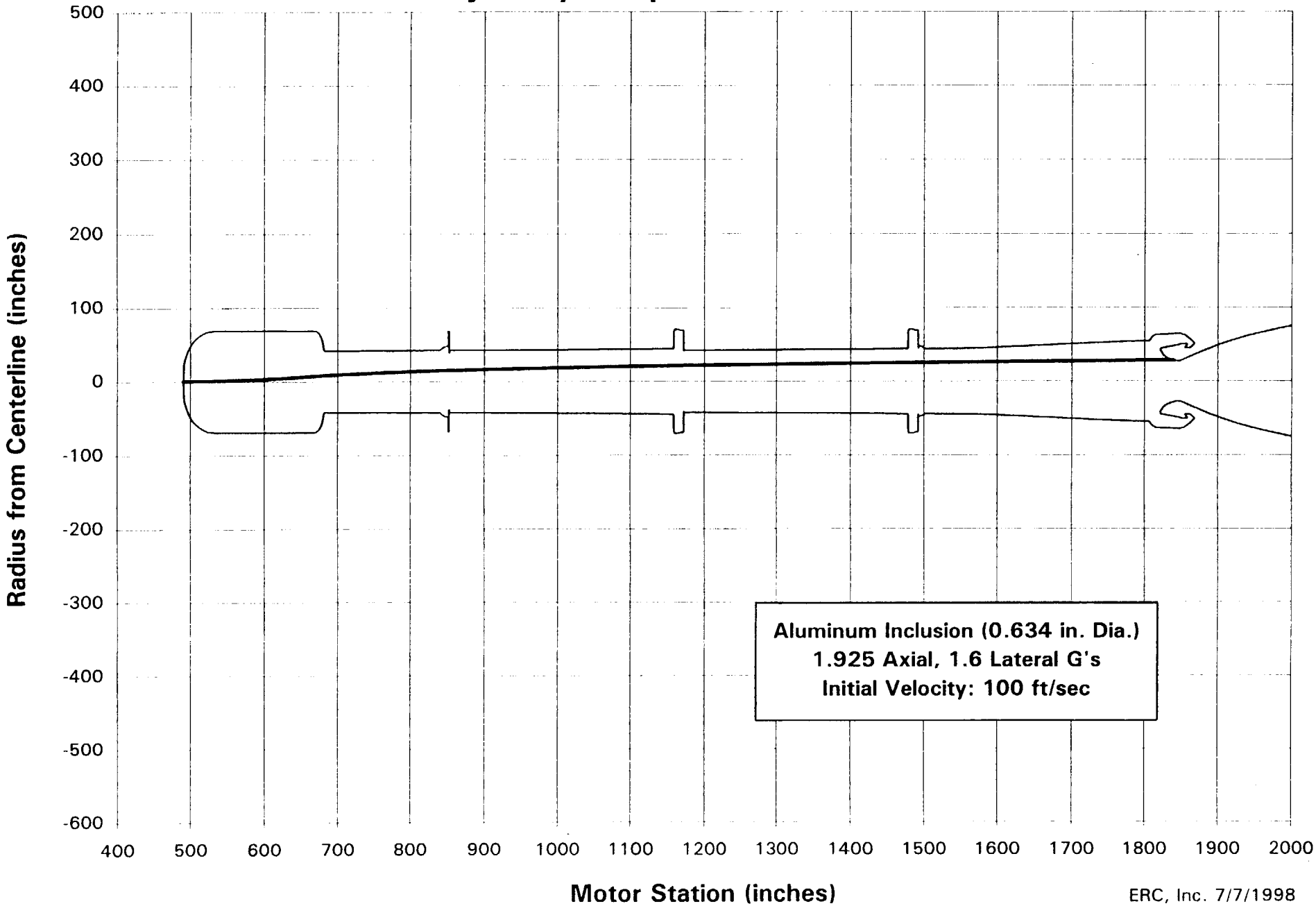

ERC, Inc. 7/7/1998

Figure 21A. RSRM 33 Second Burn Time/20 Second Geometry
Trajectory of Rectangular Inclusion

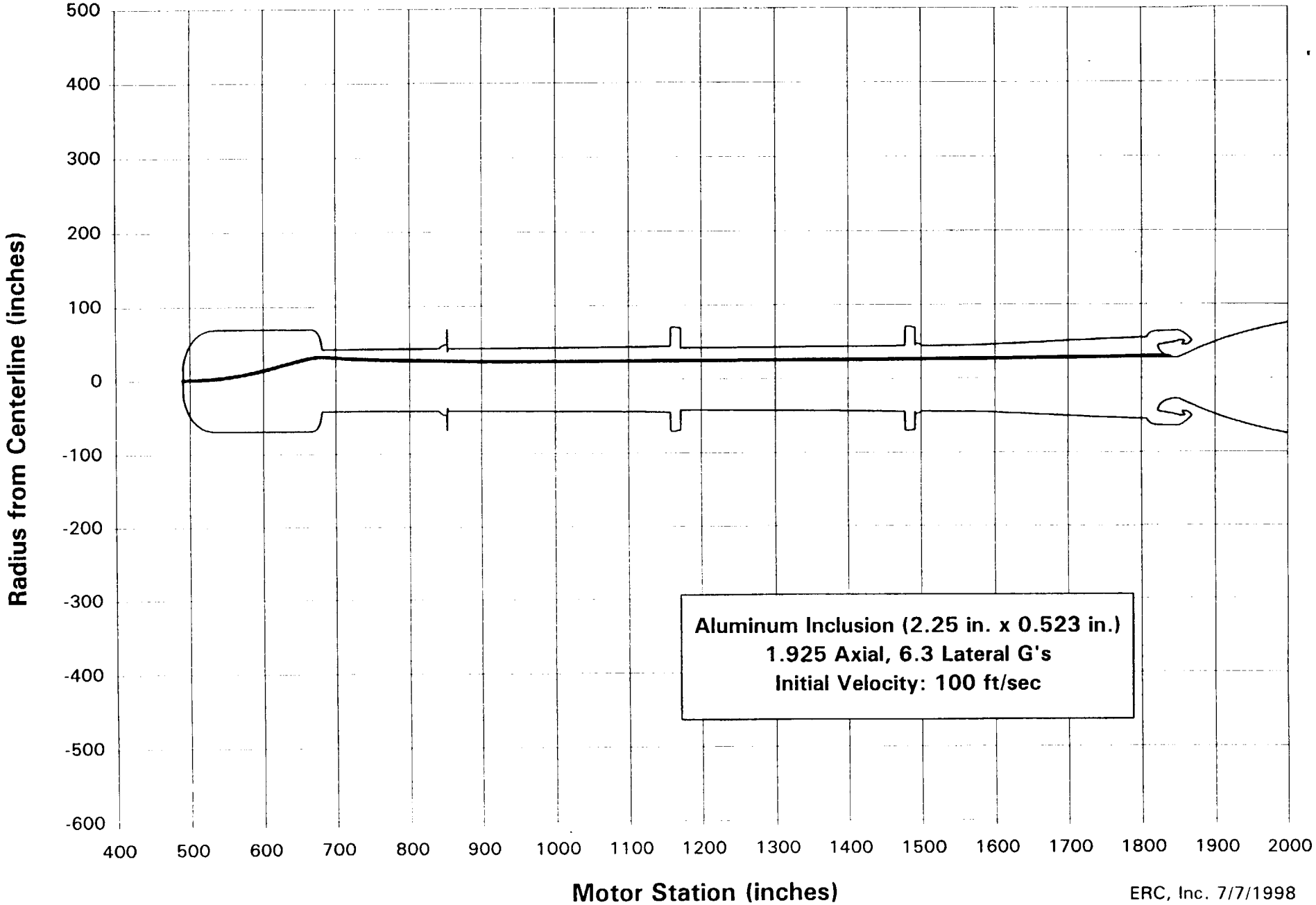

4.3 RSRM Igniter Nozzle Design Analysis

A rapid response task was initiated during late March 1998 related to the flow field in the new design of the RSRM Igniter. The task was to determine the pressure along the wall in the igniter nozzle. This pressure distribution was given to NASA/MSFC to be used in assessing the fluid dynamic induced pressure stresses on the nozzle.

Two computational grids were used to compute the flow field in the igniter nozzle. The grid resolution for the nominal grid was determined based on two criteria: 1) the grid was constructed with sufficient resolution to provide a sufficiently accurate resolution of the flow field, and 2) the grid resolution was constrained to a minimum number of grid cells so that the flow field solution could be determined in a minimum amount of time since the completion of this task was time critical. A solution was obtained from the nominal grid. This solution was used for early analysis of the nozzle pressure loading. The solution was also compared to a Thiokol CFD solution that used a coarser resolution grid. There was a significant difference in the solutions obtained using the nominal grid and the coarser Thiokol grid. For this reason, an even finer grid than the nominal grid was constructed to study the affects of grid dependence in the solution. The finer grid was used to compute the flow field solution in the nozzle and all the results are compared in this analysis.

The nominal computational grid, Figure 1, illustrates the geometry of the nozzle. The figure shows one-half of the flow domain with the centerline of the nozzle running along the bottom of the plot and the inlet to the far left of the figure. The nozzle begins with an abrupt vertical wall that is smoothed into a circular arc that forms the nozzle entrance ramp. There is a long straight section from the nozzle throat to the point where the nozzle angle opens up to form the nozzle exit contour. The length of the port section upstream of the nozzle was 6 inches. The radius of this section of the nozzle was also 6 inches. The radius of curvature of the entrance ramp was 1 inch. The throat radius was 3.0125 inches. The length of the flat segment from the throat to the abrupt angle change in the nozzle exit ramp was 0.352 inches. The angle of the nozzle exit ramp was 27.2 degrees. This angle was continued down the nozzle exit 1.23 inches to the end of the insert piece that forms the nozzle exit cone. The actual shape of the ending segment of the nozzle past the 1.23 inch point downstream of the throat was rounded. However, since no information was available at the time of the analysis on the actual shape, a long straight section was added onto this length out to the known exit radius of the nozzle. The computed wall and centerline pressures were only used up to the point that was 1.23 inches downstream of the abrupt angle change.

The nominal nozzle grid has 125 axial grid cells. There are 80 radial grid cells in the inlet region and 40 radial grid cells in the nozzle region. The nominal grid is shown in Figure 1. Figure 2 shows an enlargement in the region of the throat, which is the critical area observed in the analysis. Figure 3 shows an overall view of the refined

computational grid containing 175 axial grid cells. There are 110 radial grid cells in the inlet region and 50 radial grid cells in the nozzle region. Figure 4 shows an enlargement of the refined grid in the same region shown in Figure 2 for the nominal grid. These figures can be compared to show the finer grid resolution in the refined computational grid. The grid is much closer to the nozzle wall and the refined grid has many more axial grid lines in this region.

The mass flow rate at the nozzle inlet is fixed at 400.0 lbm/s, as calculated from the theoretical C* at an MEOP of 2159 psia. A Culick velocity profile is also enforced at the nozzle inlet. The nozzle wall boundary condition was assumed to be a non-slip boundary condition with wall functions being used to resolve the flow near the wall. A supersonic outlet boundary condition was used at the nozzle exit. The analysis was performed using an equilibrium gas. The equilibrium chemistry code, CET86S was used to compute the thermochemisty for the problem. The flame temperature of the gas was computed to be 5355 degrees Rankine at a maximum expected chamber pressure of 2159 psia. Other thermochemistry properties used from the equilibrium chemistry solution include:

1) $\gamma = 1.19$ (ratio of specific heats)
2) $\mu = 5.152 \times 10^{-5}$ lbf-s/ft^2 (viscosity)
3) $M_{wt} = 26.2$ (molecular weight)

Both CELMINT and FDNS were used to compute the flow field solutions and pressure distributions for the igniter nozzle.

Figure 5 shows a color raster plot of the Mach number in the nozzle. Figure 6 shows a color raster plot of the pressure field in the nozzle. Figure 7 shows the geometry of the nozzle as plotted on the same scale used to illustrate the remaining figures that detail the analysis. Figure 8 shows a plot of the pressures in the nozzle for various solutions. The figure shows the wall and centerline pressures computed using the nominal grid. Pressures computed using both CELMINT and FDNS are shown in the figure. The computed pressure fields are similar except in the region from the throat to just downstream of the abrupt angle change in the nozzle. The FDNS pressure values are accepted as the better prediction of the wall pressure since the turbulence model used in FDNS is recognized to be superior to that in CELMINT. The wall pressures computed by Thiokol are also shown in the figure. The pressure computed by Thiokol is close to that predicted by FDNS and CELMINT except in the throat region where there is a very significant difference in the predictions. Some of the difference may be due to the lower resolution in the grid used by Thiokol. The figure also shows the 1-D pressure predictions which fall between the centerline and wall pressures since they are in effect and average in the pressure across a nozzle cross-section. The rise in pressure at the nozzle wall along the flat section of the throat is demonstrated in all three CFD runs although more prominently in the CELMINT and FDNS runs due to the better resolution of the nominal grid over the Thiokol gird. There is a rapid fall in the

wall pressure at the abrupt angle change downstream of the throat. Figure 9 shows a plot of the Mach number that corresponds to the pressure plot shown in Figure 5. The same features are present in this figure. There is a continuous increase in the centerline Mach number which is less affected by the local wall geometry changes. There is an abrupt change in the Mach number near the wall in the throat region. The Mach number decreases near the wall along the flat section aft of the throat in the nozzle and there is an abrupt increase in the Mach number near the wall at the point where the nozzle angle changes. Figure 10 shows a comparison of three flow field solutions. The CELMINT solution for the nominal grid is shown with the FDNS solution for the nominal grid. Also shown, is the refined grid solution computed by FDNS. The refined grid shows more detail in the flow solution than the course grid solution. The pressure drop at the abrupt angle change in the nozzle exit geometry is sharper and the pressure rise along the flat section of the nozzle is greater. There is also a noticeable dip in the wall pressure just downstream of the abrupt angle change in the nozzle followed by a recovery of the wall pressure to agree with the other solutions. This figure demonstrates the importance of grid resolution in computing accurate flow field solutions for problems where there are abrupt geometry changes in the nozzle. The refined grid should be used to obtain the best resolution of the wall pressure in this nozzle. The differences in the nozzle pressure field demonstrated by the refined grid solution may be of a significant magnitude when assessing pressure loading on the nozzle.

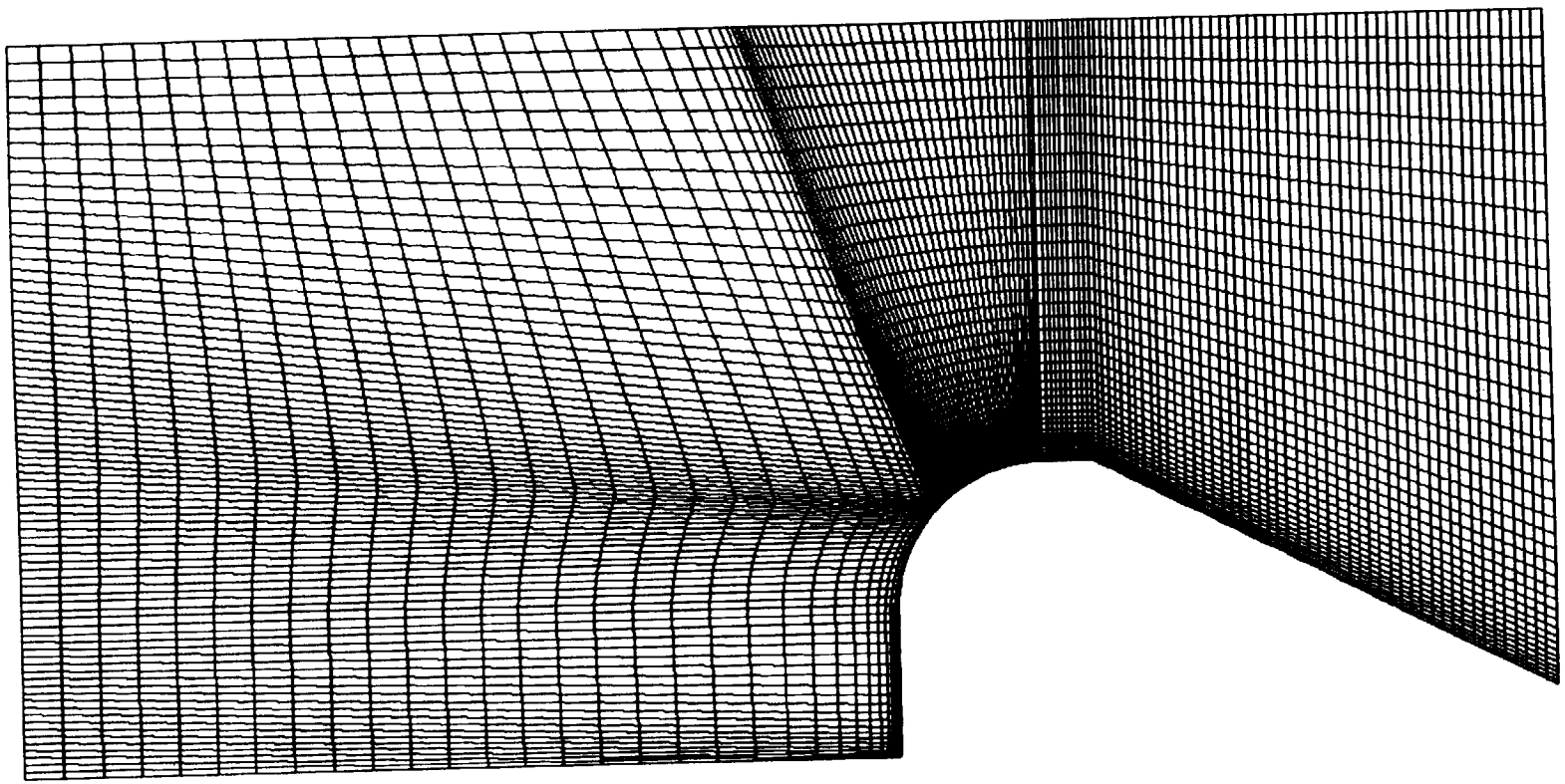

Figure 1. RSRM Igniter Nozzle, Nominal Grid

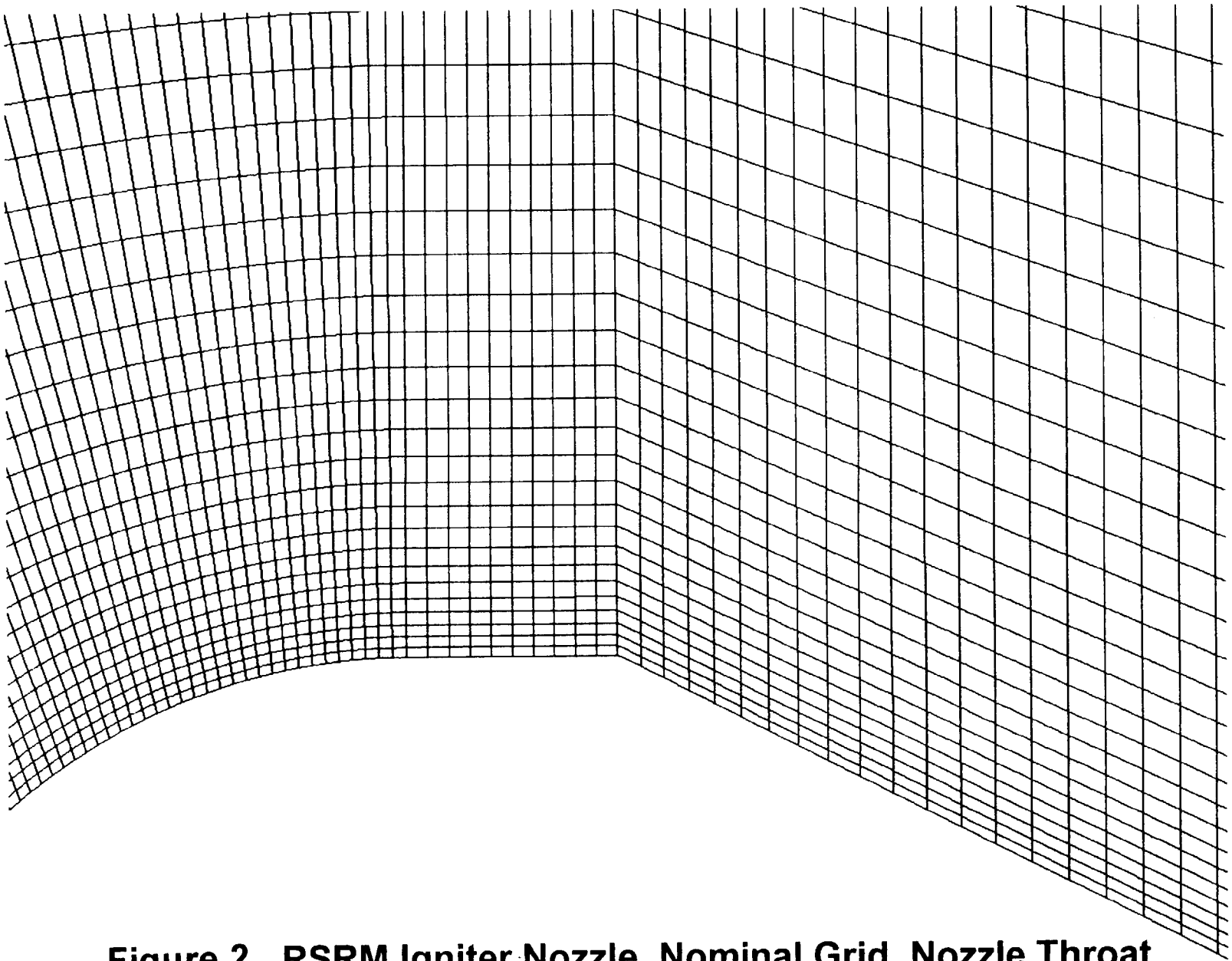

Figure 2. RSRM Igniter Nozzle, Nominal Grid, Nozzle Throat

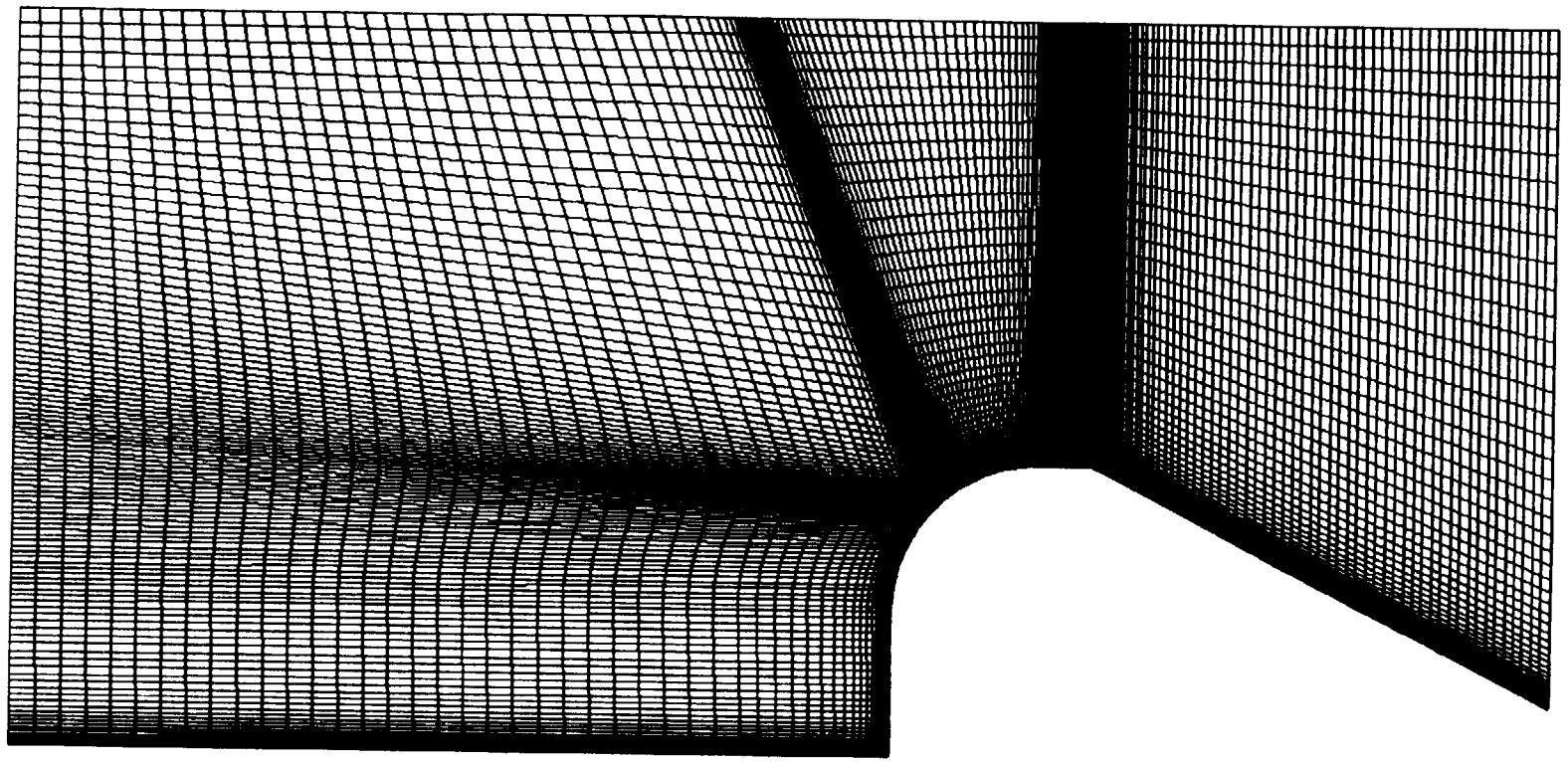

Figure 3. RSRM Igniter Nozzle, Refined Grid

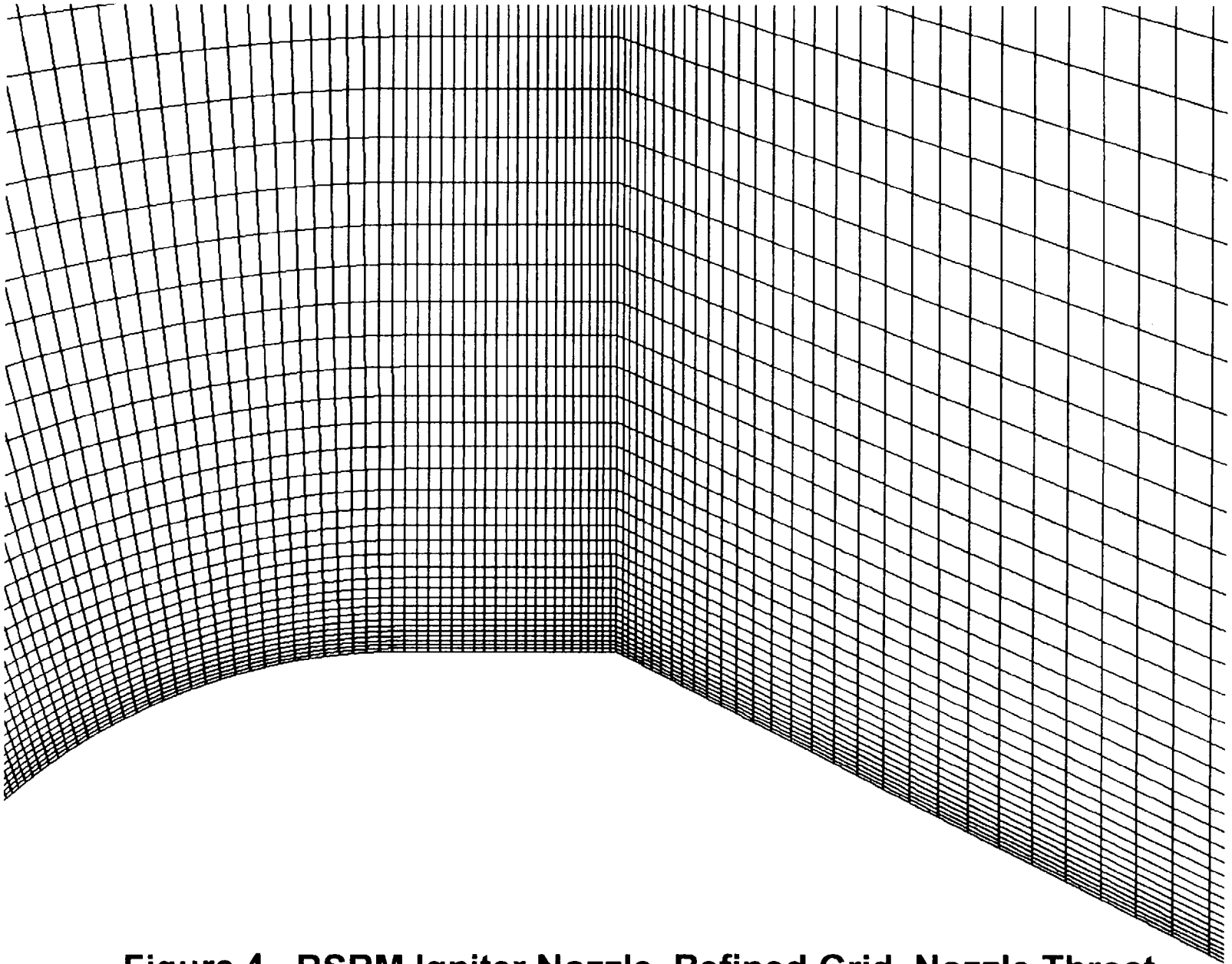

Figure 4. RSRM Igniter Nozzle, Refined Grid, Nozzle Throat

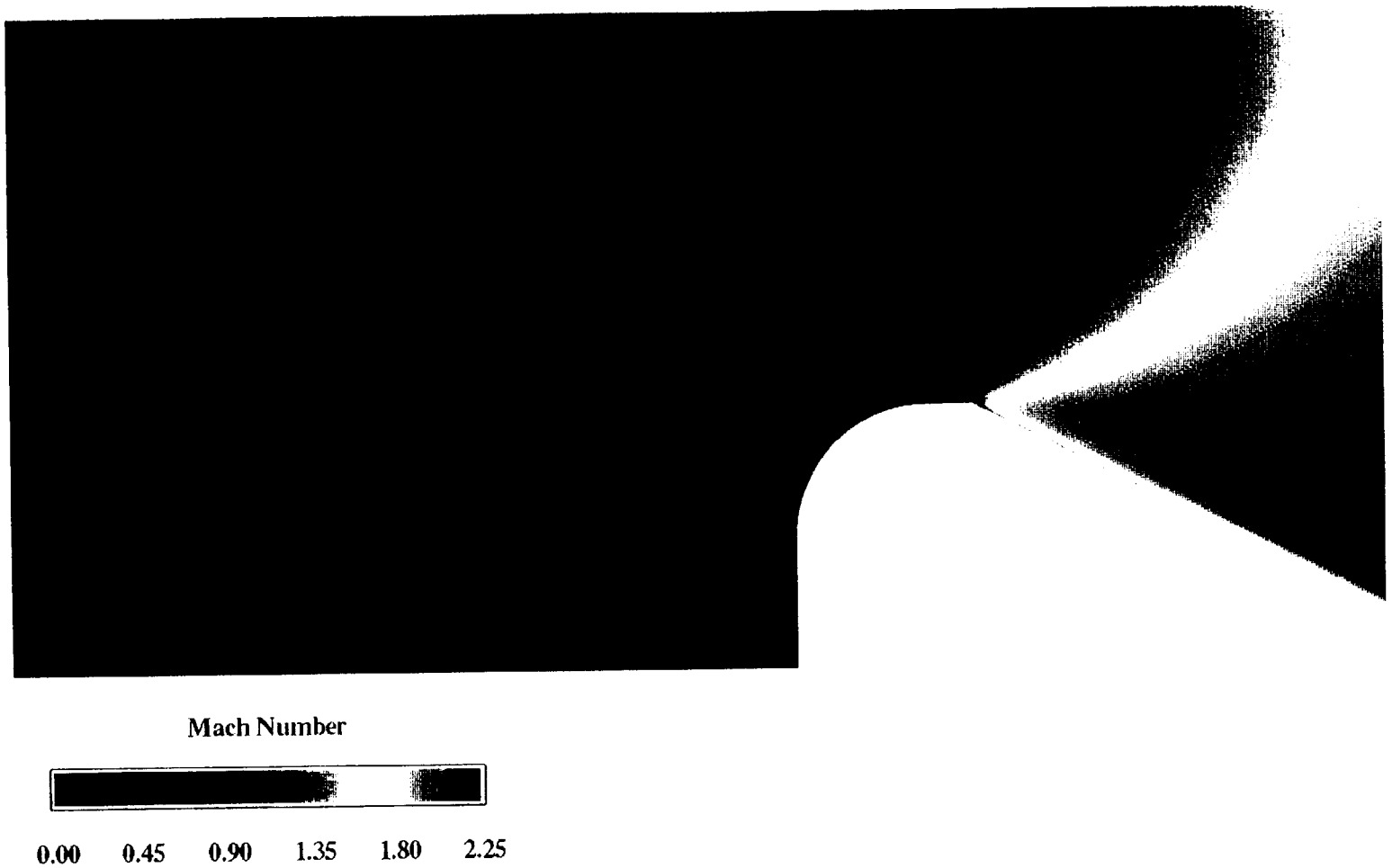

Figure 5. RSRM Igniter Nozzle, Mach Number

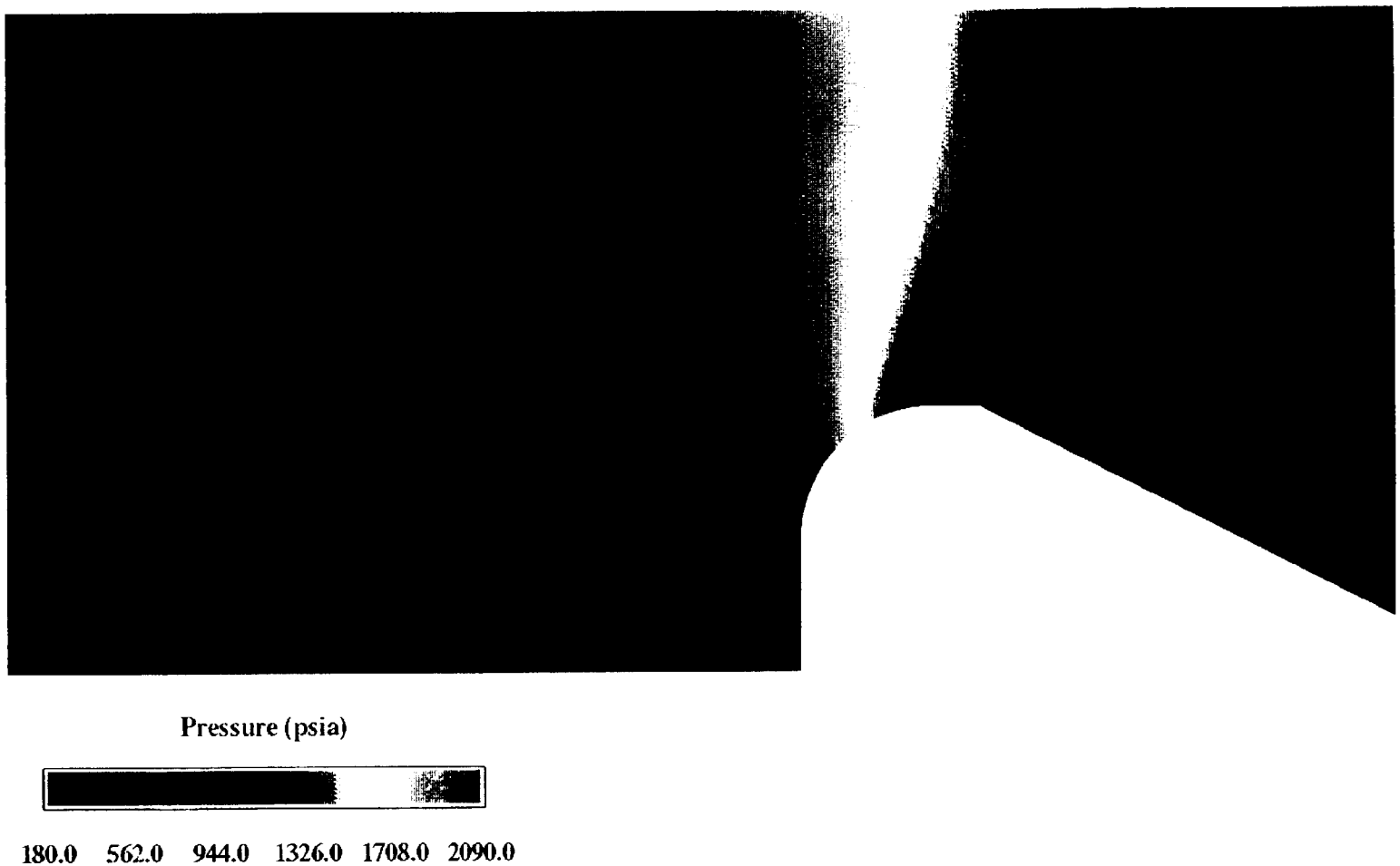

Figure 6. RSRM Igniter Nozzle, Pressure

Figure 7. RSRM Igniter Nozzle Geometry

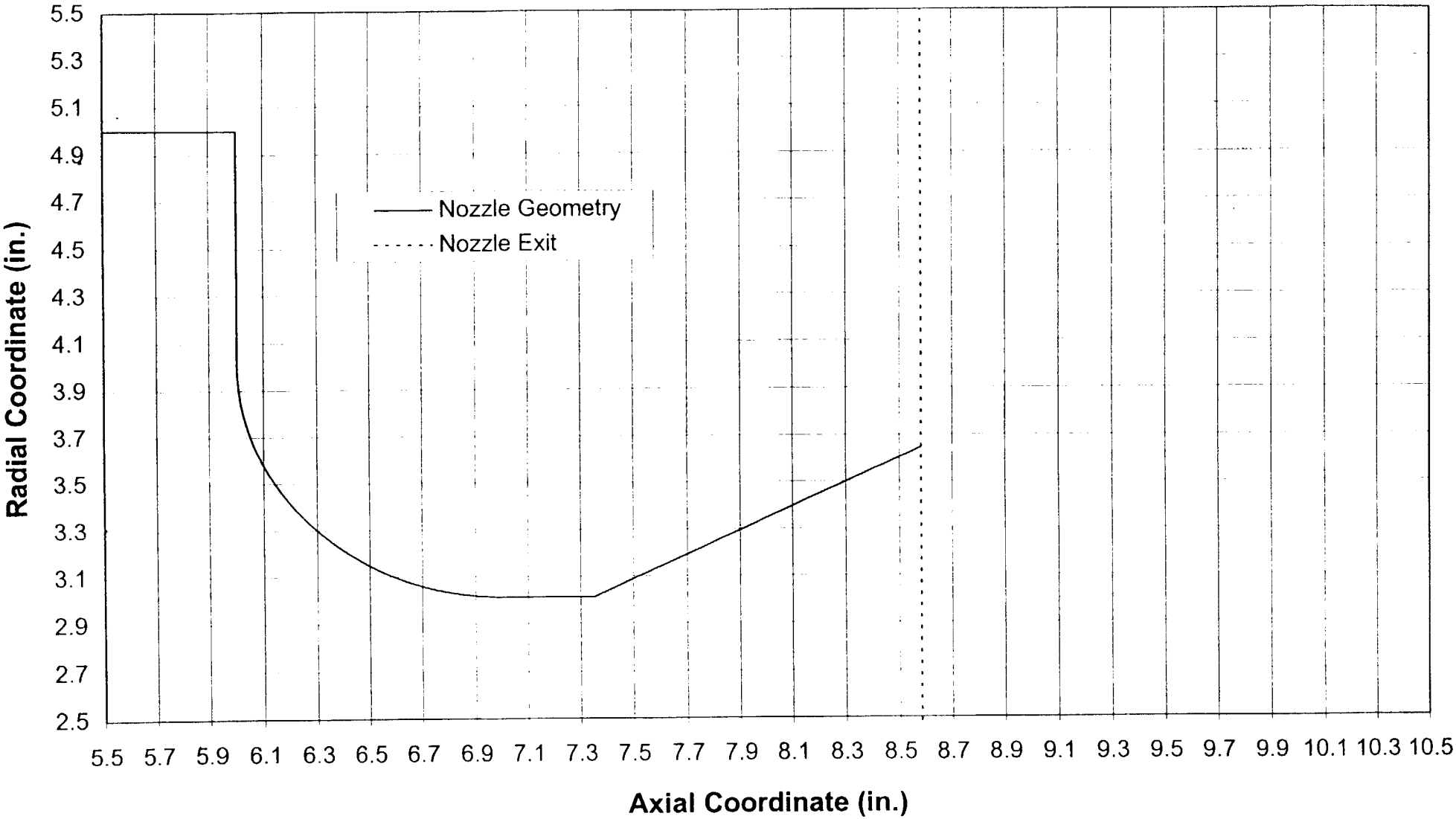

ERC Inc. 5/8/98

Figure 8. RSRM Igniter Nozzle CFD Analysis
Pressures Based on MEOP (2159 psia)

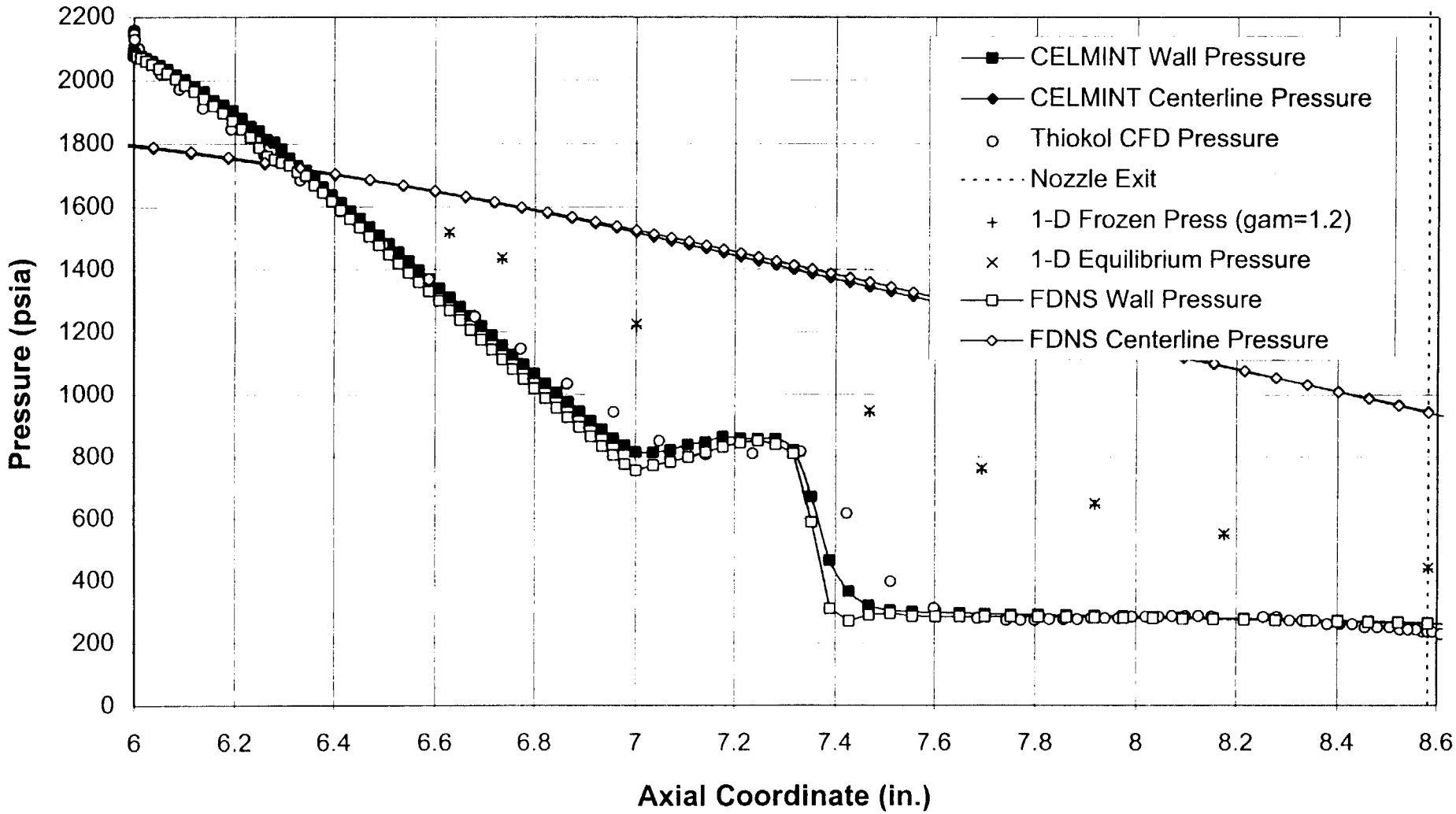

ERC Inc. 5/8/98

Figure 9. RSRM Igniter Nozzle Analysis
CFD Mach Number

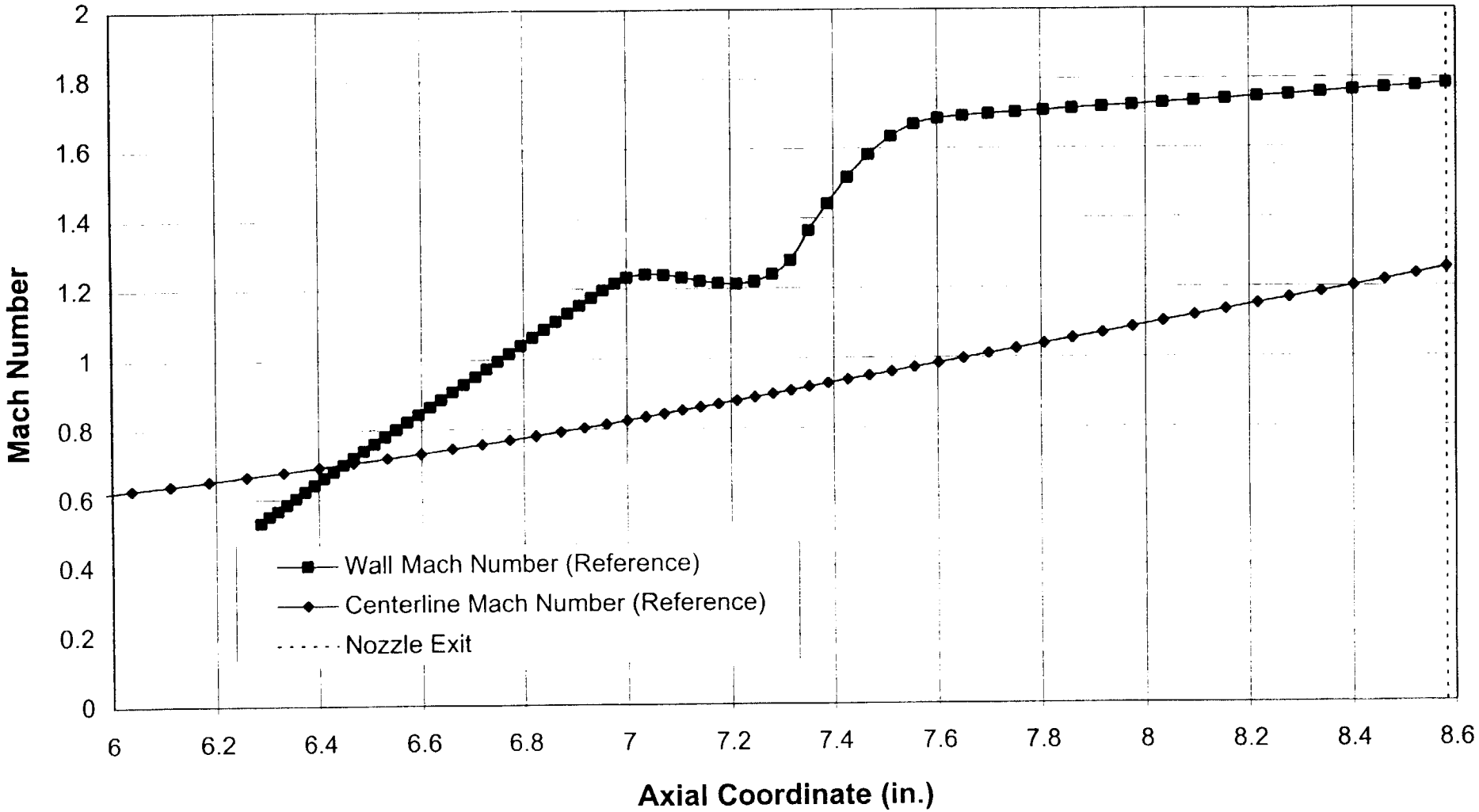

ERC Inc. 5/8/98

Figure 10. RSRM Igniter Nozzle Analysis
Comparison of Course and Fine Grid CFD Pressures

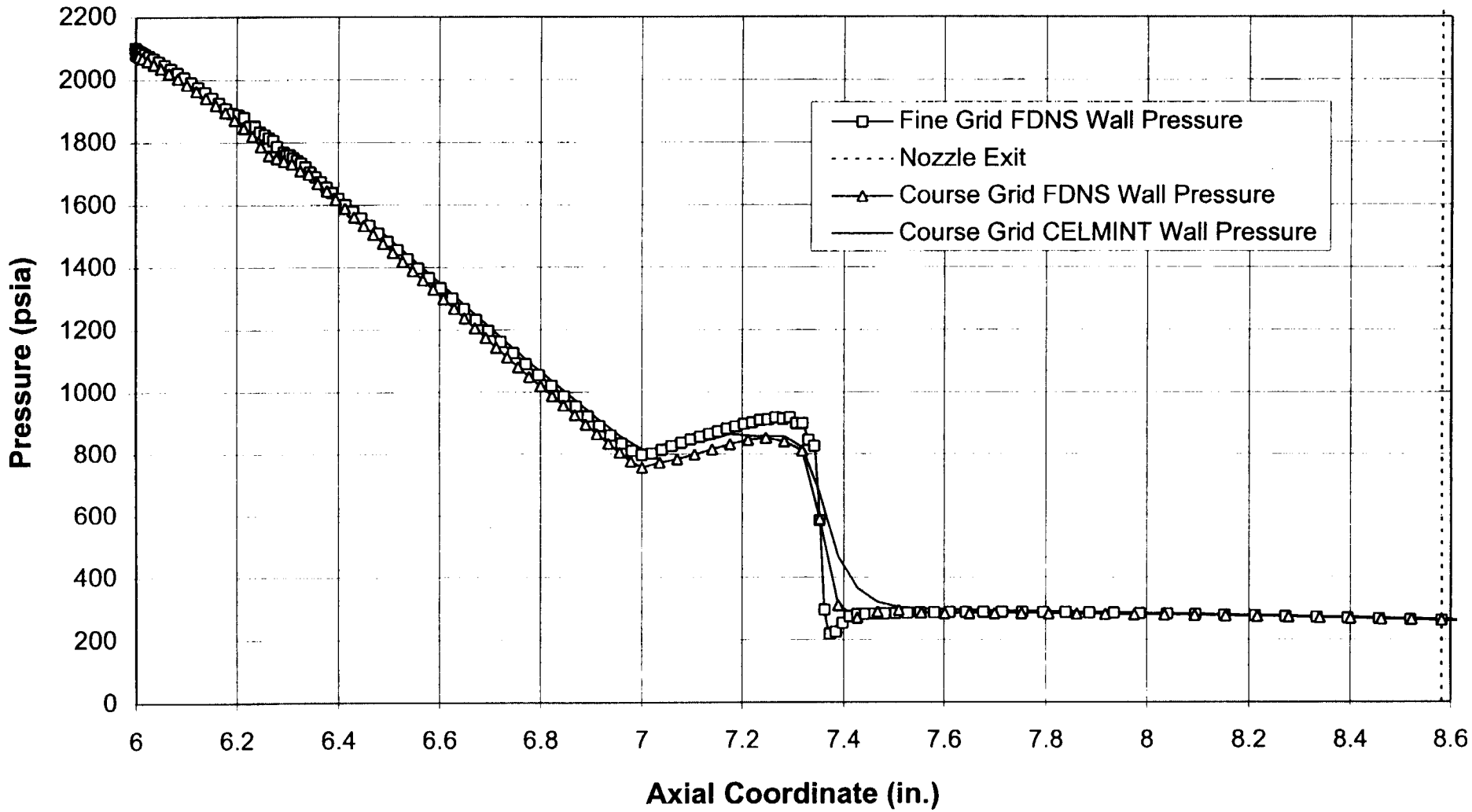

ERC Inc. 5/8/98

4.4 Nozzle Joint 4 Erosion Anomaly

ERC performed CFD work to support the Nozzle Joint 4 Abnormal Erosion Investigation. The analyses included were: 1) an erosion analysis performed as a function of motor burn time to investigate the heat transfer induced erosion enhancement caused by an initial 0.25 inch spall on the throat ring at the throat ring/forward exit cone interface, 2) an analysis of the pressure loads associated with a 0.4 inch initial spall on the throat ring at the throat ring/forward exit cone interface, 3) an investigation into the effects of a 1.0 inch high polysulfide bump on the local environment in the region of the throat ring/forward exit cone interface, 4) a two-dimensional analysis of a hemispherical 1.0 inch high polysulfide bump on a flat plate and, 5) a three-dimensional analysis of two 1.0 inch high polysulfide bumps located four inches apart on a flat plate. CELMINT was the main CFD code used to perform the analyses discussed but some initial runs with FDNS were made for the investigation involving a polysulfide bump on a flat plate.

The general nozzle geometry configuration used for all the analyses discussed except the analysis involving a polysulfide bump on a flat plate is shown in Figure 1A. The illustrates that the solutions discussed in this report were obtained by solving for only the aft end of the motor flow field so that more grid could be concentrated in the region of the flow field of most interest while allowing the total grid size to be minimized in order to provide rapid response to the overall nozzle investigation. The accuracy of the overall solution was maintained by using partial motor inlet boundary conditions obtained from a solution for the complete motor flow field. The geometry that was used to obtain the complete motor flow field solution is shown in Figure 2A. Axial and radial velocity profiles were used along with the port mass flow rate at the partial motor inlet plane to provide boundary conditions for the momentum and continuity equations. The total mass flow rate including the aft corner propellant grain was 9429 lbm/second. Radial profiles for the turbulence kinetic energy and dissipation rate were also used at the partial motor inlet plane to provide boundary conditions for the κ–ε equations. The combustion flame temperature was used as the thermal boundary condition for the energy equation. Table 4.4.1 shows the basic thermochemistry properties used in this analysis.

Table 4.4.1 Thermochemistry Properties Used in All CFD Analyses

Motor Property	
Viscosity	6.189×10^{-5} lbm/sec-ft
Molecular Weight	28.373
Specific Heat Ratio	1.1366
Flame Temperature	6098 °R

The first analysis discussed involved a spall on the nozzle throat ring. Given some initial spall geometry, the investigation team wanted to know how the initial spall would erode with time in the vicinity of joint 4. The erosion of the initial spall was determined as a function of motor burn time by the following iterative process. Flow field and heat transfer coefficients were computed for both a nominal eroded nozzle geometry and the initial spalled nozzle geometry (0th iteration geometry). The ratio of the heat transfer coefficients for the nominal and spalled nozzle geometries was computed so that an erosion enhancement rate was determined. The erosion enhancement rate represents the increase or decrease in erosion for the spalled geometry over the nominal geometry. This enhancement rate was applied to the nominal nozzle erosion rate (which is known from test data) to extrapolate the erosion of the nozzle to some later burn time. The time step over which the enhancement rate was applied was constrained to a value small enough so that a constant enhancement rate over the time step would remain valid. The erosion of the nozzle was calculated over the chosen time step to obtain a first iteration geometry. A flow field and corresponding heat transfer coefficients were then computed for the new geometry. New enhancement rates were calculated for the new geometry and used to extrapolate the erosion to a later burn time. This iterative scheme was continued until the motor web time was reached.

The flow field and heat transfer coefficients were computed for the basic eroded nozzle geometry shown in Figure 1A. These results are not shown in this report. The flow field and heat transfer coefficients were also computed for the basic geometry shown in Figure 1A, but with a spall on the throat ring at joint 4 as illustrated in Figure 3A (0th iteration geometry). The spall depth at joint 4 was 0.25 inches and the spall wedge out occurred along the lay-up ply line. The length of the spall upstream of joint 4 was 0.63 inches. The solution for the 0th iteration geometry is not shown in this report. The 0th iteration geometry enhancement rates were computed for locations along the nozzle spall geometry, as shown in Table 4.4.2. Figure 4A shows the location of the points 1 to 7 corresponding to those shown in Table 4.4.2. In order to extrapolate the nozzle erosion to a later time using the enhancement rates computed, nominal nozzle erosion rates were required. A nominal erosion rate of 4.146×10^{-3} inches/second was applied over the specified time step to yield nominal nozzle erosion as shown in Table 4.4.3. The enhancement factors were applied to the nominal erosion at the point locations 1 to 7 to obtain the 1st iteration geometry shown in Figure 5A. The initial spall occurred at approximately 10 seconds so that the 0th iteration geometry was the 10 second burn time geometry. The enhancement rates shown in Table 4.4.2 were applied over a time step of 10.0 seconds so the 1st iteration geometry is the 20 second burn time geometry.

Table 4.4.2 Throat Ring Spall Geometry, 0th Iteration, 10 Second Geometry

Point Location	Enhancement Factor
1	1
2	0.5
3	0.1
4	0.5
5	2.1
6	4.5
7	1

Table 4.4.3 RSRM-56 CFD Nominal Nozzle Erosion

Solution	Time (sec)	Δ Time (sec)	Δ Erosion$_{nominal}$ (inches)
0	10	0	0.033168
1	20	10	0.04146
2	25	5	0.02073
3	55	30	0.12438
4	85	30	0.12438
5	120	35	0.14511

A flow field solution was computed for the 1st iteration geometry. The calculated enhancement rates are shown in Table 4.4.4. Figure 5A shows the corresponding point locations associated with Table 4.4.4. A 5.0 second step time was used to calculate the 2nd iteration geometry shown in Figure 6A. A smaller step time was used for this iteration than for the previous iteration because a larger step time caused the erosion to change the spall geometry too much.

Table 4.4.4 Throat Ring Spall Geometry, 1st Iteration, 20 Second Geometry

Point Location	Enhancement Factor
1	1
2	1.35
3	0.4
4	2
5	5
6	1

A flow field solution was calculated for the 2nd iteration geometry and the calculated enhancement rates are shown in Table 4.4.5. Figure 6A shows the corresponding point locations associated with Table 4.4.5. A 30.0 second step time was used to calculate the 3rd iteration geometry shown in Figure 7A.

Table 4.4.5 Throat Ring Spall Geometry, 2nd Iteration, 25 Second Geometry

Point Location	Enhancement Factor
1	1
2	0.9
3	0.8
4	0.4
5	0.4
6	1
7	1

The flow field solution for the 3rd iteration geometry was obtained and used to calculate the enhancement rates shown in Table 4.4.6. Figure 7A shows the corresponding point locations associated with Table 4.4.6. A 30.0 second step time was used to calculate the 4th iteration geometry shown in Figure 8A.

Table 4.4.6 Throat Ring Spall Geometry, 3rd Iteration, 55 Second Geometry

Point Location	Enhancement Factor
1	1
2	1
3	0.6
4	0.3
5	0.3
6	1
7	1

The 4th iteration geometry was the final geometry for which a flow field solution was obtained. The enhancement rates shown in Table 4.4.7 were used to calculate the final 5th iteration geometry by using a 35 second step time. Figure 8A shows the corresponding point locations associated with Table 4.4.7. Figure 9A shows a compilation of the various iteration geometries to show the erosion of the nozzle from the initial spall to web time. The figure shows the nominal erosion upstream and

downstream of the spall at the far left and right corners of the plot. This is the erosion the nozzle would have undergone if the spall had not occurred. The figure also shows the progressive wash out of the spall as computed from the heating enhancement factors computed from the flow field solutions.

Table 4.4.7 Throat Ring Spall Geometry, 4th Iteration, 85 Second Geometry

Point Location	Enhancement Factor
1	1
2	0.91
3	0.91
4	1.2
5	0.94
6	1.0

The computations of the nozzle geometry erosion assumed that there was only an initial spall and no subsequent spalling of the nozzle surface in the vicinity of joint 4.

In order to compare the nozzle flow fields in the joint 4 vicinity as erosion of the spall progresses, a series of figures showing the velocity field in the vicinity of joint 4 will be presented. Figures 10A to 14A show the velocity field in the joint 4 vicinity for the 10, 20, 25, 55, 85 second burn time erosion stages computed and discussed for geometry iterations 0 to 4. There is a large recirculation region created by the spall cavity for the 0th and 1st geometry iterations shown in Figures 10A and 11A, respectively. The supersonic flow stream in the nozzle moves over the top of the cavity. There is some impingement at the top corner of the forward exit cone face in the 0th iteration geometry and an increased amount for the 1st iteration geometry. The recirculation region becomes smaller as erosion progresses from iteration to iteration until the 4th iteration geometry shows no recirculation. The flow stream fully expands into the spall cavity at this stage.

The static pressure was also needed along the nozzle surface for the initial spall geometry to investigate thermal and pressure loading along the spall surfaces and in joint 4. Figure 15A shows the complete nozzle wall static pressure contour from a point on the nozzle entrance ramp upstream of the throat to the nozzle exit. Figure 16A shows the wall static pressure variation in the vicinity of nozzle spall. Figure 17A shows the geometry of the initial spall with various locations along the spall labeled. The pressure drops initially as the flow expands into the spall cavity at the beginning of the spall. After an initial expansion, the pressure rapidly returns to the pre-expansion value and rises slowly to a value associated with the pressure in the bottom of the spall at joint 4. Pressure rises rapidly along the forward exit cone face exposed by the spalling of the throat ring. The pressure rise along the face is about 45 psi as shown in Figure

18A which shows just the pressure along the forward exit cone face from the bottom of the spall to the top corner of the forward exit cone face. Figure 19A shows a plot of the velocity along the forward exit cone face. The velocity rises rapidly from the bottom of the spall to a maximum value and then begins to fall again to a minimum point. The velocity rises from the minimum point to the top corner of the forward exit cone face. The non-monatomic shape of the velocity along the face is because of the attachment of the flow near the top corner of the forward exit cone face to form the recirculation region in the spall cavity. The minimum velocity point shown in the figure represents a point near the flow reattachment.

An analysis was performed on an initial spall geometry similar to the one discussed in section C. Figure 20A shows the initial spall depth of this configuration was 0.4 inches and the length of the spall was 0.998 inches. This configuration was analyzed to determine the pressure distribution in the spall region in order to determine the propensity for hot gasses to be driven into joint 4. The boundary conditions for this problem are the same as discussed in section B. Figure 21A shows the overall nozzle grid used to obtain a solution for this geometry. Figure 22A shows the grid spacing in the vicinity of the spall. Figure 23A shows the velocity field in the spall region. Just as in the case of the 0.25 inch deep spall previously discussed there is a prominent recirculation region present in the spall cavity. The length of the spall cavity is greater for the 0.4 inch deep spall than for the 0.25 inch spall and the flow associated with the 0.4 inch spall expands a little more into the spall cavity than seen in the 0.25 inch spall case. The flow reattaches along the forward exit cone face at a point near the top corner of the face. Figure 24A shows a plot of the Mach number in the vicinity of the spall up to a value of one. The plot illustrates the delineation between subsonic and supersonic flow. Notice the small yellow region near the wall downstream of the spall which is not seen upstream of the spall. This illustrates how the velocity profile near the wall is disturbed downstream of the spall for a significant distance. Figure 25A shows the pressure in the region of the spall and how the spall greatly affects the local pressure field. The flow initially expands into the spall cavity and then the presence of a shock is seen just downstream of the beginning of the spall. Figure 26A shows the pressure along the nozzle surface from a point along the nozzle entrance ramp to the nozzle exit. Figure 27A shows the static pressure along the nozzle surface in the vicinity of the spall. The plot is similar in structure to that seen in Figure 16A which shows the wall pressure for the 0.25 inch spall. Figure 28A shows the pressure along the forward exit cone face from the bottom of the spall to the top corner of the forward exit cone face. The pressure rise is a little more for this spall configuration than for the 0.25 inch spall. The pressure rise is more than 50 psi for this configuration. The pressure in the bottom of the spall cavity is also higher for the 0.4 inch spall configuration than for the 0.25 inch configuration.

The presence of polysulfide bumps in the vicinity of joint 4 prompted an interest in pressure and heating loads on a 1.0 inch polysulfide bump in the nozzle. The geometry considered was the nominal nozzle geometry with a 1 inch radius bump centered at joint 4. Figure 29A shows the geometry of the bump considered in this analysis. Figure

30A shows the overall grid used in this analysis while Figure 31A shows an enlargement of the grid in the region of the bump. The boundary conditions used in the analysis were the same as discussed previously in this section. Figure 32A shows the velocity field in the vicinity of the bump. There is a small recirculation in front of the bump and flow rapidly accelerates over the bump. Figure 33A delineates the supersonic and subsonic regions of the flow by plotting supersonic flow as red. The shock standoff distance in front of the bump was a little more than two inches. The acceleration of the flow as it passes over the bump is more visible in this figure. The flow is supersonic as it nears the top of the bump and remains supersonic as the flow expands down the bump except for a small compression region at the end of the ramp on the backside of the bump. Figure 34A shows the pressure field in the vicinity of the bump. Again, this figure shows that the shock stands off a large distance in front of the bump. Notice that the effect of the bump extends far away from the bump in the radial direction. The investigation team also wanted to know whether the bump would be blown off by the fluid dynamic pressure loading on the bump. In support of this analysis the static pressure along the surface of the bump was used to determine the mechanical loading on the bump. A plot of the pressure along the bump surface is shown in Figure 35A.

Two- and Three-Dimensional analyses of hemispherical bumps on a flat plate were also analyzed. The two-dimensional portion of this analyses was completed and the overall grid is shown in Figure 36A. An enlargement of the grid in the vicinity of the bump is shown in Figure 37A. A supersonic boundary condition was used at the inflow boundary. The velocity, temperature, and the density were specified at this boundary. These inlet boundary conditions were determined by averaging the conditions across the port from the RSRM nozzle geometry. Far field boundary conditions were used at the boundary at the top of the page shown in Figure 36A. Supersonic exit boundary conditions were used at the outlet boundary (the right side boundary of Figure 36A). Figure 38A shows the velocity field in the vicinity of the bump is very similar to the velocity field shown in Figure 32A for the nozzle bump problem. Separation of the flow does occur behind the bump for this configuration since the bump is modeled here as a half circle instead of having a ramp on the backside. The Mach number plot, Figure 39A, delineates the supersonic flow as red. Figure 40A shows the pressure field in the vicinity of the bump. Again, except for the backside of the bump, the flow field for the two-dimensional bump on a flat plate is similar to the nozzle bump problem as expected. The heat transfer enhancement rate for this 2-D bump is shown in Figure 41A. Enhancement rates for only the front half of the bump are shown. The enhancement factor increases from the nominal value of one in front of the bump except for the stagnant flow very close to the corner between the bump and the flat plate. The enhancement factor then increases rapidly as flow moves over the bump to a maximum value near the top of the bump.

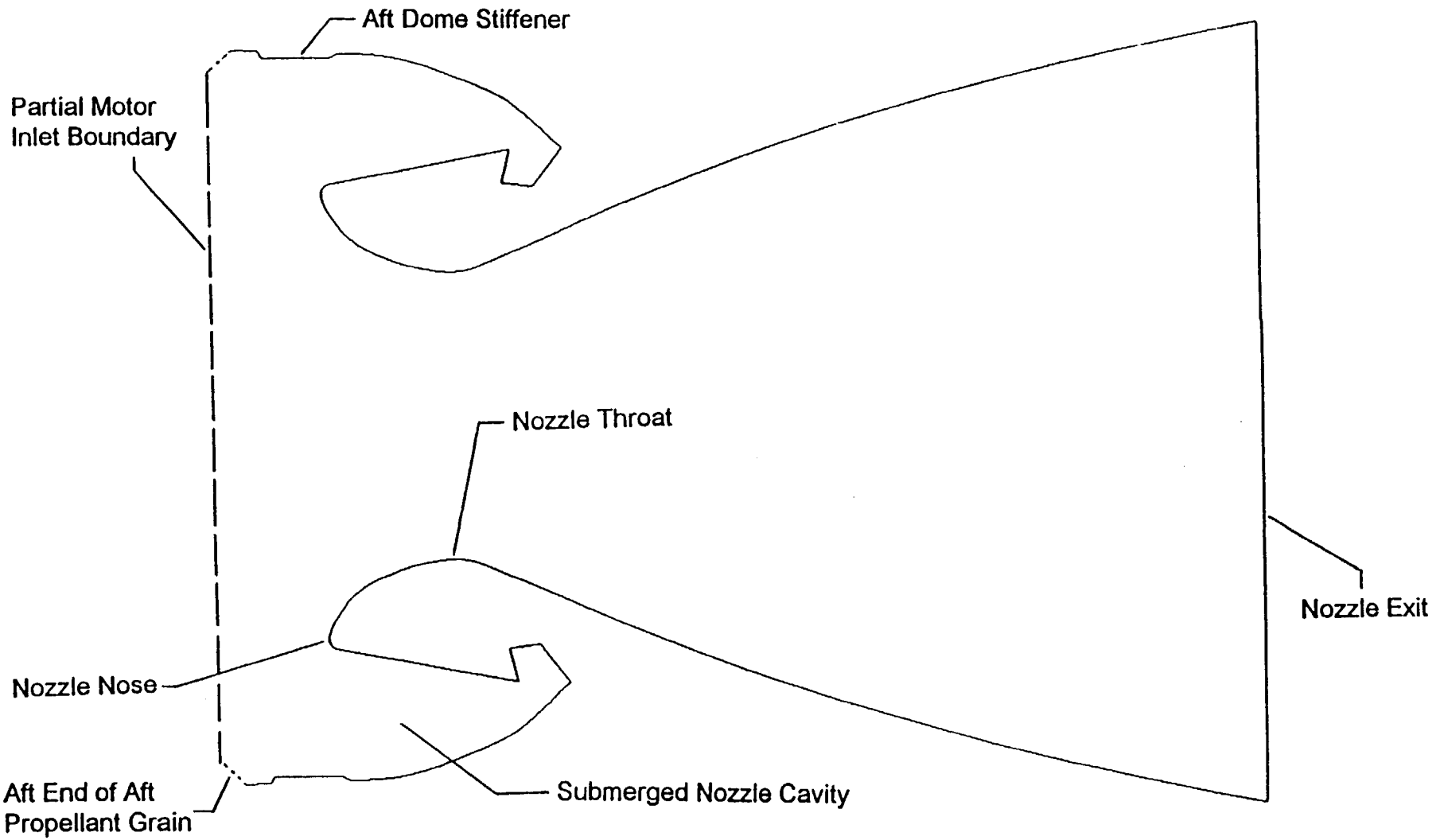

Figure 1A. General Motor Geometry Used to Compute the Various Nozzle Solutions

Figure 2A. RSRM 65 Second Full Motor Geometry

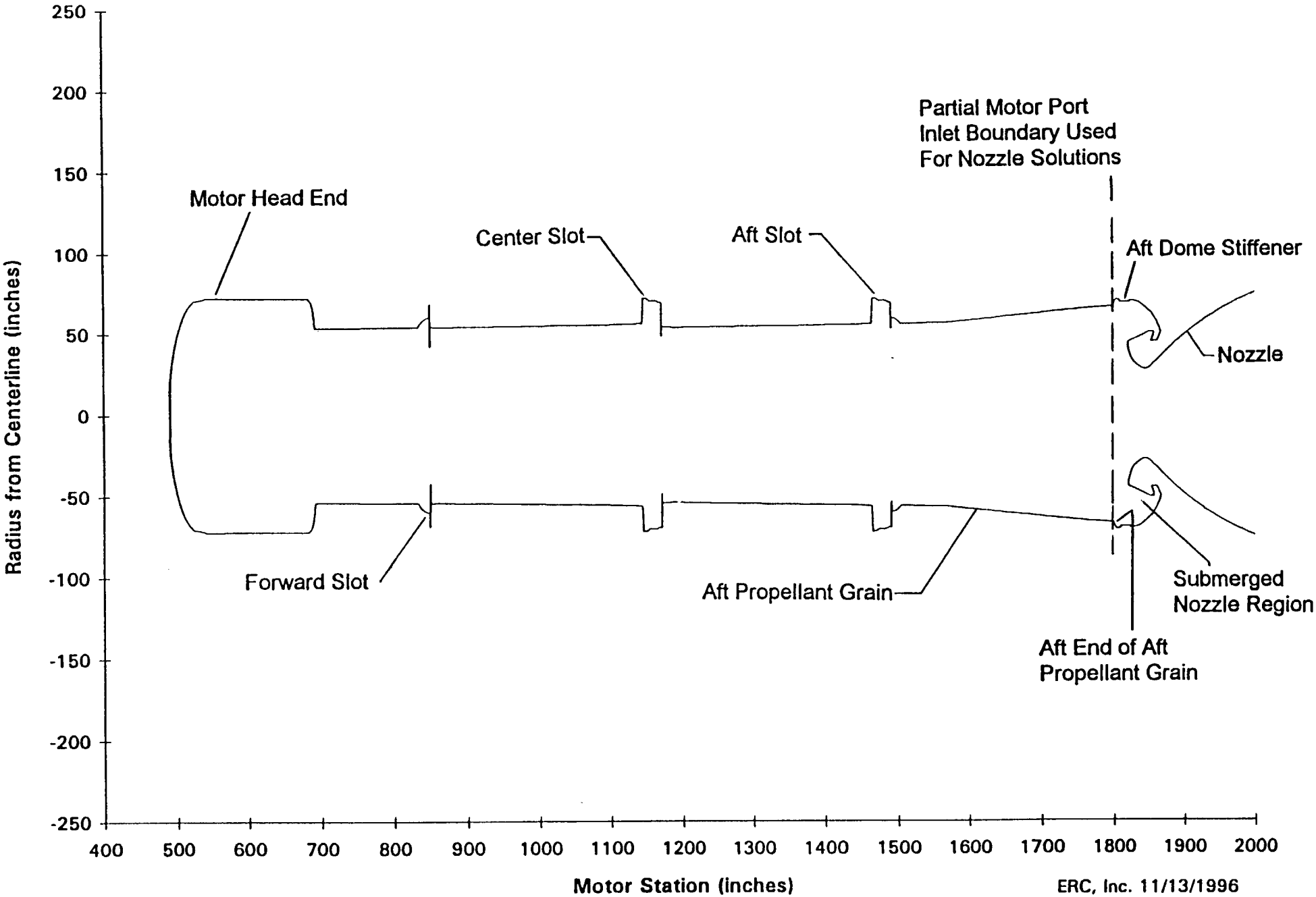

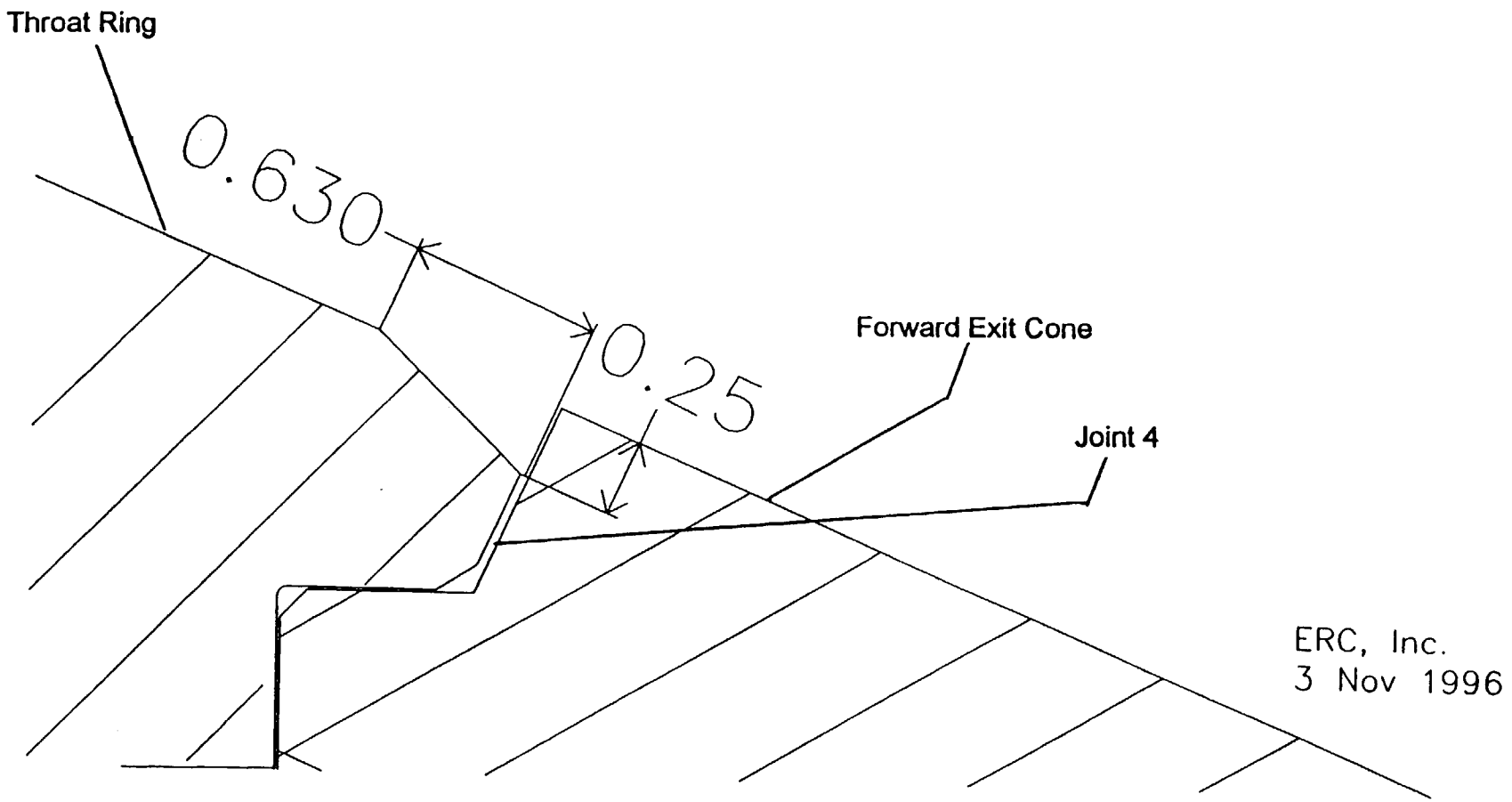

Figure 3A. Throat Ring Spall Scenario Geometry, 0.25 Inch Spall

Figure 4A. RSRM Throat Ring 0th Iteration Spall Geometry Enhancement Factor Locations

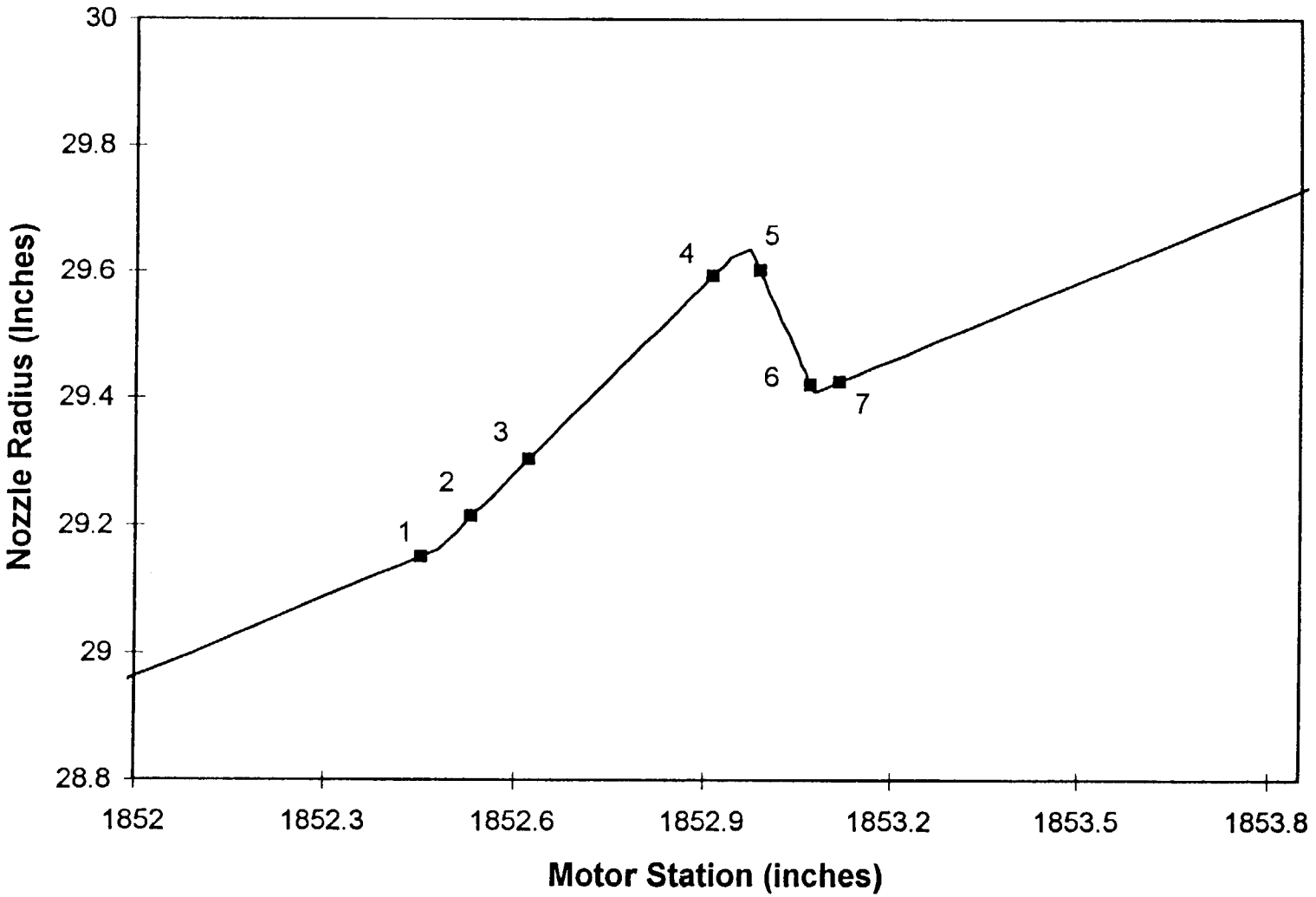

ERC Inc. 1/23/97

Figure 5A. RSRM Throat Ring 1st Iteration Spall Geometry Enhancement Factor Locations

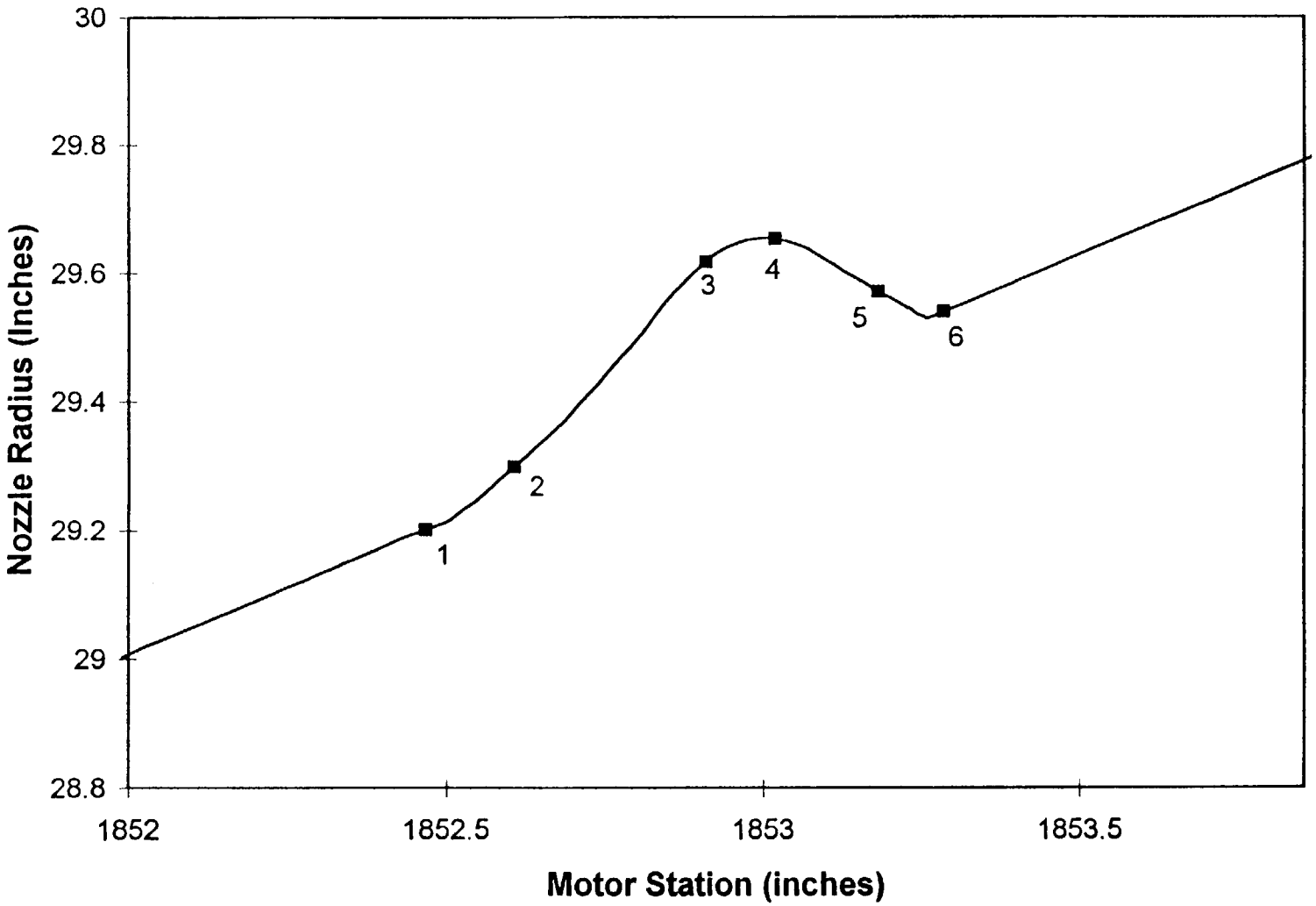

ERC Inc. 1/23/97

Figure 6A. RSRM Throat Ring 2nd Iteration Spall Geometry Enhancement Factor Locations

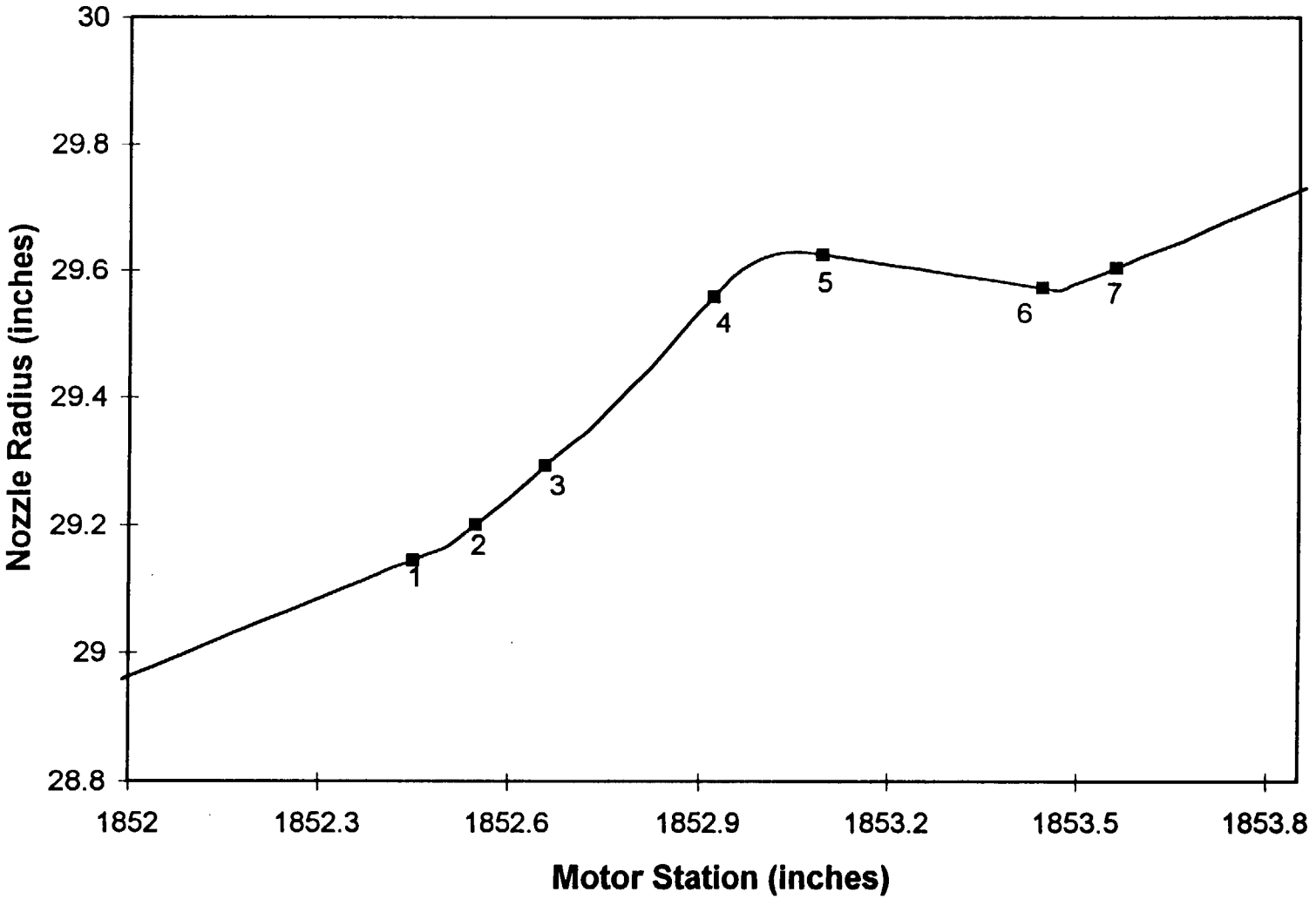

ERC Inc. 1/23/97

Figure 7A. RSRM Throat Ring 3rd Iteration Spall Geometry Enhancement Factor Locations

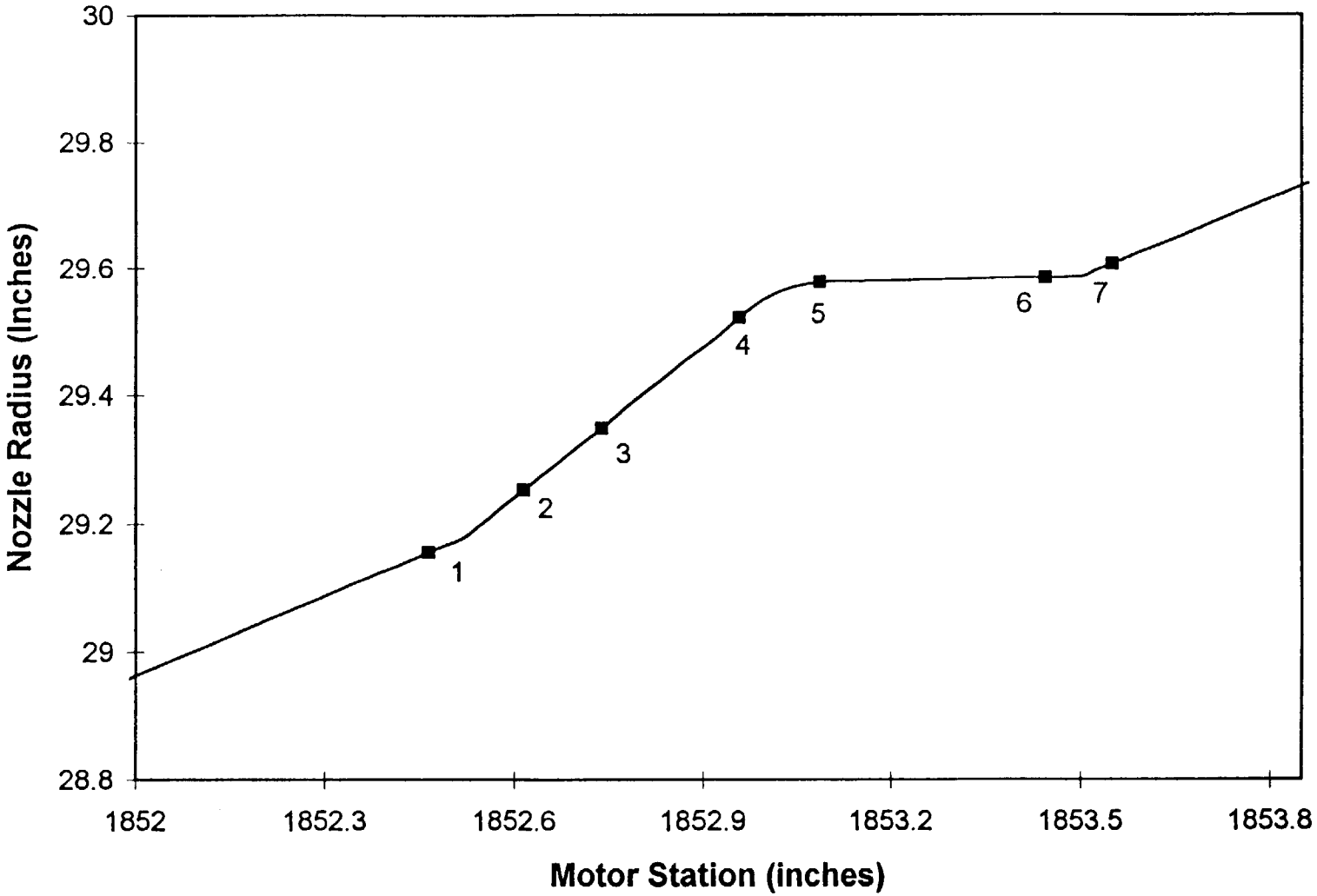

ERC Inc. 1/23/97

Figure 8A. RSRM Throat Ring 4th Iteration Spall Geometry Enhancement Factor Locations

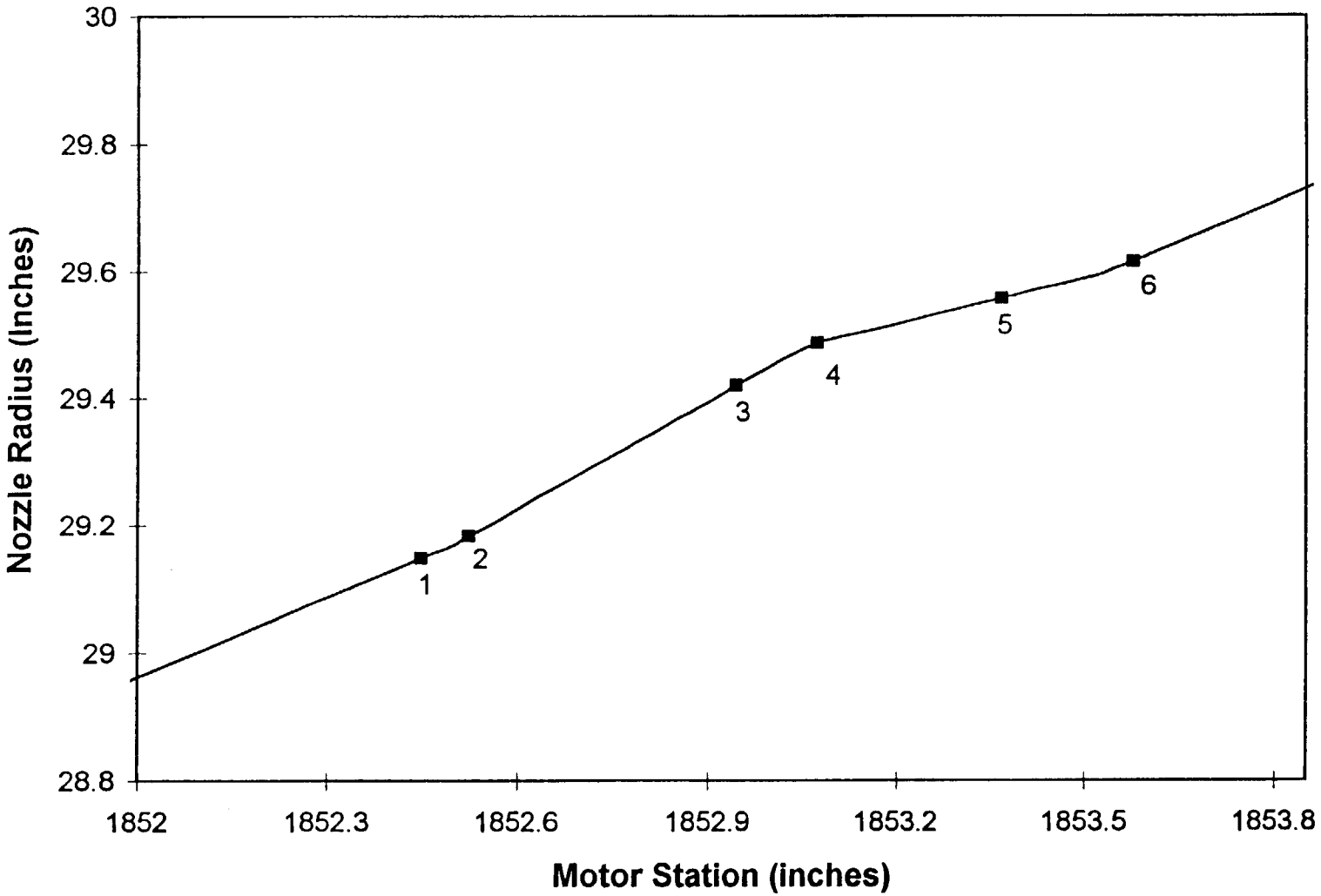

ERC Inc. 1/23/97

Figure 9A. RSRM Throat Ring Spall Geometry Erosion History

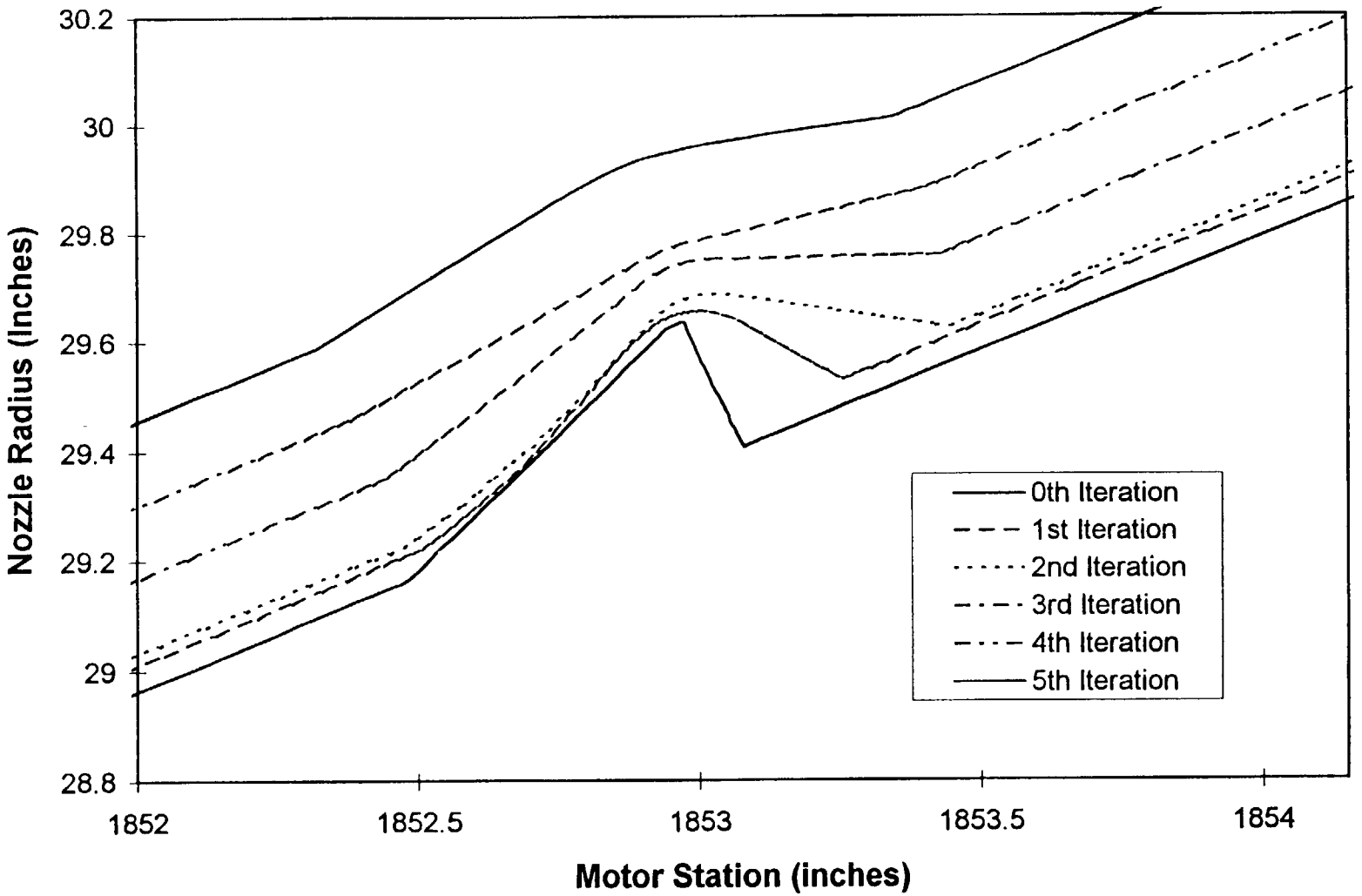

ERC Inc. 1/23/97

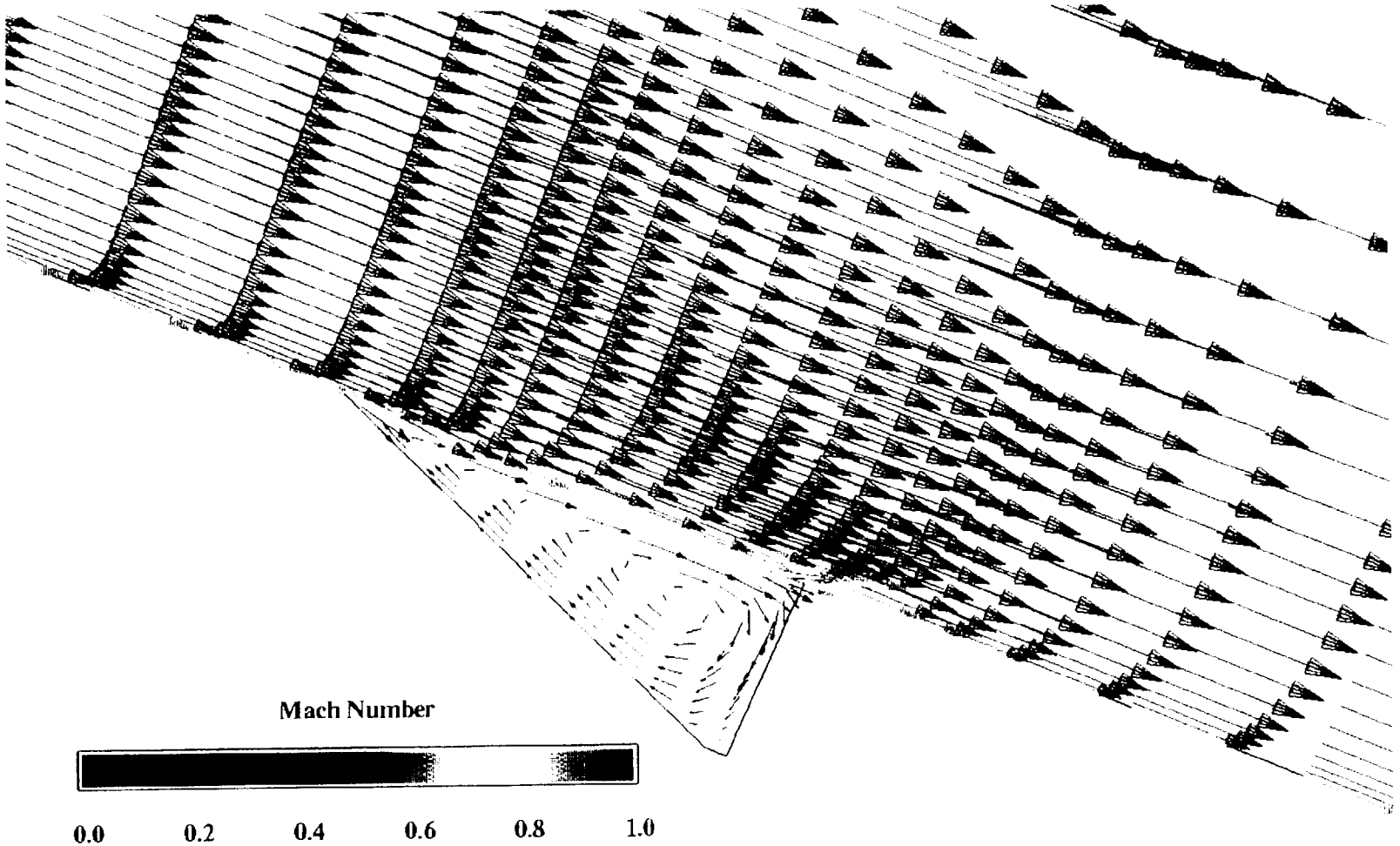

Figure 10A. RSRM Throat Ring 0th Iteration Spall Geometry Spall Depth, 0.25 Inches

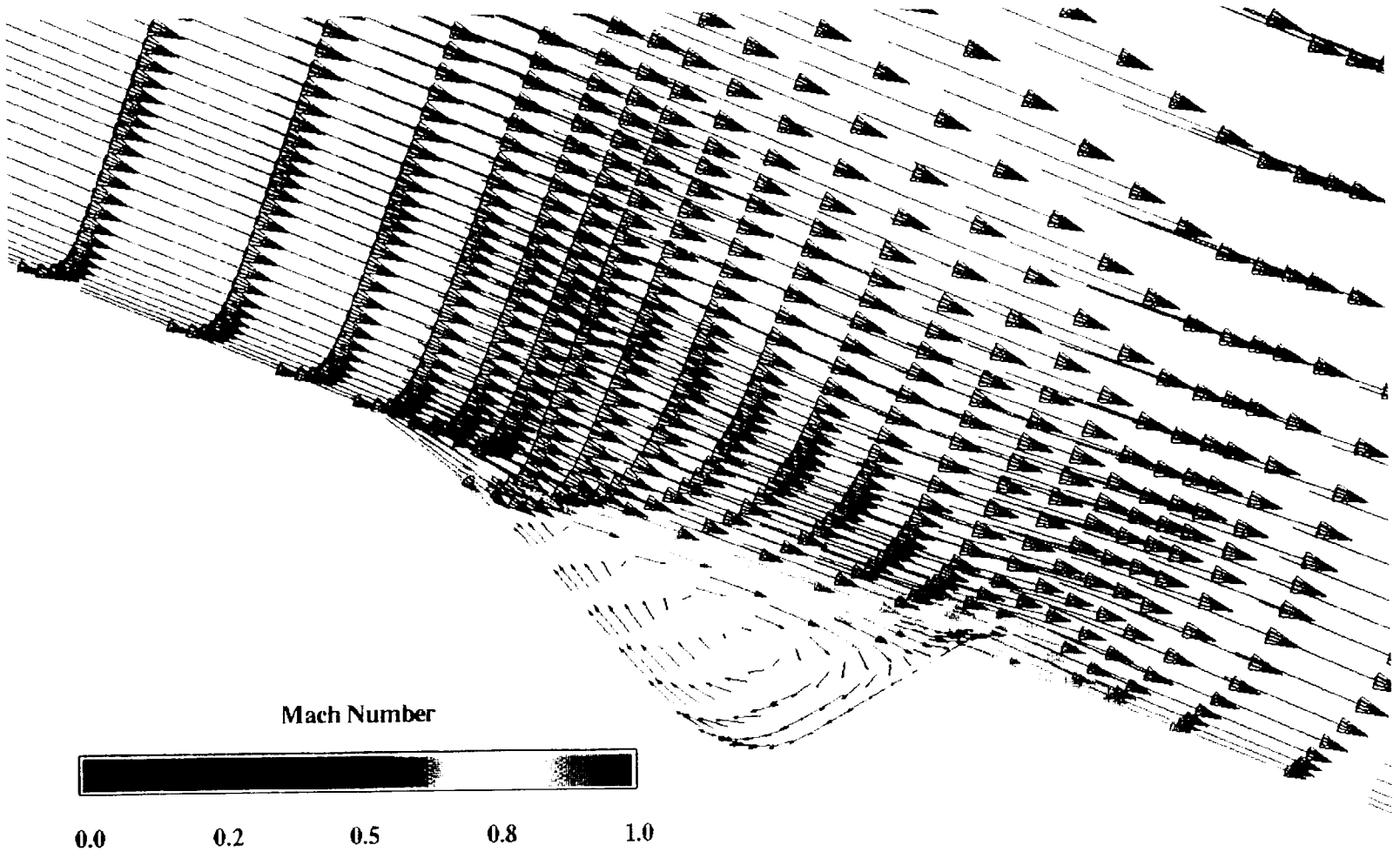

Figure 11A. RSRM Throat Ring 1st Iteration Spall Geometry Spall Depth, 0.25 Inches

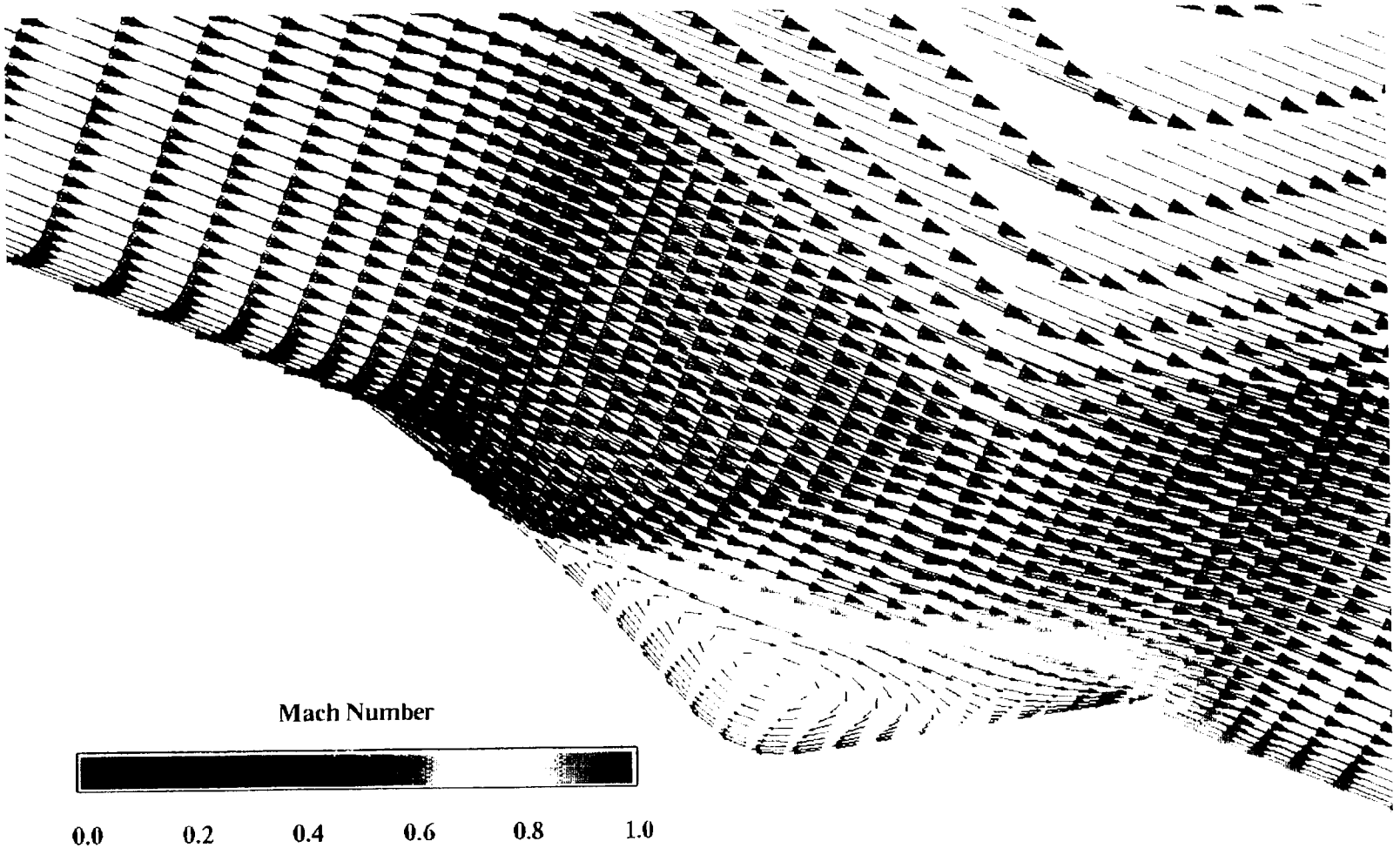

Figure 12A. RSRM Throat Ring 2nd Iteration Spall Geometry Spall Depth, 0.25 Inches

ERC, Inc.

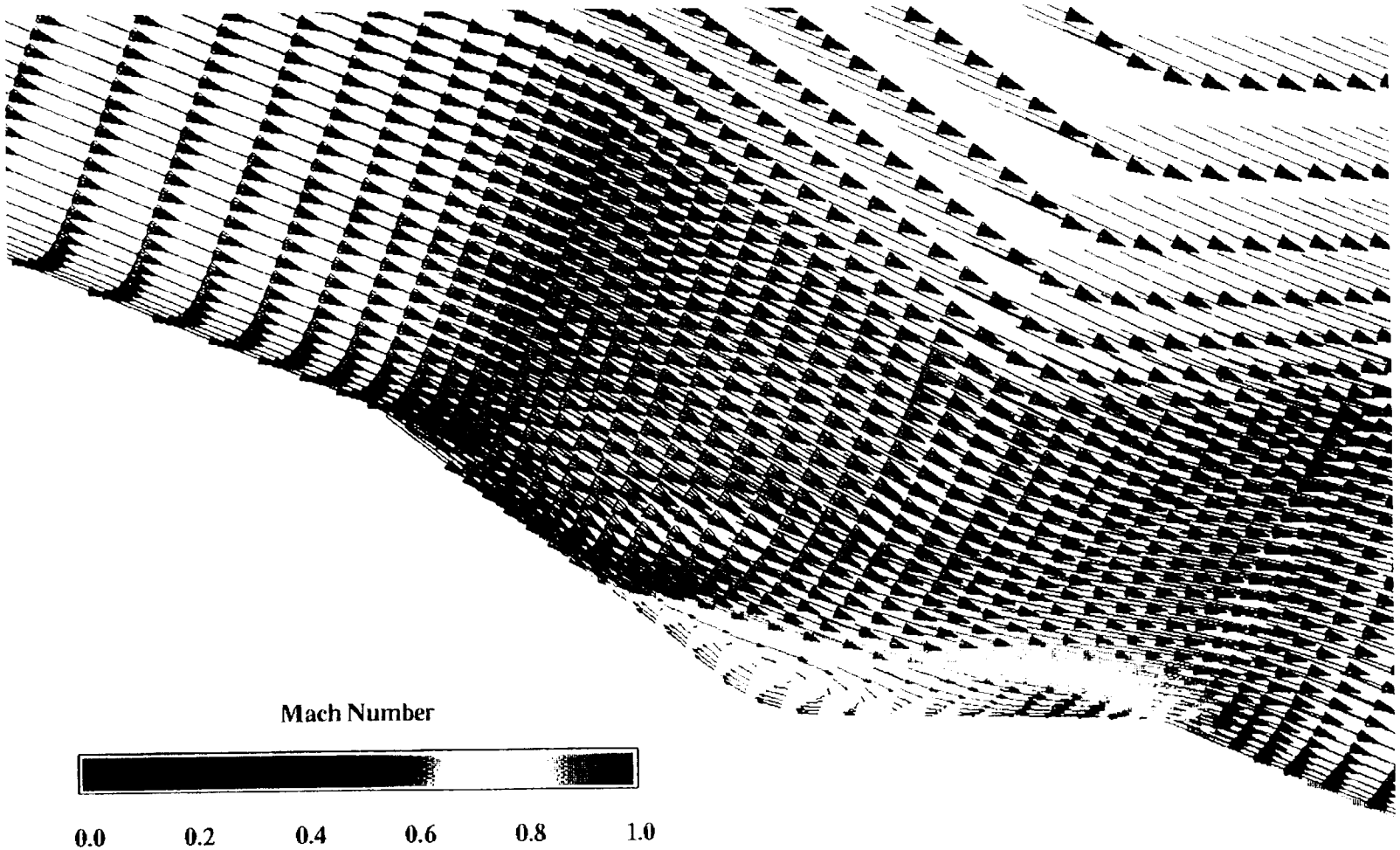

Figure 13A. RSRM Throat Ring 3rd Iteration Spall Geometry Spall Depth, 0.25 Inches

ERC, Inc.

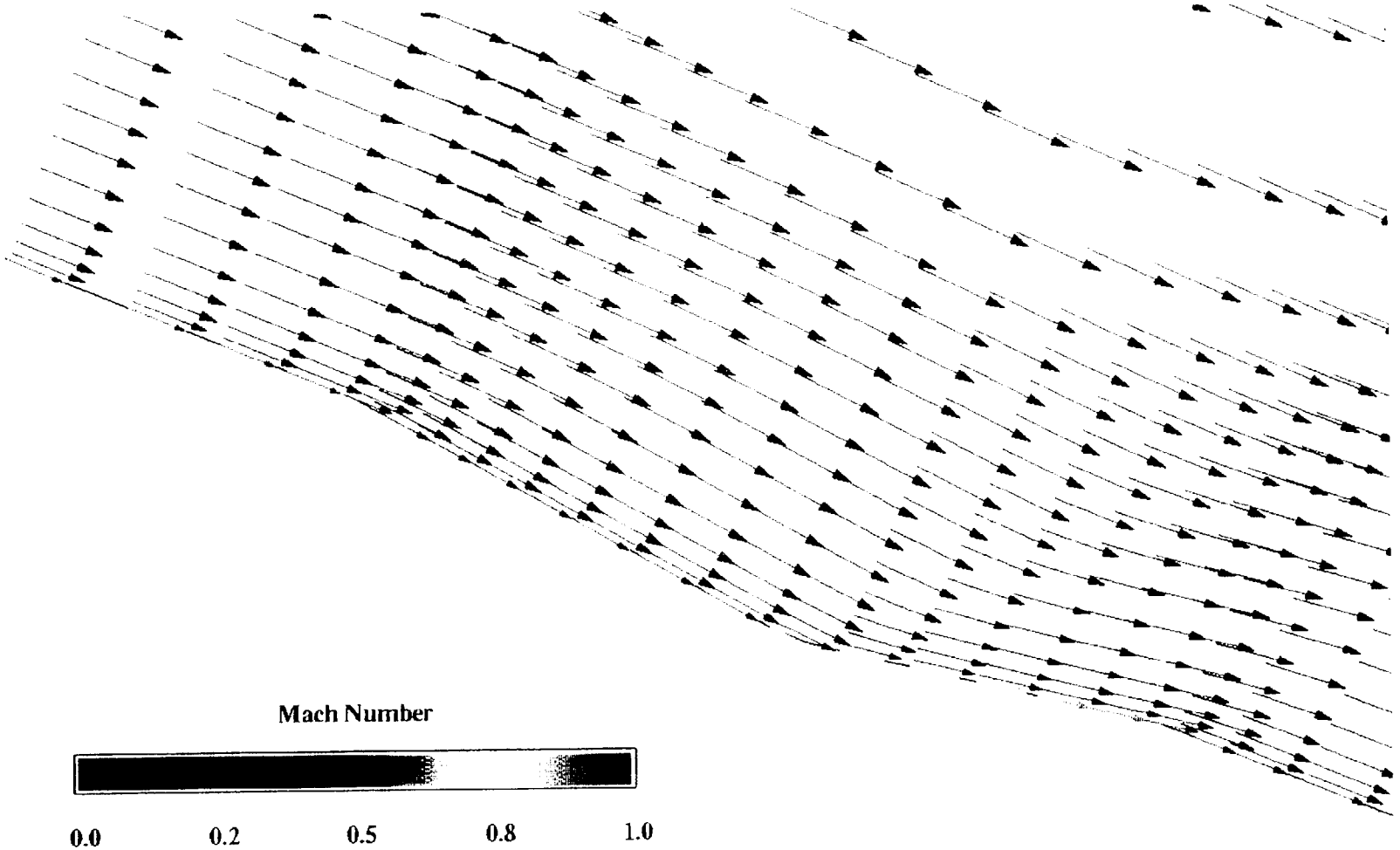

Figure 14A. RSRM Throat Ring 4th Iteration Spall Geometry Spall Depth, 0.25 Inches

ERC, Inc.

Figure 15A. Throat Ring Spall Scenario Static Wall Pressure Spall Depth, 0.25 Inches

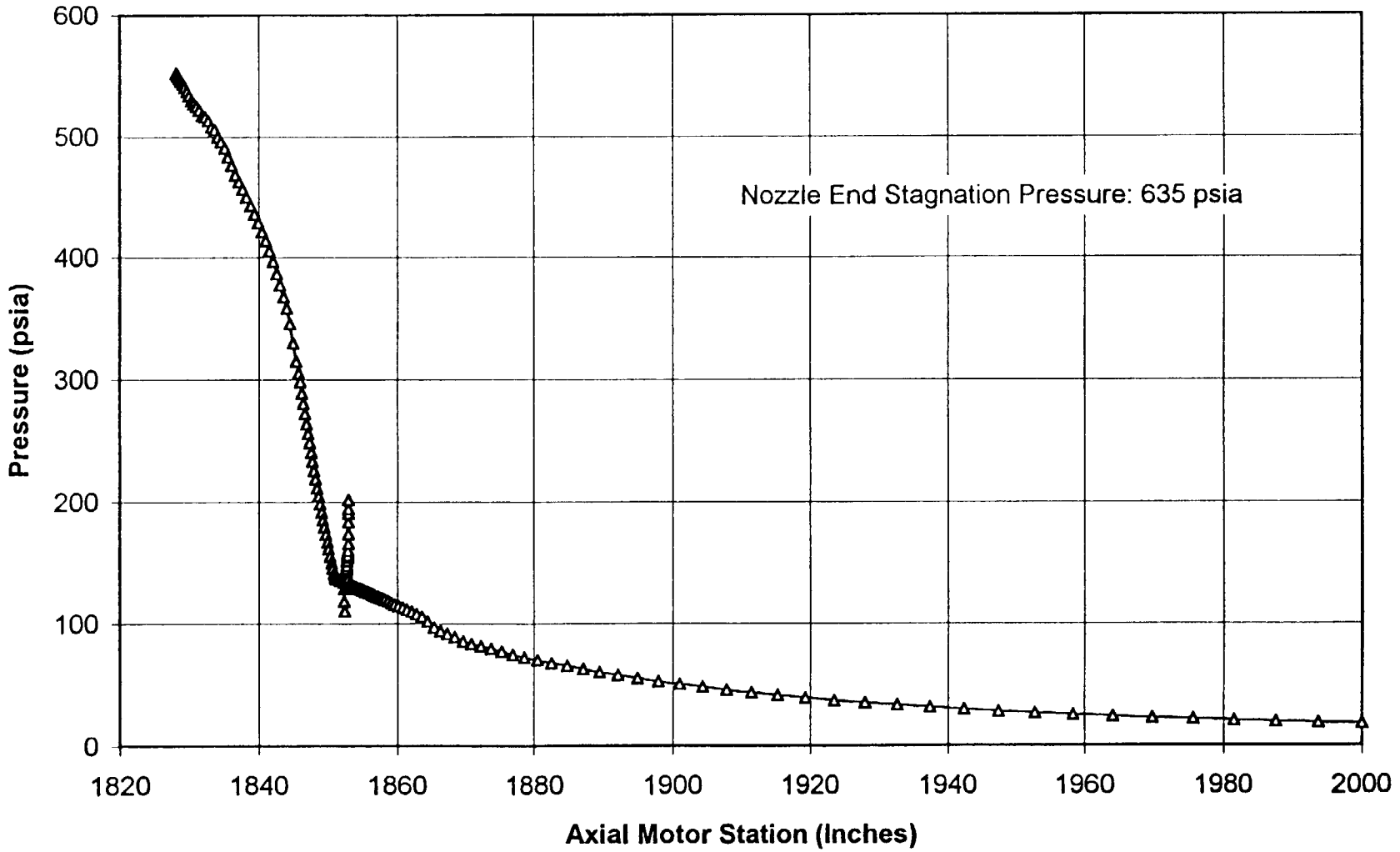

ERC Inc. 1/23/97

Figure 16A. Wall Pressure in Joint 4 Region
Throat Ring Spall Depth, 0.25 Inches

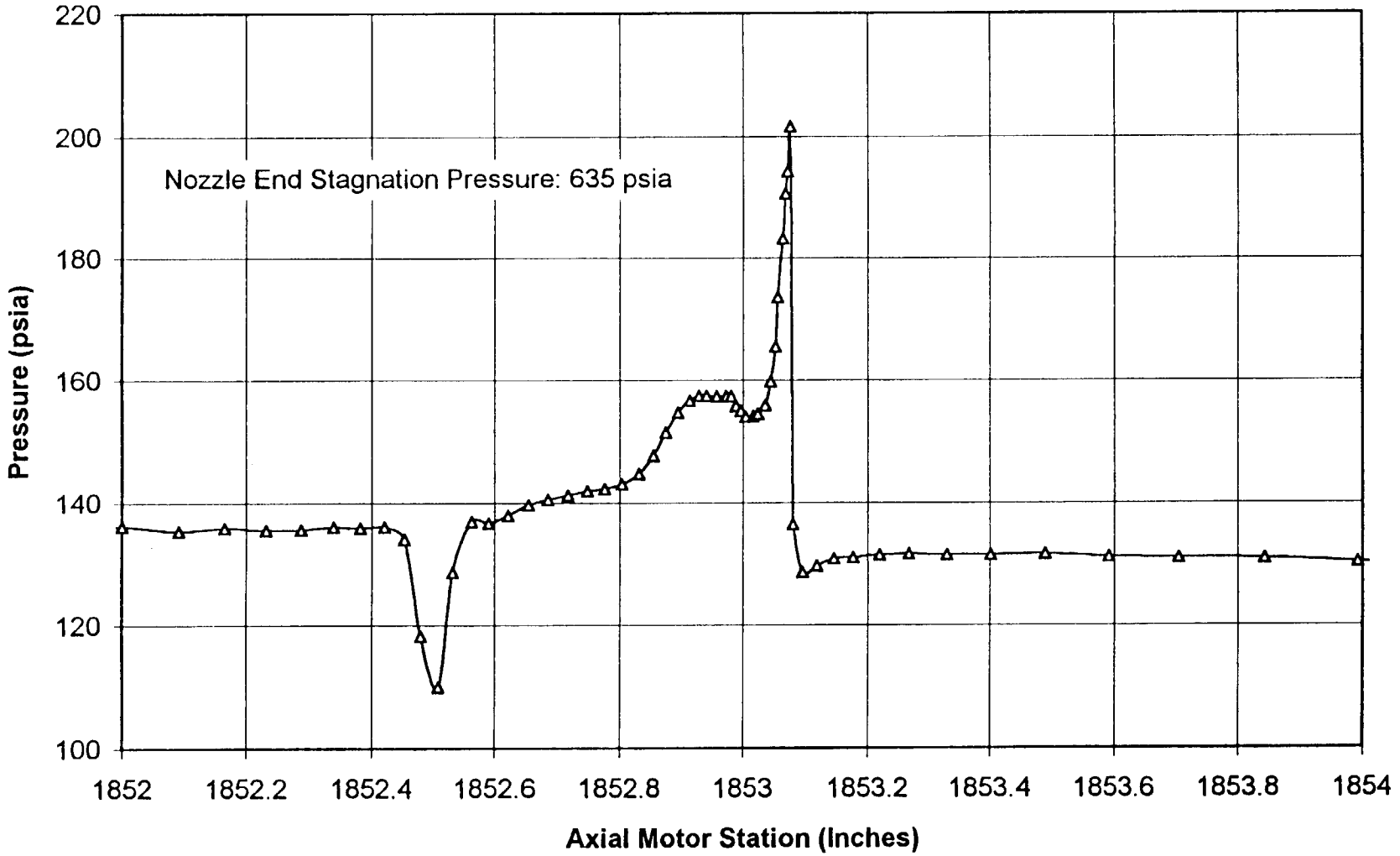

ERC Inc. 1/23/97

Figure 17A. Initial Spall Geometry
Throat Ring Spall Depth, 0.25 Inches

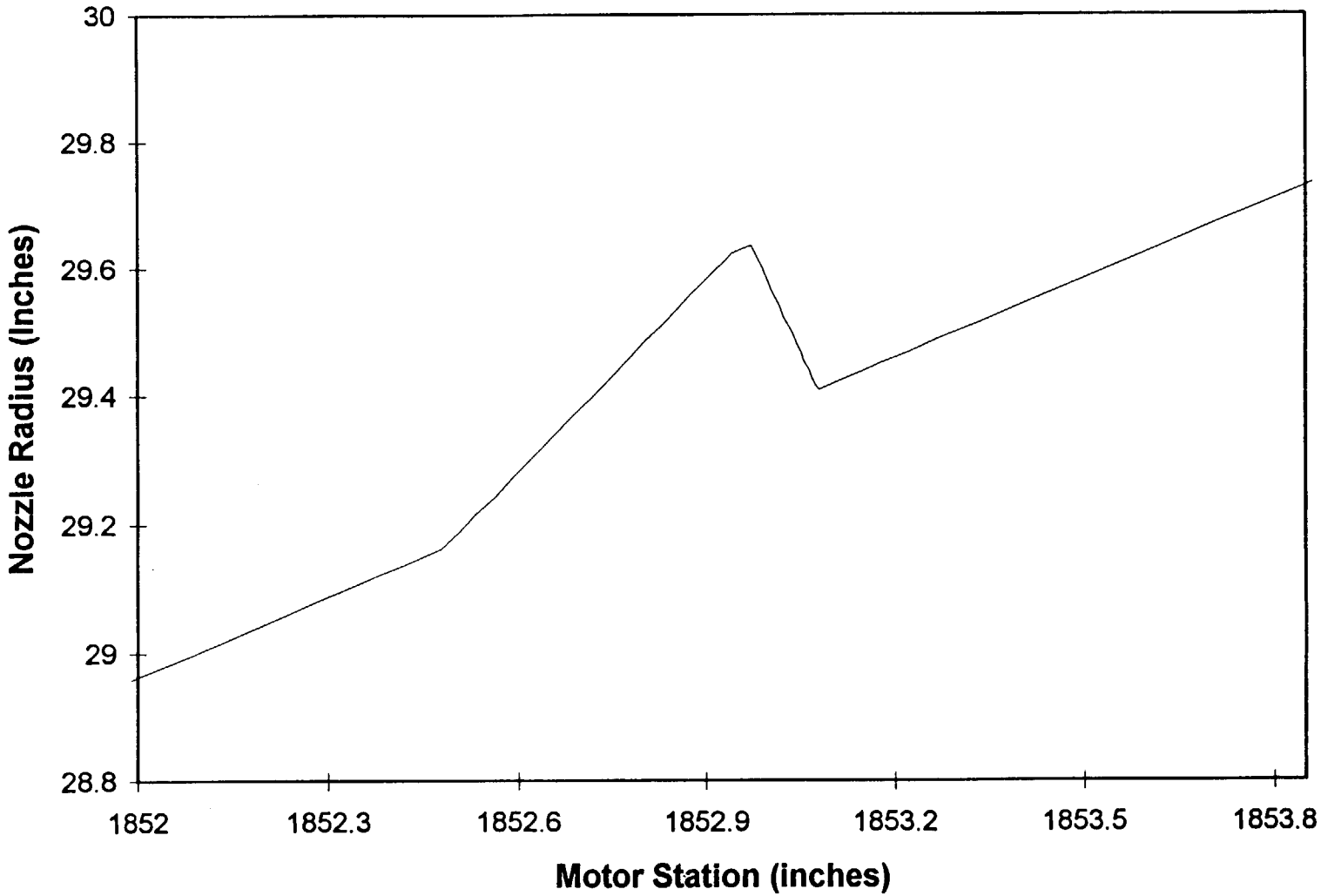

ERC Inc. 1/23/97

Figure 18A. Throat Ring Spall Scenario
Static and Total Pressure Along Spall Face
Spall Depth, 0.25 Inches

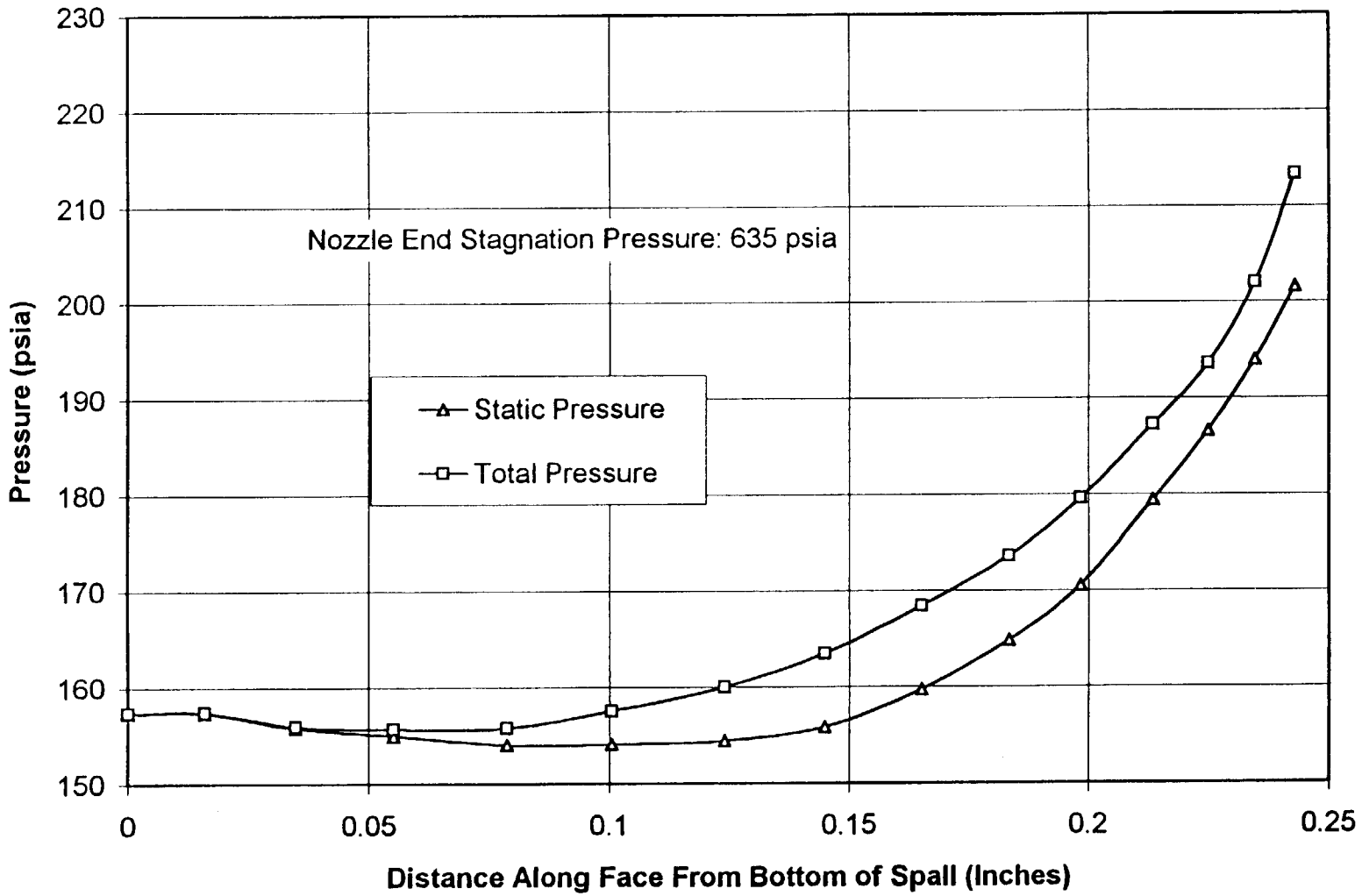

ERC Inc. 1/23/97

Figure 19A. Throat Ring Spall Scenario
Velocity Magnitude Along Spall Face
Spall Depth, 0.25 Inches

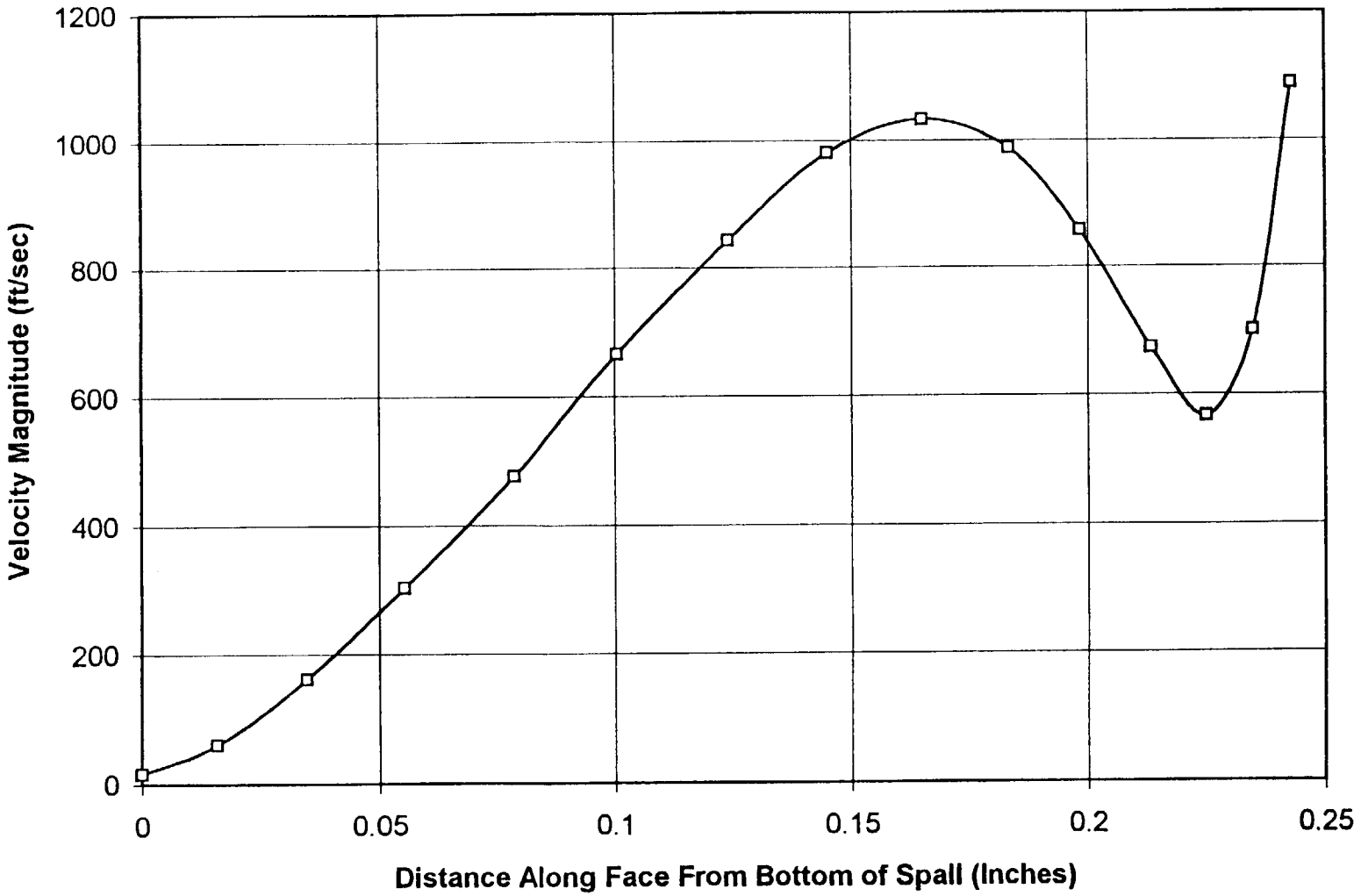

ERC Inc. 1/23/97

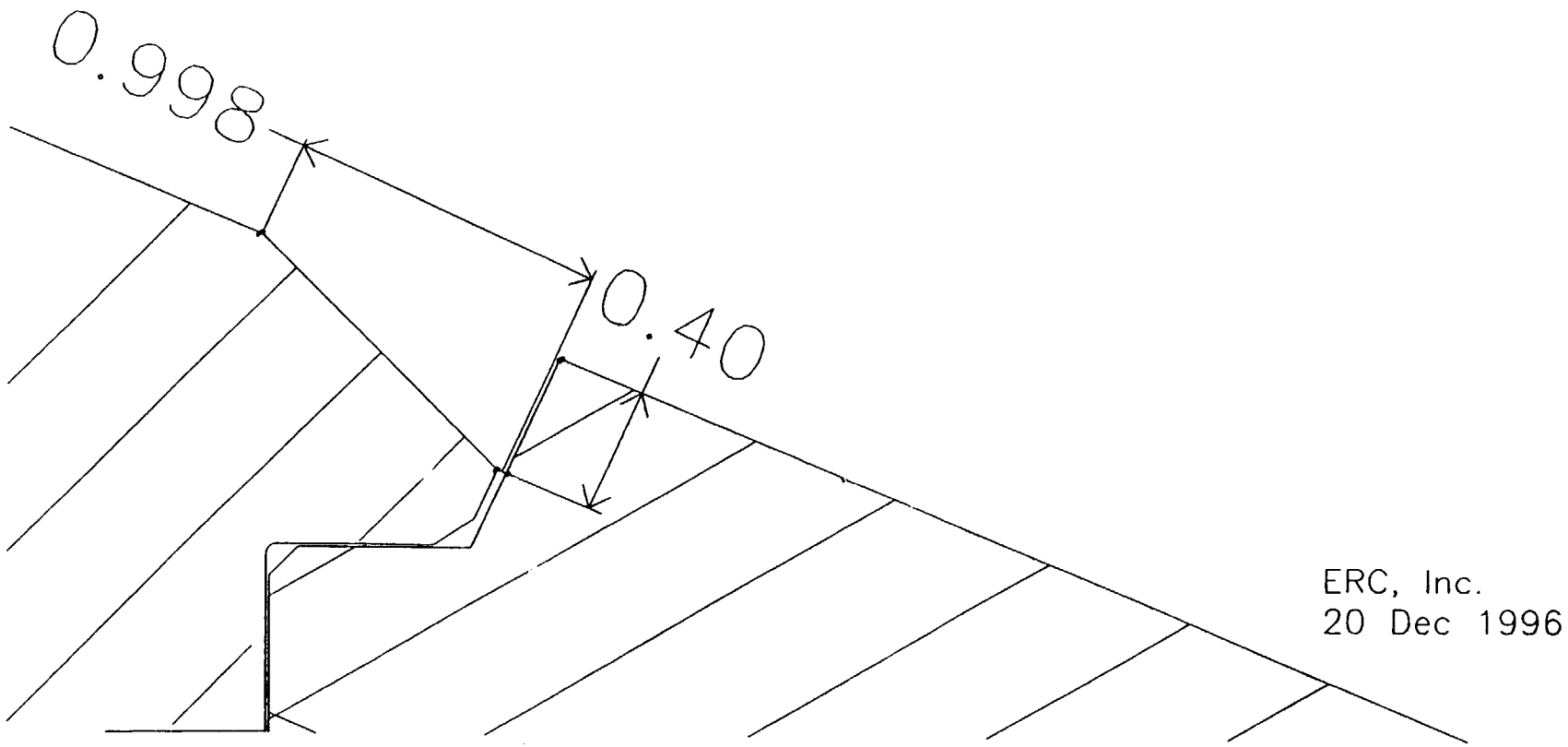

Figure 20A. Throat Ring Spall Geometry, 0.4 Inch Spall Scenario

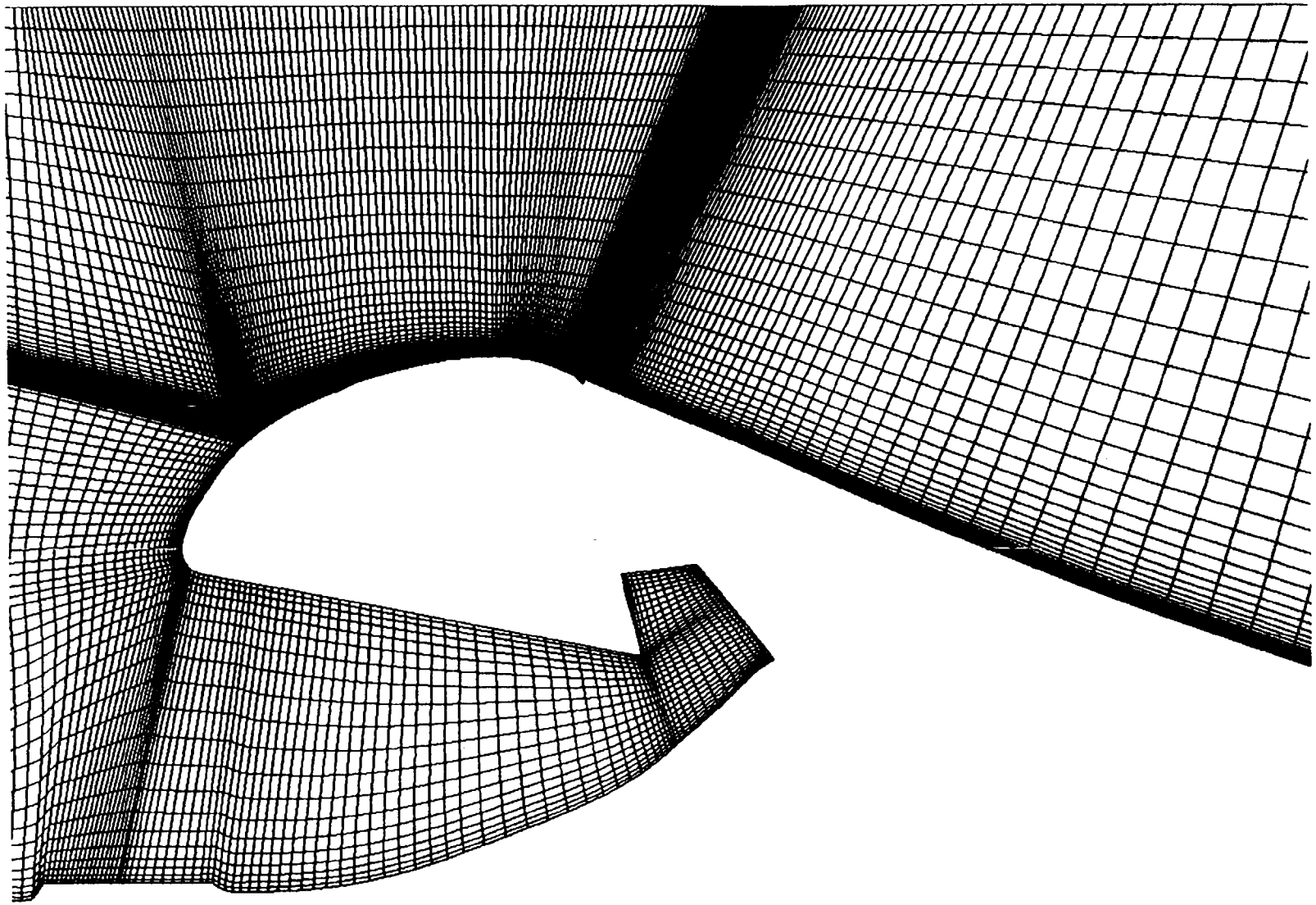

Figure 21A. Throat Ring Spall Computational Grid, 0.4 Inch Spall Scenario

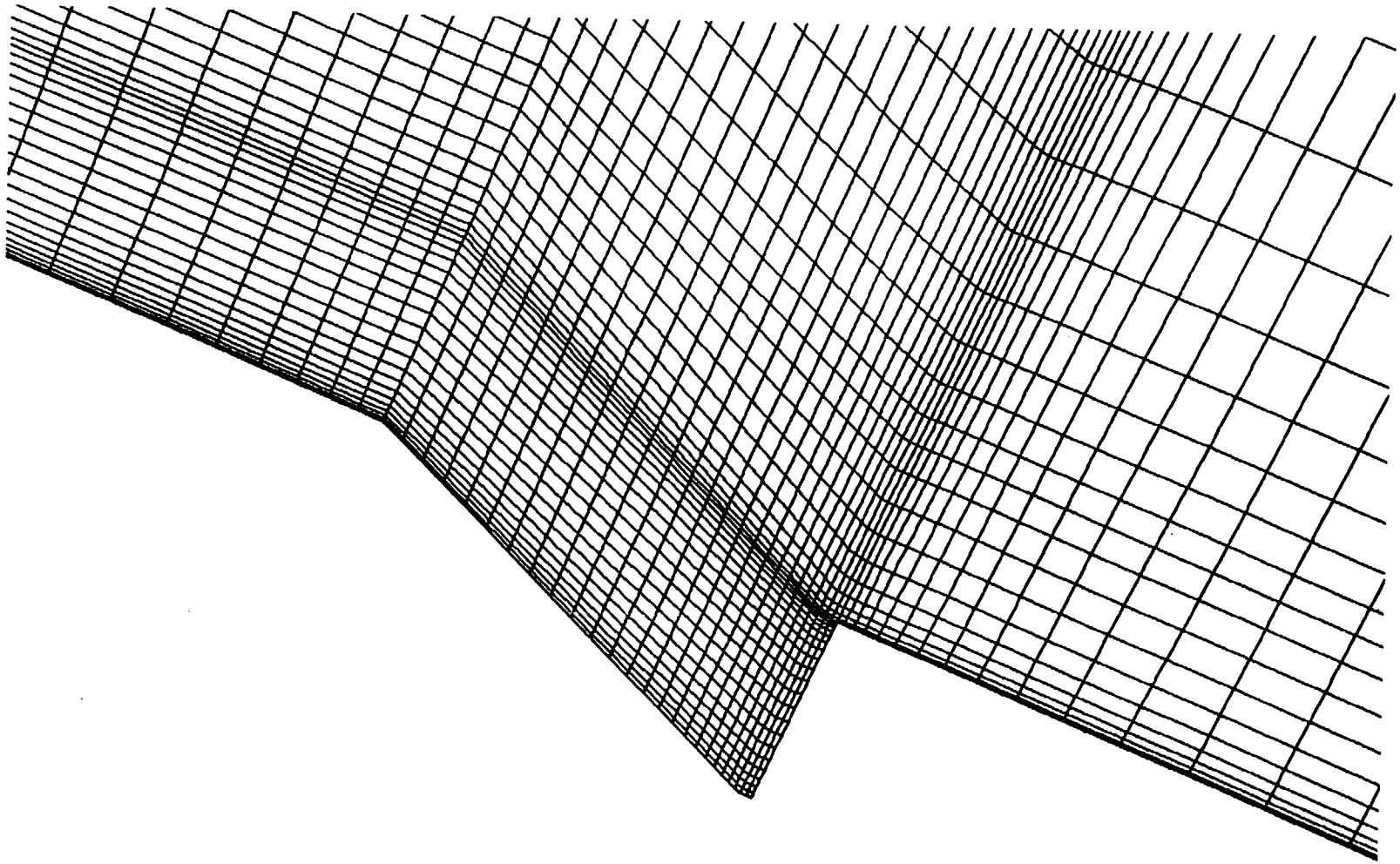

Figure 22A. Throat Ring Spall Computational Grid, 0.4 Inch Spall Scenario Enlargement in the Joint 4 Region

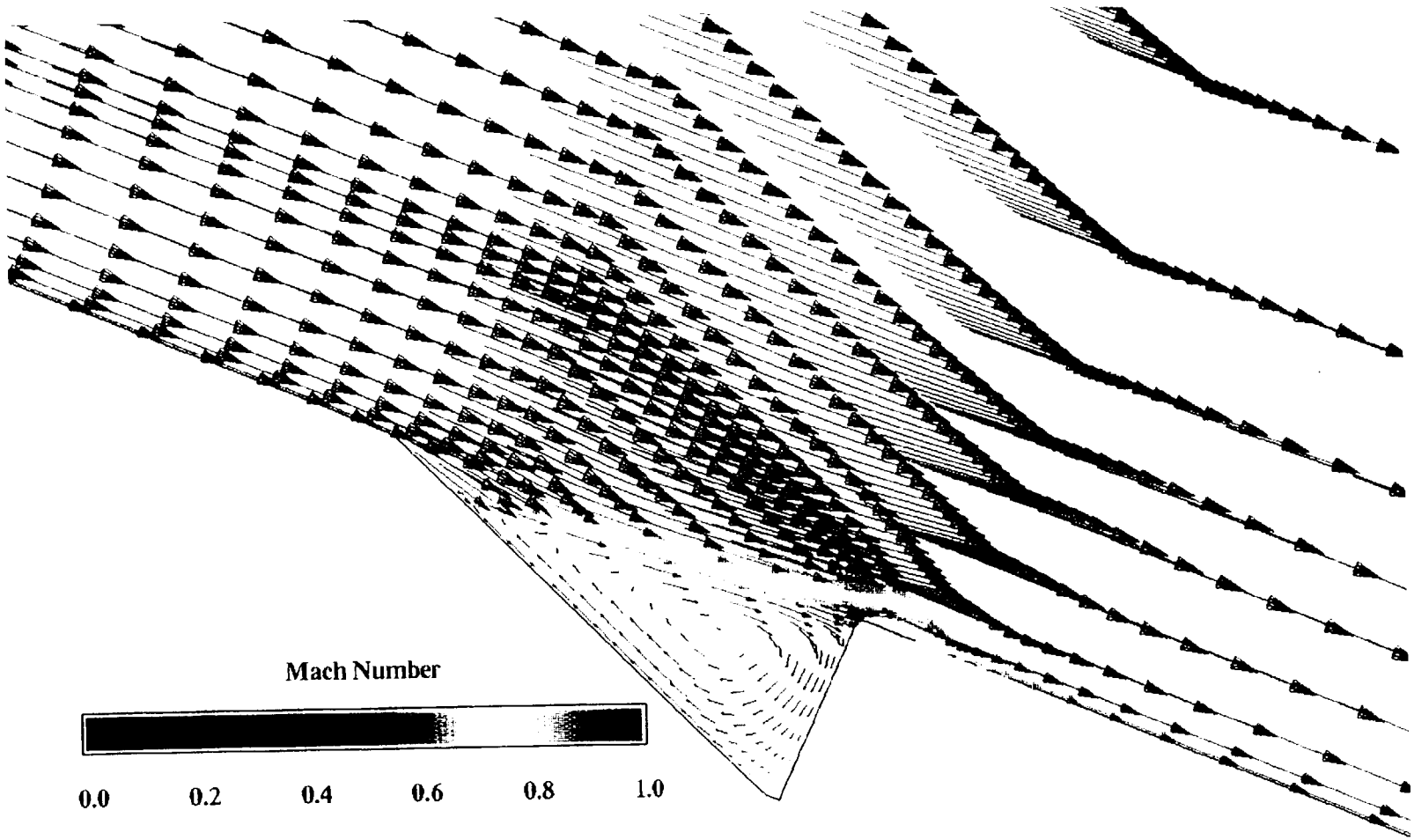

Figure 23A. Velocity Field in the Joint 4 Region Throat Ring Spall Scenario, 0.4 Inches

ERC, Inc.

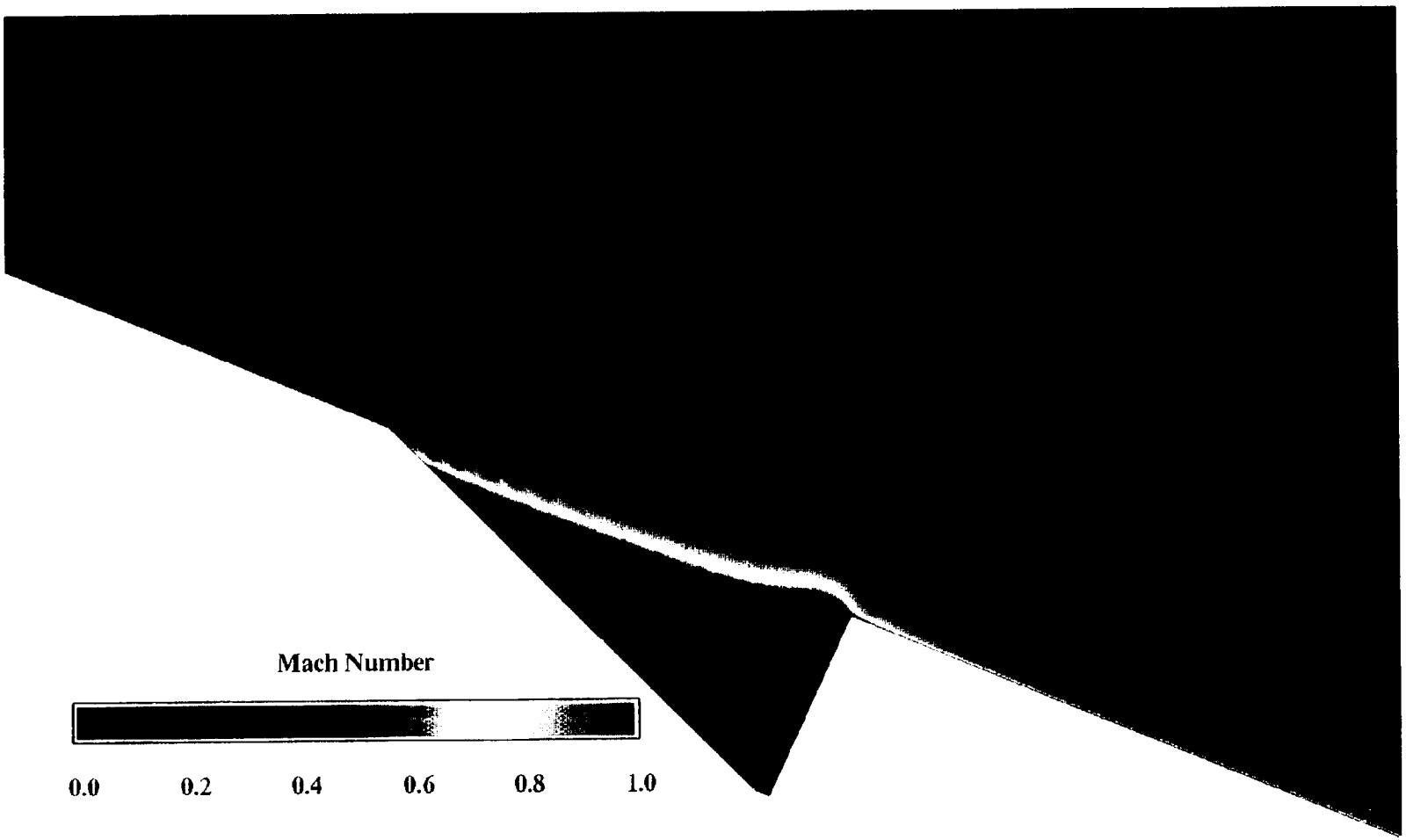

Figure 24A. Mach Number in the Joint 4 Region Throat Ring Spall Scenario, 0.4 Inches

ERC, Inc.

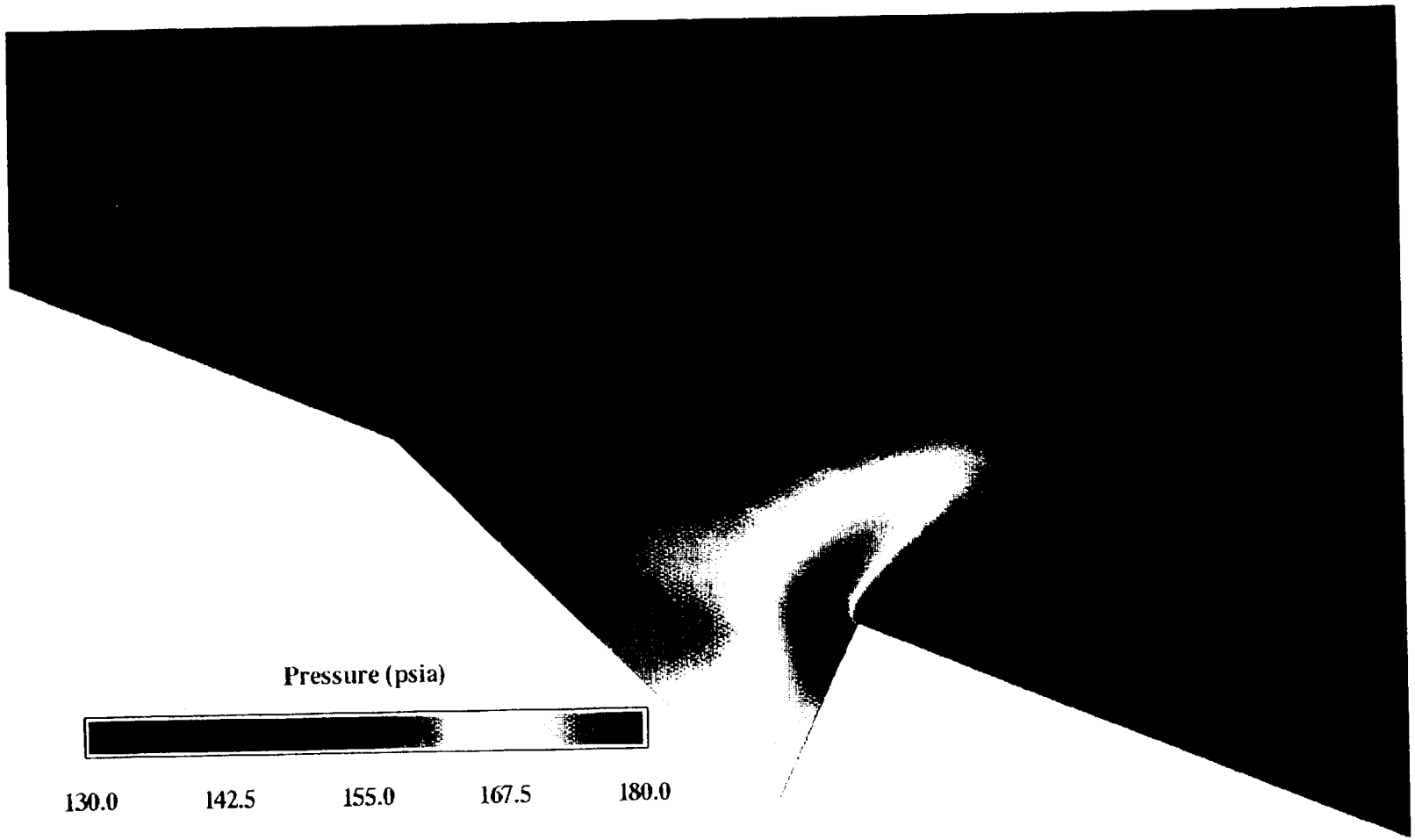

Figure 25A. Pressure in the Joint 4 Region Throat Ring Spall Scenario, 0.4 Inches

ERC, Inc.

Figure 26A. Static Pressure Along the Nozzle Wall
Throat Ring Spall Depth, 0.4 Inches

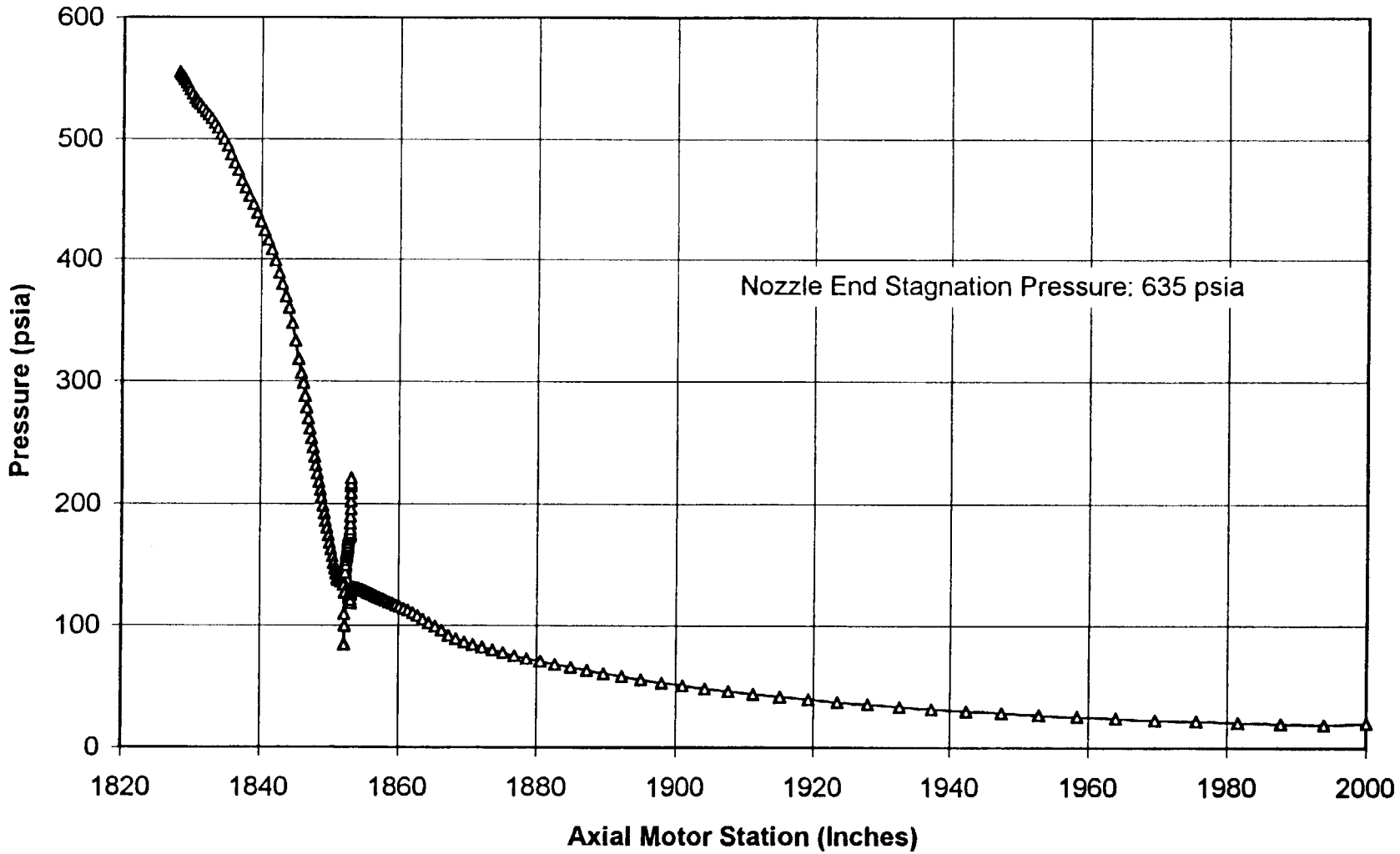

ERC Inc. 1/23/97

Figure 27A. Wall Static Pressure in the Joint 4 Region Throat Ring Spall Depth, 0.4 Inches

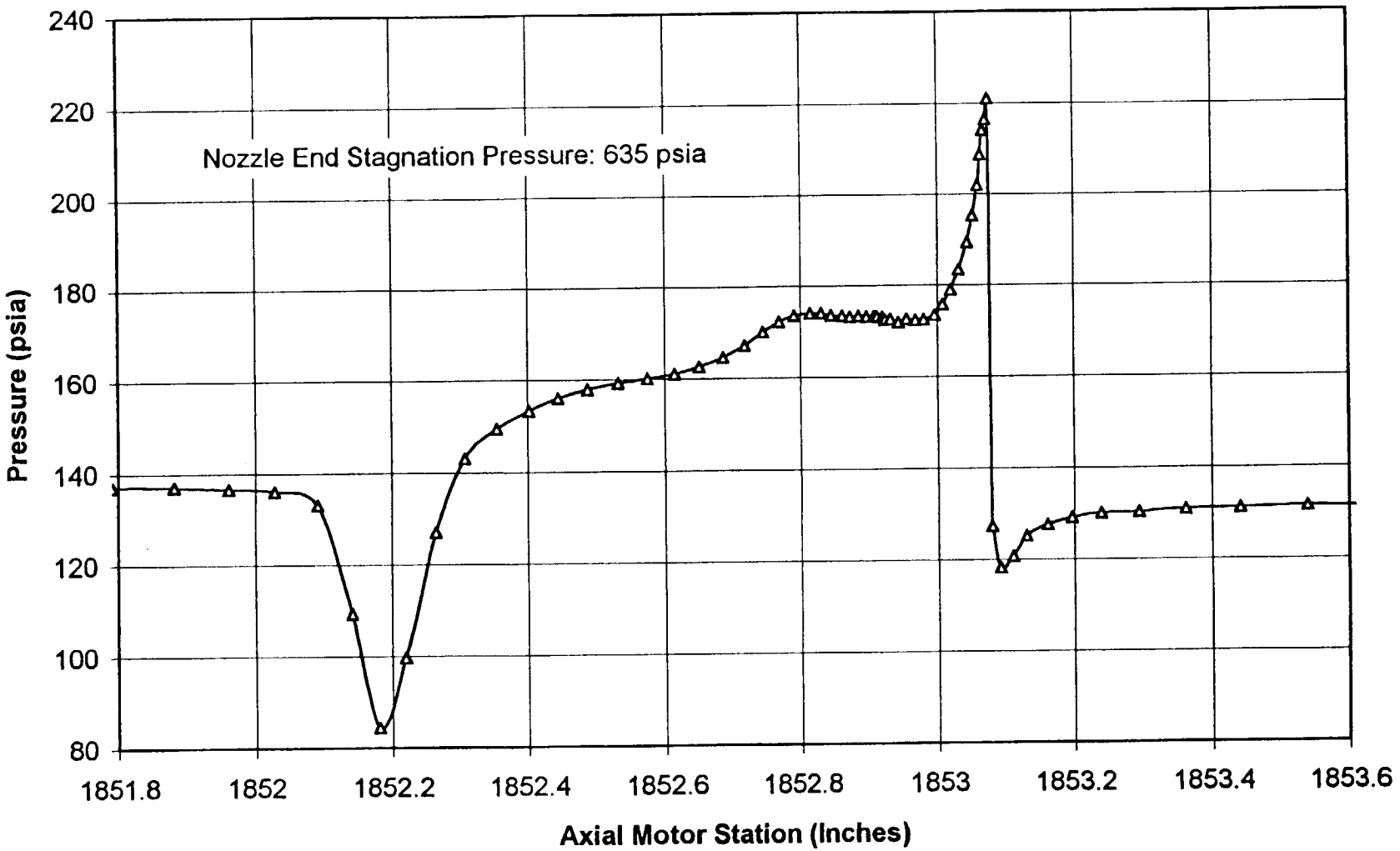

ERC Inc. 1/23/97

Figure 28A. Static Pressure Along Forward Exit Cone Face Throat Ring Spall Depth, 0.4 Inches

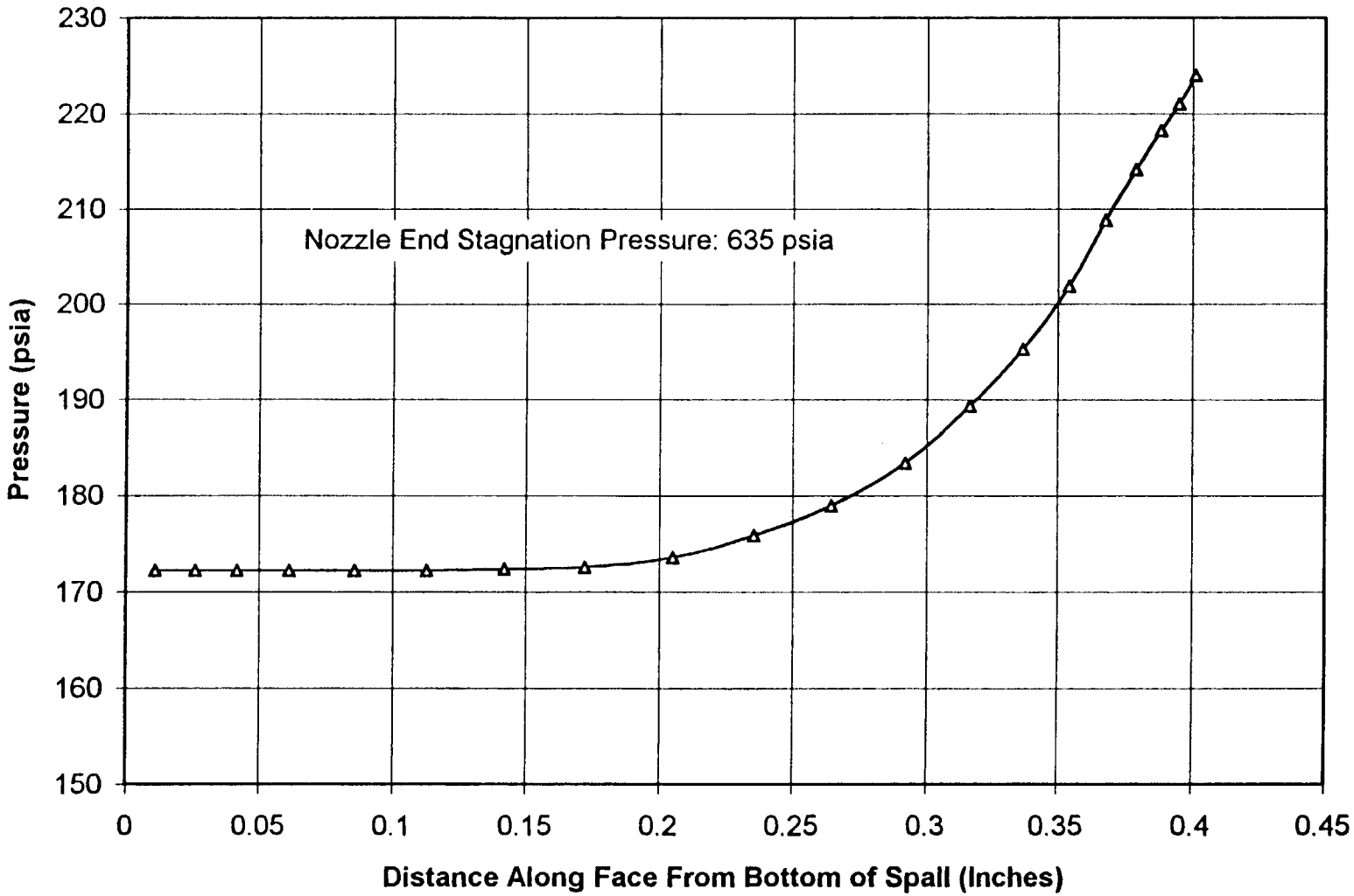

ERC Inc. 1/23/97

Figure 29A. Polysulfide Nozzle Bump Geometry
Bump Height, 1.0 Inches

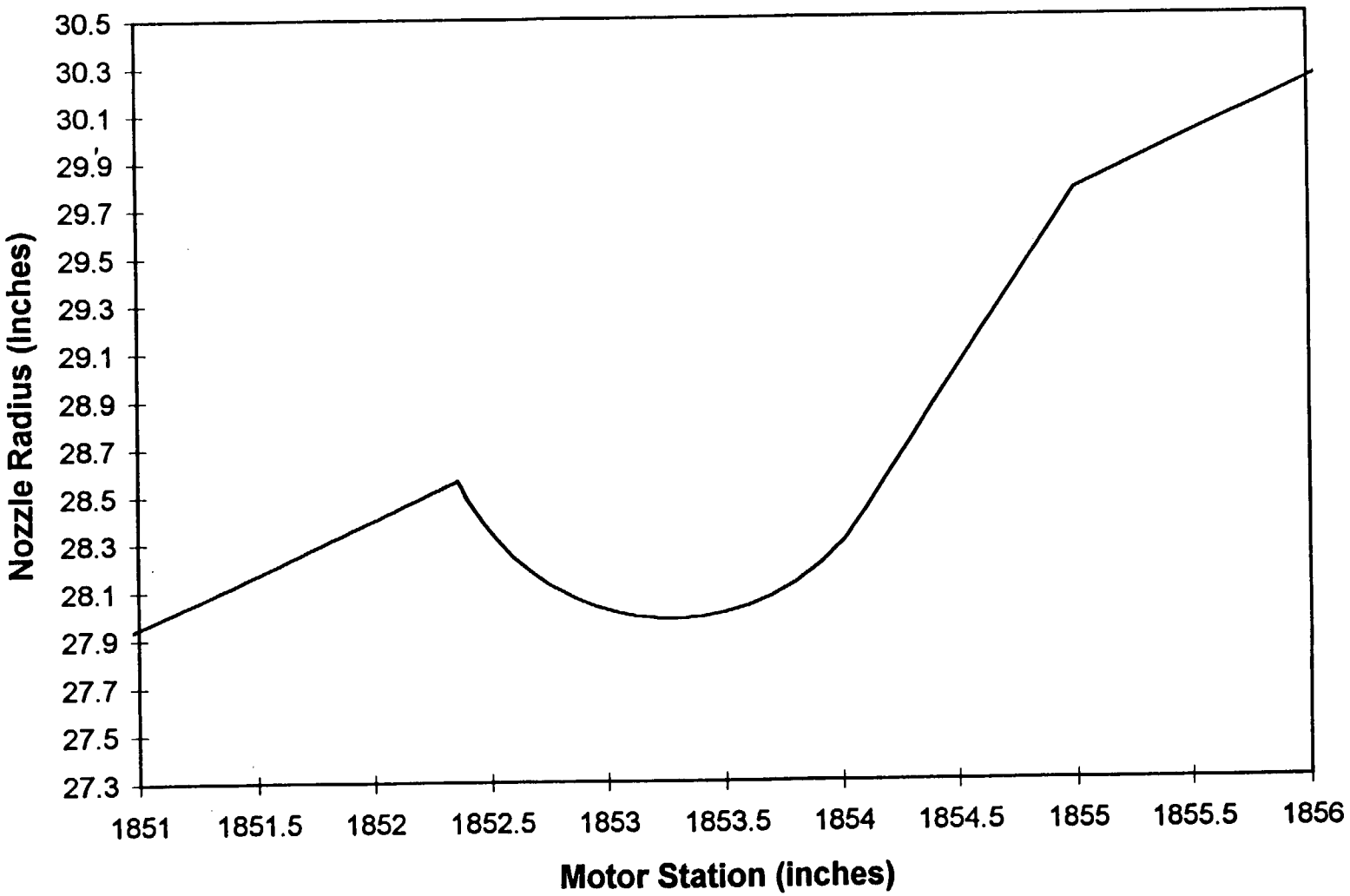

ERC Inc. 1/23/97

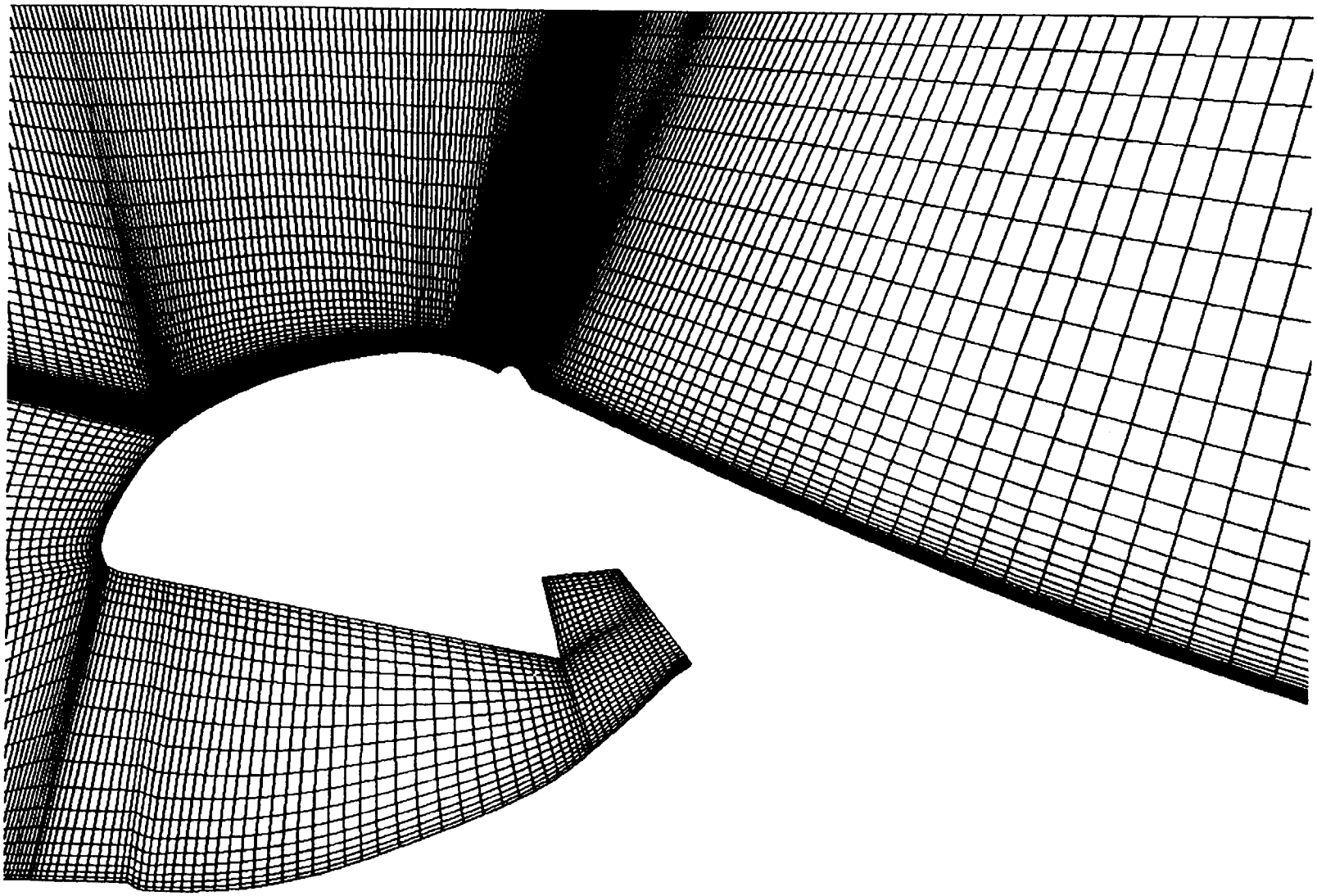

Figure 30A. Polysulfide Bump Computational Grid
Bump Height, 1.0 Inches

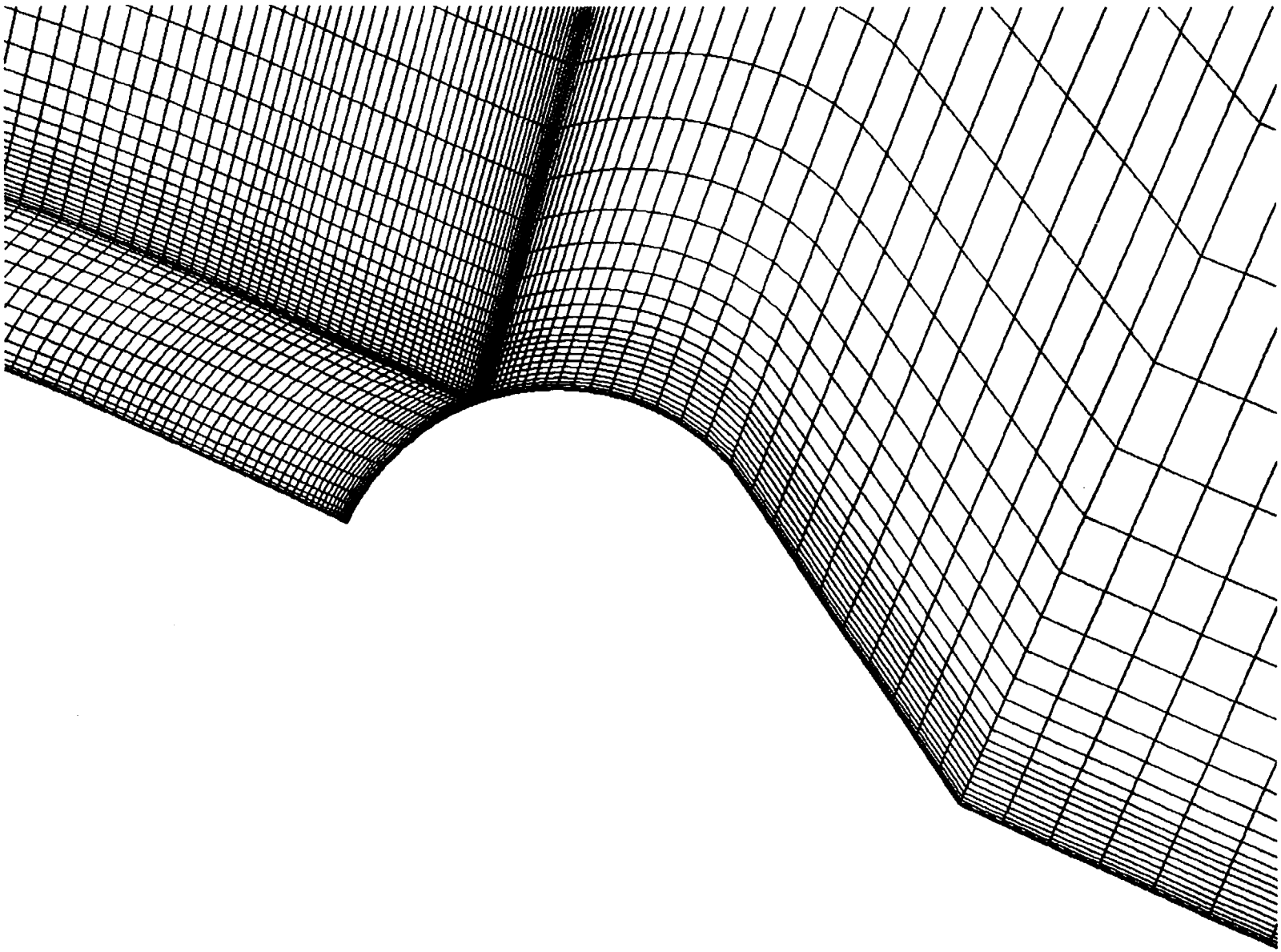

Figure 31A. Enlargement of Polysulfide Bump Computational Grid Bump Height, 1.0 Inches

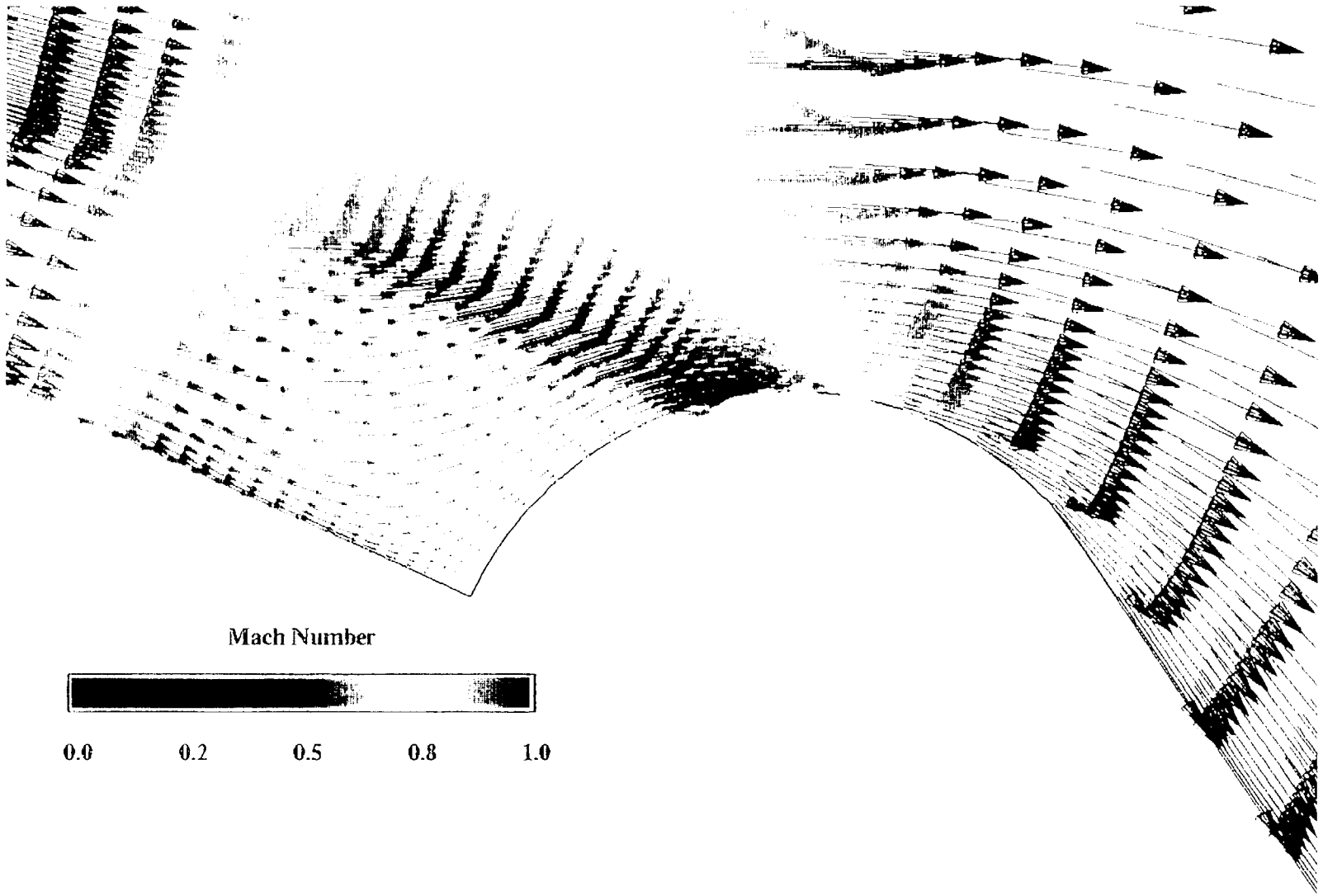

Figure 32A. Velocity Field in the Region of the Polysulfide Bump Bump Height, 1.0 Inches

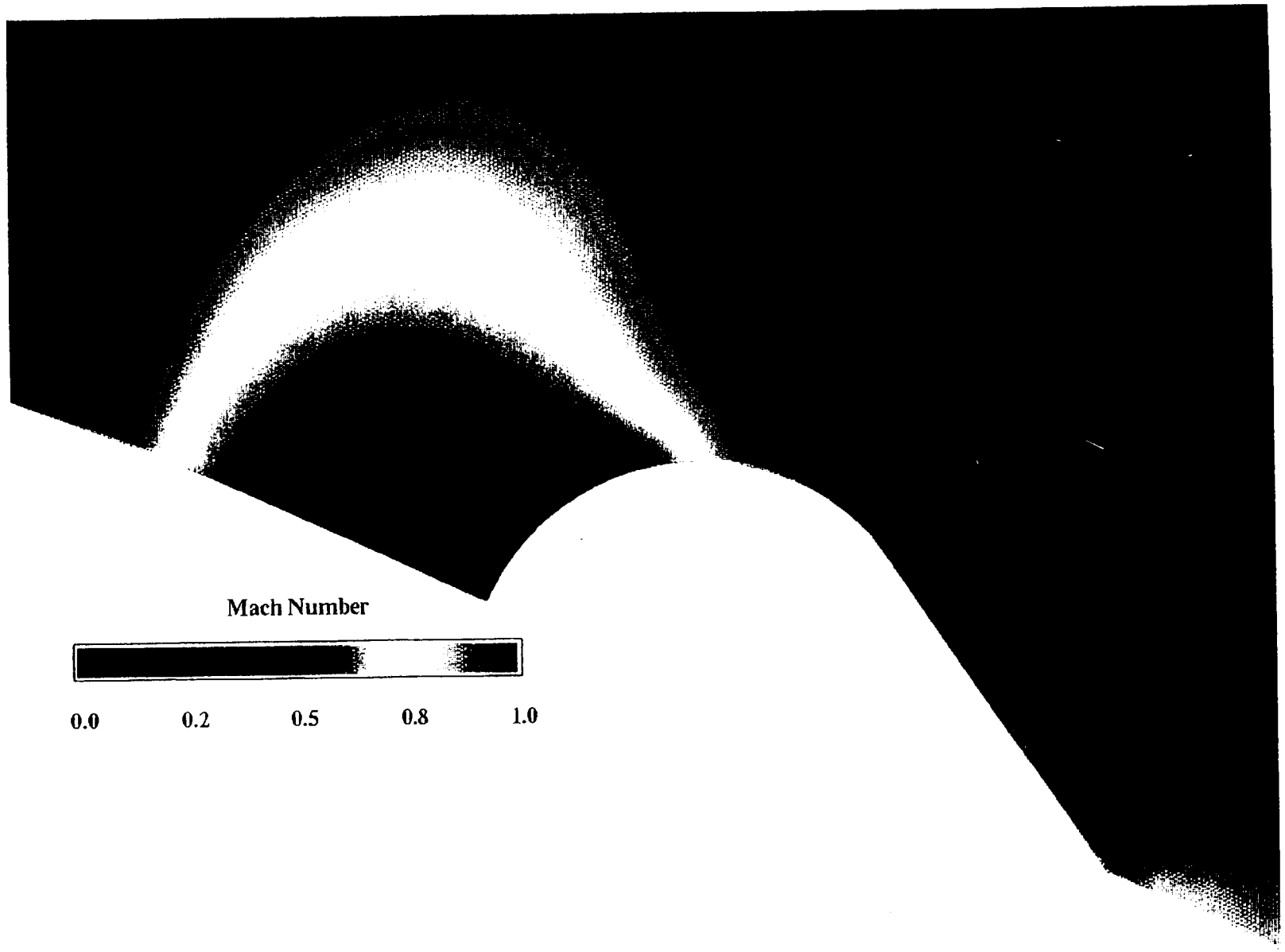

Figure 33A. Mach Number in the Region of the Polysulfide Bump
Bump Height, 1.0 Inches

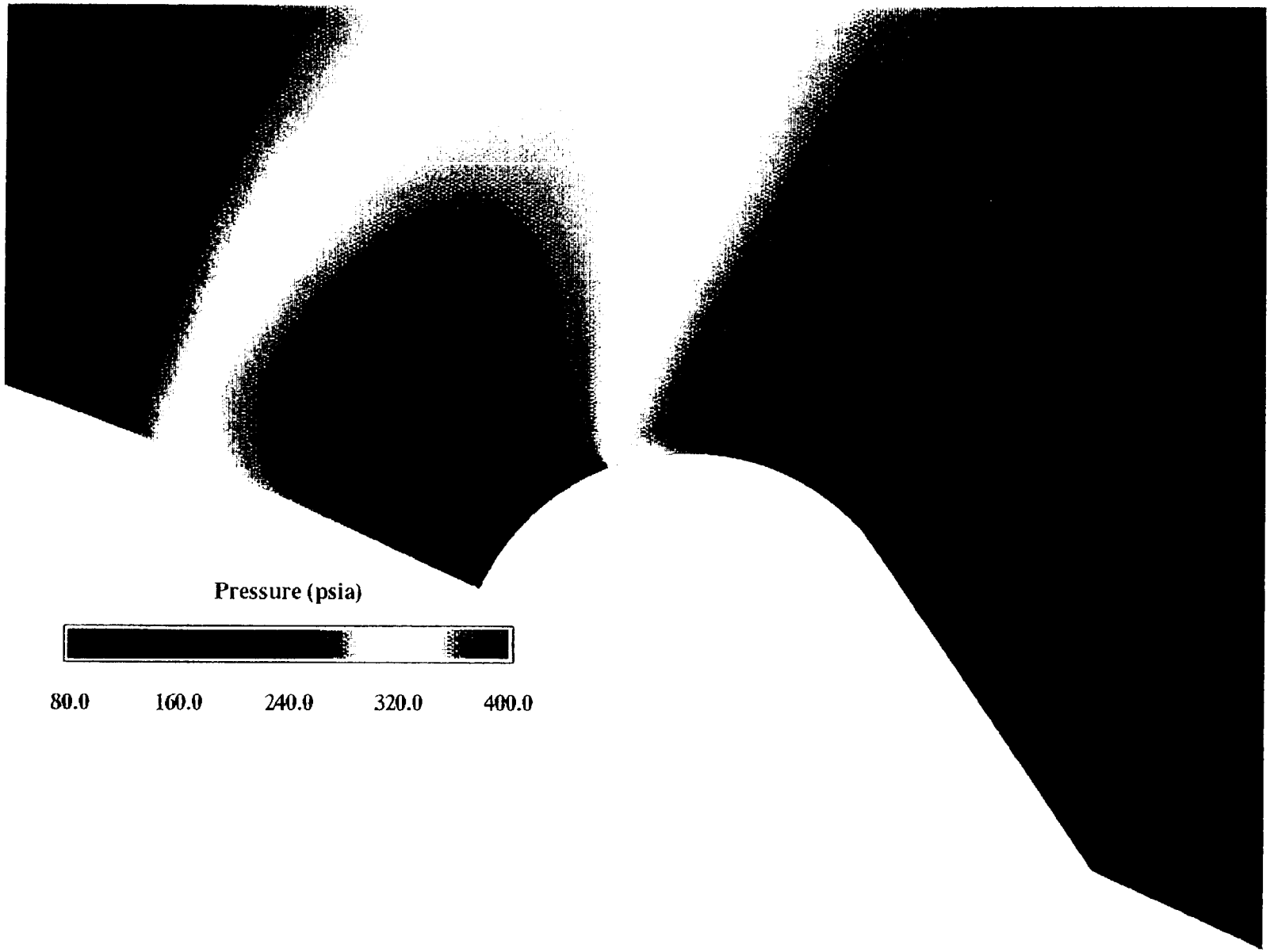

Figure 34A. Pressure in the Region of the Polysulfide Bump
Bump Height, 1.0 Inches

Figure 35A. RSRM Joint #4 Polysulfide Residue Analysis
Wall Pressure Profile

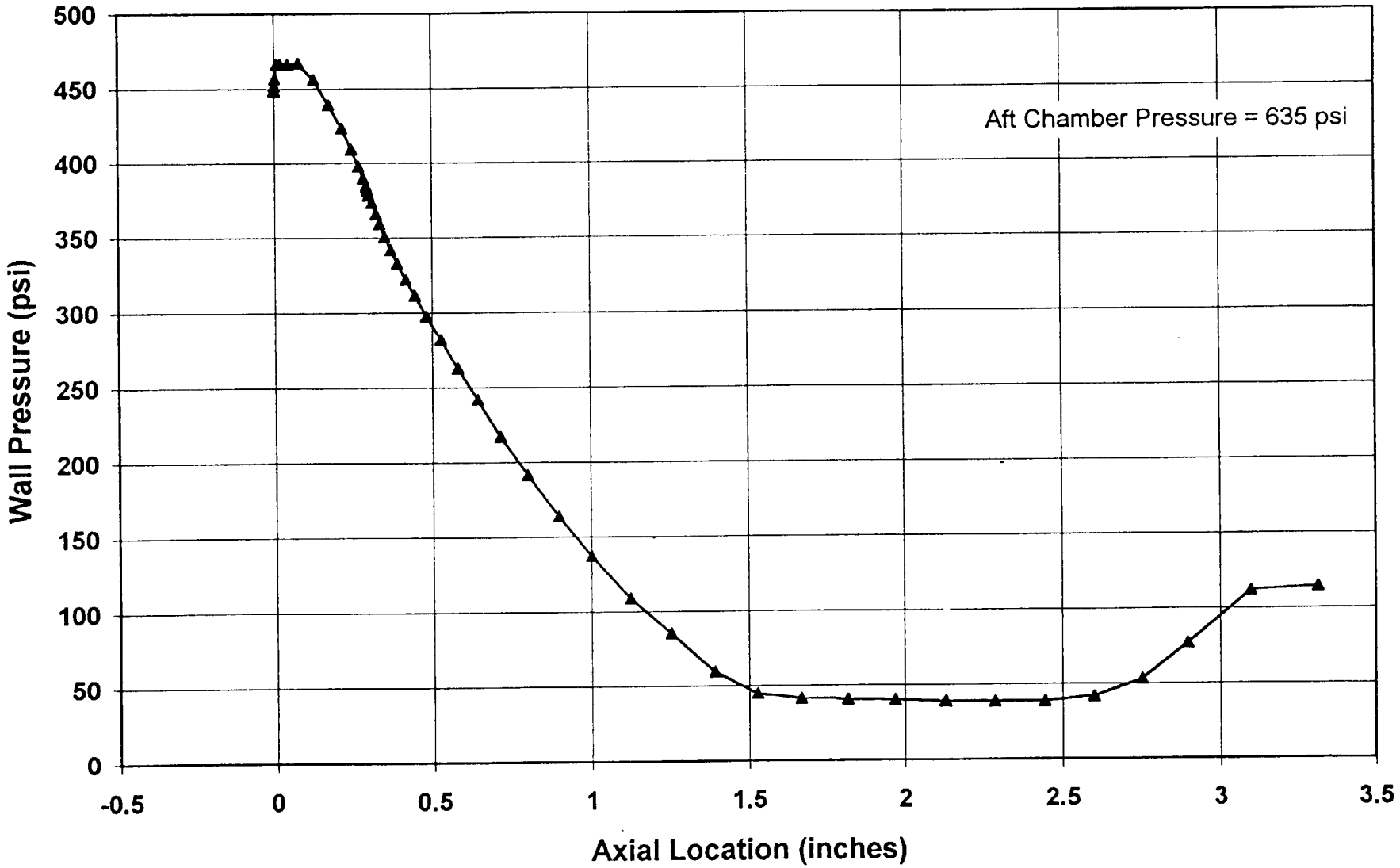

ERC, Inc. 1/8/1997

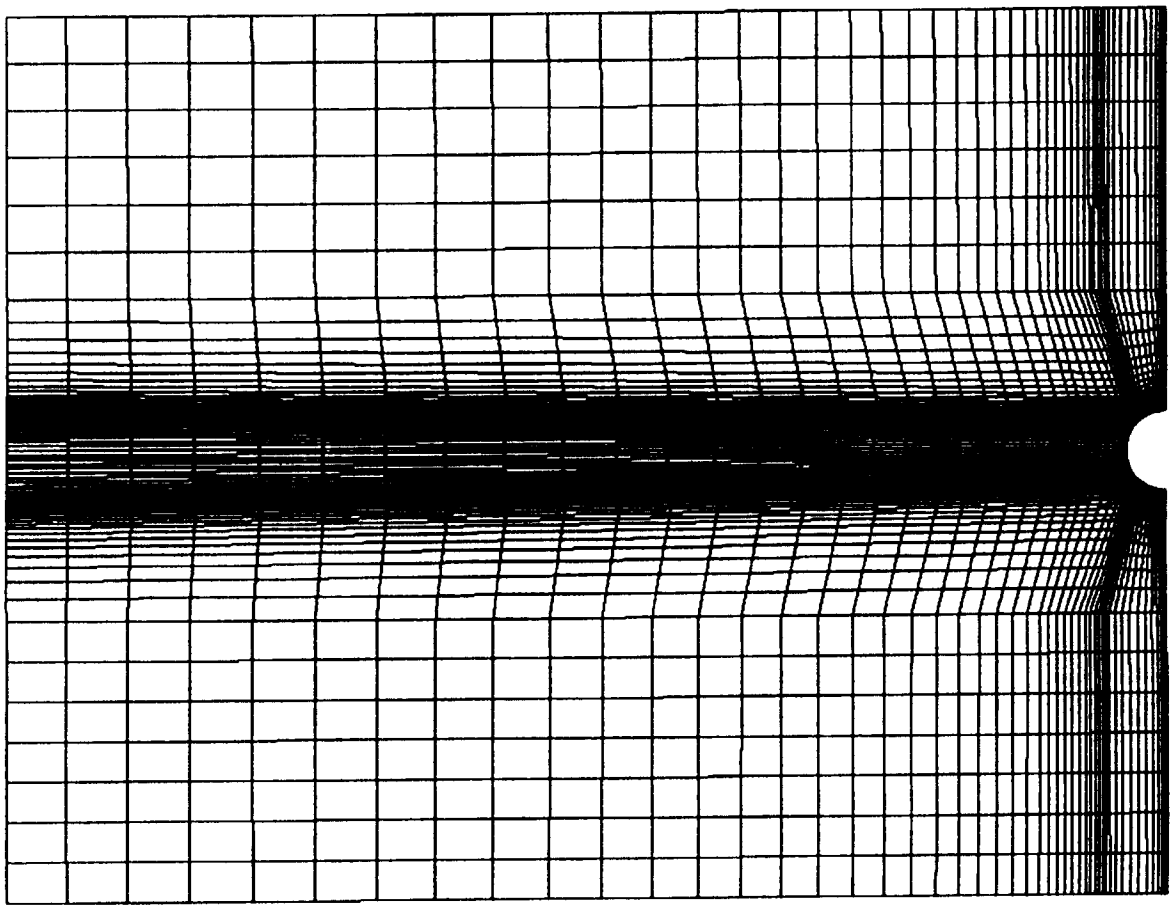

Figure 36A. Computational Grid for a Polysulfide Bump on a Flat Plate Bump Height, 1.0 Inches

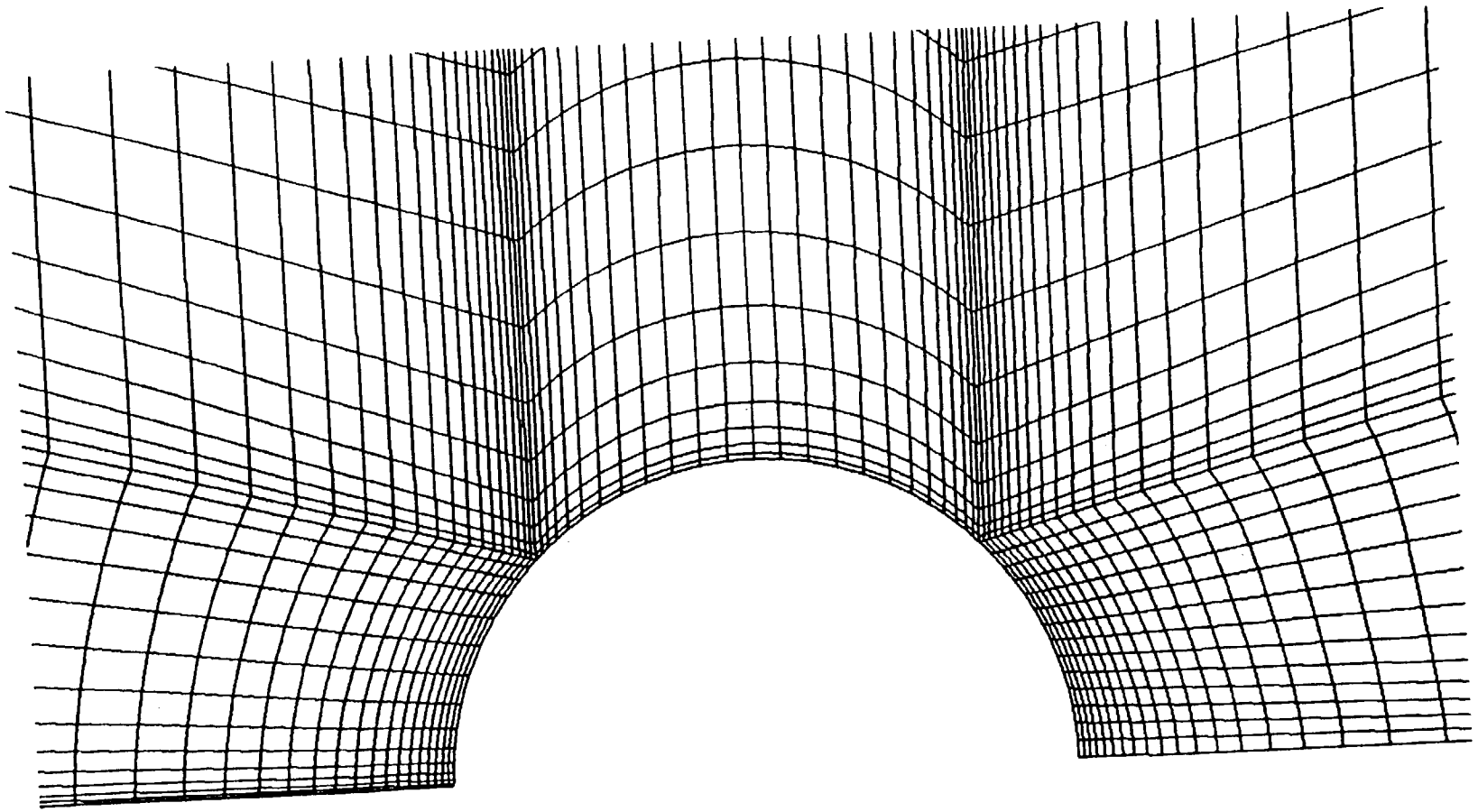

Figure 37A. Computational Grid Enlargement of the Flat Plate Bump Bump Height, 1.0 Inches

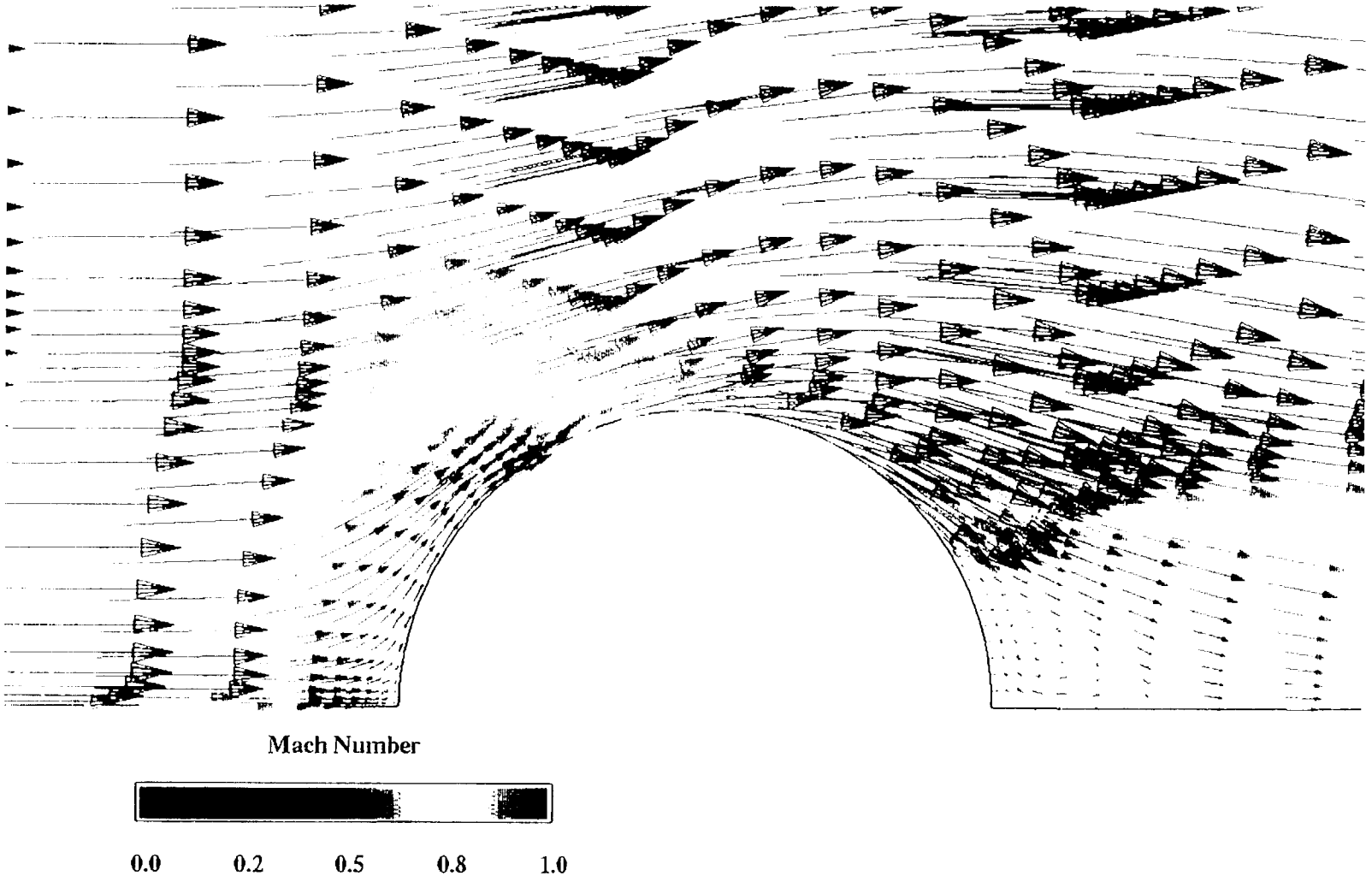

Figure 38A. Velocity Field Near the Polysulfide Bump Flat Plate Bump Height, 1.0 Inches

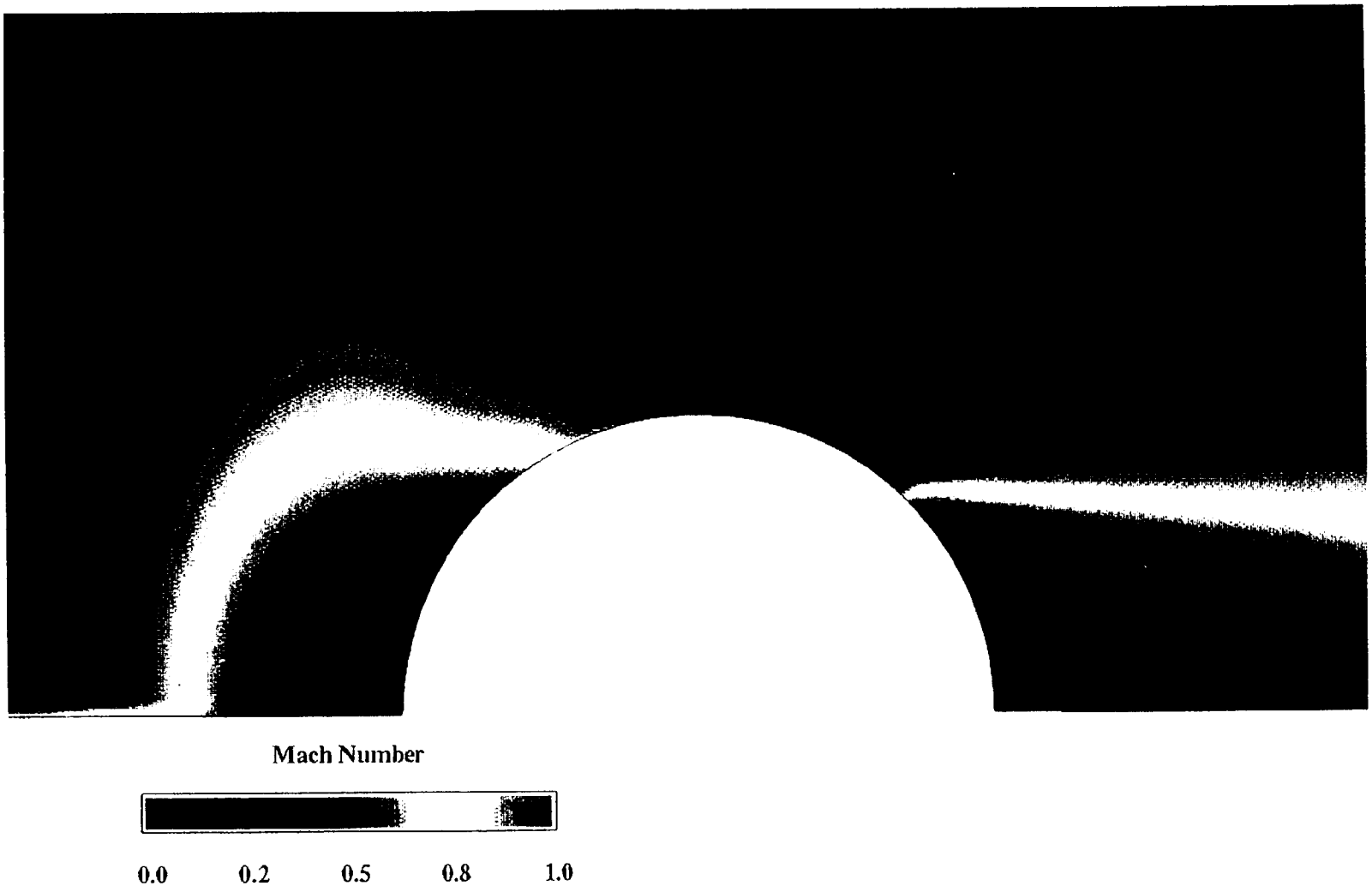

Figure 39A. Mach Number Near the Polysulfide Bump Flat Plate Bump Height, 1.0 Inches

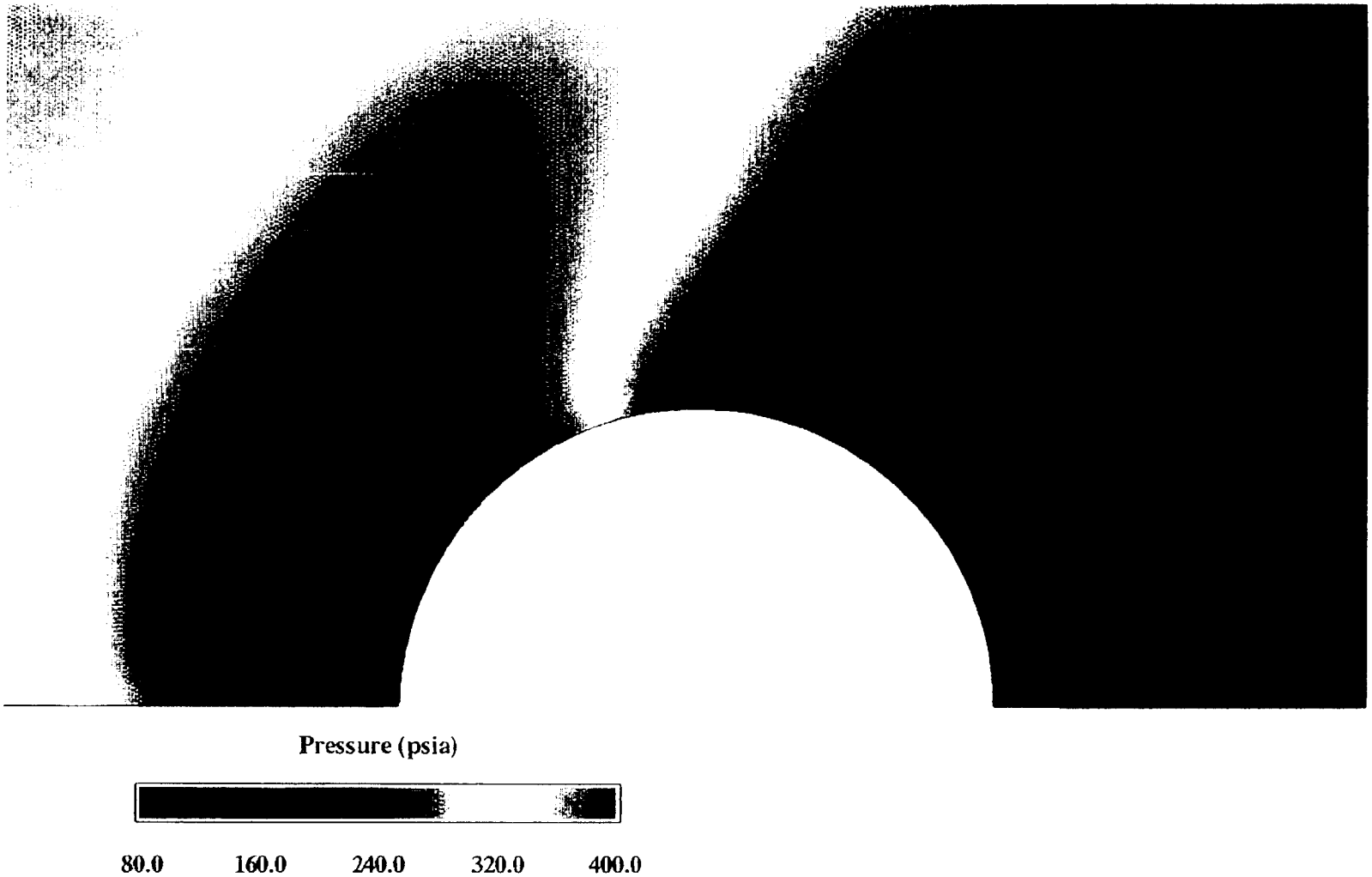

Figure 40A. Pressure Near the Polysulfide Bump Flat Plate Bump Height, 1.0 Inches

Figure 41A. RSRM Joint #4 Polysulfide Residue Analysis Convective Heating Enhancement Factor

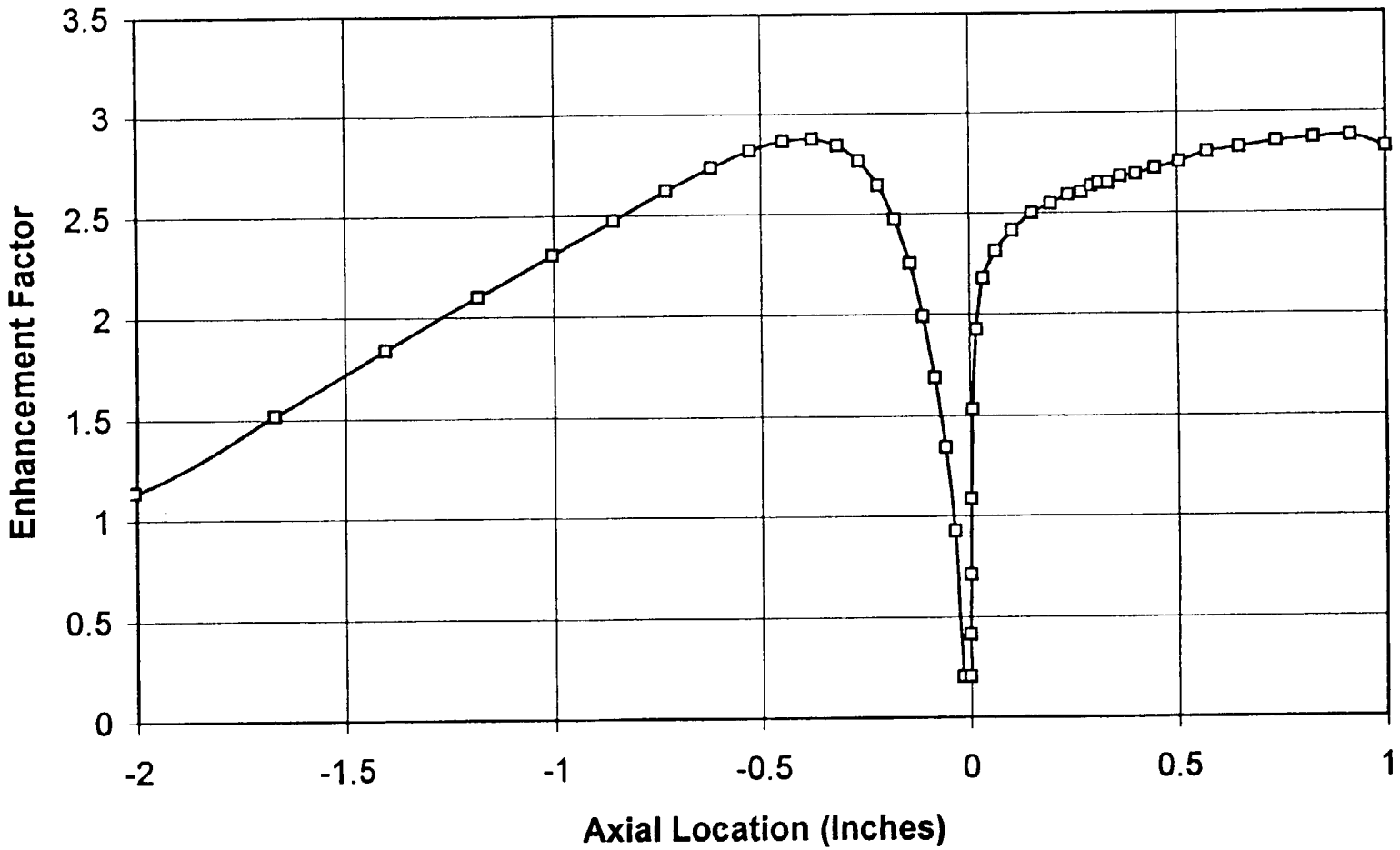

ERC Inc. 1/23/97

4.5 RSRM Full Motor Port Slag Accumulation Analysis

An analysis of the RSRM full motor port at multiple burn times was conducted by ERC, Incorporated. The major purpose of this analysis was to compute the slag accumulation rates in the motor as a function of motor burn time. These computed slag accumulation rates could then be used to form a curve that can be integrated to obtain the total slag accumulation in the motor as a function of burn time. The burn times chosen include 33, 50, 65, 80, and 110 seconds.

Since previous work on this project was performed, several changes in the internal motor geometry and problem boundary conditions occurred. These changes prompted the recomputation of the slag accumulation rates for all the burn times mentioned in the previous paragraph. The main changes affecting the computations were as follows: 1) New information was obtained from Thiokol on both the height and thickness of the motor inhibitors as a function of burn time. 2) Updated aluminum oxide particle size distribution data was obtained from Thiokol 5-inch spin motor related quench bomb work. 3) The operation of the distributed combustion model used in CELMINT was also improved and the capability to consider partial aluminum combustion at the propellant surface was added to the code.

Because of previous work for the pressure perturbation and the FSM-5 insulation erosion investigations, the updated 80 second burn time geometry and computational grid was already available for computation of the slag accumulation in the motor. Therefore, slag accumulation for the 80 second burn time was computed first. This section also summarizes results for the 50 second burn time geometry and discusses the updating of the 33 second burn time geometry and computational grid. The 65 and 110 second burn time geometries, respectively, will be updated later as time permits. Figure 1A shows the complete updated motor geometry for the 80 second burn time. Figures 2A and 3A show the updated motor geometries for the 50 second and 33 second burn times respectively.

Slag accumulation for the 80 second burn time geometry is reported first. The computational grid used to compute the two-phase flow solution was 465 axial grid cells by 65 radial grid cells.

The analysis was performed as a two-phase CFD analysis using the CELMINT distributed combustion model with partial aluminum combustion at the propellant surface. The equilibrium thermochemisty model was used to compute the composition and properties of the combusting gas flow. Table 4.5.1 shows the RSRM propellant formulation used by the equilibrium code to compute the flow mixture properties.

Table 4.5.1 RSRM Propellant Formulation used for the Thermochemistry Computations

Propellant Ingredient	Percent Weight
NH_4ClO_4	69.82%
Fe_2O_3	0.18%
$C_{6.884}H_{10.089}O_{0.278}N_{0.264}$	14.0%
Al	16.0%

Mass flow rate boundary conditions were used at the propellant surfaces. ERC obtained these conditions from SPP ballistic runs made by Sverdrup. Table 4.5.2 shows the mass flow rates applied as boundary conditions along the various propellant surfaces.

Table 4.5.2 Mass Flow Rates For 80 Second Web Time

Forward Segment	1501 lbm/sec.
Forward Center Segment	2659 lbm/sec.
Aft Center Segment	2654 lbm/sec.
Aft Segment	2803 lbm/sec.
Total Mass Flow Rate	9617 lbm/sec.

The particle size distribution used to compute the two-phase flow solutions for this and all other burn times was taken from 5-inch spin motor test related quench bomb measurements. The size distribution is as prescribed by the distribution shown in Figure 4A. The figure shows fine, nominal and course particle size distributions computed for different propellant mixes. The nominal particle size distribution was used in analyzing slag accumulation for all the burn times computed. The caps fraction (The fraction of burning aluminum which remains as discrete phase in the form of aluminum oxide.) was 28.33%. As previously stated, this analysis considers partial aluminum combustion (39% unburned aluminum) at the propellant surface. This means that the particles released from the propellant surface are composed of 54.5% aluminum and 45.5% aluminum oxide as computed from the mass flow rate and combustion boundary conditions.

Table 4.5.3 shows the slag accumulation rates for the various locations of interest in the motor for the particular boundary conditions used in the analysis. Further adjustments to the discrete phase particle boundary conditions may be investigated as time permits.

Table 4.5.3 Slag Accumulation Rates in the 80 Second Motor

Motor Location	Accumulation Rate (lbm/sec)
Head End	11.5
Forward Slot	3.5
Center Slot	3.0
Aft Slot	14.4
Submerged Nozzle	39.0

The second two-phase CFD solution computed was for the 50 second burn time. the computational grid was composed of 465 axial grid cells by 65 radial grid cells.

Just as for the 80 second burn time solution, the analysis was performed as a two-phase analysis using the CELMINT distributed combustion model with partial aluminum combustion at the propellant surface. The same equilibrium thermochemisty model and boundary conditions were used as discussed in Table 4.5.3.

Mass flow rate boundary conditions were used at the propellant surfaces. These conditions were obtained from SPP ballistic runs made by Sverdrup. Table 4.5.4 shows the mass flow rates from the various propellant surfaces used in this analysis

Table 4.5.4 Mass Flow Rates For 50 Second Web Time

Forward Segment	1490 lbm/sec.
Forward Center Segment	2557 lbm/sec.
Aft Center Segment	2548 lbm/sec.
Aft Segment	2834 lbm/sec.
Total Mass Flow Rate	9429 lbm/sec.

The boundary conditions on the discrete phase particles were identical to those used for the 80 second burn time problem.

Table 4.5.5 shows the slag accumulation rates for the various locations of interest in the motor.

Table 4.5.5 Slag Accumulation Rates in the 50 Second Motor

Motor Location	Accumulation Rate (lbm/sec)
Head End	0.2
Forward Slot	0.7
Center Slot	1.7
Aft Slot	5.8
Submerged Nozzle	33.4

Computation was initiated for the 33 second burn time solution. The computational grid used was composed of 462 axial grid cells by 70 radial grid cells.

The analysis was performed as a two-phase analysis using the CELMINT distributed combustion model with partial aluminum combustion at the propellant surface. The equilibrium thermochemisty model was used to compute the composition and properties of the combusting gas flow. The same propellant formulation as shown in Table 4.5.1 was used for this problem.

Mass flow rate boundary conditions were used at the propellant surfaces. These conditions were obtained from SPP ballistic runs made by Sverdrup. Table 4.5.6 shows the mass flow rates from the various propellant surfaces used in this analysis

Table 4.5.6 Mass Flow Rates For 33 Second Web Time

Forward Segment	3328 lbm/sec.
Forward Center Segment	2233 lbm/sec.
Aft Center Segment	2219 lbm/sec.
Aft Segment	2760 lbm/sec.
Total Mass Flow Rate	10540 lbm/sec.

The boundary conditions on the discrete phase particles were identical to those used in the 50 and 80 second burn time problems.

This analysis of the 33 second burn time was interrupted by other more pressing analyses to be completed as time permits.

Figure 1A. RSRM Motor Geometry, 80 Second Burn Time

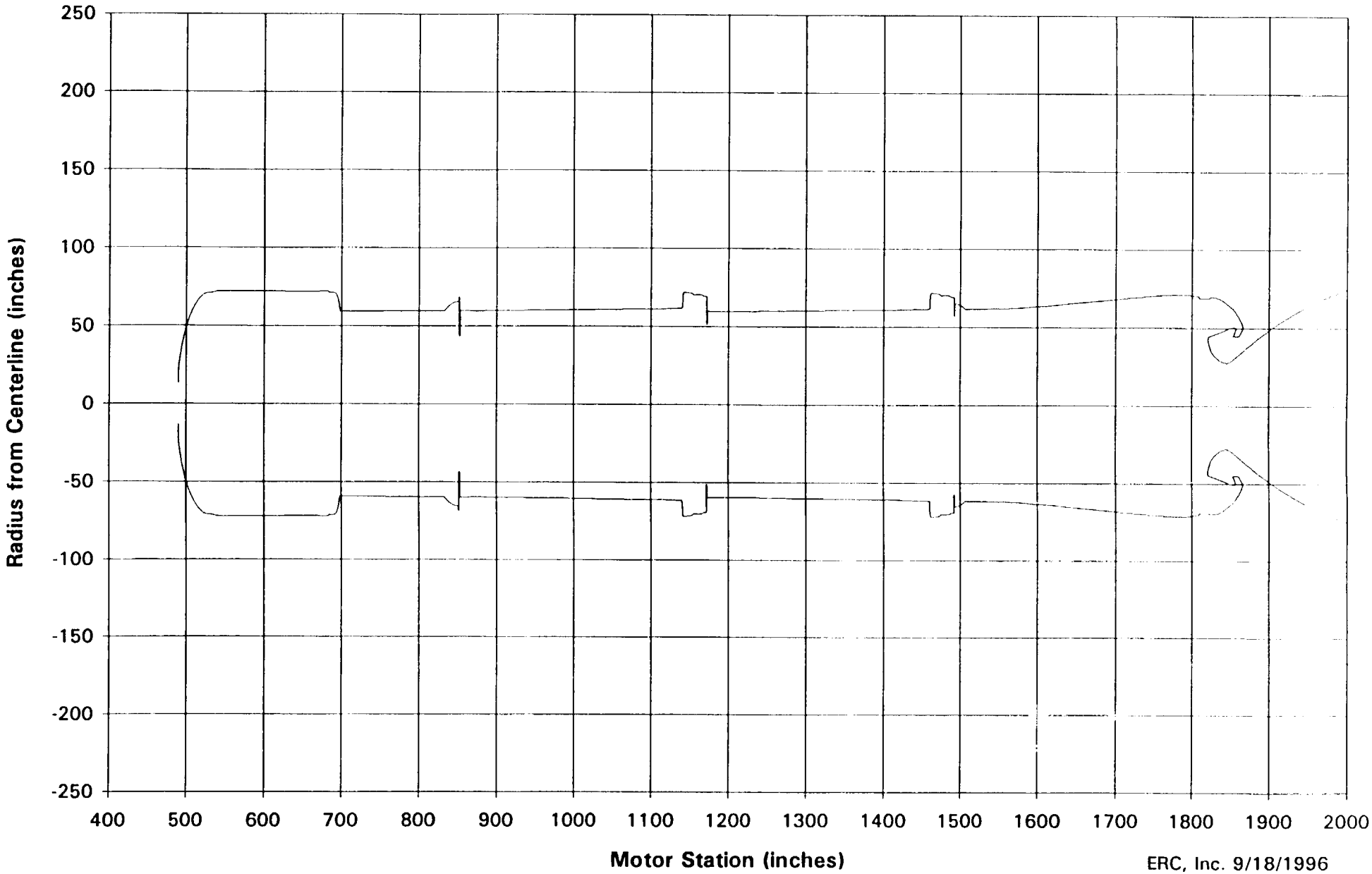

Figure 2A. RSRM Motor Geometry, 50 Second Burn Time

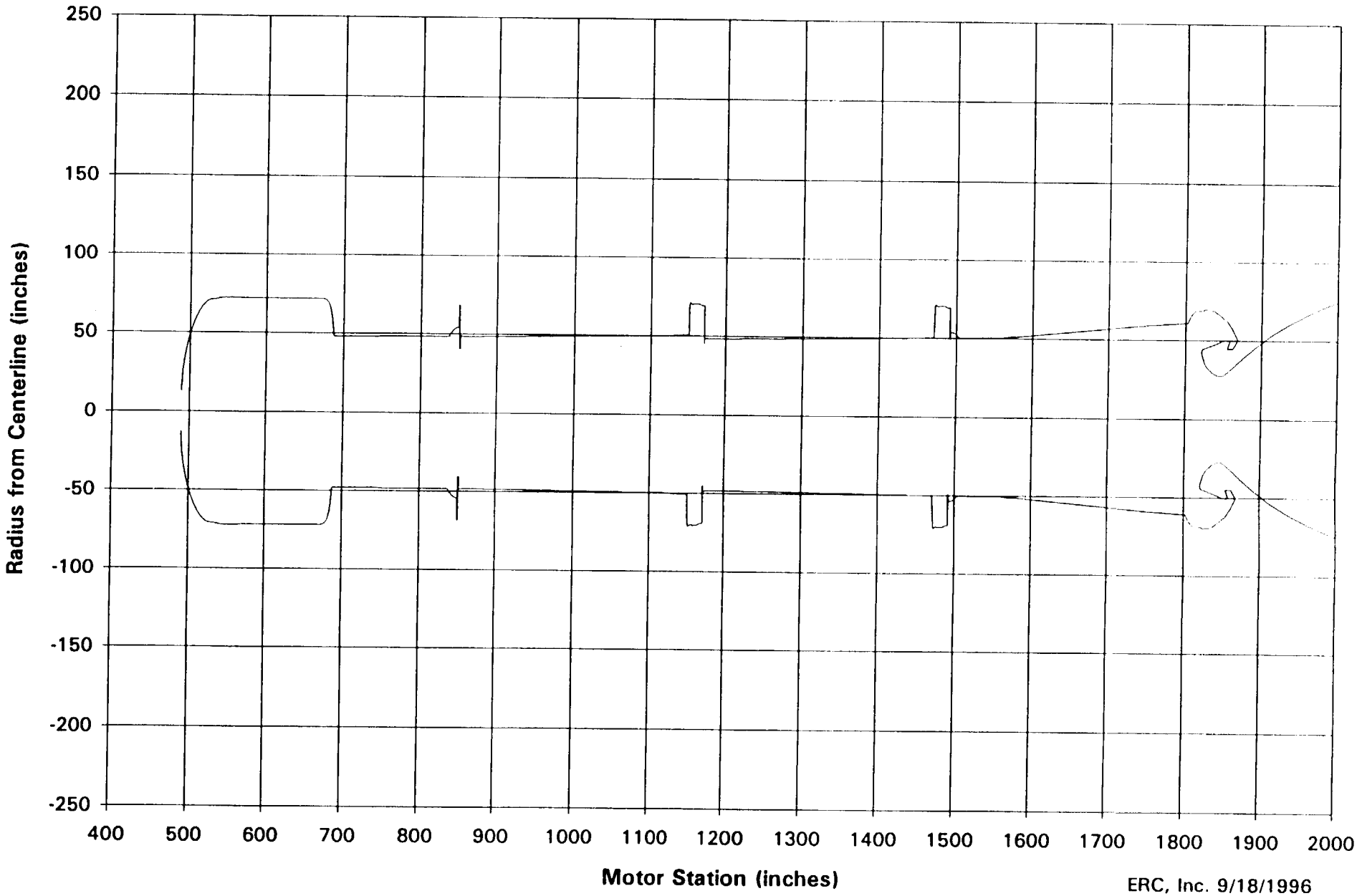

Figure 3A. RSRM Motor Geometry, 33 Second Burn Time

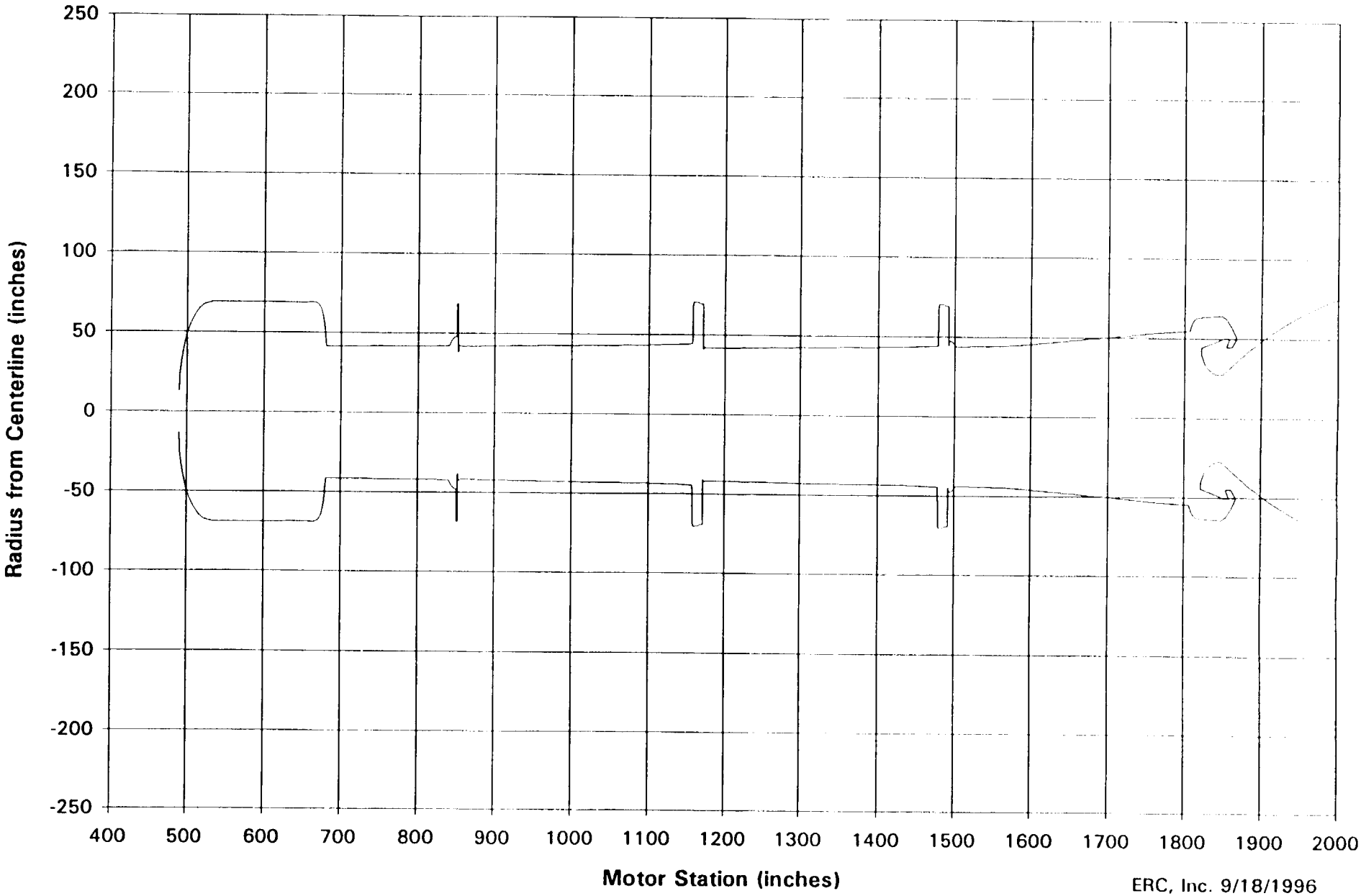

Figure 4A. Particle Distribution Data

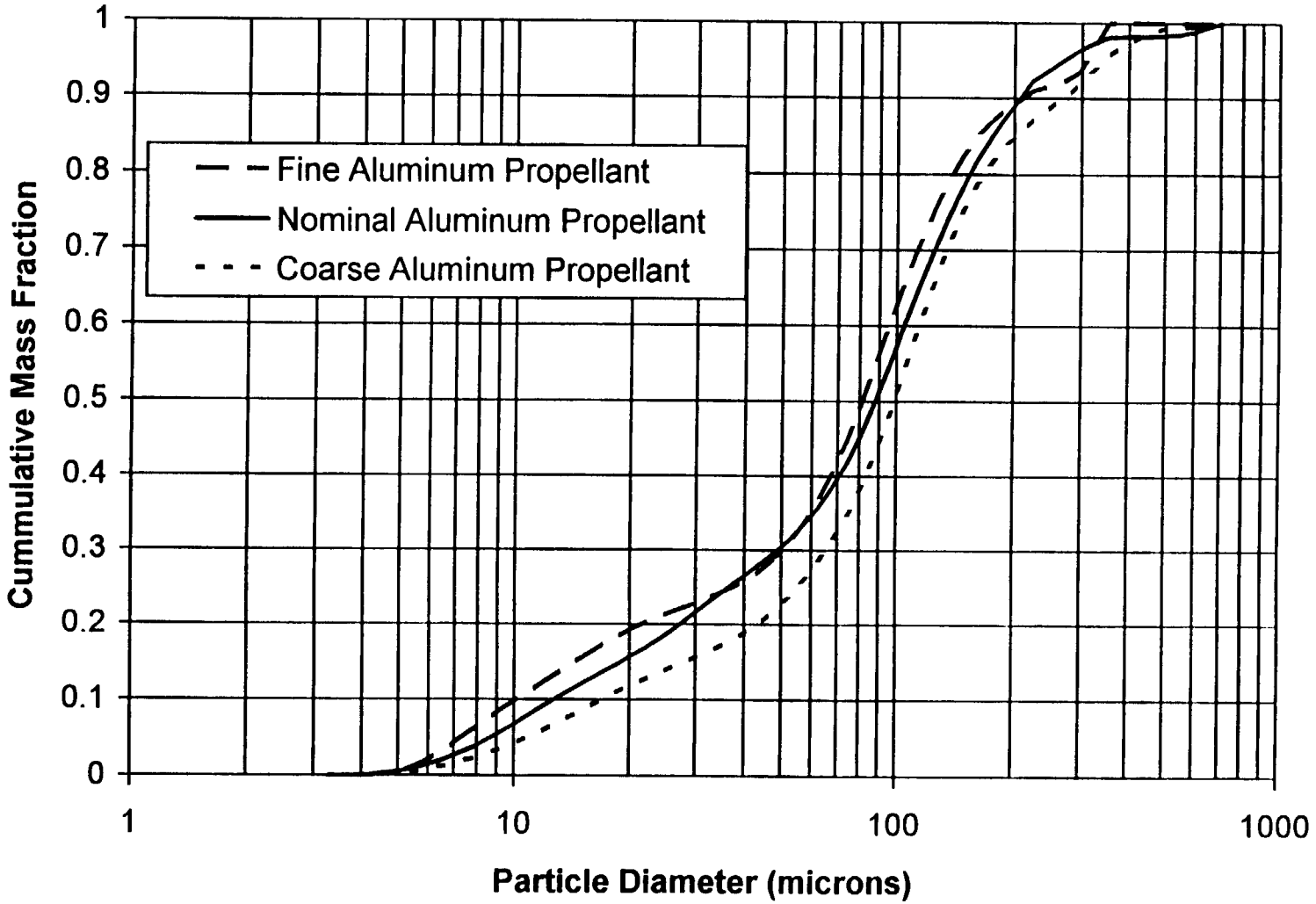

ERC, Inc.

4.6 RSRM Motor Analysis of Two-Phase Flow in the Aft Segment/Submerged Nozzle Region

The first full scale test of asbestos-free insulation materials being developed for RSRM occurred with the static firing of FSM-5. Two materials containing Kevlar substitute fiber were tested in the aft dome of the motor in the region shown in Figure 1A. Figure 1A shows both the initial and post-test eroded contours for the FSM-5 submerged nozzle. The Kevlar fiber containing materials were substituted in the aft dome by placing a 7% Kevlar material over one-half of the circumference of the aft dome and an 11% Kevlar material over the remaining half of the dome. Both materials experienced higher than expected erosion in a narrow zone extending around the entire circumference and located close to the case/nozzle joint, as shown in Figure 1A. This zone of high erosion was closer to the case/nozzle joint and much deeper than previously experienced with the carbon fiber filled EPDM insulation currently used at this location in flight motors. Additionally, the circumferential station of highest erosion was at approximately 270 degrees, which is always noted with static motor test using a "standard" nozzle vectoring duty cycle.

Some initial results of a CFD analysis investigating the RSRM case insulation erosion were performed. These results were reported to NASA for a simplified nozzle geometry at the 67 second burn time from solutions that were already available. This initial analysis was performed to provide rapid response information to the NASA investigation team until a more detailed analysis could be performed. This section of the final report presents a more extensive analysis of the aft case insulation erosion.

Two-phase CFD analyses were conducted to examine the particle/gas flow interactions in the submerged nozzle region of the RSRM. This was done in order to obtain information which could be used in explaining the excessive erosion pattern which occurred in FSM-5. These were the major objectives of the CFD analyses.

1. The first objective of the analysis was to determine the structure of the flow field underneath the submerged nozzle.

2. The analysis was also performed so that the gas flow and particle impingement environments could be defined along the surface of the case insulation in the aft dome region.

3. The analysis was performed to investigate the effects of geometry changes due to case insulation erosion and nozzle gimbaling on the structure of the flow field and local environments in the aft case region.

4. The final objective of the analysis was to investigate the effect of geometry changes associated with the extra insulation thickness used in the aft dome of FSM-5 and determine if this extra insulation thickness increased the severity of the environment.

In order to accomplish these objectives, the overall RSRM case insulation analysis was divided into the following steps.

1. A two-phase CFD analysis was performed for the entire RSRM port at the 80 second burn time and trajectories of various size particles released from the entire burning surface of the aft segment were computed to determine their impact location.

2. Two-phase CFD analyses were performed to investigate different nozzle configurations. Five nozzle configurations were investigated. An initial and eroded post test geometry were analyzed for the FSM-5. An initial and eroded post test geometry were also analyzed for a representative flight motor configuration. A 3.6 degree gimbaled nozzle configuration was computed for the initial flight motor geometry. These analyses were compared to determine information pertinent to the explanation of the FSM-5 motor case insulation erosion.

3. Trajectories of slag droplets shed from the nozzle cowl/boot ring interface at the point of flow separation were computed and their impact location was analyzed.

4. The flow velocities and mass flow rates in the secondary flow recirculation region in the extreme aft case cavity adjacent to the nozzle flex boot were computed for all the cases discussed under step 2.

The first step of the analysis investigating the aft dome case insulation erosion was to perform a two-phase CFD analysis of the entire RSRM motor port at the 80 second burn time. This analysis was performed to determine the structure of the flow field in the submerged nozzle region and the disposition of particles released from the propellant surfaces. The internal motor geometry used to compute the entire motor port solution is shown in Figure 2A. This figure shows the velocity magnitude for the entire motor port length. Velocities of over 5000 ft/sec occur within the computational domain in the nozzle but the plotted velocity magnitude was limited to only 500 ft/sec in order to better illustrate the acceleration of the lower velocity flow in the motor port. The figure shows all the main features of the internal motor geometry relevant to the computation of the flow field of interest. In addition to computing the structure of the flow field in the submerged nozzle region and determining the disposition of particles released from the propellant surface, this full motor port solution was also used as a partial motor inlet boundary condition for the analyses involving the various nozzle geometry configurations. The various nozzle geometry configuration solutions were performed for only the aft segment of the motor beginning at the aft slot. These partial motor solutions could be computed more quickly because of the drastic reduction in computational grid cells resulting from not recomputing the flow field upstream of the aft slot. The full motor port solution was applied as the partial motor inlet boundary

condition for each of the nozzle geometry configurations. These boundary conditions automatically satisfied the condition that the flow field upstream of the aft slot remain the same for all the nozzle geometry configurations. Figure 3A shows the flow field velocity vectors in the submerged nozzle region. There are several important flow field structural features apparent in the figure. The flow field separates from the aft propellant grain. This causes a recirculation to develop in the area forward of the case/dome joint stiffener. The dividing streamline between the port flow and the flow underneath the nozzle begins at the end of the aft propellant grain and reattaches on the underneath side of the nozzle near the nozzle nose. A large recirculation region is present in the cavity underneath the nozzle with strong rearward velocities present along the underneath side of the nozzle. There is also a counter rotating secondary recirculation present in the extreme aft cavity formed by the separation of the main cavity recirculation region from the cowl/boot ring interface. This secondary recirculation can be more easily seen in Figure 4A which is an enlargement of the extreme aft cavity. The dividing streamline between the main and secondary recirculation regions reattaches on the case insulation opposite the boot ring. The next paragraph discusses the disposition of particles released from the aft propellant grain. The structure of the flow field underneath the nozzle as seen in Figures 3A and 4A should be keep in mind throughout this discussion since the large rearward velocities along the nozzle underneath provide a transport mechanism for slag to collect in the nozzle aft cavity.

The two-phase CFD solution of the entire motor port was used to determine trajectories of particles released from the forward, forward center, aft center and aft propellant grains. Particles ranging in diameter from 10 microns to 600 microns were considered in this analysis. It was determined that particles from the forward, forward center and aft center propellant grains do not impact underneath the submerged nozzle regardless of the size of the particles. This is due to the structure of the flow created by the inhibitor stubs extending from the downstream face of the forward, center and aft slots. Particles emanating from these propellant segments either impact the inhibitor stubs or are directed toward the motor centerline so that they do not impact the underneath surfaces of the nozzle. Particles from the aft propellant segment do impact the underneath side of the nozzle as illustrated in Figures 5A, 6A, and 7A. Plots for these particles are shown since they represent most of the discrete phase particles in the motor domain. Approximately 95% of the discrete phase particle mass is represented by particle diameters below 200 microns. Figure 5A shows the trajectories of 50 micron diameter particles which are released from the aft propellant segment. Figure 6A shows trajectories for 100 micron diameter particles and Figure 7A shows trajectories for 200 micron diameter particles. The aft-most particle release locations for which particles impact the nozzle underneath are labeled on each of these figures. These figures illustrate and support the following conclusion. Particles released from the aft propellant segment do not impinge directly on the nozzle case insulation but impinge on the nozzle underneath side. This observation coupled with the knowledge that slag collects in the rear section of the submerged nozzle leads to the following conclusion. Particles from the aft propellant segment impact the underneath side of the nozzle and

form a melt layer of slag which is driven rearward by the large rearward velocities in the recirculation region underneath the nozzle, see Figure 3A. This melt layer is driven rearward along the surface underneath the nozzle to a point in the region of the cowl/boot ring interface at which droplets are sheared off due to flow separation near the extreme aft cavity of the nozzle. The disposition of these droplets will be studied in the next portion of this analysis. Another observation can be made regarding these conclusions. Since the flow field structure shown in Figure 3A is not present at early motor burn times, the shedding of slag from the cowl/boot ring interface and subsequent collection of slag in the aft dome occurs during the latter half of motor burn. This is because both the gas phase flow and movement of discrete particles are directed toward the nozzle nose during the first half of motor burn when propellant is still burning in the nozzle underneath cavity.

As a next phase of the analysis of the aft dome case insulation erosion, trajectories of slag droplets shed from the region of the cowl/boot ring interface were studied for various nozzle geometries. The exact location of the release point at which a slag droplet would be sheared from the nozzle underneath surface was not known but the separation of the flow from the cowl/boot ring interface (as shown in Figure 8A) makes this a probable location. Droplets of various sizes were released from several grid cells in the region of the cowl/boot ring interface to study the effect of release location on the droplet trajectory. The nominal release location that will be shown in plots is the cowl/boot ring interface. Also, since the exact size of the released droplets was unknown, a range of droplet diameters that varied from 500 microns to 3000 microns was analyzed. The 2000 micron diameter droplet is shown in the plots summarizing the results unless otherwise specified since it adequately represents the results presented.

The first nozzle geometry configuration considered was the initial flight geometry. Figure 9A shows the flow field in the extreme aft cavity underneath the nozzle. The figure also shows the trajectory of a slag droplet released from the cowl/boot ring interface. Droplets sheared from the slag melt layer near the cowl/boot ring interface impact near the nozzle/case joint shown in the figure. Figure 10A shows the flow field and slag droplet trajectory for the initial FSM-5 nozzle geometry. The droplet impacts in the same region as occurred for the initial flight geometry. The location of the center of the extreme aft cavity secondary recirculation is in a slightly different location for the two configurations but the flow velocities along the aft dome case insulation and along the flex boot are similar. It is concluded from this comparative analysis that the extra thickness of case insulation used in the FSM-5 does not significantly impact the severity of the flow or particle impingement environment. The gas flow and particle impingement environments are similar for the initial FSM-5 and initial flight motor geometries.

Figure 11A shows the flow field and slag droplet trajectory for the post test eroded FSM-5 nozzle geometry. Figure 10A and Figure 11A can be compared. Note that the impact location of the slag droplet has not been significantly altered. Note also that the droplets impinge on the aft case insulation in the highest region of erosion observed in

the FSM-5 nozzle. The weak secondary flow field in the extreme aft cavity has been significantly altered by the nozzle erosion but the primary disposition of the slag droplets has not been significantly altered. A similar result is also apparent if Figure 11A and Figure 12A are compared. Figure 12A shows the flow field and slag droplet trajectory for the post test flight motor geometry. The primary impact location of the slag droplet has not changed significantly and is still close to the nozzle/case joint. The secondary recirculation in the extreme aft cavity is significantly different from the FSM-5 secondary recirculation due to the large differences in the extreme aft cavity geometry. A detailed discussion of slag droplet disposition as a function of droplet size is discussed later for the eroded nozzle configurations because the full analysis showed that there is an increased propensity for slag to be carried into the flex boot region for the FSM-5 eroded nozzle configuration.

The last comparison made is for the initial flight motor geometry at 0 degrees and 3.6 degrees gimbal angle. The gimbaled nozzle configuration discussed is the open or windward side of the nozzle with the boot ring gimbaled forward toward the nozzle nose. Due to gimbaling, the distance between the case insulation and the boot ring is greater for the 3.6 degree gimbal configuration of the nozzle. This shifts the main recirculation underneath the nozzle further aft and changes the secondary recirculation position and strength. Figure 13A shows the flow field for the gimbaled nozzle configuration. The velocities along the case insulation wall are greater over most of the case wall. Figure 14A shows a plot of the mass velocity along the surface as a function of distance from the nozzle/case joint forward along the case insulation, for the 0 degree and 3.6 degree gimbal configurations. The inflection points in the curves between 8 and 9 inches from the nozzle/case joint represent the reattachment points for the secondary recirculation on the case insulation wall. The mass velocities along the nozzle flex boot are also greater for the 3.6 degree gimbal configuration. The strength of the secondary recirculation is significantly stronger for the 3.6 degree gimbal configuration. This is illustrated by Figure 15A which shows the integrated mass flow rate from the center of the recirculation region to the nozzle fixed housing. The increased mass flow rate in the secondary recirculation also provides a mechanism for increased slag transport to the flex boot region for the gimbaled configuration. The comparison of the 0 degree and 3.6 degree configurations shows that the CFD results for these configurations agree with the test data in predicting a more severe erosion environment at the 270 degree circumferential angle.

An analysis investigating the affect of varying the droplet diameter and release location along the underneath side of the nozzle was performed. Figure 16A (flight motor) and 17A (FSM-5) show trajectories for 1000 and 2000 micron diameter droplets released from the nozzle cowl/boot ring interface and two grid stations downstream of the interface. The velocity along the underneath side of the nozzle drops rapidly after flow moves rearward of the interface so that droplets released aft of the interface are accelerated much more slowly in the rearward direction. The narrow lines in the figures represent the 1000 micron diameter trajectories and the wider lines represent the 2000

micron diameter trajectories. The three release locations along the boot ring are represented by the color scheme in Table 4.6.1.

Table 4.6.1 Color Code for the Droplet Release Location Analysis

Location	Release Location	Color
1	Cowl/Boot Ring Interface	Black
2	One Grid Cell Downstream of Interface	Red
3	Two Grid Cells Downstream of Interface	Green

The 1000 micron droplet released from location 1 impacts near the nozzle/case joint for both the FSM-5 and flight motor eroded geometry configurations. The 1000 micron droplet released from location 2, just aft of the cowl/boot ring interface, is carried into the region of the flex boot for the FSM-5 configuration. The 1000 micron droplet released from the most aft location 3 of the FSM-5 configuration, does not have enough rearward velocity to pass through the secondary recirculation. This droplet impacts the case insulation near the secondary flow recirculation reattachment point. All the 1000 micron diameter droplets released from all locations impact the case insulation near the nozzle/case joint for the flight motor. This is because the velocities are greater along the cowl and forward portion of the boot ring than for the FSM-5 configuration. This occurs because the main recirculating flow underneath the nozzle has moved further rearward as illustrated by the rearward movement of the center of the secondary recirculation for the flight motor, Figure 16A. The results for the 2000 micron droplet trajectories for the FSM-5 are similar but shifted slightly because of the greater weight of the 2000 micron droplets. The droplets released from locations 1 and 2 in this case impact the case insulation near the nozzle/case joint. The droplet released from the most aft location is carried into the region of the flex boot. All the 2000 micron diameter droplets for the flight motor released from the three locations impact near the nozzle/case joint. This analysis shows that the FSM-5 configuration has more potential for transporting slag to the flex boot region. This agrees with the FSM-5 test results. More erosion in the flex boot was evident for the FSM-5 nozzle than seen in the flight motor nozzle.

The major conclusions related to excessive erosion of the case insulation in FSM-5 will now be summarized. The excessive erosion of the case insulation in the aft dome region must occur during the last half of the motor burn since the flow recirculation region in the aft cavity region does not exist at early burn times due to the forward direction of the flow driven by the presence of burning propellant underneath the nozzle. Particulate from the burning surface of the propellant in the motor port upstream of the nozzle do not impact the case insulation on the aft dome directly. Instead, aluminum oxide particulate from the burning surface of the propellant aft segment strikes the underneath surface of the nozzle near the nose tip late in motor burn where they collect to form a melt layer. The melt layer is driven aftwards toward the nozzle cowl and boot ring by the flow in the recirculation region underneath the

nozzle. As this melt layer reaches the region of the cowl/boot ring interface, slag droplets are sheared from the surface and impact the case insulation near the nozzle/case joint. This creates a severe particle impingement environment on the aft dome case insulation near the nozzle/case joint for both the FSM-5 and flight motor configurations. One would therefore hypothesize that the asbestos-free insulation has a lower resistance to a direct particle impingement environment than the carbon filled EPDM insulation used in the current flight motors. Excessive case insulation erosion in static motor FSM-5 results in changes to the recirculating flow in the extreme aft cavity region that increases slag transport and heating to the nozzle fixed housing and flexible boot surfaces not observed in the eroded flight nozzle. Support was also found for the greater erosion at the 270 degree circumferential angle observed in static test firings. This increased erosion is caused by a more severe environment induced by the "standard" nozzle vectoring duty cycle

This analysis provides strong support to show the necessity for using two-phase CFD analysis techniques to define the environments for new or modified SRM configurations. These kinds of analyses can reduce design risks and assist in planning higher fidelity subscale tests to evaluate potential motor problems.

Figure 1A. FSM-5 Initial and Eroded Nozzle Geometry Contours

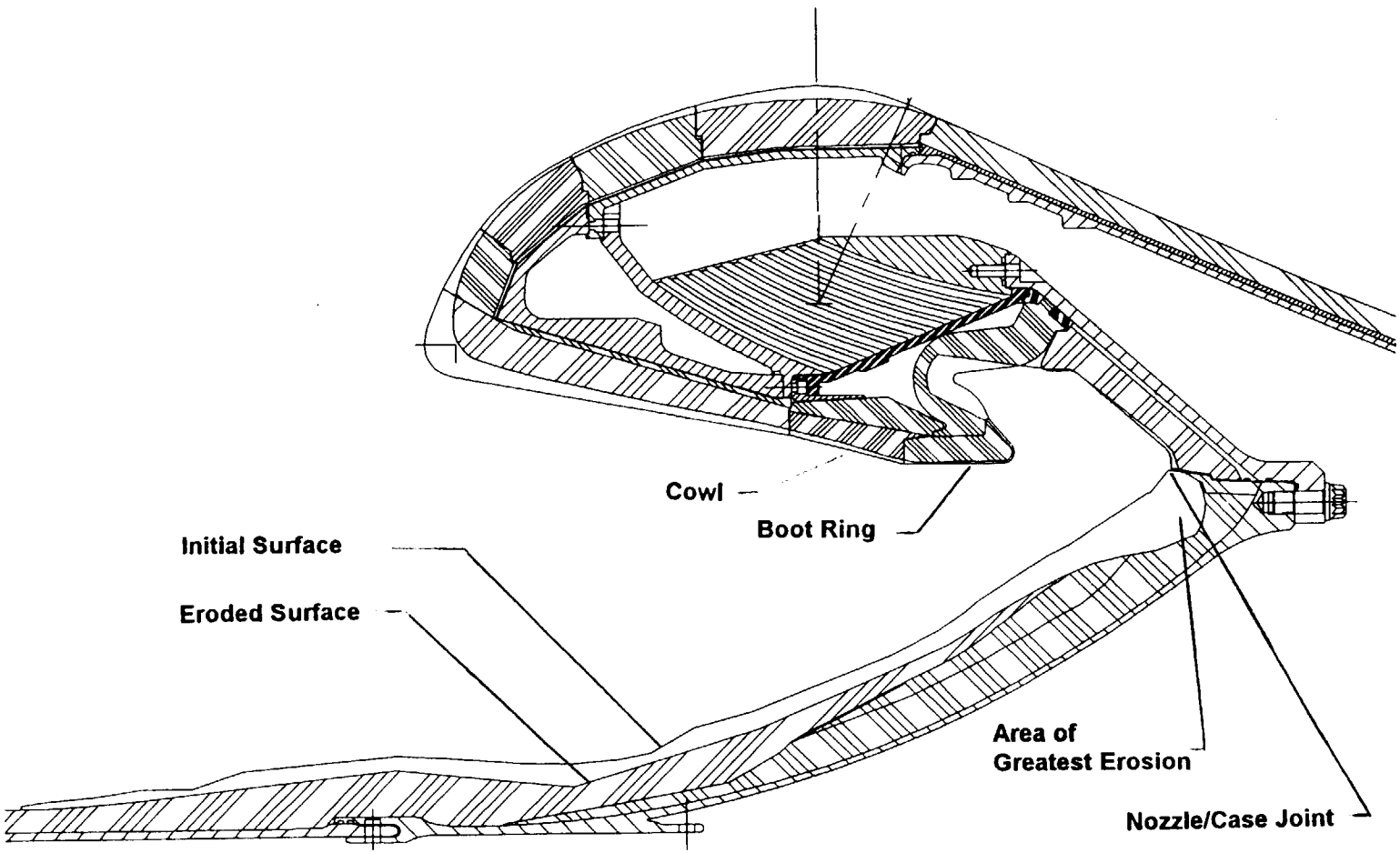

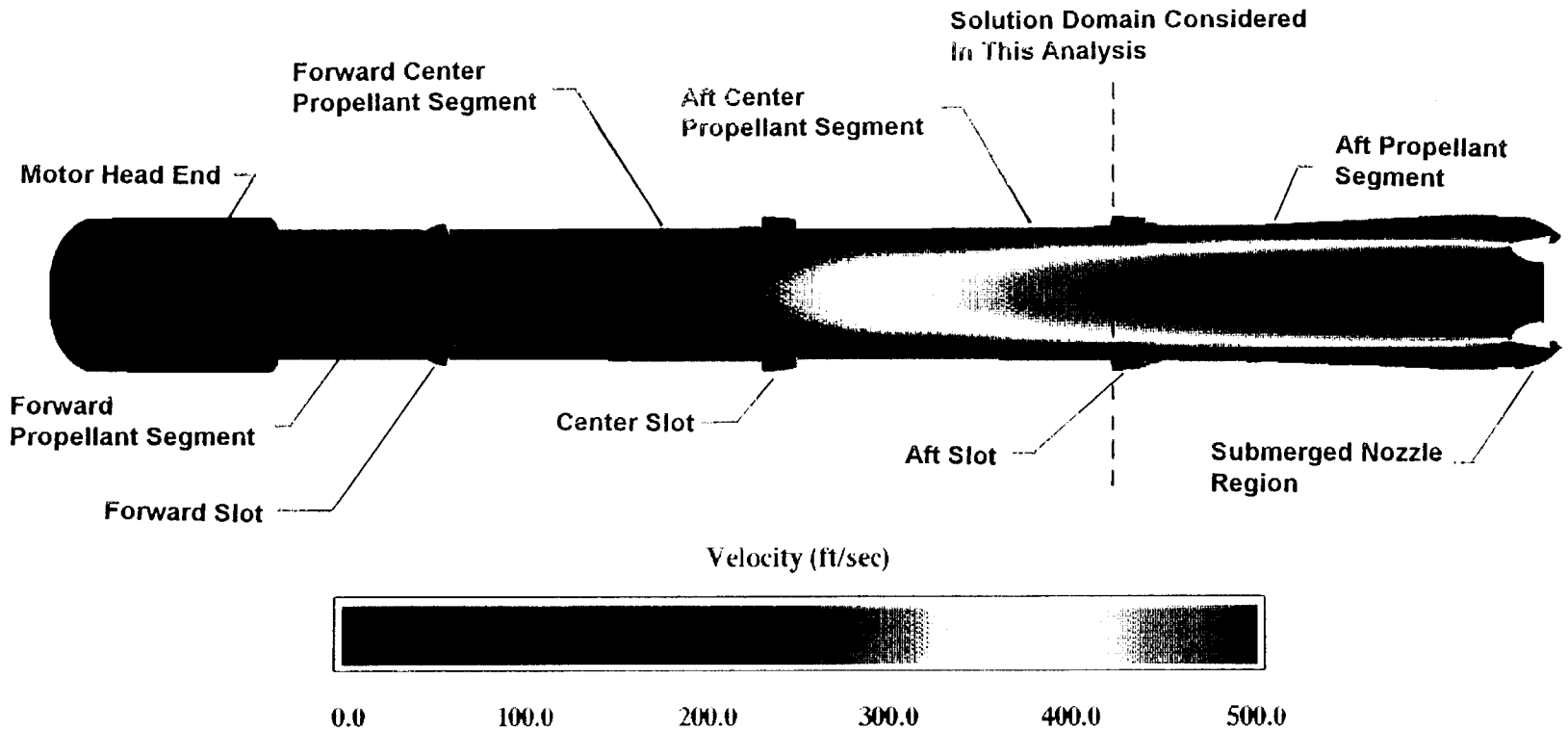

Figure 2A. RSRM Full Motor Port 80 Second Burn time, Velocity Magnitude

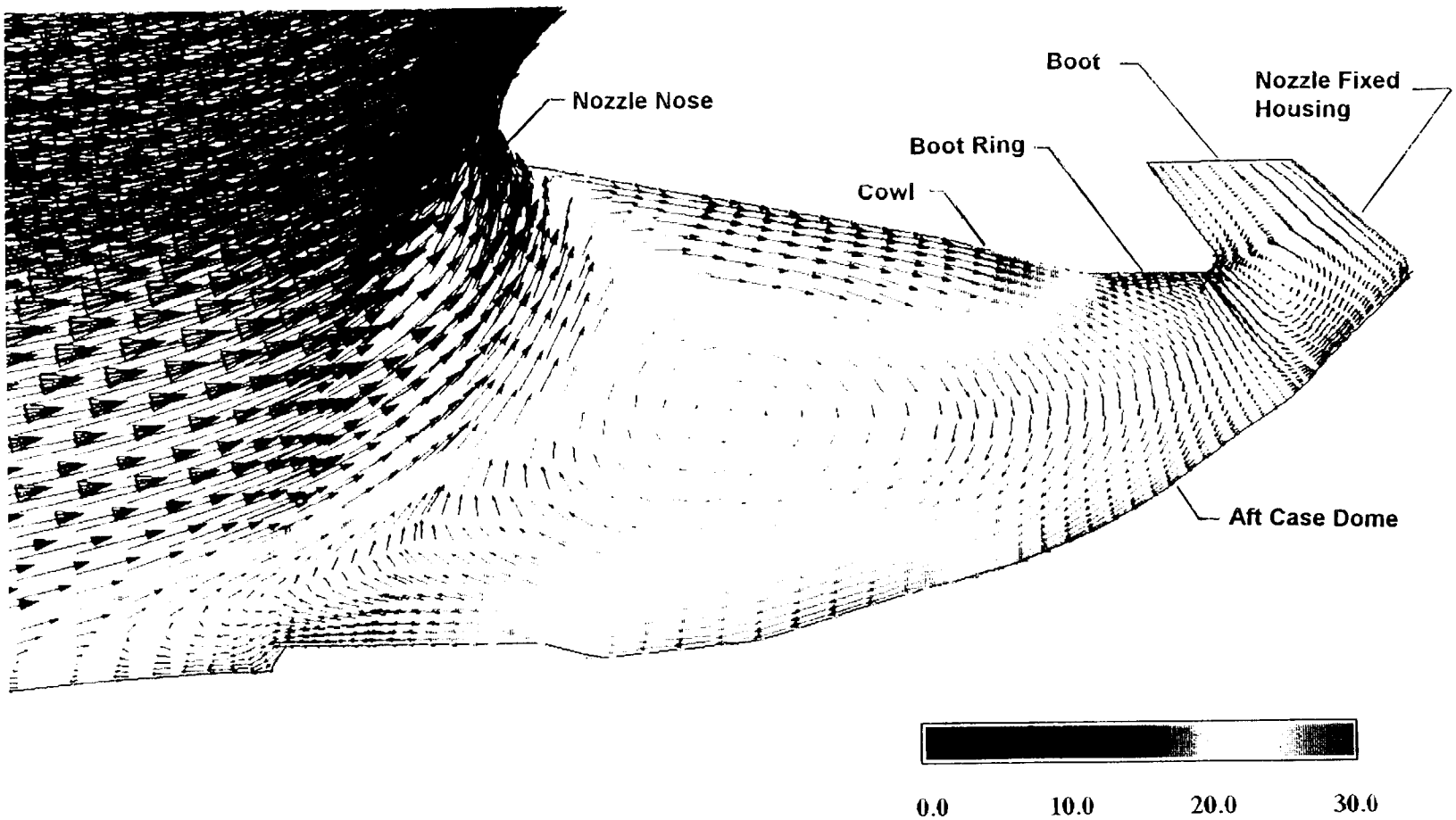

Figure 3A. Initial Flight Nozzle Geometry, Submerged Nozzle Flow Field Features

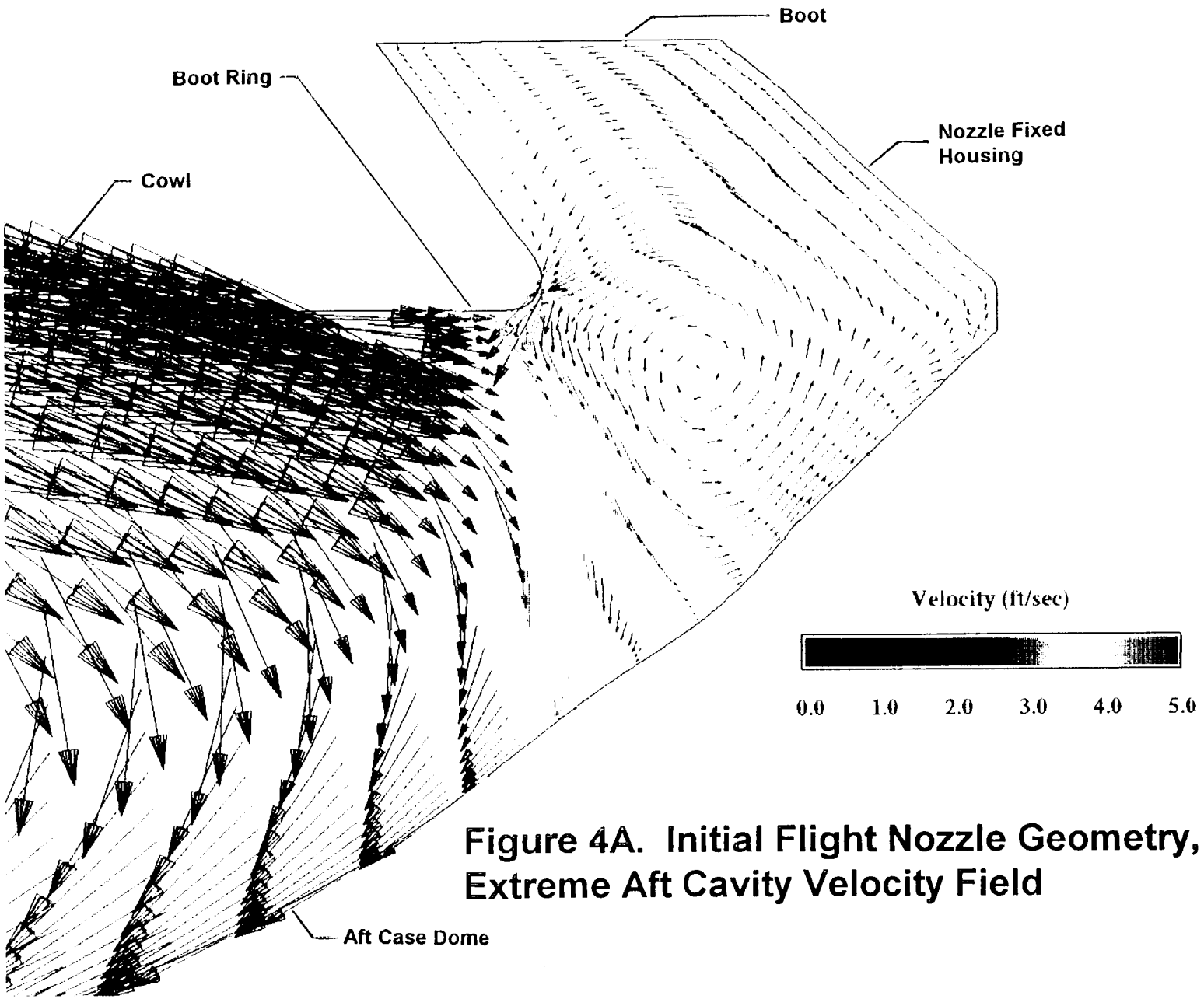

Figure 4A. Initial Flight Nozzle Geometry, Extreme Aft Cavity Velocity Field

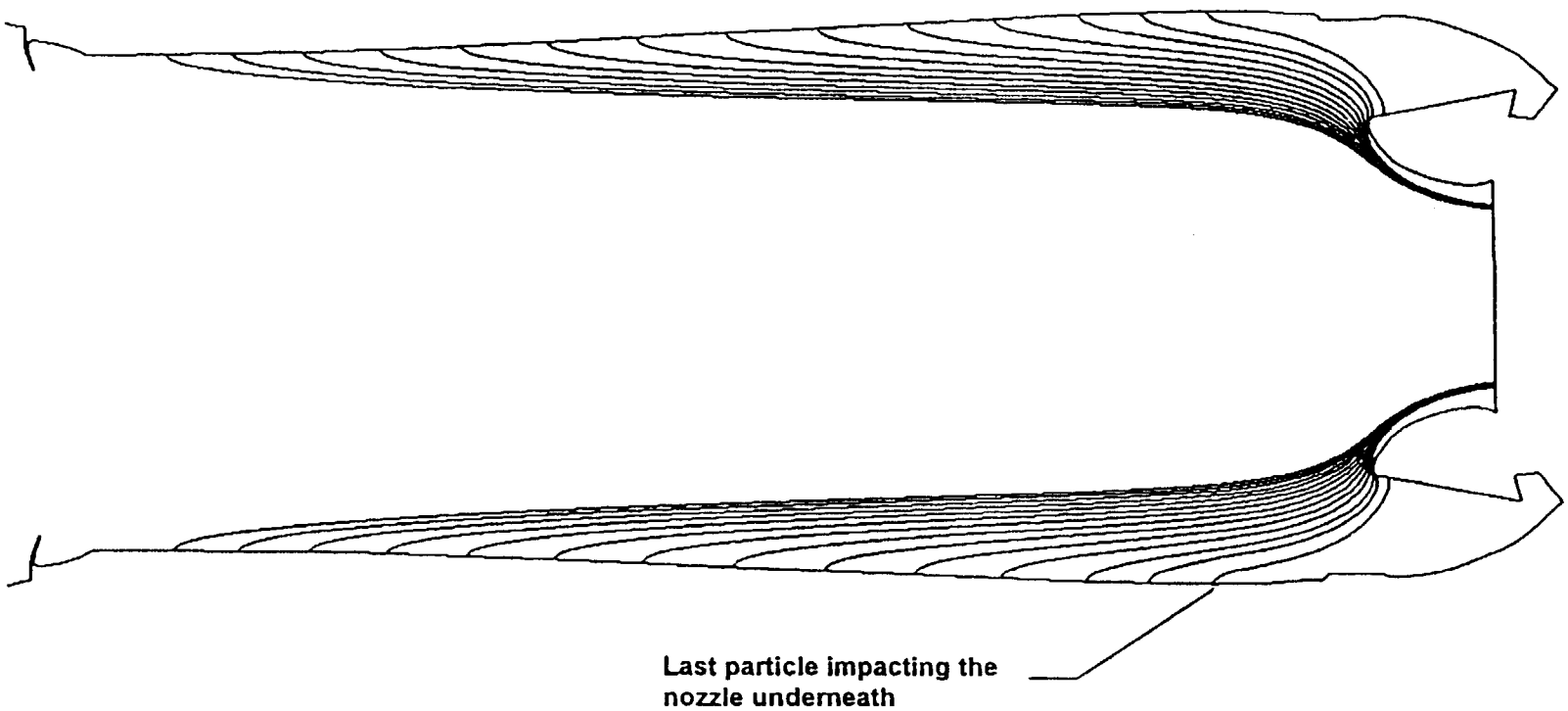

Figure 5A. 50 Micron Diameter Particle Trajectories from the Aft Propellant Grain

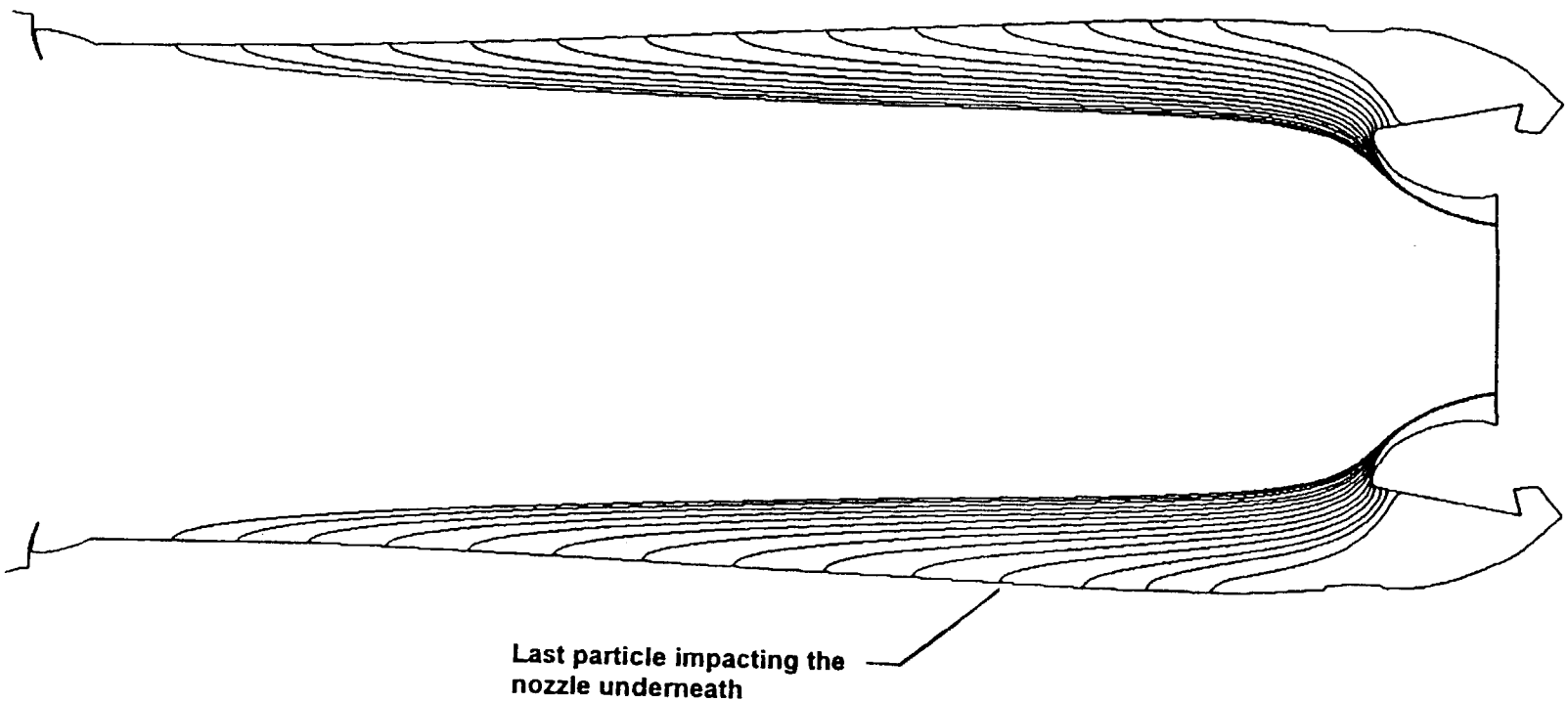

Figure 6A. 100 Micron Diameter Particle Trajectories from the Aft Propellant Grain

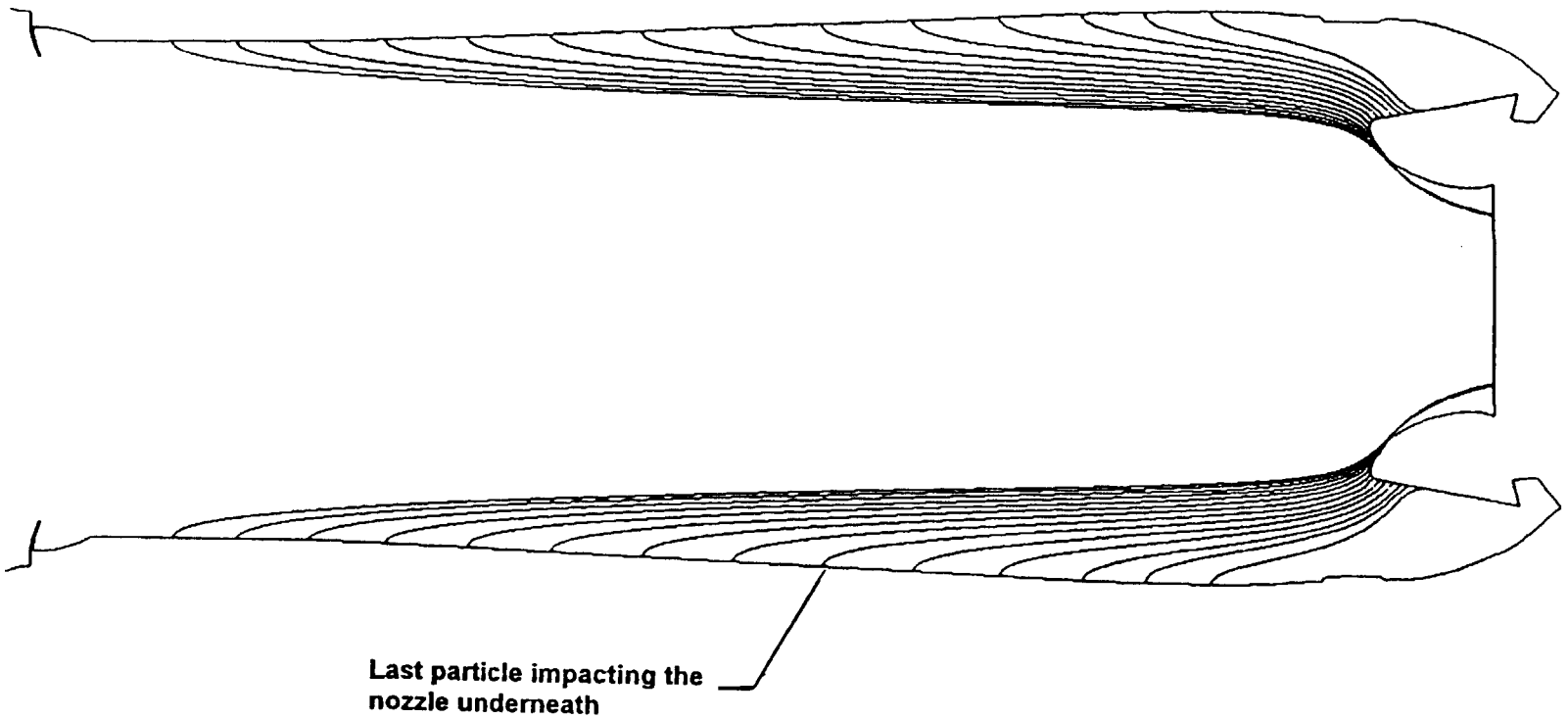

Figure 7A. 200 Mircon Diameter Particle Trajectories from the Aft Propellant Grain

Figure 8A. FSM-5 Initial and Eroded Nozzle Geometry Contours

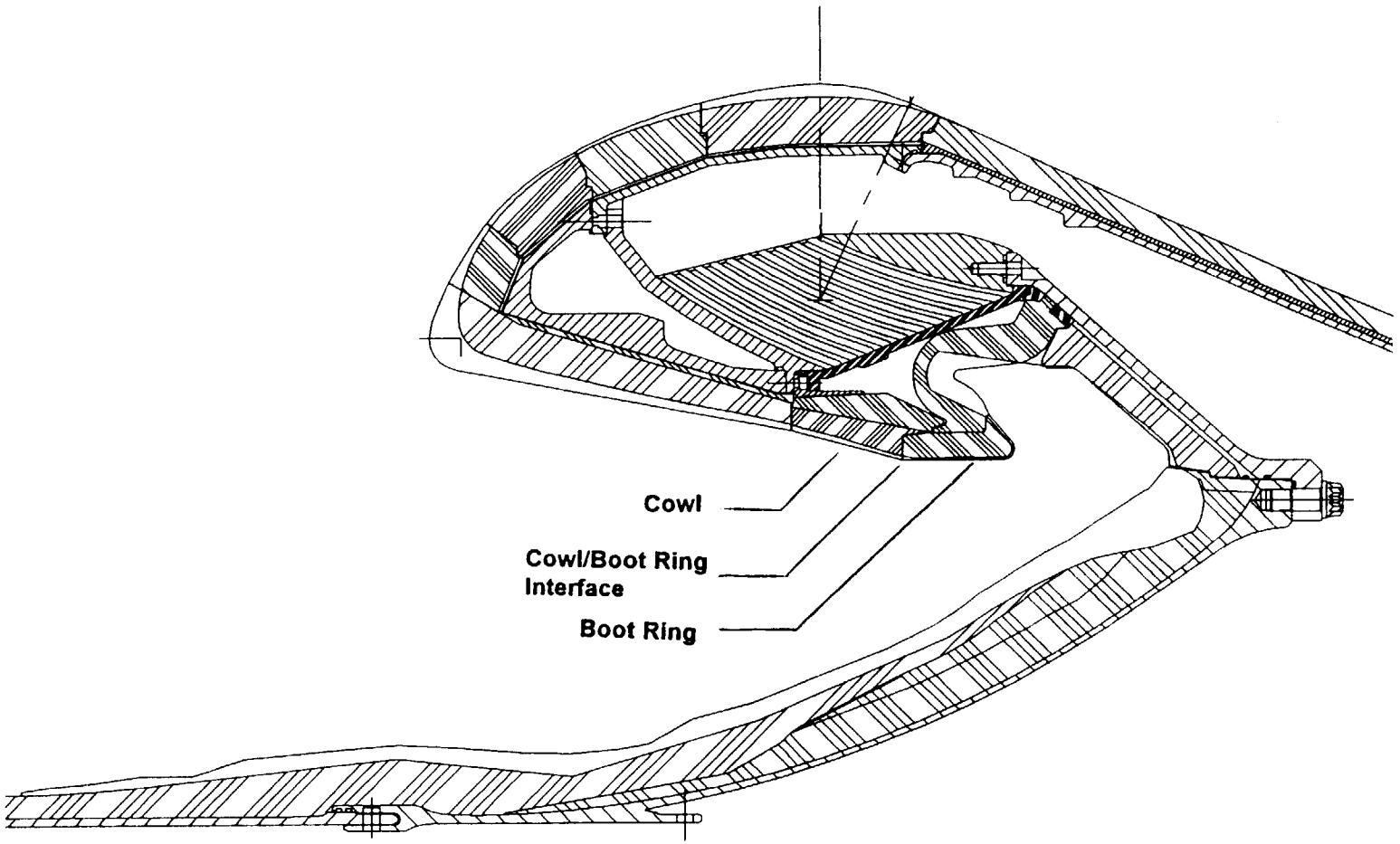

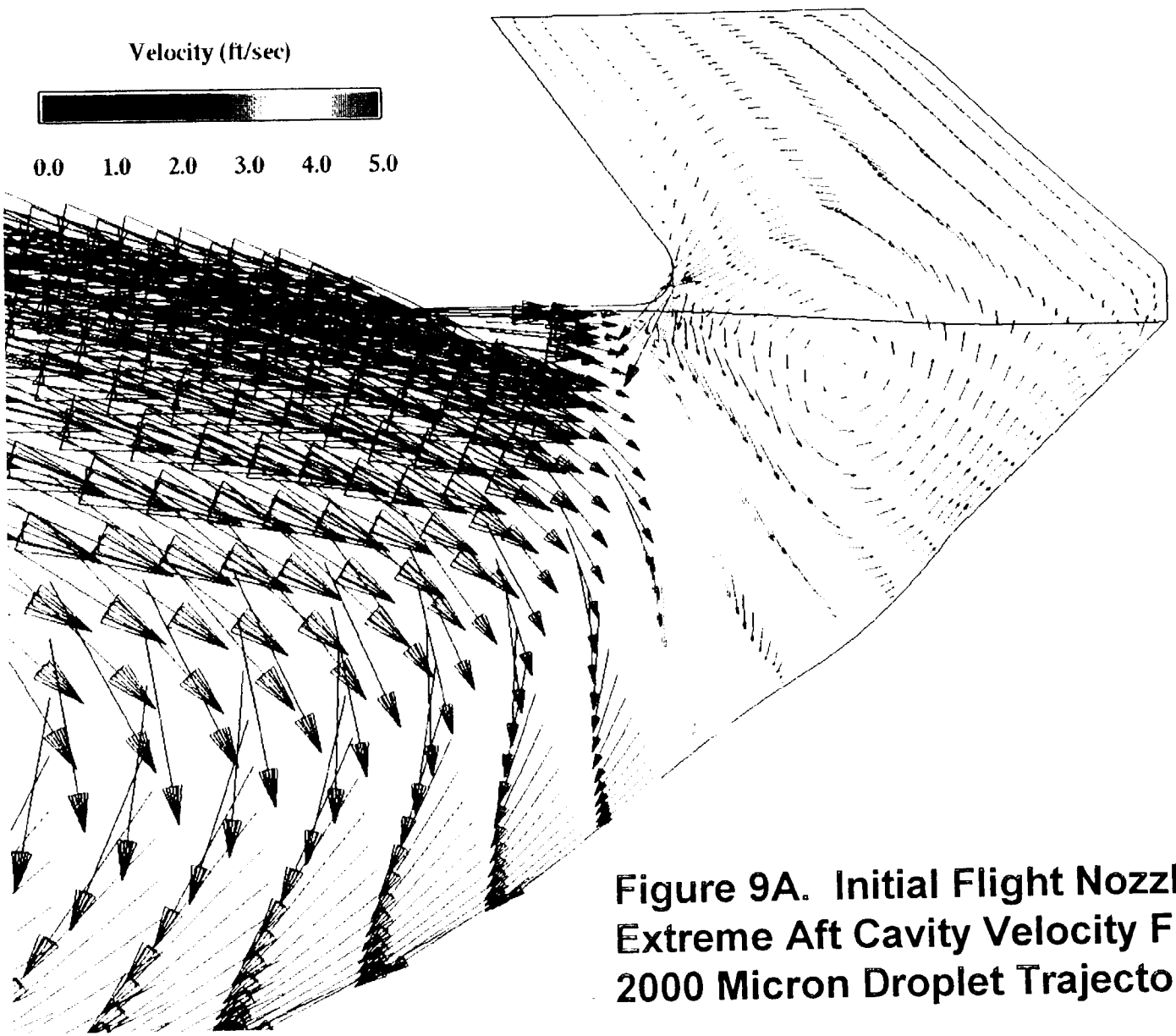

Figure 9A. Initial Flight Nozzle Geometry, Extreme Aft Cavity Velocity Field and 2000 Micron Droplet Trajectory

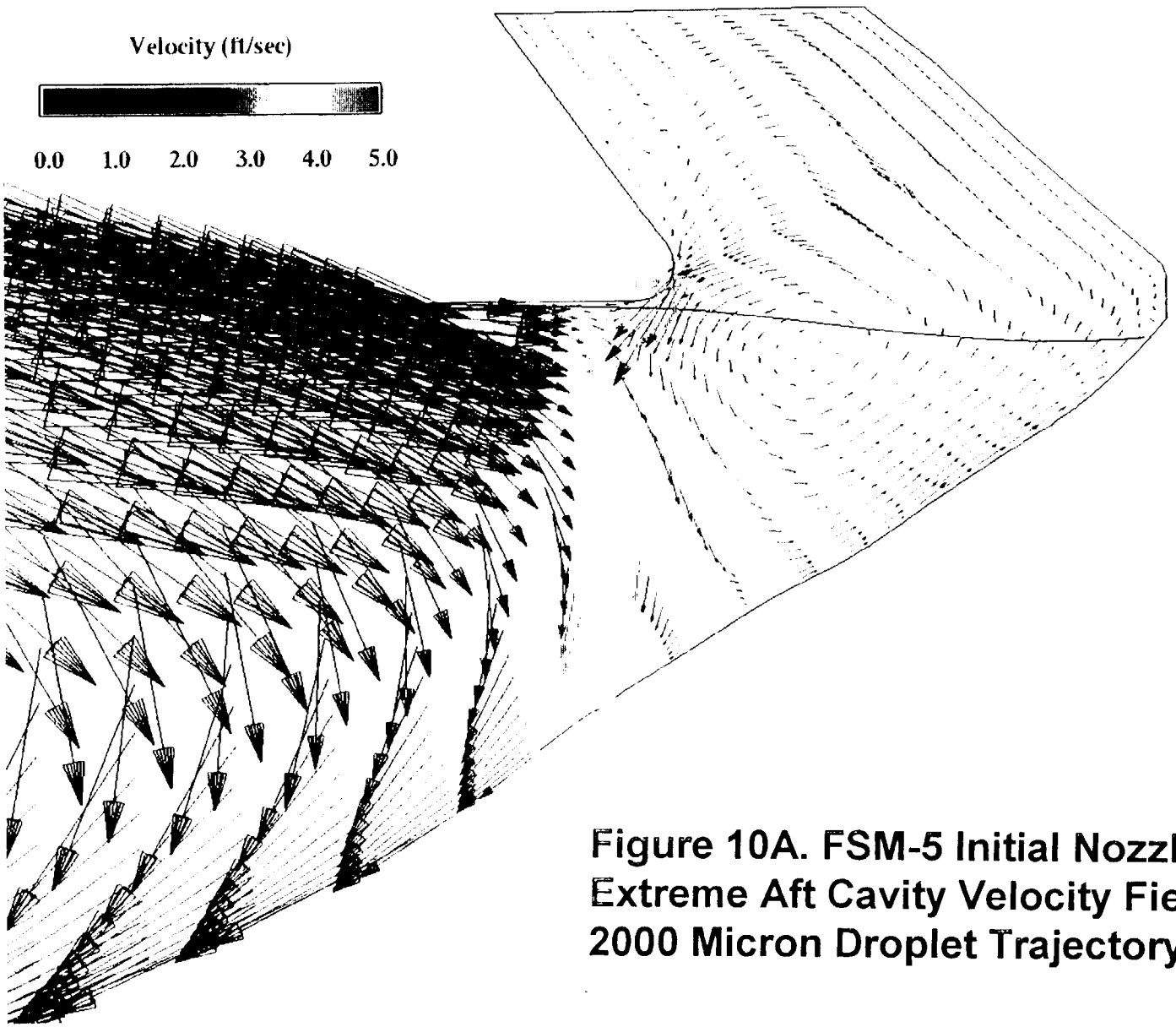

Figure 10A. FSM-5 Initial Nozzle Geometry, Extreme Aft Cavity Velocity Field and 2000 Micron Droplet Trajectory

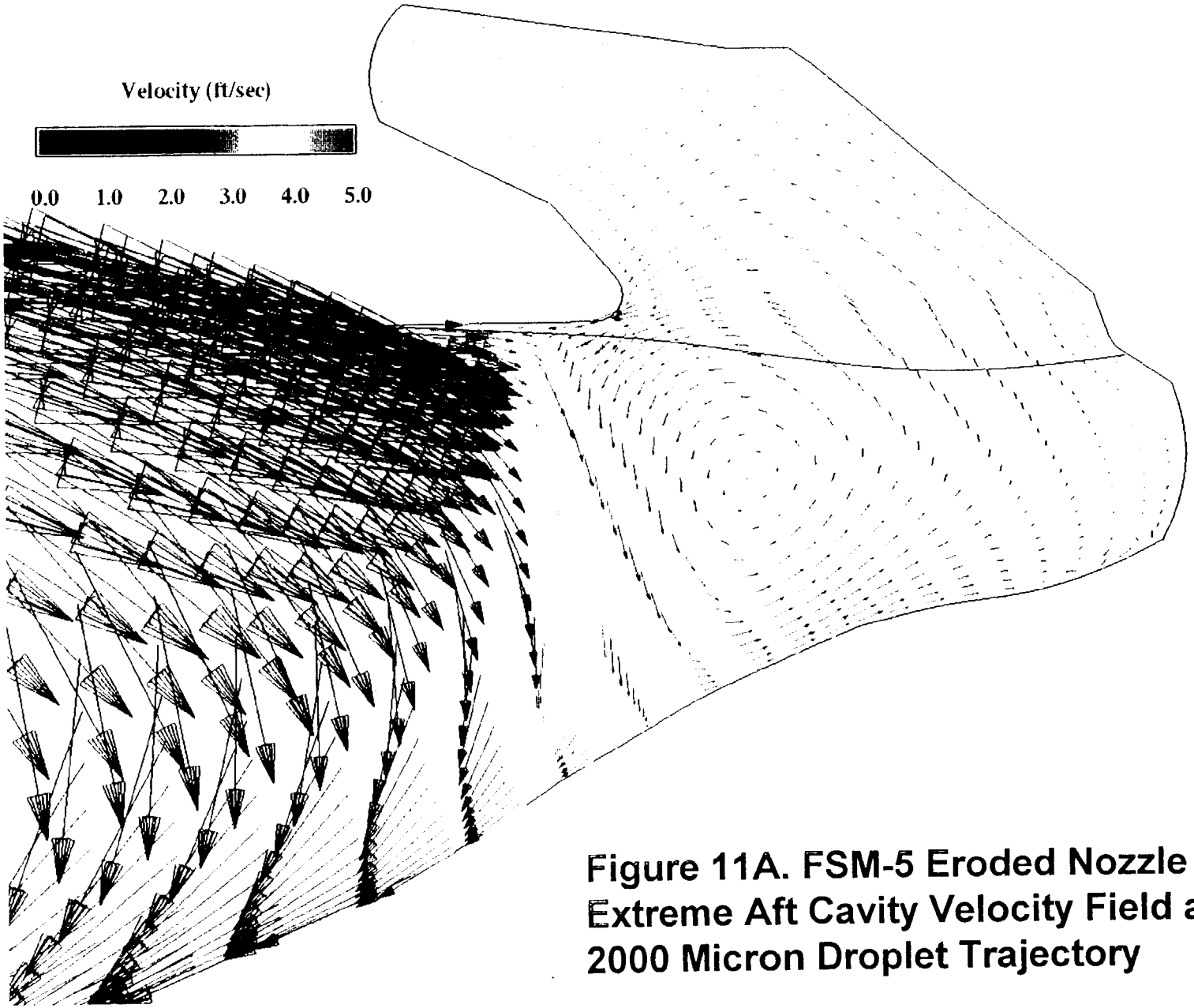

Figure 11A. FSM-5 Eroded Nozzle Geometry, Extreme Aft Cavity Velocity Field and 2000 Micron Droplet Trajectory

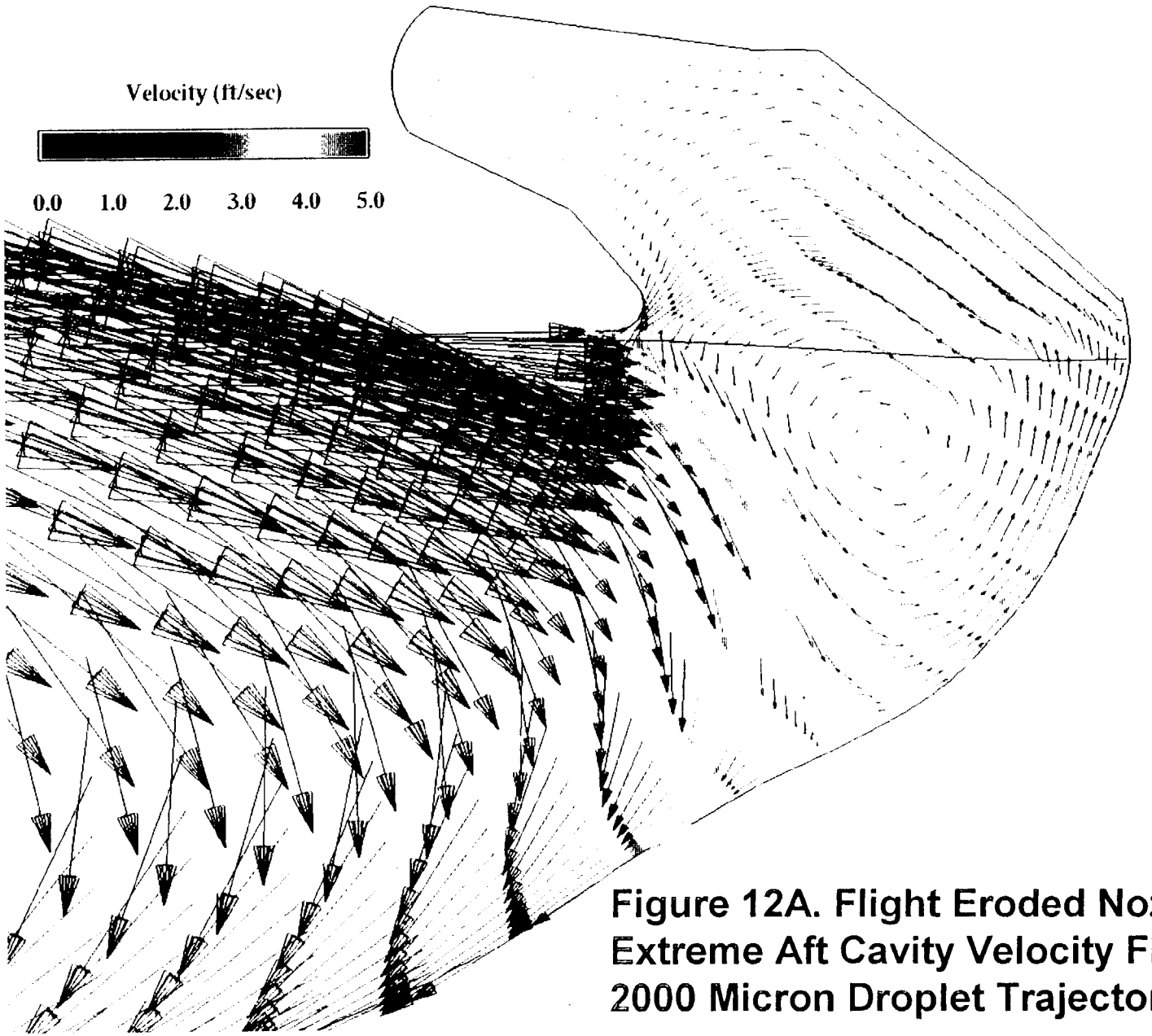

Figure 12A. Flight Eroded Nozzle Geometry, Extreme Aft Cavity Velocity Field and 2000 Micron Droplet Trajectory

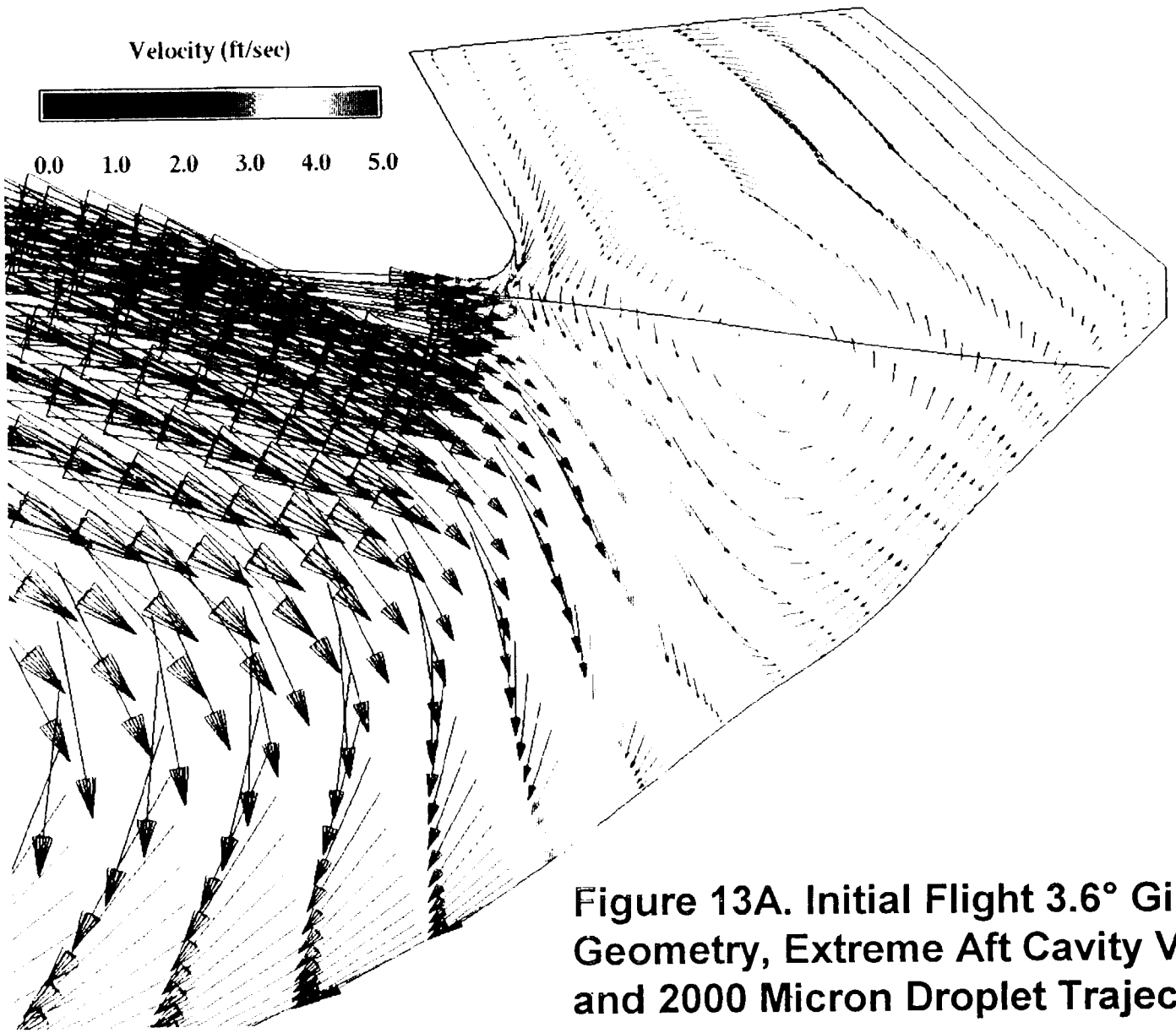

Figure 13A. Initial Flight 3.6° Gimbaled Nozzle Geometry, Extreme Aft Cavity Velocity Field and 2000 Micron Droplet Trajectory

Figure 14A. Comparison of Mass Velocities for Flight Motor Initial and 3.6 Deg. Gimbal Geometries

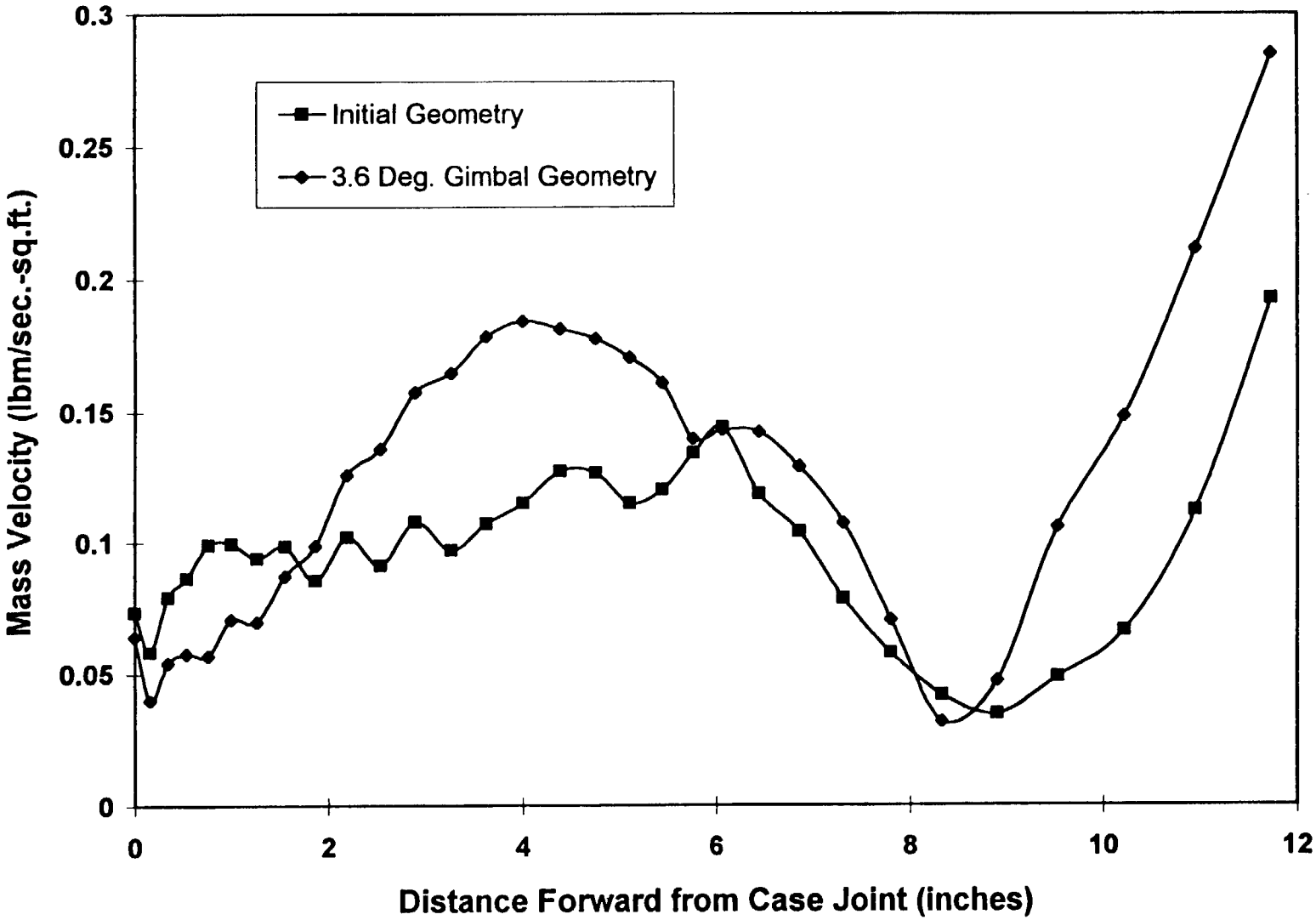

Figure 15A. Comparison of Mass Flow Rates for Flight Motor Initial and 3.6 Deg. Gimbal Geometries

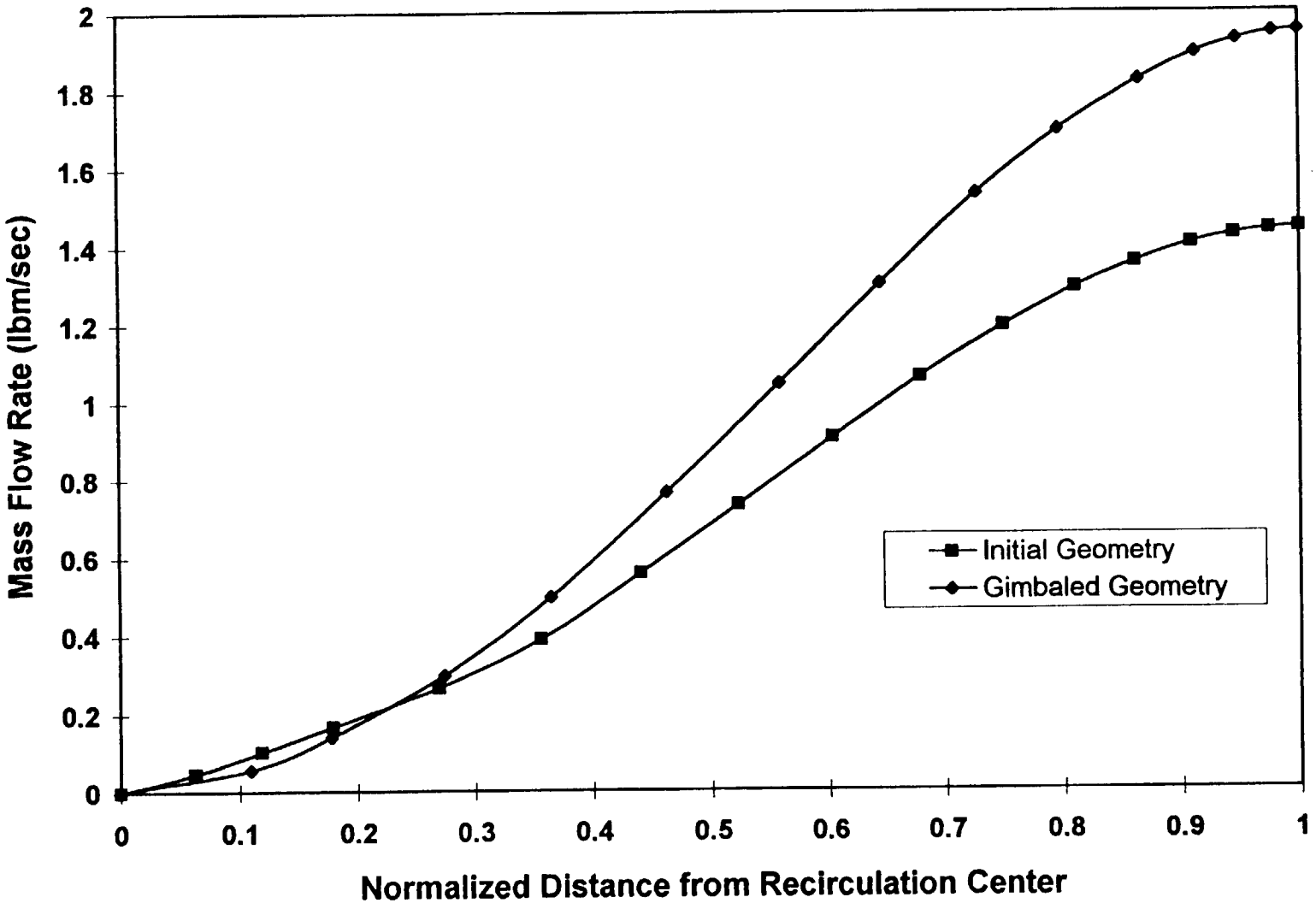

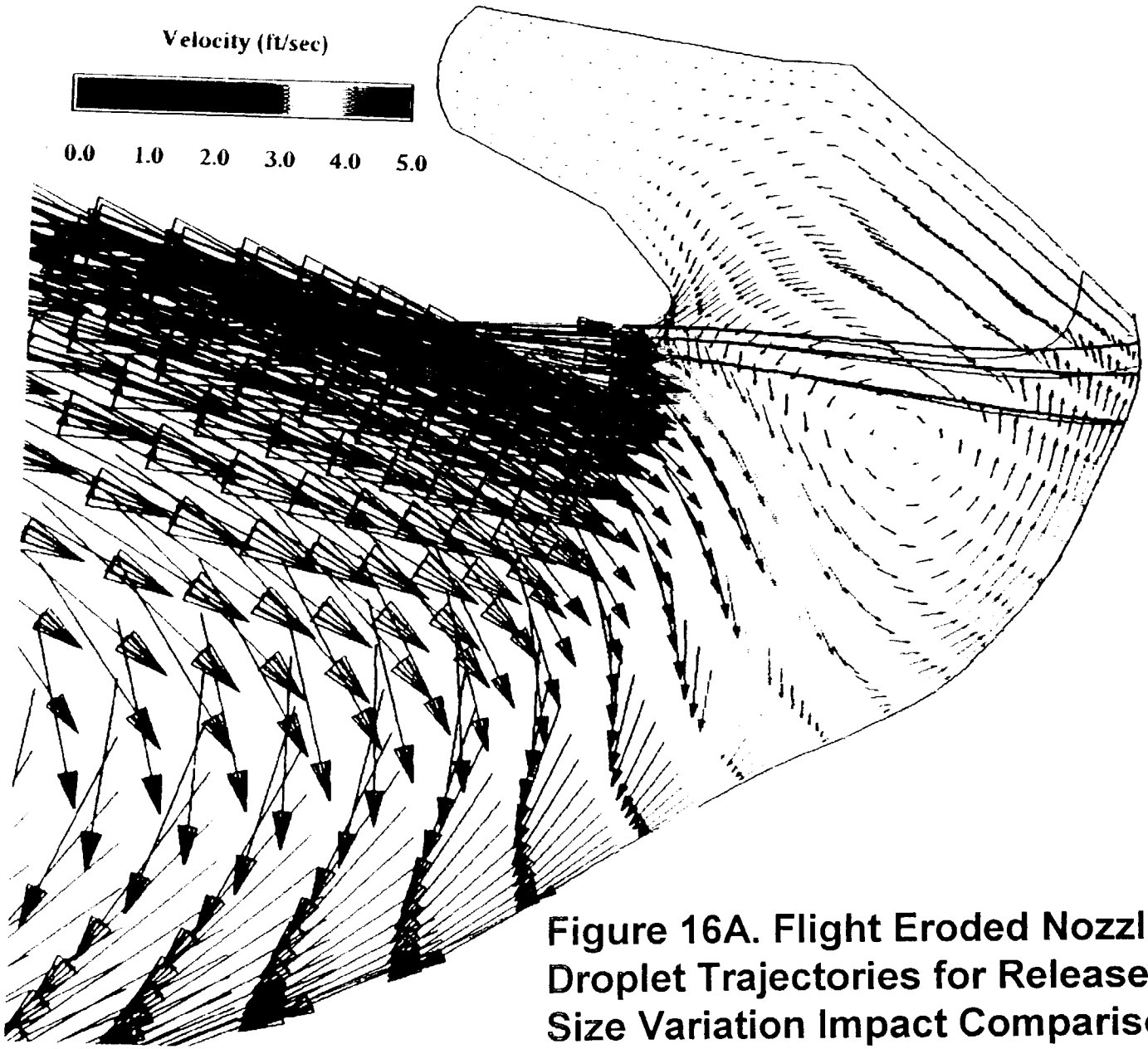

Figure 16A. Flight Eroded Nozzle Geometry, Droplet Trajectories for Release Location and Size Variation Impact Comparison

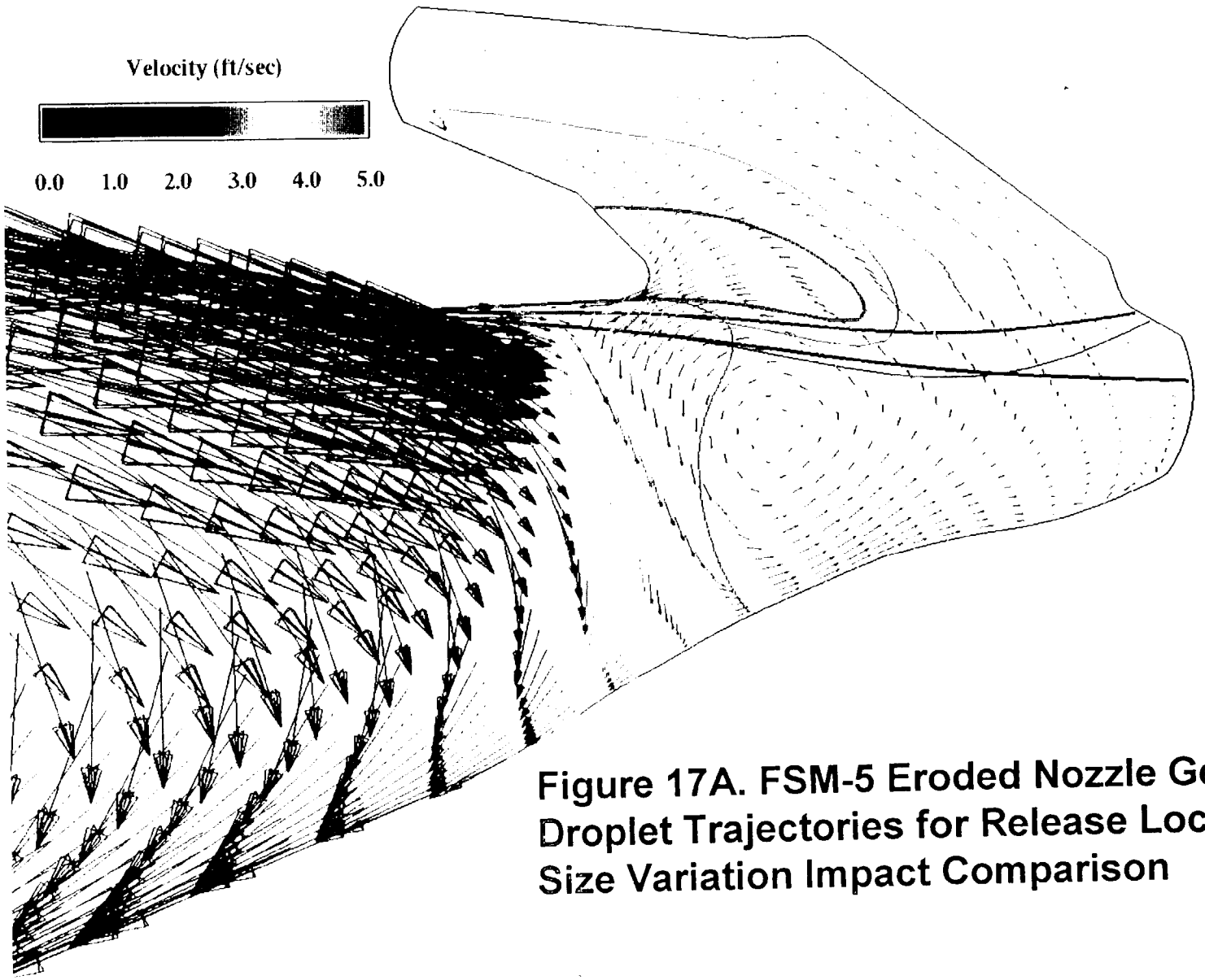

Figure 17A. FSM-5 Eroded Nozzle Geometry, Droplet Trajectories for Release Location and Size Variation Impact Comparison

4.7 Completion of 3-D Analysis of the Hot Air Nozzle Manifold

4.7.1 Introduction

Numerous analyses were performed in support of the investigation into the probable cause or causes of nozzle spalling near the aft end of the throat ring of several RSRM nozzles. The overall investigation of this motor anomaly covered a wide variety of potential causes including issues that involve carbon cloth phenolic broadgoods material properties as well as the nozzle throat ring manufacturing processes. This section summarizes one part of the overall investigation associated with the nozzle throat ring tape wrapping process. The specific purpose of this portion of the investigation was to determine if a non-uniform flow distribution at the exit of the hot air nozzle could cause uneven heating of the tape which in turn could result in non-uniform laydown of the tape layers (wrinkles and/or tape-to-mandrel gaps). Non-uniform heating of the tape might also result in other physical and thermal property non-uniformities through the throat ring billet. Early during this investigation, results showed that non-uniform hot air nozzle exit velocity profiles were likely to exist. This information was used to support the necessity for measuring the tape temperature during the actual nozzle tape wrapping process using infrared measurement techniques. These measurements confirmed that the temperature distribution across the tape was not uniform and this portion of the investigation was expanded to evaluate potential corrective action design changes to the nozzle and/or the manifold to provide uniform heating of the tape. Figure 1A shows a diagram of the nominal hot air nozzle, manifold and air supply analyzed.

A nozzle shown in Figure 1A is used to focus a stream of hot air on the nozzle tape as it is wrapped onto the nozzle mandrel. The temperature of the air at the nozzle exit is fairly uniform so that uneven heating of the nozzle tape must be caused by non-uniform convective heating associated with a non-uniform velocity distribution of the flow emanating from the nozzle. Three-Dimensional CFD (Computational Fluid Dynamics) techniques were utilized to calculate the complex flow in the canister manifold and the nozzle, thereby providing information on the uniformity of the flow emanating from the hot air nozzle. The velocity profile of the flow at the nozzle exit directly relates to the level of convective heat transfer rates for the flow impinging on the tape passing by the hot air nozzle. A non-uniform hot air nozzle exit plane velocity profile would result in uneven heating of the nozzle tape and a non-uniform temperature distribution across the width of the tape. A Non-uniform temperature distribution across the tape would result in variations in the relative tension in the tape across the width of the tape and also differences in resin staging. These non-uniformities could affect the laydown of the tape and the uniformity of properties in the billet.

The Finite-Difference Navier-Stokes (FDNS) code developed at NASA/MSFC by ESI was used to conduct this investigation. The code has been extensively tested and used

by the CFD branch at NASA/MSFC. It has proven to provide accurate flow solutions for the type of low speed recirculating flows occurring in the hot air nozzle/manifold assembly. The code is based on the full Navier-Stokes equations for three-dimensional flow fields using a finite difference algorithm for solving the non-linear governing equations using a non-staggered curvilinear grid system.

The flow in both eight and ten inch hot air nozzles and the manifolds that feed flow to these nozzles was investigated. The nominal (as-built) geometric configurations of these nozzles and manifolds were analyzed in order to determine the nozzle exit velocity distribution associated with the nominal configurations. Geometric variations to these nominal configurations were also analyzed to determine which if any combination of off-nominal conditions was capable of creating a non-uniform nozzle exit flow and thus non-uniform heating of the carbon cloth phenolic tape. Geometric variations included partial blockage of the nozzle exit and nozzle surface dents at the exit plane. In addition to geometric variations, the effect of flow non-uniformity at the nozzle inlet (manifold/nozzle interface) was also studied. Finally, a redesign of the nominal nozzle/manifold configurations was performed to provide corrective action to the flow non-uniformities at the nozzle exit. These redesign changes were then evaluated to assure a more uniform nozzle exit flow and thus more even heating of the nozzle tape.

This section provides a summary of this investigation. Section 5.7.2 provides a summary of the most important analysis results. Section 5.7.3 provides conclusions and recommendations associated with the investigation.

4.7.2 Analysis Results Summaries

4.7.2.1 Hot Air Nozzle Analysis Summary

Since the flow results and analysis conclusions were similar for both the eight and ten inch nozzles, illustration examples will be chosen from both the eight and ten inch nozzle analyses. Figure 2A shows a top view of the nominal eight inch nozzle along the width and length dimensions of the nozzle. As with the ten inch nozzle, the eight inch nozzle expands in the width dimension. Figure 3A shows a side view of the eight inch nozzle along the height and length dimensions. The nozzle converges in this dimension as did the ten inch nozzle. There is also a one inch long rectangular section on the exit end of the eight inch nozzle. The eight inch nozzle has only a single noncircular inlet hole for the flow as opposed to the double inlet hole configuration used in the ten inch nozzle. This is illustrated in Figure 4A. As was the exit region for the ten inch nozzle, the eight inch nozzle is a rectangular area of the dimensions shown in Figure 5A.

For the case of uniform inlet flow to the nozzles, the nozzle exit flow associated with both the eight and ten inch nominal nozzles shows higher velocities in the center of the nozzle. Figure 6A shows a view of the nominal eight inch nozzle flow field across the width dimension of the nozzle and Figure 7A shows a view of the nominal eight inch

nozzle flow field across the height dimension of the nozzle. Figure 6A shows the flow separation on the wall just downstream of the inlet plane which results in lower velocities near the edge of the nozzle exit plane. There is about a 15% variation in the velocity across the width of the nozzle at the exit plane.

Further flow analyses were performed using a non-uniform inlet velocity profile to determine how the inlet flow to the nozzle affects the flow at the exit. The velocity profile at the nozzle inlet is expected to be non-uniform since the upstream flow from the manifold and supply piping is highly non-uniform due to the complexity and turning of the flow as it enters the nozzle. An estimated inlet velocity profile shape was used to represent the flow distortion due to the flow turning into the nozzle from the canister manifold. The velocity profile across the width direction varied such that the normalized velocity profile across the exit varied from 0.75 to just over 1, as shown in Figure 8A. (The vertical dimension of 0.0 corresponds to the center of the nozzle in the height dimension.) The non-uniform inlet velocity used in this portion of the nozzle analysis did create significant variations in the nozzle exit velocity with the exit velocity being greater on one side of the nozzle than the other. Measured temperature profiles across the carbon cloth phenolic tape showed the same trends, with the high velocity and the maximum temperatures occurring on the mandrel side of the tape. This infrared data was taken by MSFC/ED61 for the TTW-3 special test wrap. The shape profiles do not have similarity, but this was not expected since the exit velocity profile is based on an assumed inlet flow distortion and also because the relationship between velocity and tape temperature is very nonlinear. However, one can conclude that the non-uniform tape temperature profile can be explained by the flow distortion at the nozzle exit plane.

During observation of the nozzle tape wrapping procedure it was noted that there were significant dents at the exit plane for some of the hot air nozzles. In order to determine how a dent in the nozzle might affect the nozzle exit flow, a dent like the one shown in Figure 9A was analyzed. The dent was placed one-half inch from the edge of the nozzle exit side wall and was one inch in length and one inch in width. Different dent heights were used which ranged from one-thirty-second, 1/32, to one-sixteenth, 1/16 of an inch. The dent was considered to be a smooth circular arc over the one inch in the width dimension at the nozzle exit plane and a linear variation in height was used along the length of the one inch long rectangular section. Figure 10A shows the results of this analysis for the same non-uniform nozzle inlet velocity profile as used above. A non-uniform inlet velocity profile has already been shown to skew the shape of the nozzle exit velocity profiles. Figure 10A shows that a dent in the nozzle further skews the shape of the exit velocity profiles. The figure illustrates how the exit velocity profile shape is distorted as a function of both inlet velocity profile and the existence of a dent. It is obvious that the dent is an undesirable feature since it significantly enhances the exit plane velocity profile distortion and would result in higher convective heating rates to the nozzle tape where the dents were located. This would be true with or without the inlet plane velocity distortion.

During observation of the tape wrapping process it was noted that as the nozzle tape passes by the hot air nozzle exit before it goes under the mandrel roller, on occasion it moves closer to one side of the nozzle exit than the other thus partially blocking the nozzle exit on one side. In order to examine this effect on the uniformity of the nozzle exit flow, a percentage of one side of the nozzle area was blocked as shown in Figure 11A. Figure 11A shows a 75% nozzle area blockage on one side of the nozzle. A 50% blockage was also simulated and similar results were obtained. Figure 12A shows the nozzle velocity profiles in the width direction for the 75% area blockage case. The velocity is highly skewed to the outer edge of the non-blockage side of the nozzle. The much higher velocities on the non-blockage side of the nozzle would support a higher convective heating rate along the edge of the nozzle tape as it rolls past the non-blockage side of the nozzle. Therefore, it would be highly desirable to maintain the nozzle tape at some reasonable uniform distance from the nozzle exit and avoid the effective blocking of a portion of the nozzle exit opening.

A redesign concept of the nominal eight inch hot air nozzle was developed that would provide a more uniform exit velocity distribution without regard to the uniformity of the inlet velocity distribution. Figure 13A shows a width dimension view of the final redesigned eight inch nozzle. The nozzle is rectangular in this dimension and does not have diverging side walls in the width dimension as the nominal nozzle had. Figure 14A shows a side view of the redesigned nozzle. This is similar to the nominal nozzle design in that the nozzle converges in this direction, but the one inch long straight wall rectangular section has been removed from the exit end of the nozzle. The nozzle converges on a constant angle continuously to the nozzle exit. Figure 15A shows that the nozzle inlet area has been expanded to reduce the inlet velocity, which decreases the sensitivity of the nozzle to flow non-uniformity at the nozzle inlet. Figure 16A shows the velocity field in the redesigned eight inch nozzle. This figure shows that the flow separation present on the side wall for the nominal nozzle has been eliminated for this redesigned nozzle and that a very uniform velocity profile is achieved at the nozzle exit plane. Figure 17A shows a plot of the velocity profile at the nozzle exit to illustrate that the exit velocity profile is much smoother than for the nominal nozzle. This exit profile was produced using the original non-uniform inlet velocity profile shown in Figure 8A for the nominal nozzle. The nozzle exit velocity profile for the redesigned nozzle is even smoother than that of the nominal nozzle having a completely uniform inlet velocity profile.

The redesigned nozzles are much less sensitive to inlet flow non-uniformity caused by the manifold or inlet design but the larger nozzle inlet used on the redesigned nozzles requires a manifold redesign. In this analysis, the redesign of the manifold to create a smoother nozzle inlet flow was also considered.

4.7.2.2 Hot Air Manifold Analysis Summary

The flow field in the nominal (as built) eight inch nozzle manifold was analyzed in order to determine the exact non-uniformity of the velocity profile at the nozzle entrance. Since the flow results and analysis conclusions were similar for both the eight and ten inch nozzles and because the use of the ten inch nozzle in the tape wrapping process has been discontinued, only the manifold for the eight inch nozzle was analyzed. Figure 18A shows a three-dimensional isometric view of the nominal manifold which is geometrically a right circular cylinder. In order to show the inside of the manifold, one-half of the manifold domain is shown in the figure by bisecting the manifold at the centerline of the manifold inlet and outlet. This bisection occurs at the lengthwise center of the cylindrical manifold. Figure 19A shows a side view of the nominal manifold with dimensions. There are two holes in the side of the manifold cylindrical wall. The round hole is the inlet to the manifold with a diameter as shown. The rectangular hole is the manifold outlet. The inlet and outlet holes do not directly oppose one another. The centers of the holes are instead separated circumferentially by an angle of 105 degrees. There is also a cylindrical solid rod that extends down the centerline of the manifold. Figure 20A shows a top view of the nominal manifold. A nozzle damper with a 90 degree sector shape is attached to the solid cylindrical rod located on the manifold centerline. The manifold damper was not considered in the analysis because it was estimated that this component would further increase the predicted flow distortions.

The velocity field at the manifold outlet (which is the inlet to the hot air nozzle) is very non-uniform in the radial, circumferential and axial directions as would be expected from the complex flow geometry of the nominal manifold. Figure 21A shows the velocity field in a cross-section of the cylindrical manifold. The cross-section is located near the bottom of the manifold exit in the lengthwise dimension. The flow is highly non-uniform in all directions at the manifold exit, which has already been shown to have a significant effect on the nozzle exit flow uniformity. Figure 22A shows a three-dimensional iso-metric color raster plot of the radial velocity at the manifold outlet. The radial velocity component is shown because it corresponds to the predominant flow direction in the nozzle. The figure shows that there is significant variation of the radial velocity in all directions at the nozzle outlet. The peak radial velocities are also toward the edge of the outlet and have a magnitude of 91 feet/second. The circumferential and axial velocity magnitudes at the manifold exit are also very large and vary diagonally across the outlet. The axial velocities vary by 80 feet/second across the outlet and the circumferential velocities vary by 138 feet/second across the outlet.

A modification of the standard manifold was considered to reduce distortions of the flow at the manifold outlet. The modified manifold uses the basic nominal manifold dimensions except that the manifold inlet feeds flow from the end of the manifold instead of through the side as shown in Figure 23A. This figure shows one-half the manifold domain cut through the center of the manifold along the length of the manifold.

The black area in the figure is the manifold outlet, which is identical to the nominal manifold outlet. The circular lower end of the cylindrical manifold geometry is the inlet to the modified manifold configuration. The arrows show the predominant direction of the flow. Figure 24A shows the velocity field in a cylindrical cross-section of the manifold. The cross-section is located at the same lengthwise manifold location as the cross-section shown in Figure 21A. A direct comparison of Figures 21A and 24A shows that modification of the standard manifold design with a bottom fed inlet significantly improves the flow uniformity at the manifold outlet. For this modified inlet manifold, the flow is much more unidirectional which tends to make the flow at the manifold outlet more uniform in all directions, especially the axial and circumferential directions. The peak magnitude of the radial velocity at the manifold outlet is reduced by only 11 feet/second but the overall radial profile is smoother and more uniform for the modified inlet manifold. The circumferential velocity variation at the outlet has been reduced to 70 feet/second. The axial velocity variation is more for this configuration but large variations are confined to near the upper and lower lips of the outlet and the overall axial velocity variation across the outlet is smoother.

A further design refinement was considered by lengthening the manifold outlet such that it would be compatible with the redesigned eight inch hot air nozzle as described in the above section on the nozzle analysis results. Thus this redesigned manifold is also a right circular cylinder as shown in the isometric view, Figure 25A. The dimensions of the redesigned manifold are shown in the side view, Figure 26A, and in the top view, Figure 27A, of the manifold. The redesigned manifold is longer than the standard manifold in order to fit the redesigned eight inch nozzle but the diameter of the cylindrical configuration remains the same. The greater manifold length has the added benefit of providing more plenum volume to settle and turn the flow coming into the manifold. The redesigned manifold is fed from the end of the cylindrical manifold and the manifold exit is both longer and wider than the nominal manifold exit. The redesigned manifold flow velocities are lower and more uniform than for the nominal manifold because the flow is feed through a larger opening in the end of the manifold. The flow in the cross-sections down the length of the manifold are similar to those for the modified inlet nominal manifold. The redesigned manifold has the added benefit of more manifold outlet area. This yields lower outlet velocity magnitudes, a smoother turning of the flow out the manifold outlet and a more uniform outlet flow. Figure 28A shows a color raster plot of the radial velocities at the redesigned manifold outlet. The maximum radial velocity at the manifold outlet is reduced to 25 feet/second compared to 80 - 90 feet/second for the nominal and modified inlet manifolds. The maximum variation of circumferential velocity at the manifold outlet has been reduced to 22 feet/second and the variation of the axial velocity has been reduced to 29 feet/second. The redesigned manifold creates a much more uniform inlet flow field for the nozzle.

4.7.3 Conclusions and Recommendations

Several conclusions were drawn from the analysis results:

1) The standard canister manifold produces significant flow distortions at the nozzle entrance plane with the flow velocities distorted in the plane of the flow turning.

2) Even with a uniform entrance flow to the hot air nozzle, flow separations on the diverging flow walls result in significant flow non-uniformities at the exit plane with higher velocities at the center of the nozzle.

3) With the actual distorted flow at the nozzle entrance as supplied by the standard canister manifold, the flow is significantly distorted at the exit plane with higher velocities on the outside of the effective flow turning radius. This would result in higher heating rates on one side of the nozzle. This matches, qualitatively, the measured non-uniform temperature distribution across the width of the carbon cloth phenolic tape.

4) The dents observed in the nozzle and the effective partial nozzle blockage of the flow by the tape itself can also result in non-uniform nozzle exit flow velocities which could cause non-uniform convective heating rates to the nozzle tape.

5) The uniformity of the hot air nozzle exit flow and conversely the heating rates across the width of the carbon cloth phenolic tape could be immensely improved by using the redesigned nozzle and the redesigned manifold as described in the analysis.

Therefore, the recommendations are as follows:

1) The recommended configuration of the hot air nozzle and manifold would be the redesigned eight inch nozzle and the redesigned manifold. This configuration would yield the optimal nozzle exit flow uniformity, which in turn translates to more even heating of the nozzle tape.

2) The hot air nozzles should be maintained free of dents, especially in the region near the nozzle exit.

3) It is also recommended that tape feed controls and procedures be used which will preclude blockage of the hot air nozzle by the tape during the wrapping process.

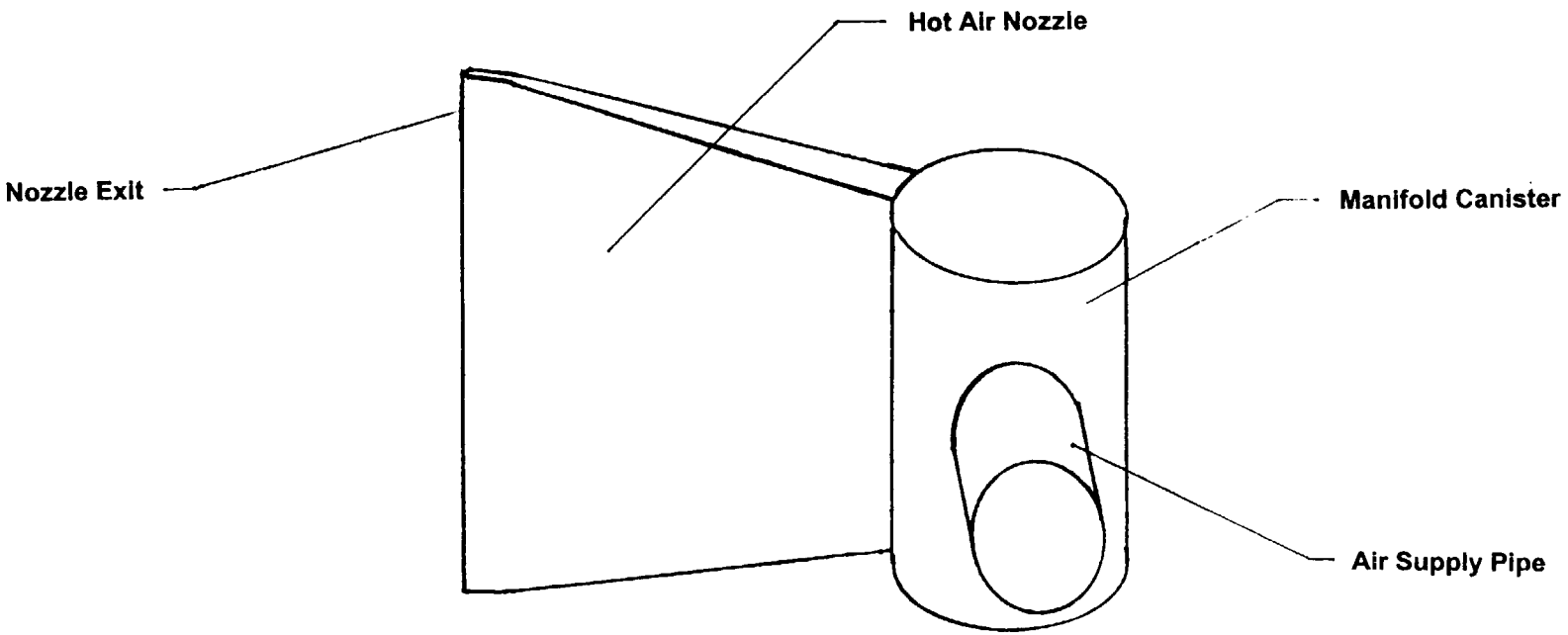

Figure 1A. Diagram of the Manifold Inlet, Manifold, and Nozzle

Figure 2A. Eight Inch Hot Air Nozzle Geometry, Top View

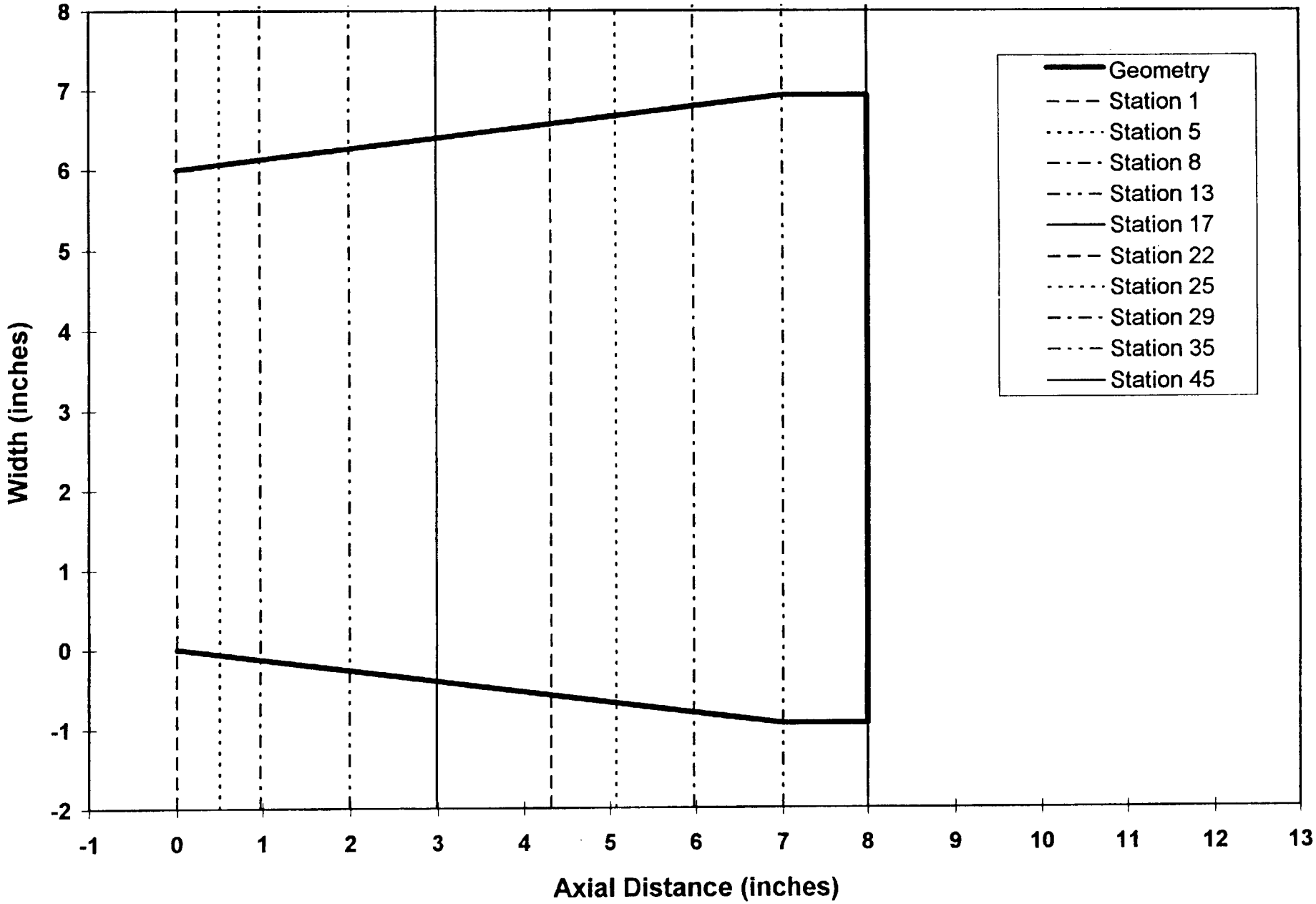

ERC, Inc. 7/10/1997

Figure 3A. Eight Inch Hot Air Nozzle Geometry, Side View

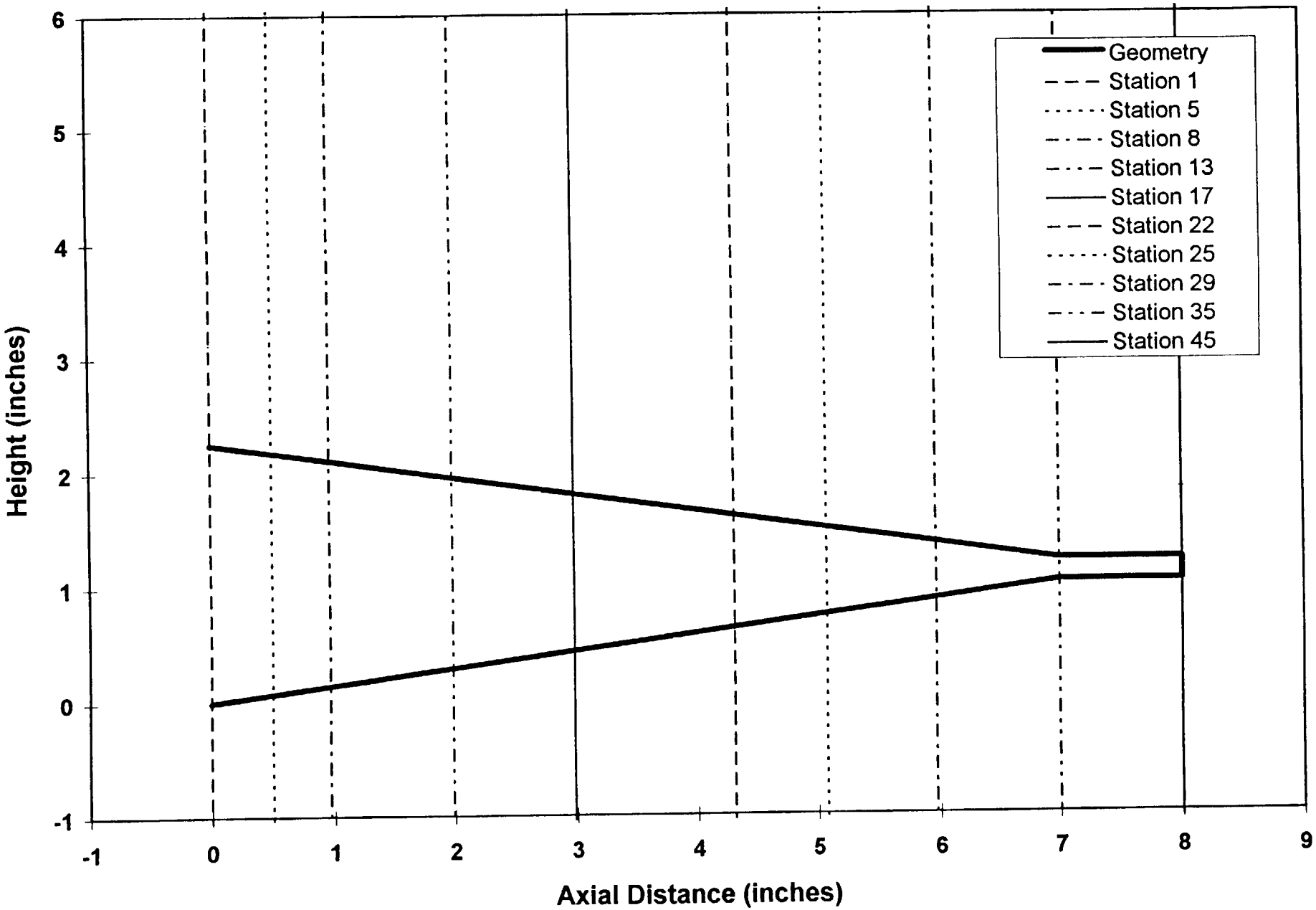

ERC, Inc. 7/10/1997

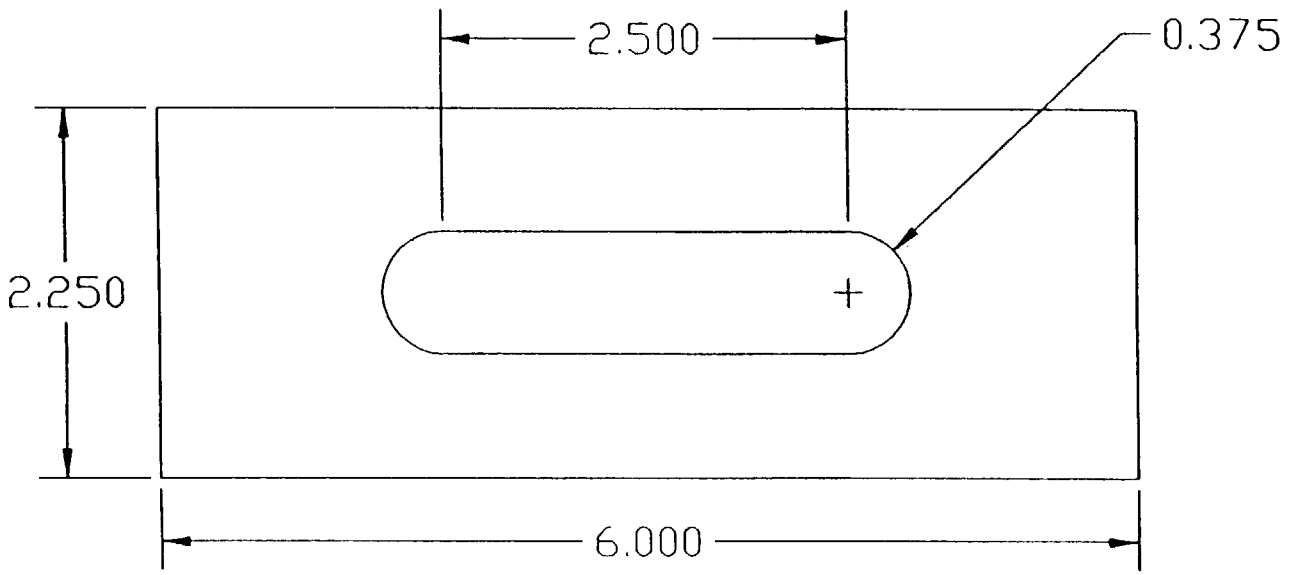

Figure 4A. Eight Inch Hot Air Nozzle Geometry, Inlet

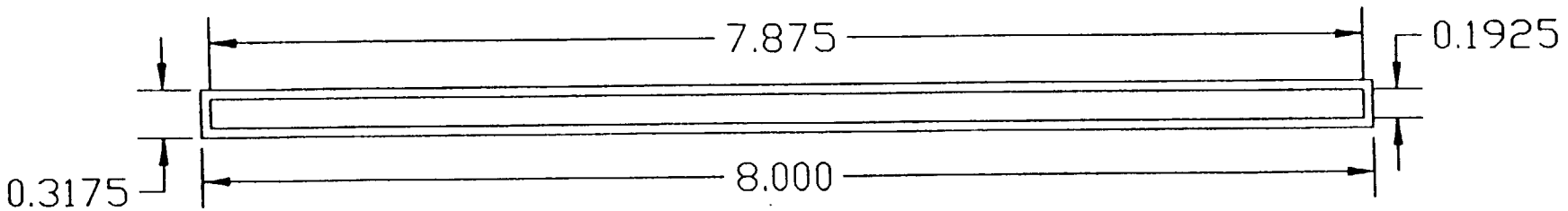

Figure 5A. Eight Inch Hot Air Nozzle Geometry, Exit

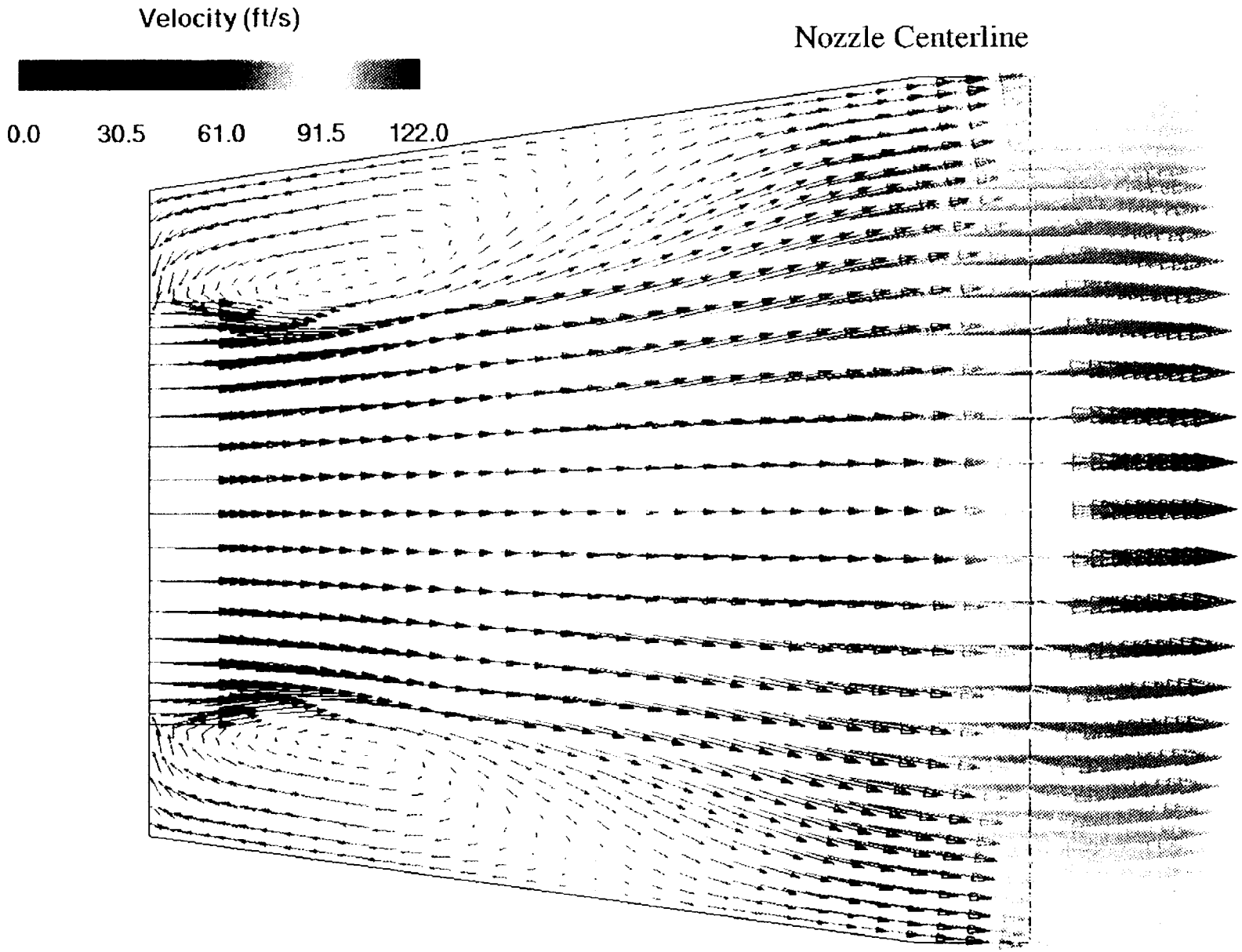

Figure 6A. Nominal Eight Inch Nozzle Flow Field, Uniform Inlet Velocity

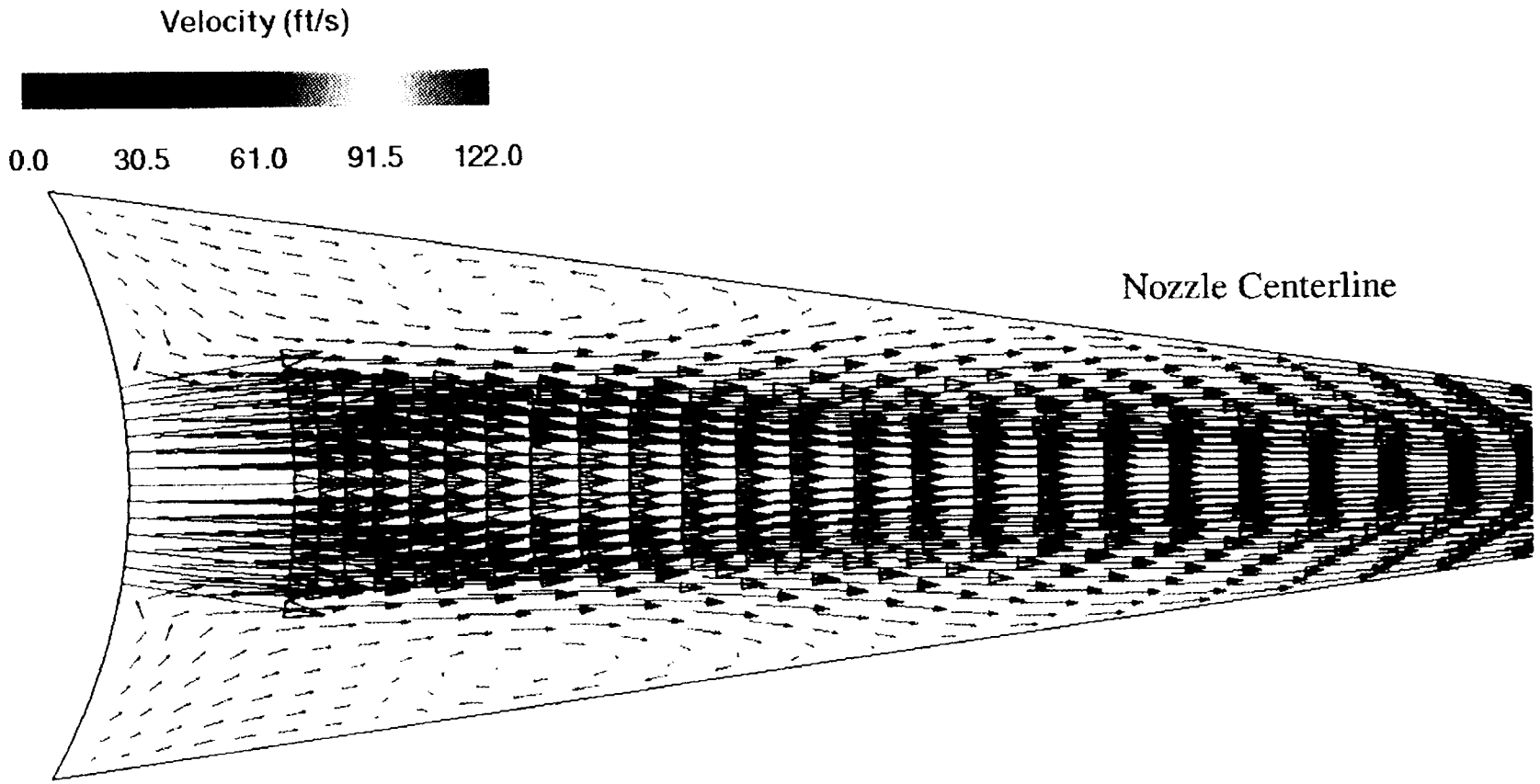

Figure 7A. Nominal Eight Inch Nozzle Flow Field, Uniform Inlet Velocity

Figure 8A. Eight Inch Nozzle Exit Plane Axial Velocities Non-Uniform Inlet Velocity

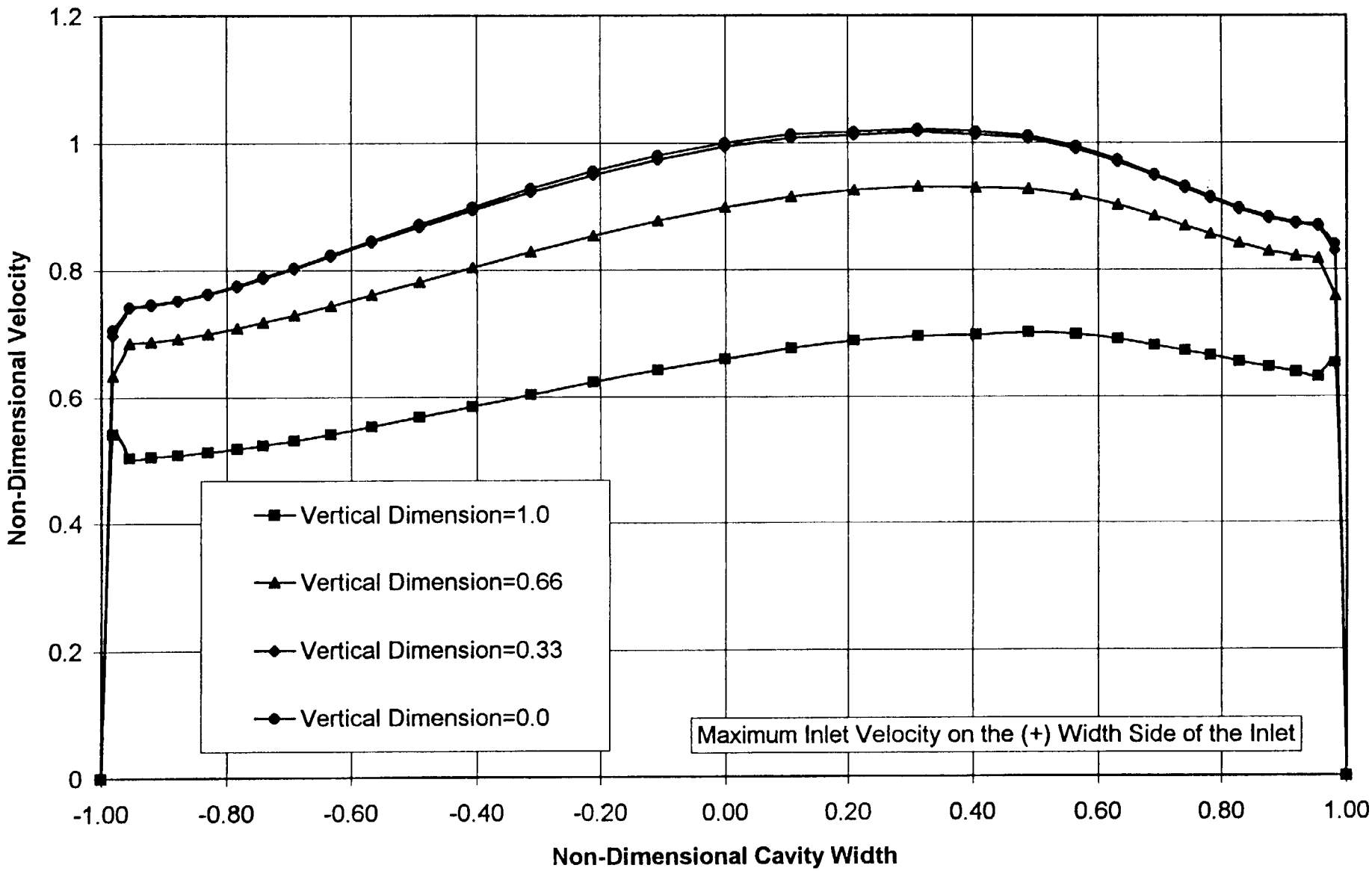

ERC Inc. 7/10/97

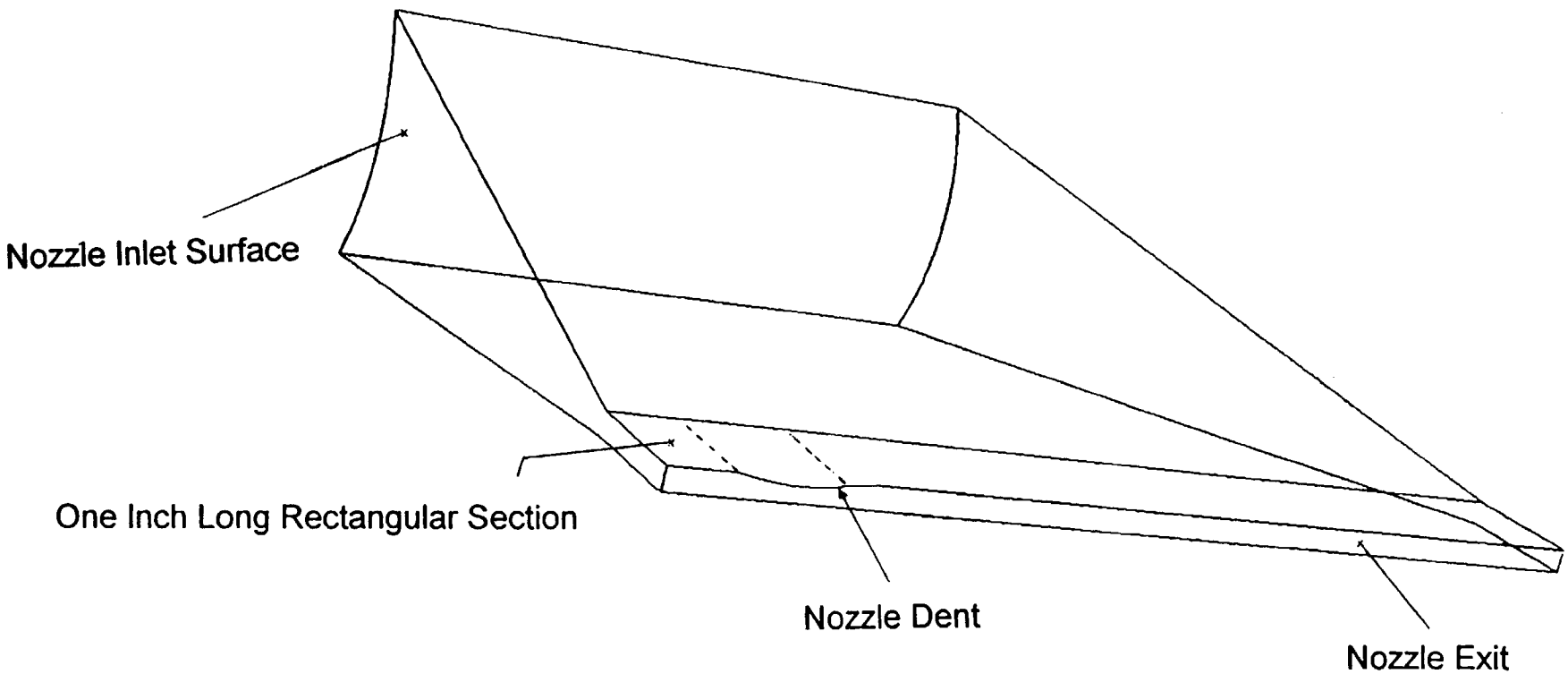

Figure 9A. Eight Inch Nozzle Dent Geometry

Figure 10A. Eight Inch Nozzle Exit Plane Axial Velocities
Non-Uniform Inlet Velocity
(1/16x1)" Dent in One Side of the Nozzle

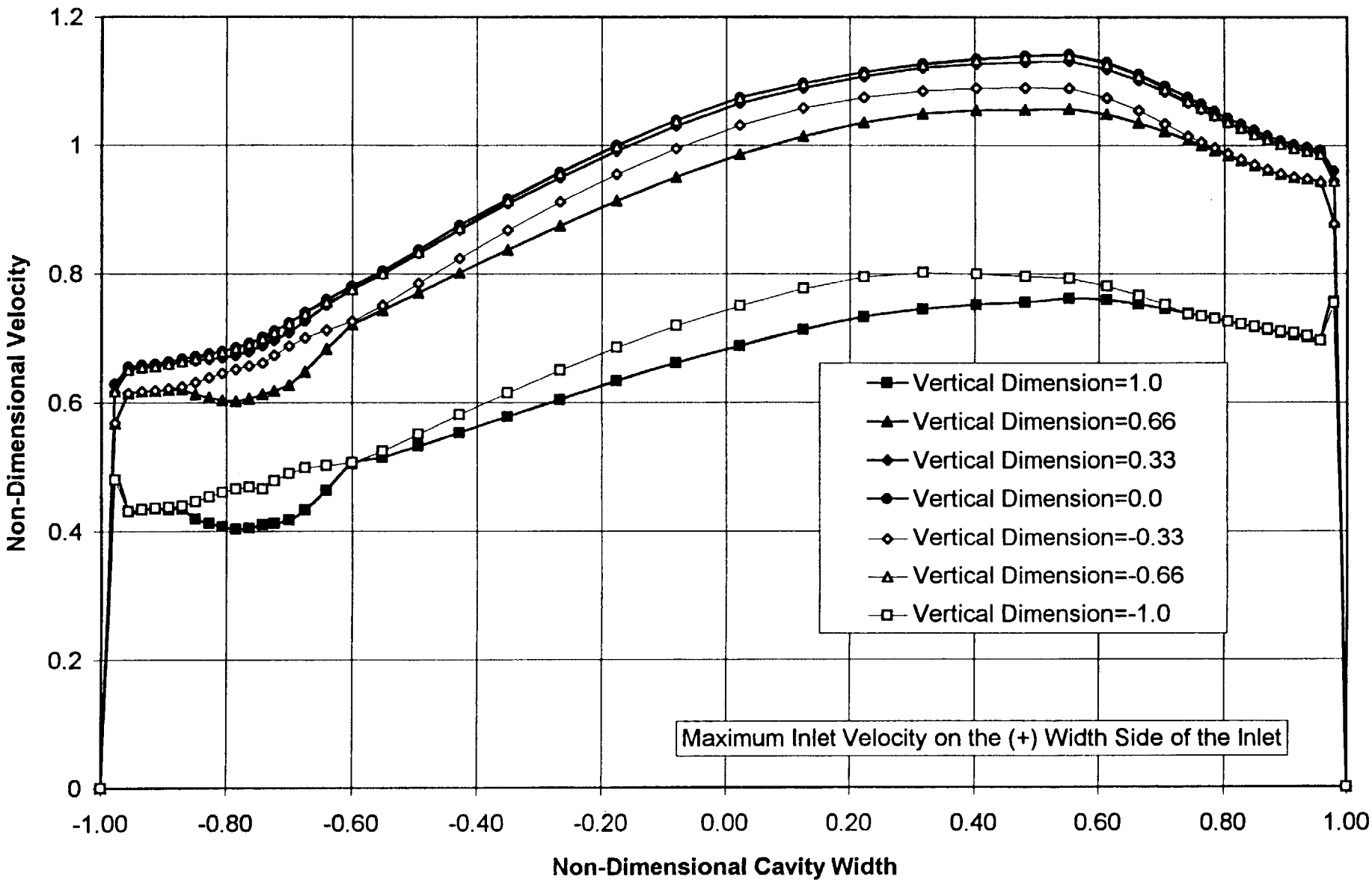

ERC Inc. 7/10/97

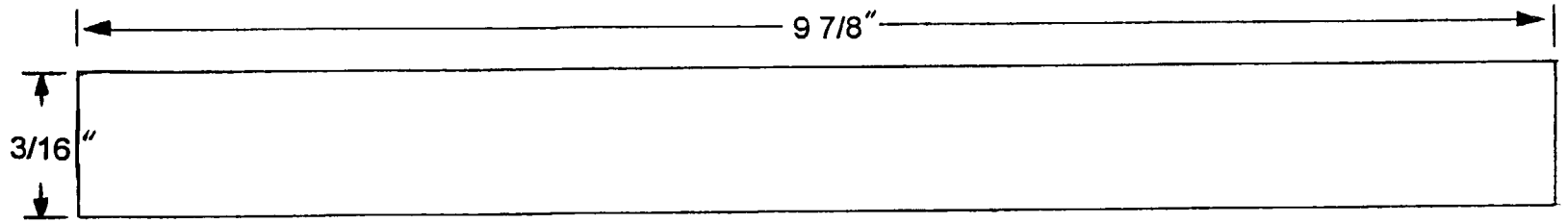

(a) Nominal Nozzle Exit Opening

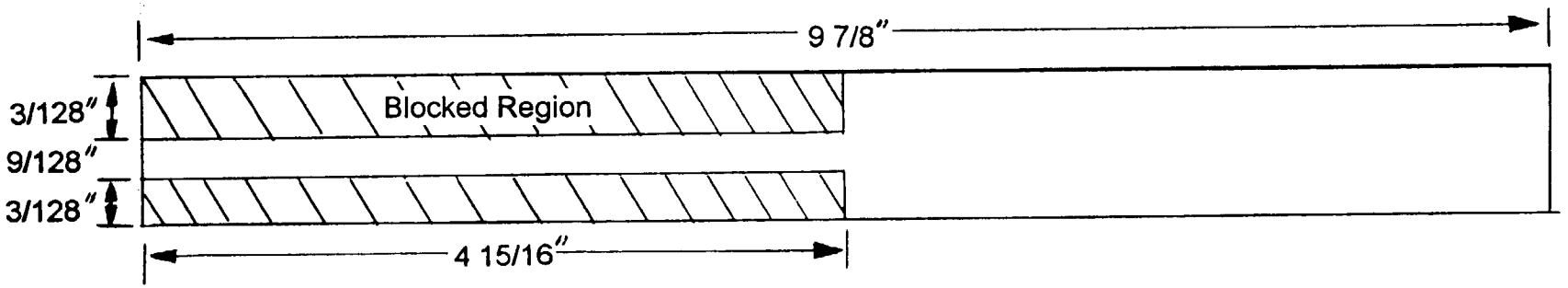

(b) Blocked Nozzle Opening

Figure 11A. Ten Inch Nozzle 75% Area Exit Blockage Geometry

Figure 12A. Ten Inch Nozzle Exit Plane Axial Velocities
75% Blockage on One Side

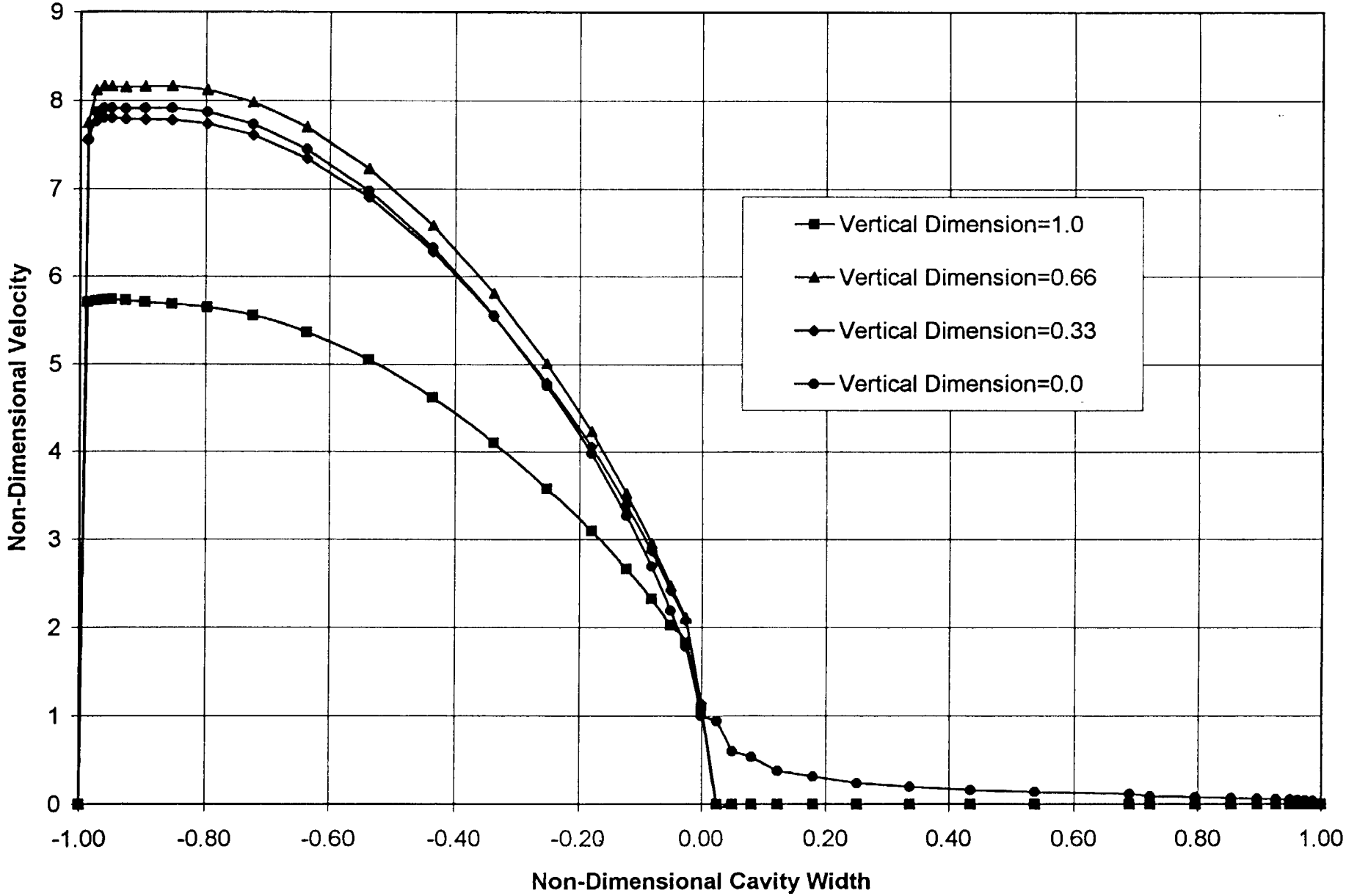

ERC Inc. 5/14/97

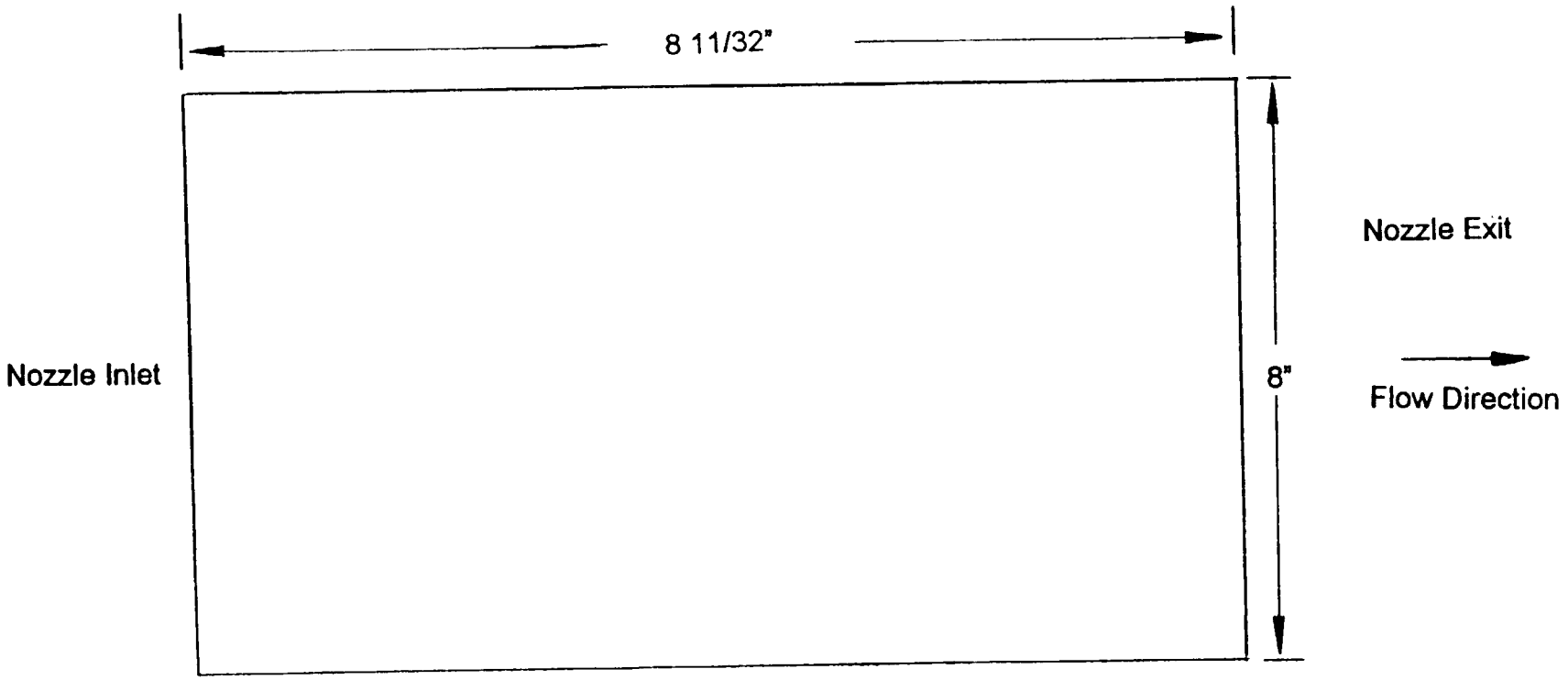

Figure 13A. Redesigned Eight Inch Nozzle, Top View

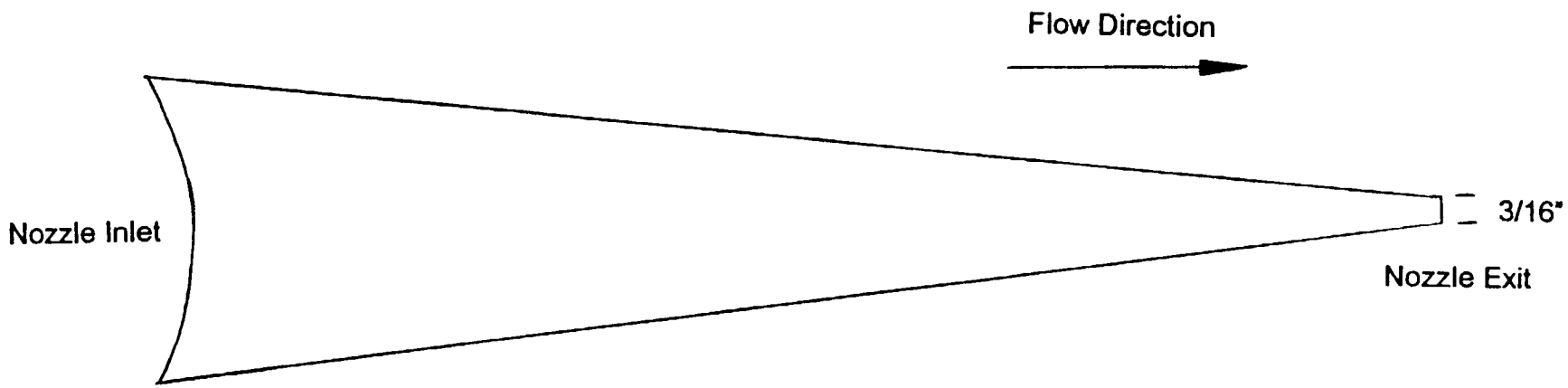

Figure 14A. Redesigned Eight Inch Nozzle, Side View

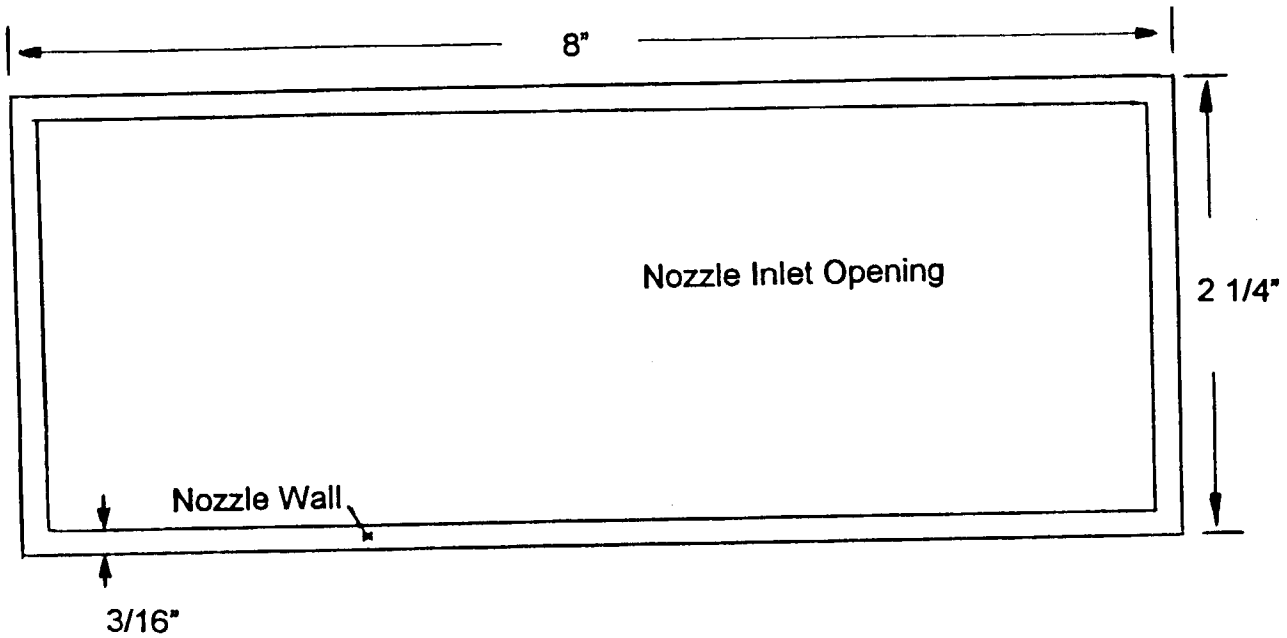

Figure 15A. Redesigned Eight Inch Nozzle, Inlet

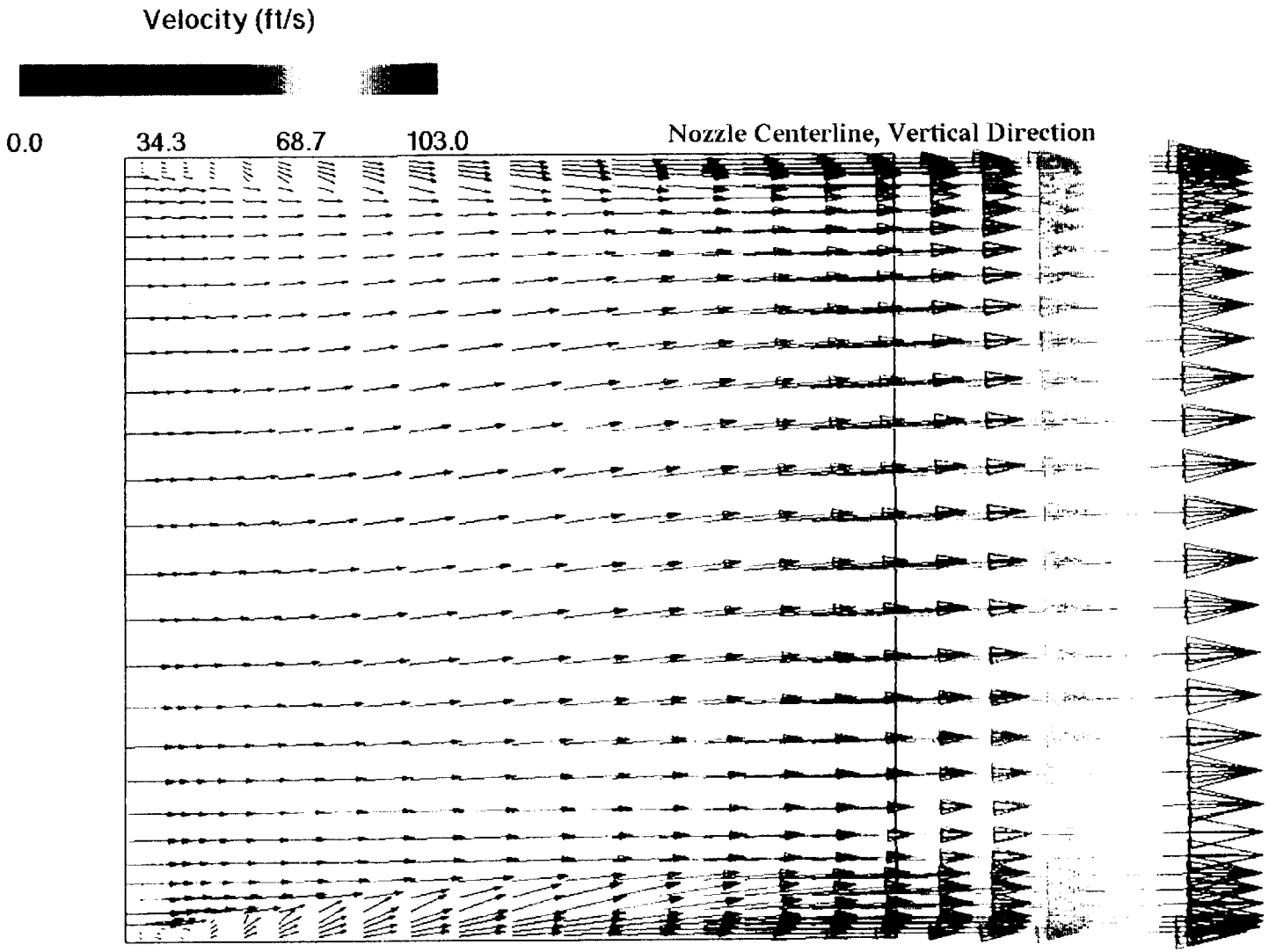

Figure 16A. Redesigned Eight Inch Nozzle Flow Field

Figure 17A. Redesigned 8 Inch Nozzle Exit Plane Axial Velocities Non-Uniform Inlet Velocity

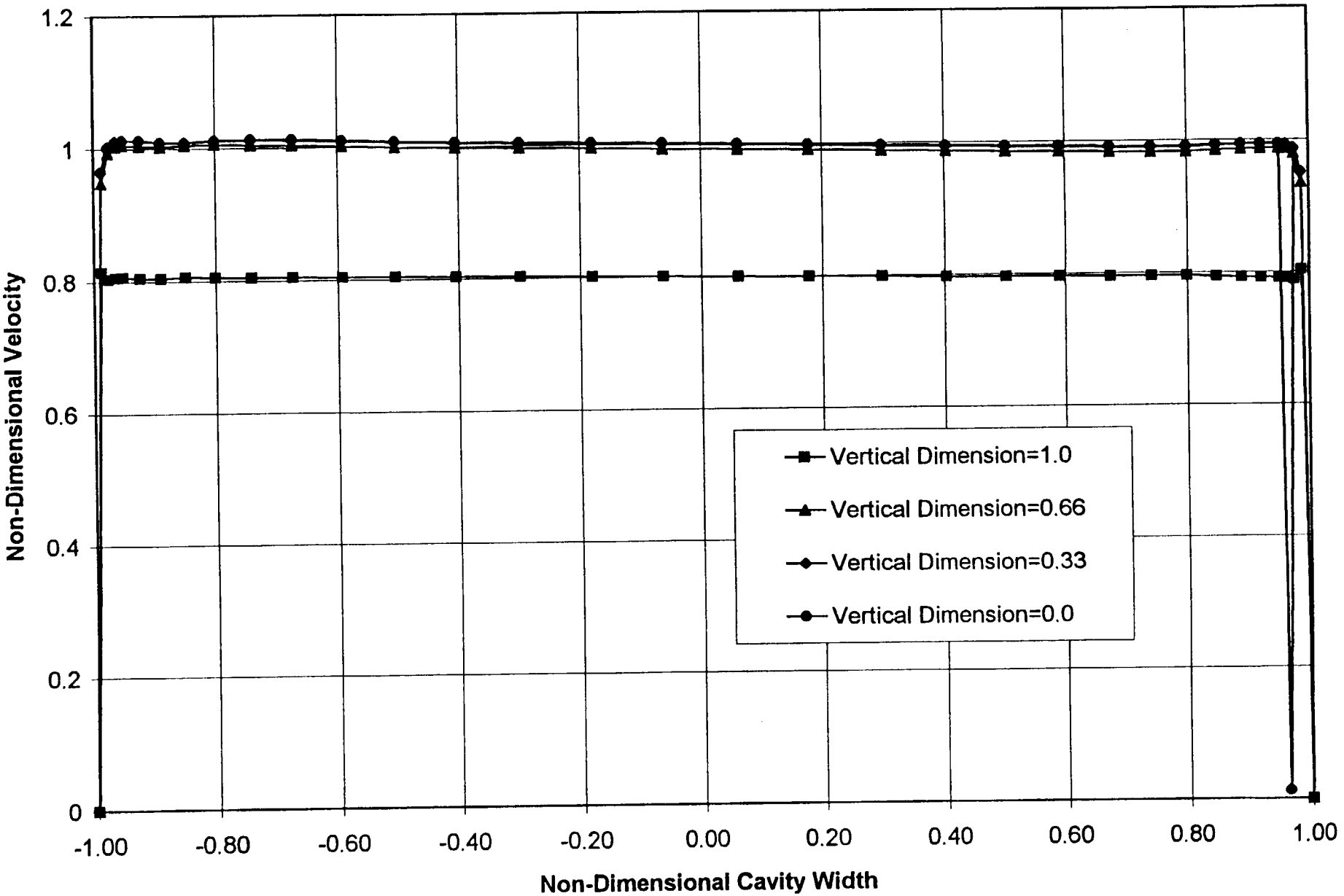

ERC Inc. 7/11/97

Figure 18A. Isometric View of the Hot Air Nominal Manifold

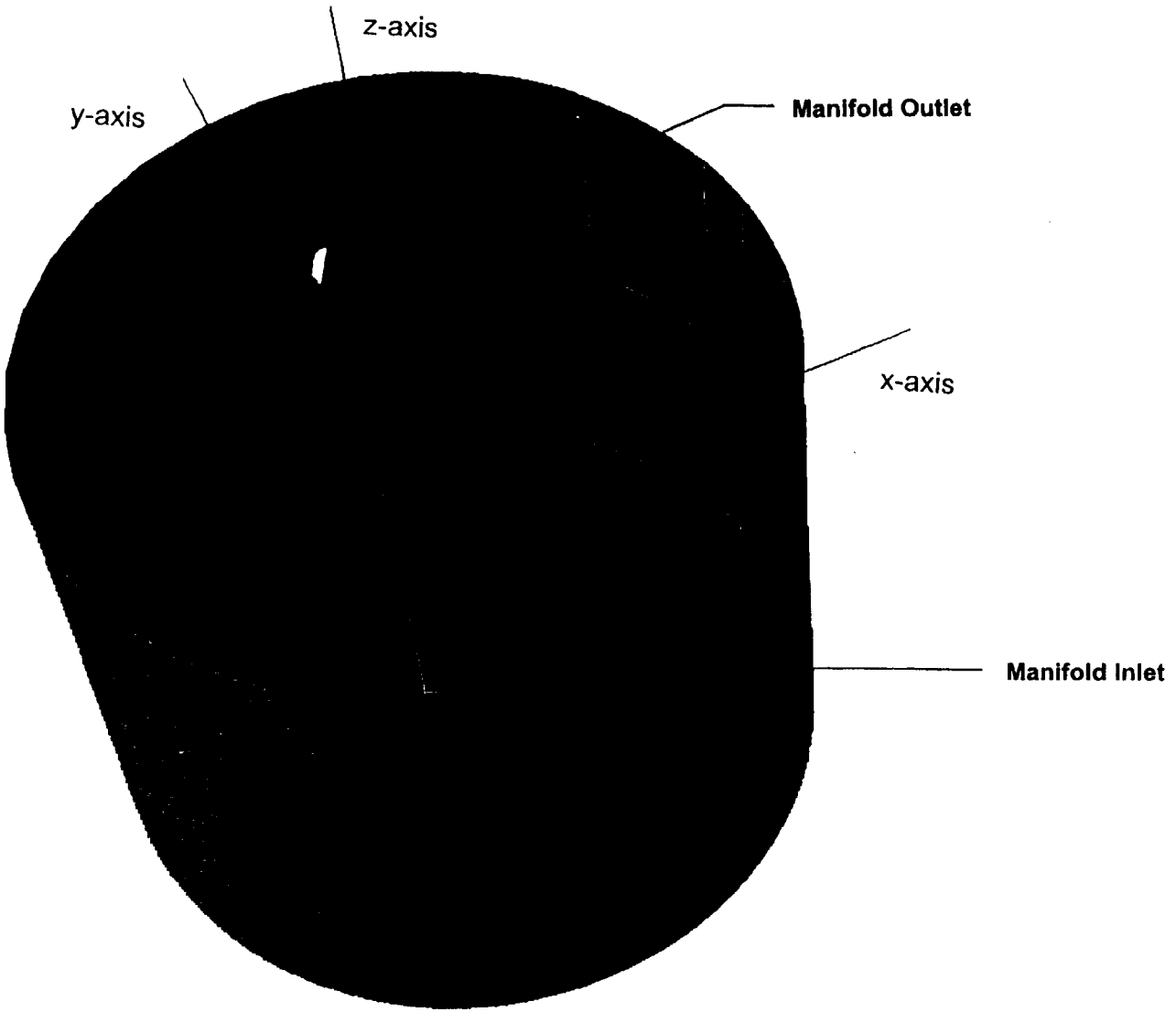

Figure 19A. Side View of the Hot Air Nominal Manifold

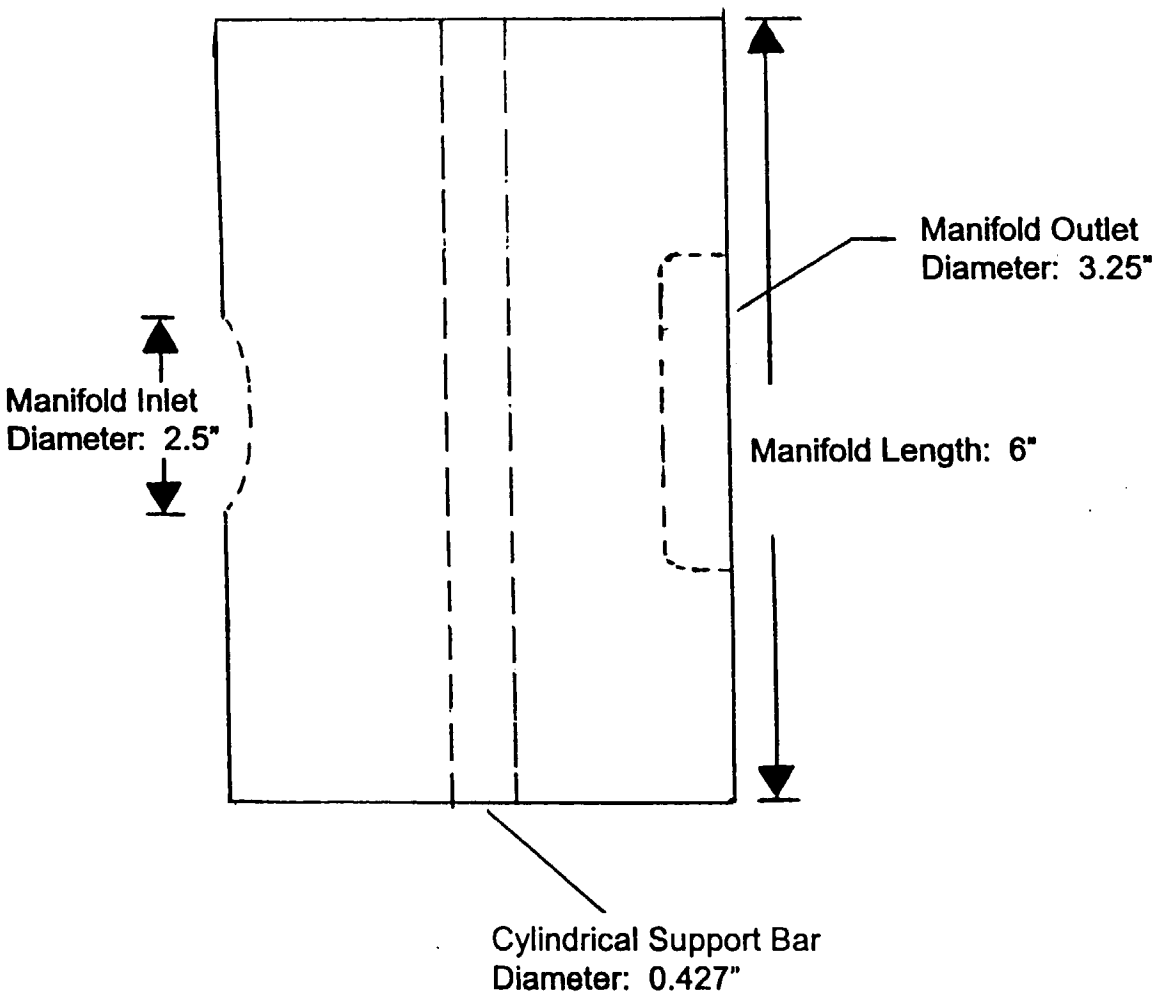

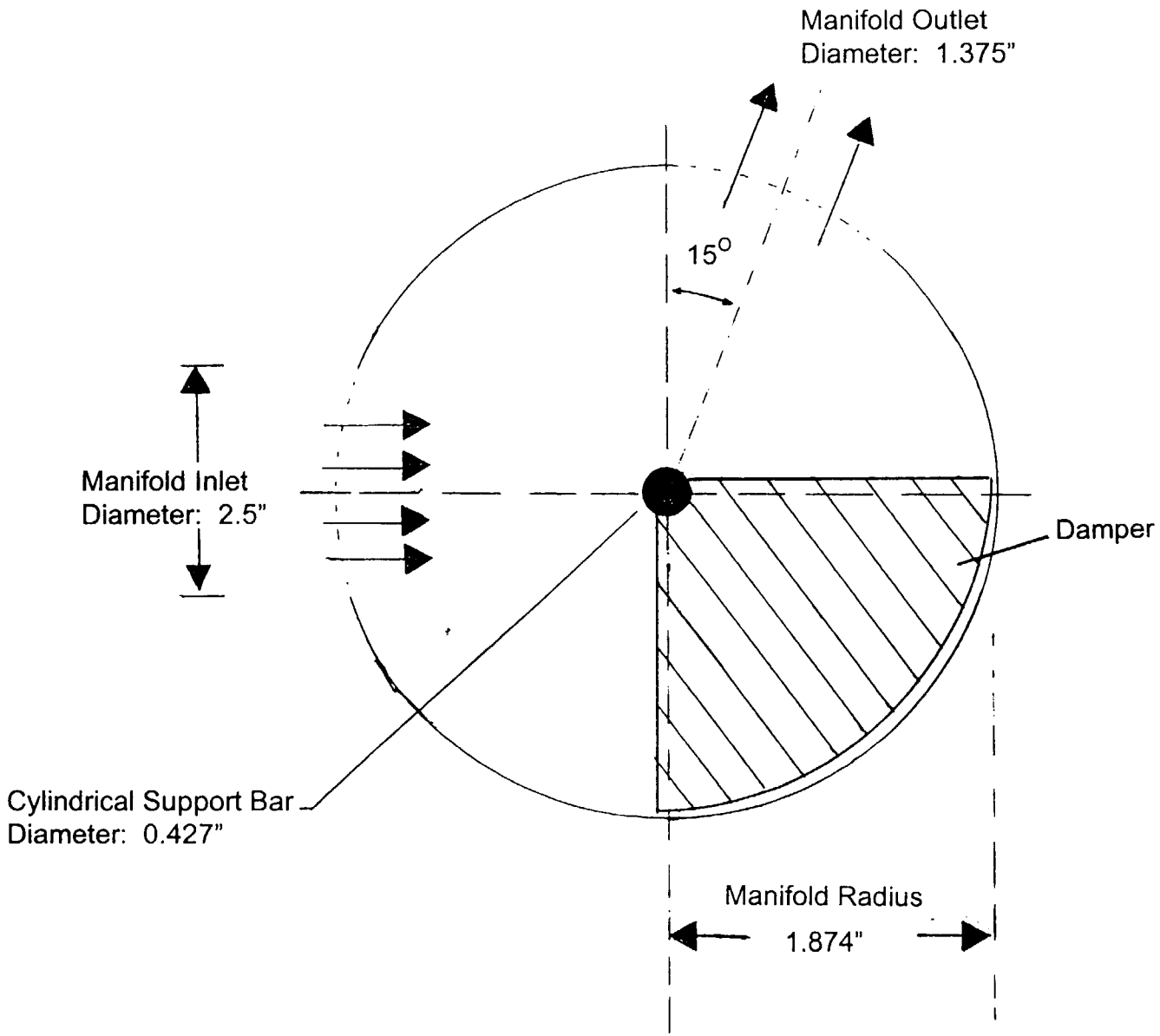

Figure 20A. Side View of the Hot Air Manifold.

Figure 21A. Nominal Manifold Velocity Field Cross-section, k=22 Axial Plane

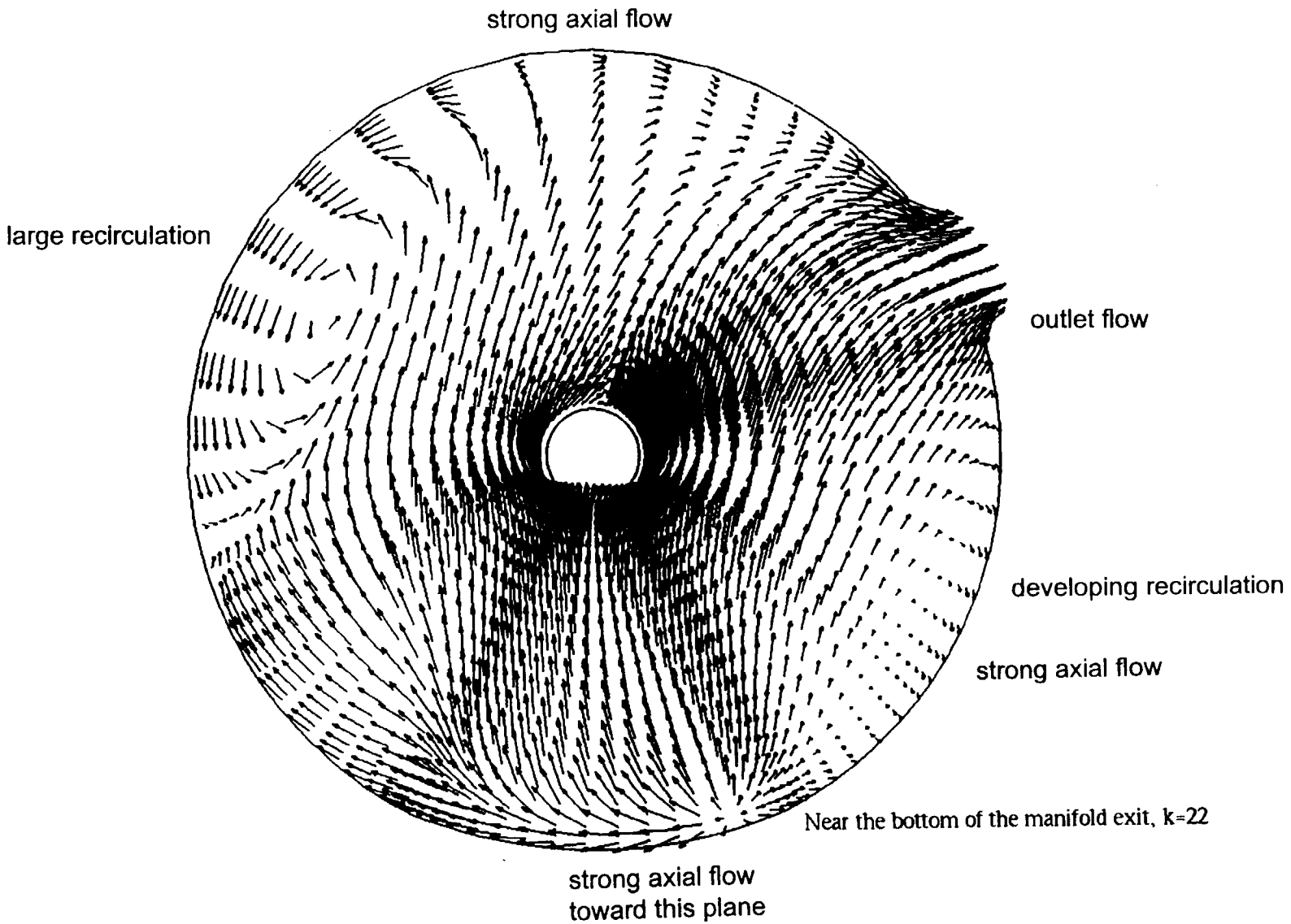

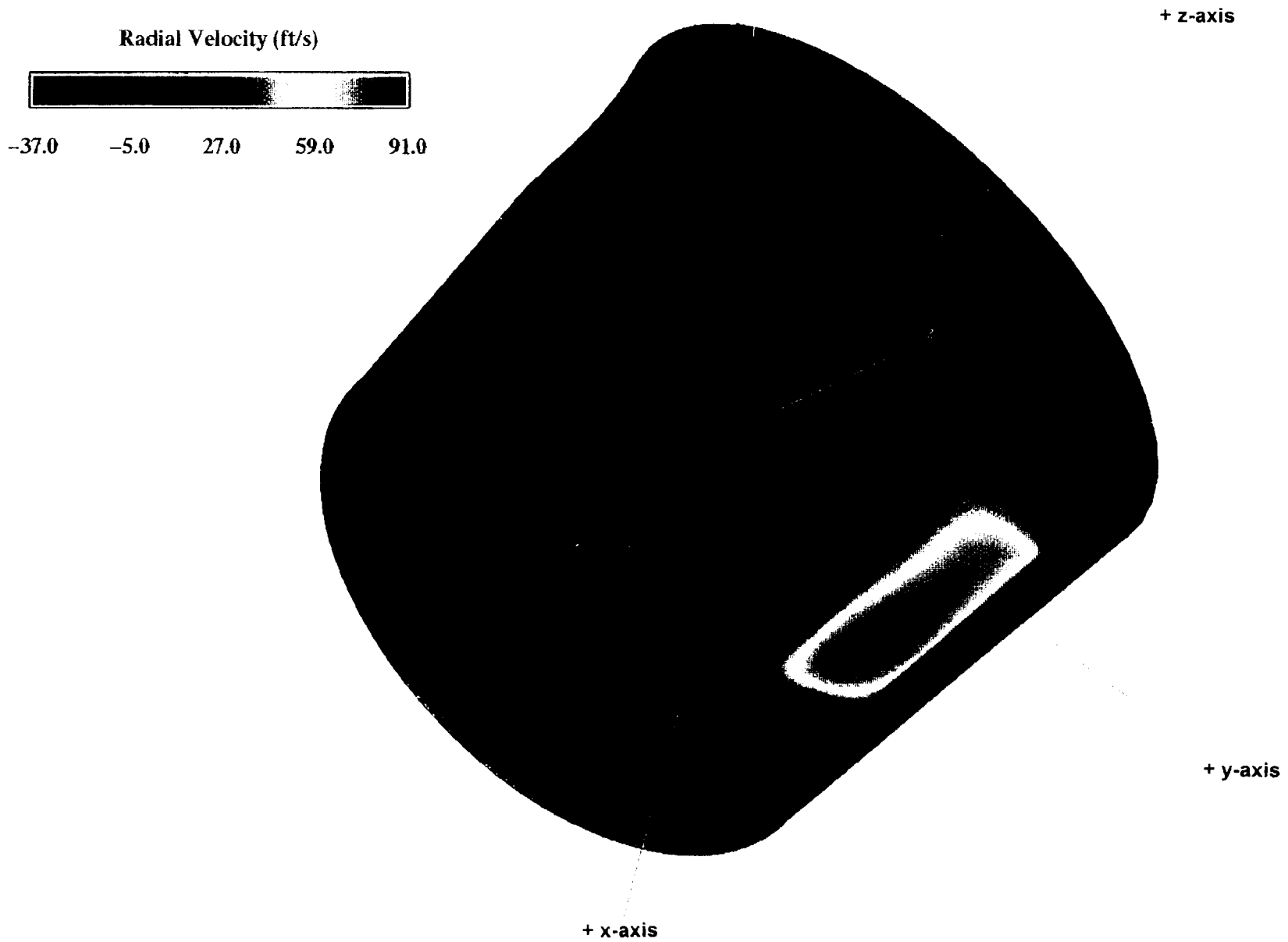

Figure 22A. Nominal Manifold, Radial Velocity at Radial Plane, j=25

Figure 23A. Isometric View of the Hot Air Modified Manifold

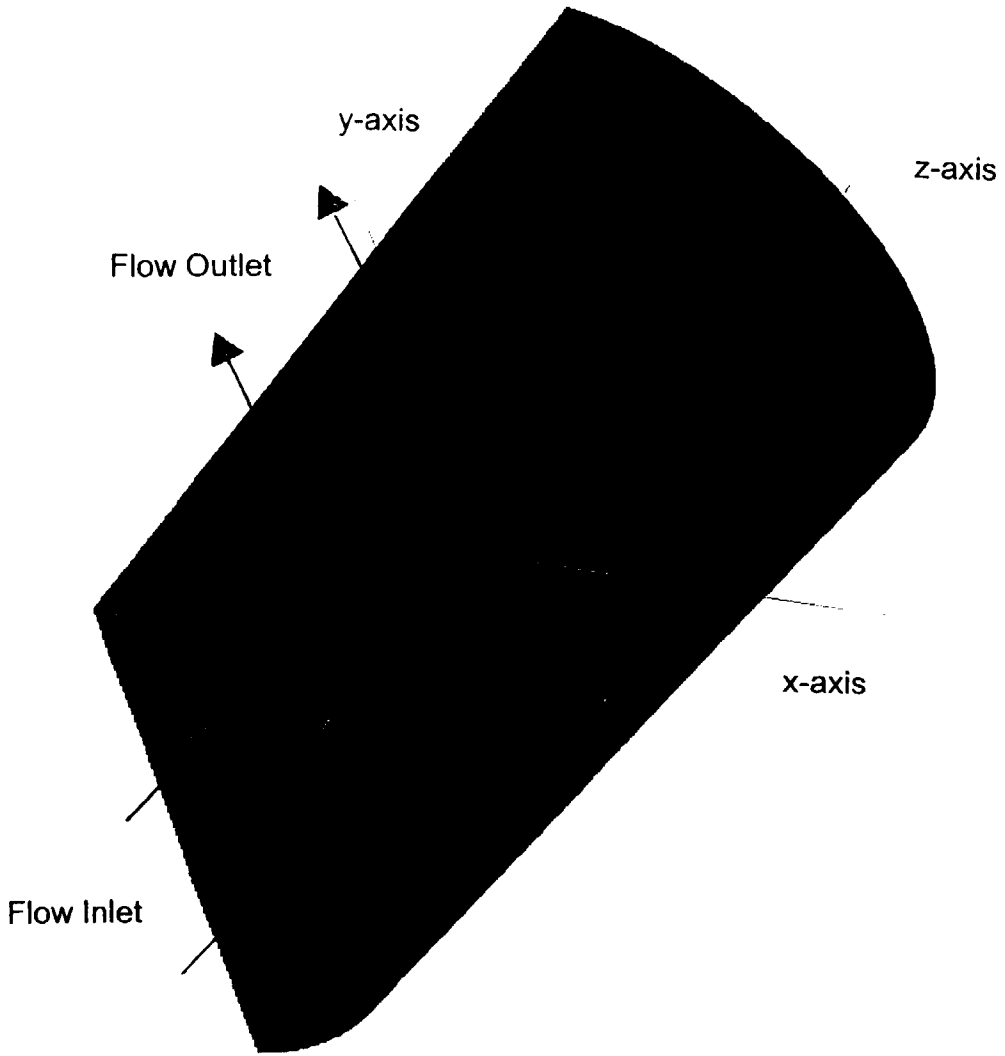

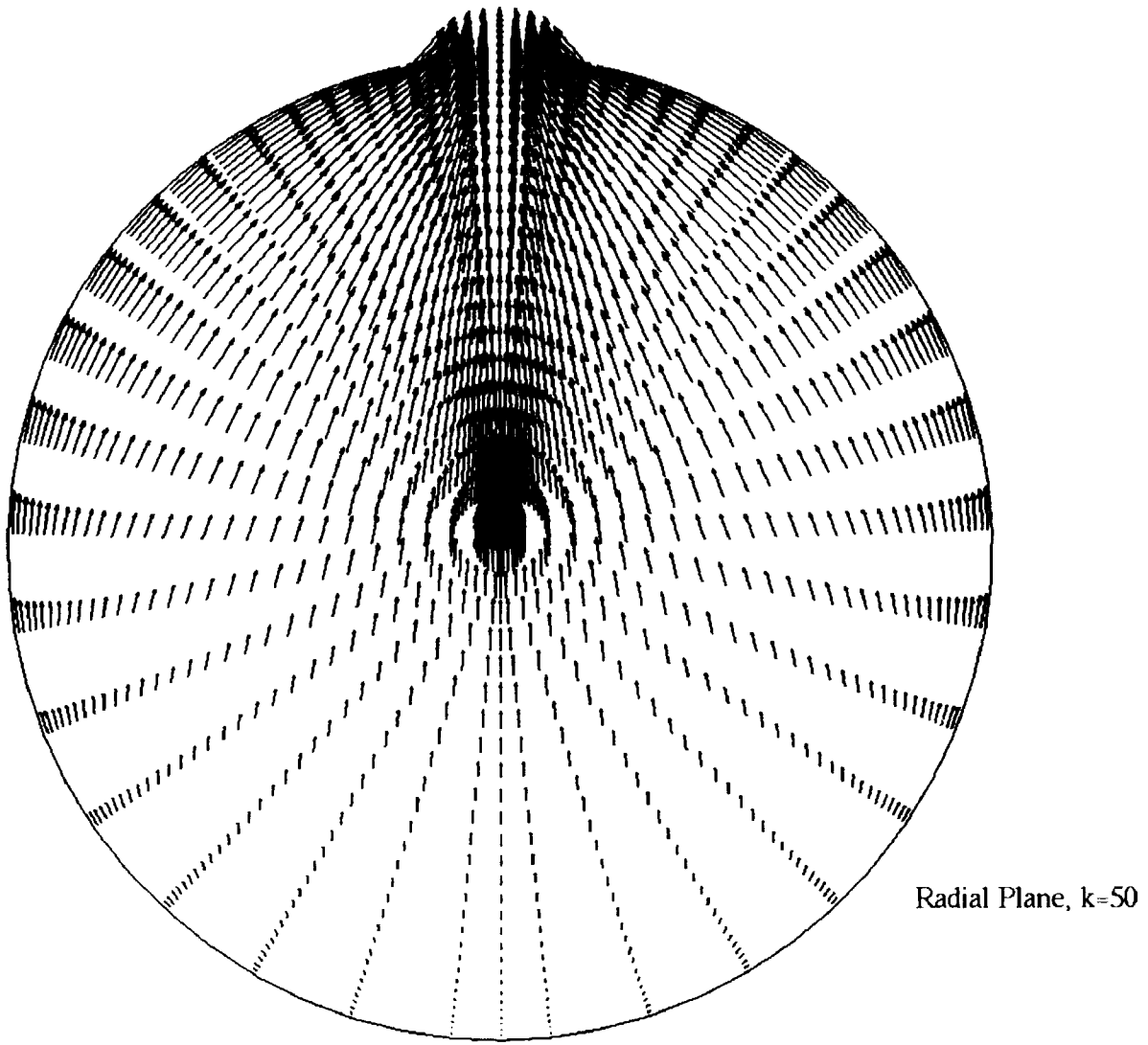

Figure 24A. Modified Manifold Velocity Field Cross-section, k=50 Axial Plane

Figure 25A. Isometric View of the Hot Air Redesigned Manifold

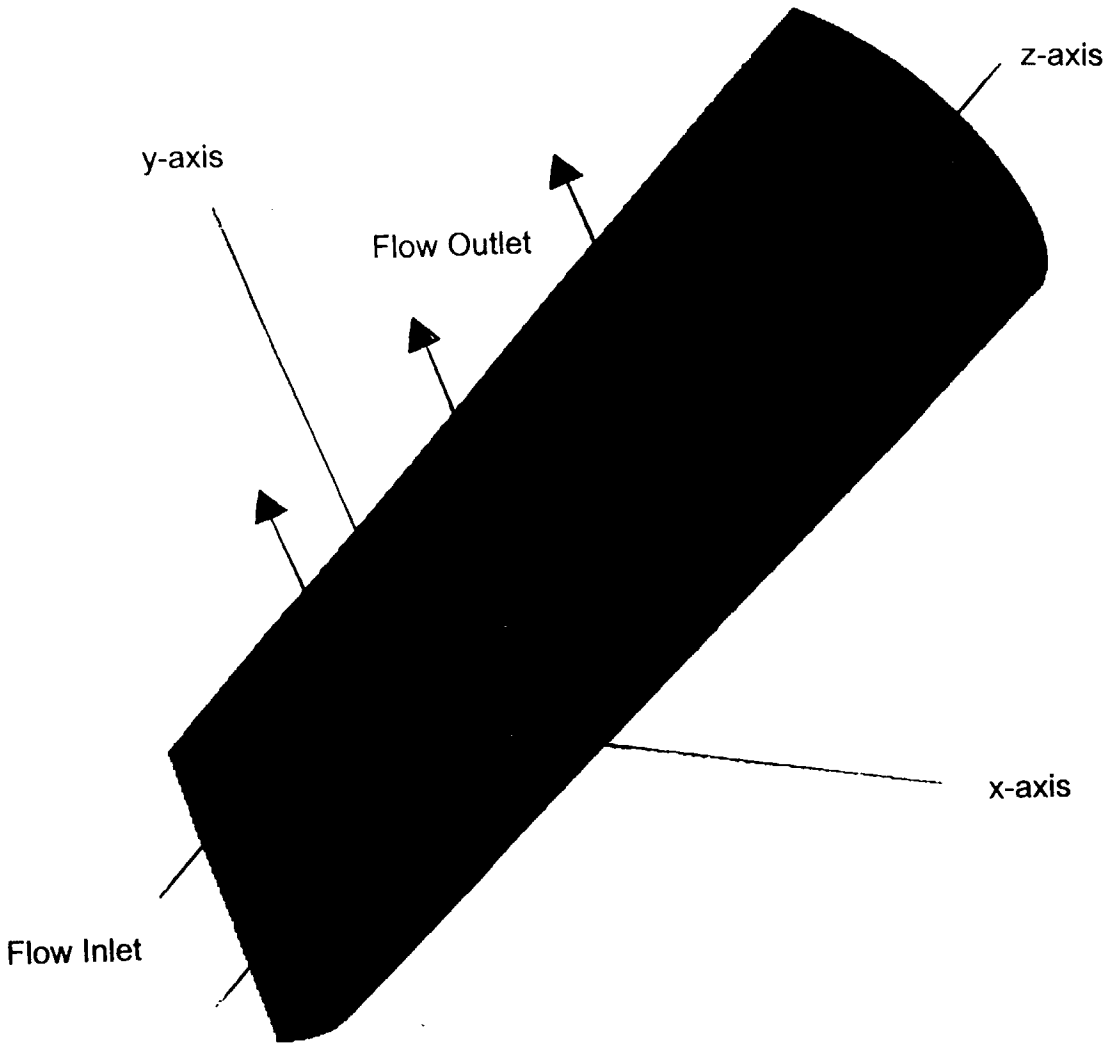

Figure 26A. Side View of the Hot Air Redesigned Manifold

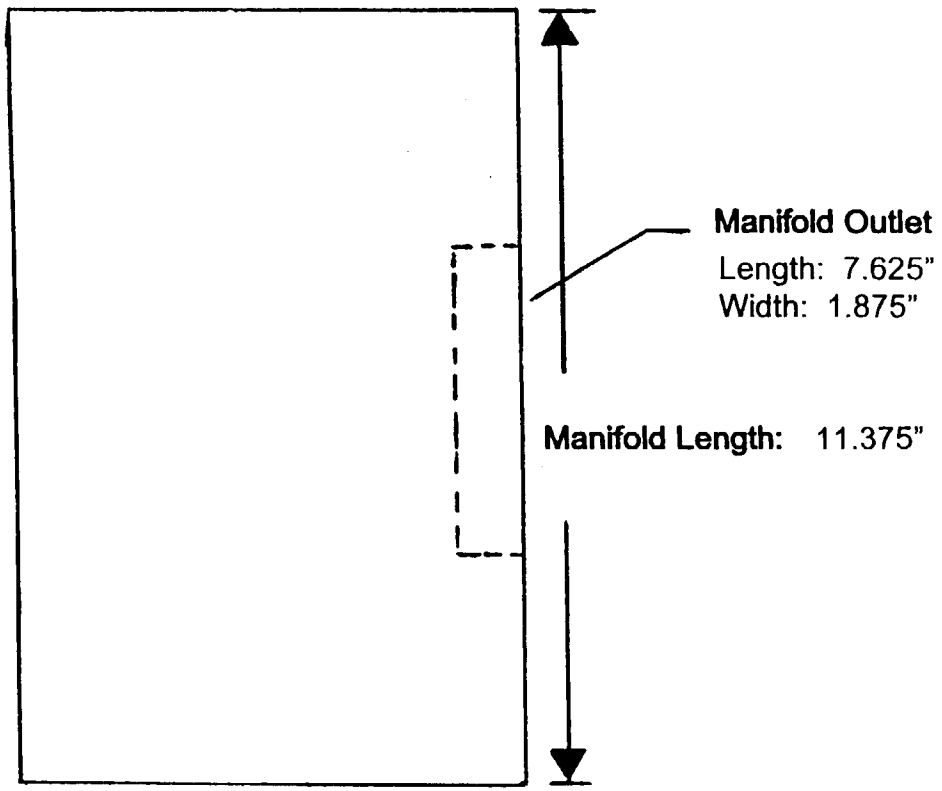

Figure 27A. Top View of the Hot Air Redesigned Manifold

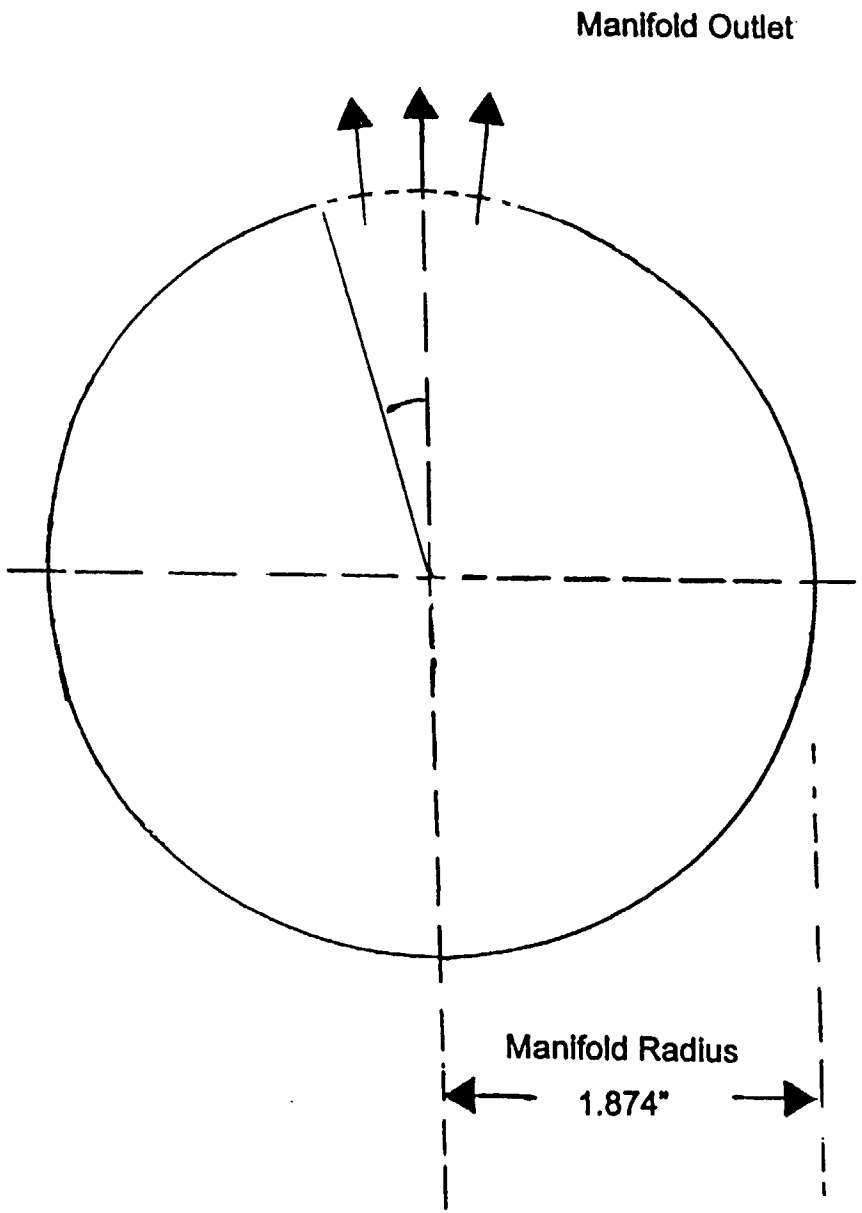

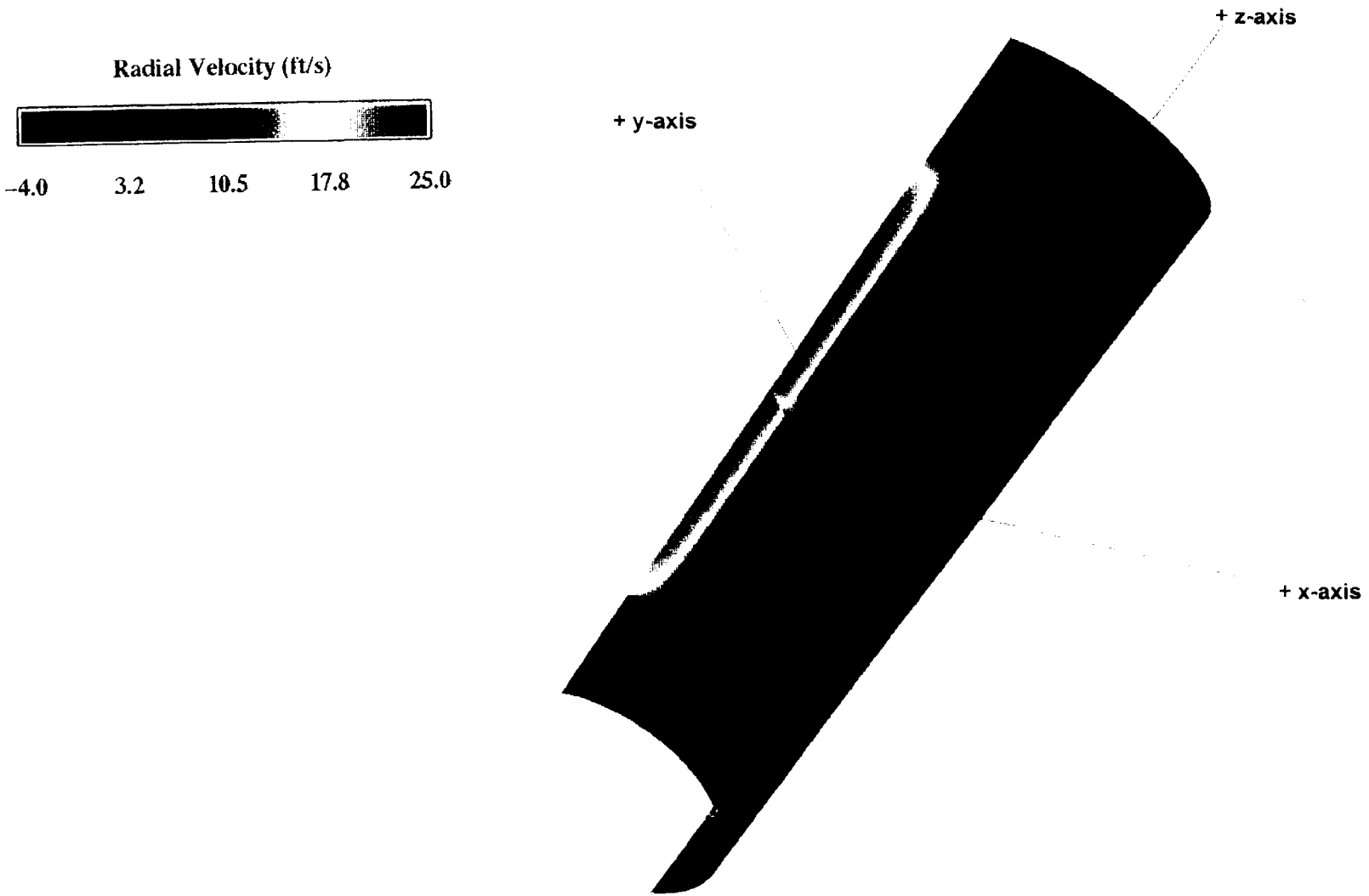

Figure 28A. Redesigned Manifold, Radial Velocity at j=30 and k=60

4.8 Bates Motor Distributed Combustion Test Case

This section of the final report presents validation results for the CELMINT code used heavily in analyses performed by ERC. The CELMINT code can compute the flow field solution of a solid rocket motor by using one of several thermochemistry model options. ERC, Inc. has used three of the available CELMINT thermochemistry models to compute flow fields of interest to NASA. First, an equilibrium thermochemistry model is available. The flow is computed as a single phase flow in this case. The code will also compute CFD solutions using two different two-phase thermochemistry models. The first of these, the surface combustion model, assumes that the aluminum in the propellant burns completely at the propellant surface. The discrete phase particles injected into the motor chamber from the simulated propellant grain are composed of aluminum oxide with no unburned aluminum remaining in the particles. This model has been used extensively in flow field calculations for problems of interest to NASA. The CELMINT code also contains a distributed combustion model which assumes that no aluminum has burned at the propellant surface. Hermsen's aluminum combustion burn rate model is used in this case to compute the burn rate of the aluminum particles as they move down the motor port. This model has become very important to many of the analyses performed by ERC since two-phase methodology is required to assess many solid rocket motor problems. Since this is an important thermochemistry model option, ERC has taken time to further validate this model by examining a distributed combustion test case, which was originally used by SRA, Inc. In order to fully document the capabilities of the CELMINT code one more thermochemistry model option will be mentioned. The CELMINT code also has the capability of employing finite rate chemistry, but this model has not been used by ERC, Inc. at this time.

The Super BATES motor case as reported by SRA, Inc. in the document entitled, Advanced Flow Field Model (Phillips Lab report number PL-TR-93-3005), was used as the distributed combustion test case. The initial grain configuration of the motor was used in this analysis. Some simplifications were made to the Super BATES motor geometry, similar to test runs reported by SRA, Inc. in the AIAA paper, 92-3509, "A Two-Phase Restricted Equilibrium Model for Combustion of Metalized Solid Propellants". The actual initial Super BATES motor geometry is shown in Figure 1A. Modifications were made to this geometry to simplify the calculation of the motor internal flow field. A 20 inch inert length of chamber was added to the end of the propellant length shown in Figure 1A. The original length of the motor chamber was 60 inches. The additional inert length extends the motor chamber length to 80 inches. The inert length was added to the Super BATES motor chamber to assure that a large percentage of the aluminum is burned upstream the motor nozzle. This is necessary in order to properly compare the one-dimensional solution to the CFD solutions. The geometry in the vicinity of the motor nozzle was also simplified. A smooth ramp from the propellant to the nozzle throat was used instead of the vertical wall connected to the nozzle shown in Figure 1A. The 45 degree angle as used in the geometry shown in

Figure 1A was maintained as the nozzle entrance ramp angle. Figure 2A shows a schematic of the Super BATES test case motor geometry. One additional change was made to the Super BATES motor geometry shown in Figure 1A. The throat radius of curvature was increased from 1.5 inches to 2.247 inches to create a smoother turning of the flow in the transonic flow region. The geometry simplifications will not have a significant effect on the flow field and will remove from the solution process any grid uncertainties associated with the original geometry.

There are several flow boundary conditions associated with the various CELMINT test cases that are common to all the cases. The boundary conditions specific to a particular case are detailed as the case results are presented. The BATES motor propellant formulation used in this analysis is shown in Table 4.8.1. The propellant contains 15% aluminum by weight. The mass flow rate boundary condition at the propellant surface was assigned such that the total mass flow rate in the motor was 96.52 lbm/sec. This corresponds to a specified propellant burn rate of 0.348 in/sec and a propellant density of 112.0 lbm/ft^3 as specified by SRA, Inc. in their analysis of this problem (Phillips Lab report number PL-TR-93-3005). The total pressure at the aft end of the motor chamber corresponding to the other motor conditions presented is 982.2 psia. The no-slip condition is applied at the inert walls of the motor and the motor walls are also assumed to be adiabatic.

Table 4.8.1 Super BATES Motor Propellant Formulation

Component	Formula	Weight Percent	Heat of Formation (cal/g-mole)
HTPB (R-45M)	C 7.332 H 10.982 O 0.58	12.84	-2970.
AP	N 1.0 H 4.0 Cl 1.0 O 4.0	71.0	-70690.
IPDI	C 12.0 H 18.0 O 2.0 N 2.0	1.06	-91360.
A-02246	C 23.0 H 32.0 O 2.0	0.10	-155000.
Aluminum	Al 1.0	15.0	0.0

Two computational grids were used in the analysis. The main computational grid was constructed with an axial resolution of 155 grid cells and a radial resolution of 60 grid cells. The axial resolution of the motor chamber from the head end to the end of the propellant was 65 grid cells. The remainder of the motor chamber that was an inert surface had an axial resolution of 30 grid cells. The nozzle entrance ramp from the end of the inert chamber surface to the nozzle throat had an axial resolution of 25 grid cells while the remainder of the nozzle exit cone had an axial resolution of 25 grid cells. This grid was used for all the solutions reported except the analysis using CELMINT version 6.05. The dimensions of the computational grid used for version 6.05 were 140 x 60. The geometry was also slightly different for this configuration in that no inert length of motor chamber was added to the end of the propellant grain.

In order to provide a validation comparison for the CELMINT computed BATES motor test cases, a one-dimensional equilibrium chemistry solution was computed using the CET86 thermochemistry code. CET86 is an equilibrium thermochemistry code developed by NASA Lewis. The one-dimensional equilibrium chemistry solution is shown in the first data column of Table 4.8.2.

Table 4.8.2 Flow Field Solution Summary for Super BATES Motor Cases Under Consideration

Gas phase Flow Parameters	Equilibrium Chem. 1-D	Equilibrium Chem. 2-D	Distributed Comb. v6.05	Distributed Comb. v6.2	Distributed Comb. v6.22
End of Grain					
Total flow rate (lbm/s)	96.52	96.91	99.50	97.95	97.00
Gas flow rate (lbm/s)	96.52	96.91	94.05	92.50	91.56
Static Pressure (psia)	981.9	1020.9	1012.4	1040.2	1033.0
Total Pressure (psia)	982.2	1021.4	1013.1	1040.6	1033.4
Total Temperature (°R)	6182	6178	6115	6107	6134
Mass Fraction of Al	0.150	.150	.1058	.1080	.1083
Mach Number	0.024	.023	.024	.022	.022
End of Port			This point		
Total flow rate (lbm/s)	96.52	97.16	was not	98.04	96.95
Gas flow rate (lbm/s)	96.52	97.16	available. A	92.59	91.51
Static Pressure (psia)	981.9	1020.5	geometry	1040.3	1032.6
Total Pressure (psia)	982.2	1021.3	without any	1040.6	1033.4
Total Temperature (°R)	6182	6176	inert length	6113	6147
Mass Fraction of Al	0.150	0.150	was used.	0.1084	0.1091
Mach Number	0.024	0.023		0.022	0.022
Nozzle Throat Plane					
Total flow rate (lbm/s)	96.52	96.84	97.67	97.60	96.49
Gas flow rate (lbm/s)	96.52	96.84	92.22	92.15	91.05
Static Pressure (psia)	565.8	591.0	603.0	600.1	596.0
Total Pressure (psia)	982.2	1024.4	995.0	987.9	980.7
Static Temperature (°R)	5818.	5812	5778	5765	5812
Total Temperature (°R)	6230	6349	6291	6273	6320
Mass Fraction of Al	0.150	0.151	0.1063	0.1089	0.1098
Nozzle Exit					
Total flow rate (lbm/s)	96.52	96.74	97.65	97.54	96.40
Gas flow rate (lbm/s)	96.52	96.74	92.20	92.09	90.96
Static Pressure (psia)	46.9	49.5	49.8	51.7	51.3
Total Pressure (psia)	953.6	859.7	748.1	682.1	678.6
Static Temperature (°R)	4287	4156	4208	4234	4271
Total Temperature (°R)	6529	6701	6678	6520	6574
Mass Fraction of Al	0.150	0.150	0.1063	0.1086	0.1095
***Convergence Status**					
Static Pressure (psi)	-	1.2	0.7	0.5	0.6
Static Temperature (°R)	-	1	11	1	3
Mass flow rate (lbm/s)	-	0.05	0.07	0.07	0.15
Mass Fraction of Al	-	-	0.0008	0.0001	0.0001

*The values shown in the row labeled "Convergence Status" are differential values computed for the last 500 iteration, ($|P_J - P_{J-500}|$, where J is the current iteration).

Note: All flow quantities shown are mass averages across the motor port at the specified axial location.

The "End of Grain" values and the "End of Port" values are the same for the one-dimensional equilibrium chemistry solution since the port area ratios at these locations are the same. The values in data column one of the table are one-dimensional calculated values of the flow quantities. All the other data columns correspond to CFD solutions and the flow field quantities shown are mass averaged flow field values. The flow quantities are mass averaged across a radial station at the specified location. For example, the static temperature contained in the row labeled, "End of the propellant grain", gives the mass average static temperature across the motor port in a plane perpendicular to the motor centerline and located at the end of the propellant grain. The last row in the table shows the convergence status of the CFD solutions. There is no convergence status shown for the one-dimensional computations since this is not an iterative solution and requires no convergence. The convergence for the CFD solutions is shown as a differential value for the mass averaged flow quantity over the last 500 iterations. In other words, the differential of static pressure shown in the second data column, 1.2 psi, is the amount the mass averaged static pressure has changed over the last 500 iterations. All the convergence differentials are computed at the end of the motor port location.

The CET86S code was used to compute the gas phase equilibrium thermochemistry for the CELMINT computed BATES motor test cases. This code is a modified version of the CET86 code. The two major modifications are:

1) A modification was made to account for the oxygen atoms that are removed from the gas phase as Al_2O_3 caps form from the burning aluminum in the particle. The thermochemistry is referred to as restricted equilibrium because the equilibrium chemistry is restricted by the oxygen atoms that are being removed from the gas phase as the aluminum burns in the motor.

2) Modifications were also made in the code to allow an equilibrium thermochemistry table to be created for use in CELMINT. The table gives the species distribution at a particular location in the motor as a function of the gas phase enthalpy and mass fraction of aluminum at that particular location.

All the modifications to the CET86 code were performed by SRA, Inc.

The first CELMINT solution computed was a two-dimensional equilibrium thermochemistry solution. Complete combustion of aluminum is assumed to have occurred at the propellant surface in this case. Therefore, the appropriate thermal boundary condition at the propellant surface is the adiabatic flame temperature of the completely burned propellant ingredients. The adiabatic flame temperature for these conditions is 6181.9 °R. The second data column of Table 4.8.2 shows a summary of the important flow field information associated with this solution. The computed mass flow rate of 96.91 lbm/sec at the end of the propellant grain was within 0.5% of the desired total mass flow rate of 96.52 lbm/sec. The error associated with this difference

can be attributed to either the need for more iterations or round off inaccuracies in the computation of the propellant area used to generate the mass flow rate per unit area boundary condition used at the simulated propellant surface. All flow quantities reported in the table for the two-dimensional equilibrium chemistry CFD solution have changed by less than one percent over the last 500 iterations.

The distributed combustion cases are the last three columns shown in Table 4.8.2. The original CELMINT code received from SRA, Inc. was version 6.05. In order to assure that no errors were introduced into the code by changes made to the original version 6.05 of CELMINT, several versions of the code were run. Three basic versions of the code were tested. The first was version 6.05. The second was CELMINT version 6.2, which is a later version of the code obtained from SRA, Inc. This code is a restructured version of version 6.05 and also contains some minor bug fixes and improvements to the code as suggested by ERC, Inc. The third version tested is CELMINT version 6.22. This is an ERC, Inc. updated version of the 6.2 code supplied by SRA, Inc. Modifications to the code consist of changes to make the initialization of the domain flow field more stable and additions to the list of possible boundary conditions available with the CELMINT code. The only difference in the three versions that should affect the converged CELMINT distributed combustion results is a change to a burn rate exponent in the Hermsen burn rate equations made between version 6.05 and version 6.2. The exponent was changed to match the correct value as specified in Hermsen's AIAA paper, 81-0038. The change was checked out and is insignificant in magnitude but the change was made to remain consistent with the documentation of the code.

In general, for all the distributed combustion cases, no aluminum is assumed to have burned at the propellant surface. Therefore, the appropriate boundary condition for the species equation is to set the mass fraction of aluminum at the propellant surface to 0.0. Also, the appropriate thermal boundary condition at the propellant surface is the adiabatic flame temperature of the completely burned propellant ingredients excluding aluminum. The adiabatic flame temperature for these conditions is 4724.3 °R. The value of the motor temperature at the end of the motor port where most of the aluminum has burned should correspond to the adiabatic flame temperature of the propellant assuming all ingredients are completely combusted, including aluminum. This temperature is 6181.9 °R. The total mass flow rate for this case is 96.52 lbm/sec as already computed. Since all the aluminum in the propellant will be injected into the computational domain as discrete phase particles, the gas phase mass flow rate is obtained by removing the 15% aluminum from the total mass flow rate. This corresponds to a gas phase flow rate of 82.04 lbm/sec and a discrete phase (aluminum particles) mass flow rate of 14.48 lbm/sec. If the aluminum in the motor burns completely, the total aluminum oxide existing at the aft end of the motor is 27.35996 lbm/sec. It is assumed in this analysis that 80% or 21.89 lbm/sec of the aluminum oxide exists as smoke in the gas phase. The remaining 20% or 5.47 lbm/sec of aluminum oxide exist as discrete phase particles.

The discrete phase aluminum particles injected at the propellant surface have a log-normal particle size distribution with a mass-mean diameter of 150μm and a standard deviation of 0.2. This size distribution was the same as used in the analysis reported by SRA, Inc. in Phillips Lab report, PL-TR-93-3005.

Basic comparative results for the three CELMINT versions are shown in Table 4.8.2. The CELMINT solutions shown in Table 4.8.2 are not completely converged but are adequately converged for the preliminary observations made with respect to Table 4.8.2. The solutions will be further converged for the later analysis discussed in this section of the final report. Some differences in the solutions are due to the initialization process which is the same for versions 6.05 and 6.2 but different for version 6.22. The mass fractions for the solutions using versions 6.05 and 6.2 were initialized with a 0.0 mass fraction of aluminum in the domain. The solution for version 6.22 was initialized with a mass fraction of 0.13 in the computational domain. The solution for version 6.05 is the least converged of the solutions but the solution values were close to the values computed by the version 6.2 code at the same stage of convergence. Also, the flow field values computed by the version 6.05 code are moving toward those computed for the other two solutions. All the flow quantities shown for the version 6.2 and version 6.22 solutions are within one percent at this stage of convergence. The detailed printout (the flow field values at each individual computational cell) of the solutions shown in Table 4.8.2 shows that some differences in the solutions still exist in the low velocity regions of the domain which are related to the initialization differences used for the two solutions. One of these areas is in the recirculation region at the port wall just downstream of the end of the propellant grain. These low velocity regions are slower to converge than the regions in which the flow is steadily moving toward the nozzle exit. The convergence of these solutions will be completed but the preliminary results indicate that the three versions of the code give consistent distributed combustion results and no code errors have been introduced into the later versions of the CELMINT code.

Based on observing the Table 4.8.2 preliminary solutions for versions 6.2 and 6.22, the total temperature achieved by the end of the port for both versions 6.2 and 6.22 is reasonably close to the adiabatic flame temperature of the propellant but this is being further investigated. Another discrepancy being investigated is the aluminum mass fraction in the gas phase, which should be approximately 0.127 for this problem but reaches a value of only 0.11. It is known from runs already made that the artificial dissipation added to the continuity equation has a significant effect on the solution, including the aluminum mass fraction, and this is being investigated.

Looking at the drop in total pressure at the nozzle exit location, the values possess the correct trend. The total pressure loss is smallest for the single-phase equilibrium chemistry run. There are no particles in the nozzle domain to cause further momentum loss as for the two-phase distributed combustion cases. The version 6.05 run losses are intermediate between the equilibrium chemistry run and the version 6.2 and 6.22

solutions, probably because the particle breakup model was not turned on for this run. The breakup model will be turned on when convergence of this run is continued and this should determine if indeed the breakup model is contributing to the total pressure loss in the nozzle. The most total pressure loss is for the two-phase version 6.2 and version 6.22 cases with the particle breakup model activated. The total pressure loss for these two cases is within one percent.

The preliminary solutions reported in Table 4.8.2 raised a number of questions associated with the two-phase CELMINT solutions. Further analysis was performed in order to answer the questions. The additional analysis involved the CELMINT distributed combustion model. The key elements of the distributed combustion model examined are: 1) the combustion model routines contained in CELMINT, 2) the thermochemistry database utilization routines contained in CELMINT, and 3) the thermochemistry database generation code, CET86S. These solution results show that the CELMINT code distributed combustion model is operating properly. The problems observed in previously computed solutions using the distributed combustion model have been associated with the following causes: 1) reduced convergence rate for the distributed combustion solutions, 2) increased sensitivity of the distributed combustion solutions to runtime parameters associated with the solution procedure and 3) improper default values for the particle breakup model. The additional distributed combustion analyses used to support the proper operation of the CELMINT code are now discussed.

The initial analyses showed that CELMINT version 6.22 solutions are essentially the same as solutions generated using previous versions of the code (versions 6.05 and 6.2). Only solution results associated with version 6.22 are subsequently discussed in this section.

The first subject addressed is validation of the thermochemistry used in CELMINT. The general two-phase combustion solution process can be described as follows. CELMINT begins the solution process for a given computational cell by using the gas phase flow variables (pressure, temperature, etc.) computed at the last time step, (n-1), to compute the discrete phase combustion processes at the new time step, n. The mass, momentum and enthalpy transferred from the discrete phase to the gas phase due to aluminum combustion are computed and loaded into interphase exchange terms. These terms appear in the gas dynamic equations as source terms and are used to couple the discrete phase to the gas phase. The gas phase enthalpy, pressure and aluminum mass fraction in a given cell are used to obtain the proper species distribution for that cell from the thermochemistry database. The species distributions for the cell along with the curve fit functions for enthalpy, specific heat and entropy are used to calculate new gas phase properties associated with the cell such as specific heat, molecular weight, etc.. These quantities are used along with the interphase exchange terms to recompute the solution at the time step, n. This general process is continued until convergence is obtained.

The operation of CET86S was checked by comparison with an independent version of the NASA Lewis CET86 thermochemistry code. This independent version of the NASA Lewis equilibrium thermochemistry code has been validated by the motor ballistics community and will be referred to here as just, CET86I. Table 4.8.2 shows the results of the analysis, which compares the CET86S AND CET86I codes. Thermochemistry conditions were computed for the Super Bates motor propellant composition under the various conditions shown in Table 4.8.3. For each of the case comparisons shown in the first column, the corresponding flame temperature and enthalpy computed by the CET86I code are shown in columns three and four. The flame temperature computed by the CET86S code at the corresponding enthalpy shown in column four is shown in column two. The first case, "No Aluminum Burned", corresponds to the assumption in which all the propellant ingredients except aluminum are burned. The aluminum remains in the propellant mixture as inert aluminum. This case corresponds to a typical solid rocket motor propellant thermal boundary condition for which it is assumed that no aluminum burns at the propellant surface. This is the CELMINT thermal boundary condition used for this distributed combustion analysis. An assumption that some fraction of the aluminum is burned at the propellant surface is also possible with the CELMINT code, but this option was not used for the results reported. The "No Aluminum Burned" case has the lowest propellant surface flame temperature for several reasons. No aluminum is burned at the surface, and therefore no heat from aluminum combustion is produced. The inert aluminum takes up space in the propellant mixture where other heat producing ingredients could be combusting. And, heat is extracted from the other burning ingredients to raise the temperature of the inert aluminum to the equilibrium surface flame temperature. The CET86S code uses an approximation to compute the surface flame temperature for the inert aluminum thermochemistry case while the CET86I code computes the equilibrium flame temperature more directly. The CET86S approximation appears to be adequate because the computed flame temperatures for the two codes are within 0.3%. The other three cases show excellent agreement between the computed flame temperatures for the two codes. The "No Aluminum Burned, No Inert Aluminum" case corresponds to the condition in which the aluminum is removed from the propellant formulation and the other ingredients are completely burned. The, "50% Aluminum Burned", case corresponds to the condition in which 50% of the aluminum in the propellant is burned. The remaining case, "All Aluminum Burned", represents conditions in which all propellant ingredients are completely burned at the propellant surface. The individual species mass fraction compositions of the gas at the thermochemical conditions corresponding to the four cases were also compared for the two codes. The comparison showed that the computed species mass fraction distributions were within a fraction of a one percent for all the cases shown.

Table 4.8.3 Comparison of CET86S and CET86I Computed Flame Temperatures for Various Aluminum Combustion Conditions

Component	Flame Temperature CET86S	Flame Temperature CET86I	Enthalpy
No Aluminum Burned (Inert Aluminum)	4666.0 °R	4653.0 °R	-435.8 cal/gm
No Aluminum Burned (No Inert Aluminum Considered)	5139.2 °R	5140.8 °R	-512.7 cal/gm
50% Aluminum Burned	5742.2 °R	5742.0 °R	-470.8 cal/gm
All Aluminum Burned	6181.6 °R	6181.2 °R	-435.8 cal/gm

The operation of the CELMINT routines that read and store the thermochemistry database and interpolate between table values were also validated. Specific values of the input values used to read the thermochemistry database were printed along with interpolated output values from the database. The desired database output values were computed manually to validate the operation of the CELMINT interpolation routines. No problems were found with any of these CELMINT routines.

Comparisons of solution results will be presented for five basic solutions. These results are shown in Table 4.8.4. All the flow field values in this table are mass averages of the flow field quantities across a radial station at the specified axial location. For example, the row labeled 'End of the propellant grain' gives mass averages of the flow field quantities radially across the port at the end of the propellant grain.

Table 4.8.4 shows a summary of the CFD solution results associated with this analysis. The first solution shown in Table 4.8.4 is a 1-D equilibrium thermochemistry solution. The solution was computed using the CET86I code and corresponds to a single-phase equilibrium thermochemistry solution assuming isentropic nozzle flow. This solution is presented as an idealized flow comparison to the distributed combustion solutions. The 1-D equilibrium thermochemisty solution provides isentropic estimates of the motor pressure and temperature without the effects of thermal and momentum lags caused by the discrete phase. The gas phase mass fraction of aluminum is 0.15 (the total fraction of aluminum in the propellant mixture) at all locations in the motor for this solution since there is only a single phase. The two-phase solutions will have reduced gas phase mass fractions since some of the aluminum resides in the discrete phase. The target mass flow rate associated with all the runs reported is 96.52 lbm/s.

The last row in Table 4.8.4 shows the convergence of the solutions. This is shown as the amount of change in the flow field variables over the last 1000 iterations. The

convergence properties for the 1-D equilibrium solution are not shown because this is not a CFD solution. The flow values for the CFD solutions are changing by less than one percent over 1000 iterations. The flow variables are also not changing in one direction but are fluctuating. To obtain further convergence at this stage, the number of discrete phase averaging steps would have to be increased significantly. This stage of convergence is very sufficient for the comparison purposes of this analysis.

Case 0	**Case A**
Artificial viscosity coefficient, continuity equation: 0.05 momentum equation: 0.5 energy equation: 0.5 turbulence equation: 0.5 species equation: 0.5 Particle Breakup Model: on with default input	Artificial viscosity coefficient continuity equation: 0.5 momentum equation: 0.5 energy equation: 0.5 turbulence equation: 0.5 species equation: 0.5 Particle Breakup Model: off
Case B	**Case C**
Artificial viscosity coefficient, continuity equation: 0.05 momentum equation: 0.5 energy equation: 0.5 turbulence equation: 0.5 species equation: 0.05 Particle Breakup Model: off	Artificial viscosity coefficient, continuity equation: 0.05 momentum equation: 0.5 energy equation: 0.05 turbulence equation: 0.5 species equation: 0.05 Particle Breakup Model: off

All of the cases shown utilize the same computational grid and boundary conditions. The differences in the solutions are due to the utilization of different solution procedure control parameters. The solution procedure control parameters that were found to have the most affect on the CFD solutions are specified for each case.

Table 4.8.4 Comparison of the version 6.22 Distributed Combustion Cases

Gas phase Flow Parameters	Equilibrium Chem. 1-D	Case 0	CASE A	CASE B	CASE C
End of Grain					
Total flow rate (lbm/s)	96.52	97.00	95.59	96.01	96.01
Gas flow rate (lbm/s)	96.52	91.56	90.12	90.54	90.54
Static Pressure (psia)	981.9	1033.0	973.0	982.0	981.8
Total Pressure (psia)	982.2	1033.4	973.5	982.4	982.3
Total Temperature (°R)	6181	6134	6165	6170	6163
Mass Fraction of Al	.15	.1083	.120	.124	.124
Mach Number	.024	.022	.023	.023	.023
End of Port					
Total flow rate (lbm/s)	96.52	96.96	95.78	95.97	95.88
Gas flow rate (lbm/s)	96.52	91.51	90.32	90.50	90.41
Static Pressure (psia)	981.9	1032.6	972.7	981.6	981.5
Total Pressure (psia)	982.2	1033.4	973.4	982.4	982.2
Total Temperature (°R)	6181	6147	6178	6190	6183
Enthalpy (cal/gm)	-435.71	-314.53	-322.18	-325.76	-327.44
Total Enthalpy (cal/gm)	-435.71	-314.53	-322.18	-325.76	-327.44
Mass Fraction of Al	.15	.1091	.121	.126	.126
Mach Number	.024	.022	.023	.023	.023
Nozzle Throat					
Total flow rate (kg/s)	96.52	96.50	92.26	95.81	95.33
Gas flow rate (kg/s)	96.52	91.05	86.80	90.34	89.86
Static Pressure (psia)	565.8	596.0	553.9	567.8	568.9
Total Pressure (psia)	982.2	980.7	932.1	972.0	970.8
Static Temperature (°K)	5818	5812	5816	5827	5872
Total Temperature (°K)	6230	6320	6340	6370	6417
Enthalpy (J/kg)	-565.01	-460.09	-486.14	-482.31	-465.34
Total Enthalpy (J/kg)	-435.71	-328.87	-349.90	-341.30	-323.85
Mass Fraction of Al	.15	.1098	.126	.126	.127
Nozzle Exit					
Total flow rate (kg/s)	96.52	96.41	91.67	95.52	95.06
Gas flow rate (kg/s)	96.52	90.96	86.22	90.06	90.06
Static Pressure (psia)	46.9	51.3	48.0	47.9	47.9
Total Pressure (psia)	953.6	678.6	669.0	764.8	777.7
Static Temperature (°K)	4288	4271	4279	4194	4234
Total Temperature (°K)	6529	6574	6604	6710	6698
Enthalpy (J/kg)	-1048.28	-943.36	-972.28	-1026.05	-987.81
Total Enthalpy (J/kg)	-435.47	-374.52	-395.32	-418.50	-370.46
Mass Fraction of Al	.15	.1095	.127	.126	.127
***Convergence Status**					
Static Pressure (psia)	-	+0.6	-0.3	+0.4	+0.04
Static Temperature (°R)	-	-5	+4	-2	-2
Mass flow rate (lbm/s)	-	+0.15	-0.13	+0.02	+0.04
Mass Fraction of Al	-	-0.0001	+0.0002	-0.00001	-0.00001

*The convergence status is the change in the variable over the last 1000 iterations at the radial station at the end of the motor chamber. Nominal parameters except as shown. Case 0: default parameters except for avisc(4)=0.05 and particle breakup model on. Case A: default parameters with no particle breakup

model. Case B: avisc(4),avisc(8) = 0.05 and no particle breakup model. Case C: same as case B except that avisc(5) = 0.05.

For all the distributed combustion cases considered, no aluminum is assumed to have burned at the propellant surface. Since this is assumed, the thermal boundary condition appropriate at the propellant surface is the adiabatic flame temperature of the completely burned propellant ingredients, including inert aluminum. The adiabatic flame temperature for these conditions is 4666 °R. The inert walls in the motor domain are treated as adiabatic. The adiabatic flame temperature in the motor, if all propellant ingredients are completely burned, is 6181 °R. Also, the aluminum mass fraction at the propellant surface is set to 0.0. The mass flow boundary conditions at the propellant surface were assigned such that the total mass flow rate in the motor is 96.52 lbm/sec as previously derived for the 1-D equilibrium thermochemistry solution.

The mass flow rate of aluminum particles injected at the propellant surface is 14.48 lbm/sec which corresponds to 15 % of the propellant weight. If the aluminum in the motor burns completely, the mass flow rate of aluminum oxide particles at the nozzle exit will be 7.75 lbm/sec. This corresponds to 20% of the initially injected aluminum burning to form aluminum oxide in the form of caps. The gas phase mass fraction of aluminum would then be .1272 if all the aluminum burns. The discrete phase particles injected at the propellant surface have a log-normal particle size distribution with a mass-mean diameter of 150 μm and a standard deviation of 0.2. This size distribution was the same as used in the analysis reported by SRA Inc. in Phillips Lab report number PL-TR-93-3005.

As previously stated, one difficulty in obtaining solutions using the CELMINT distributed combustion model is the reduced convergence rate of the species and energy equations. The other equations converge to a reasonable flow pattern in comparable times to the non-distributed combustion solutions. This problem is still being addressed but some action can be taken to increase the convergence of the species and energy equations. The convergence can be accelerated by a judicious choice of initial conditions as well as temporarily increasing the time step on the species equation.

The major problem associated with obtaining good converged distributed combustion solutions was found to lie in the particle breakup model. Case 0, shows the flow field solution when the particle breakup model is used with default model operational parameters. Case B can be directly compared to Case 0. The only difference between Case 0 and Case B is that the particle breakup model is not used in Case B. The Case 0 solution shows an excessive loss of total pressure in the motor nozzle region and the aluminum mass fraction at the aft end of the motor and in the nozzle is much lower than the 0.1272 expected assuming all the aluminum is burned. The Case B results show that the pressure and temperature at both the end of the grain and at the end of the port are close to the 1-D equilibrium chemistry solution values. Also, the aluminum mass fractional values of .124 at the end of the grain and 0.126 at the end of the port are much more consistent with almost complete combustion of the aluminum. There is

still a small fraction of aluminum (associated with the larger particles released), which is unburned at the end of the port. There are temperature and momentum lags due to the particulate phase which do cause pressure and temperature differences in the nozzle. Case A and Case C are shown as comparisons to Case B. Case A shows the effect of using the default artificial viscosity coefficient value of 0.5 on the continuity equation. The other three distributed combustion solutions use the lower value of 0.05. The use of the artificial viscosity coefficient of 0.5 on the continuity equation causes the solution to have a significant mass flow deficit at the throat. This same phenomena has been observed on all other test problems. Normally the lowest continuity equation artificial viscosity coefficient value, which will maintain a stable CFD solution is used. The pressure at the end of the grain is lower because of this mass flow error at the motor throat but the overall solution is much better than the Case 0 solution. Case C shows that there is a small but notable affect in the solution if the artificial viscosity coefficient on the energy equation is reduced to 0.05. There is slightly less pressure loss in the motor nozzle for this case and the gas phase aluminum mass fraction in the motor nozzle corresponds more closely to complete aluminum combustion.

As time permits, additional analyses will be performed to fine tune the CELMINT distributed combustion model. These analyses will be concentrated in the following areas. Solution procedure control parameter combinations that allow more rapid convergence will be sought. The distributed combustion model will be tested for the assumption of some fraction of aluminum combustion at the propellant surface instead of assuming that no aluminum burns at the surface. Dependence of the equilibrium thermochemistry tables and the CELMINT solution on the motor pressure in the nozzle region will be investigated and quantified.

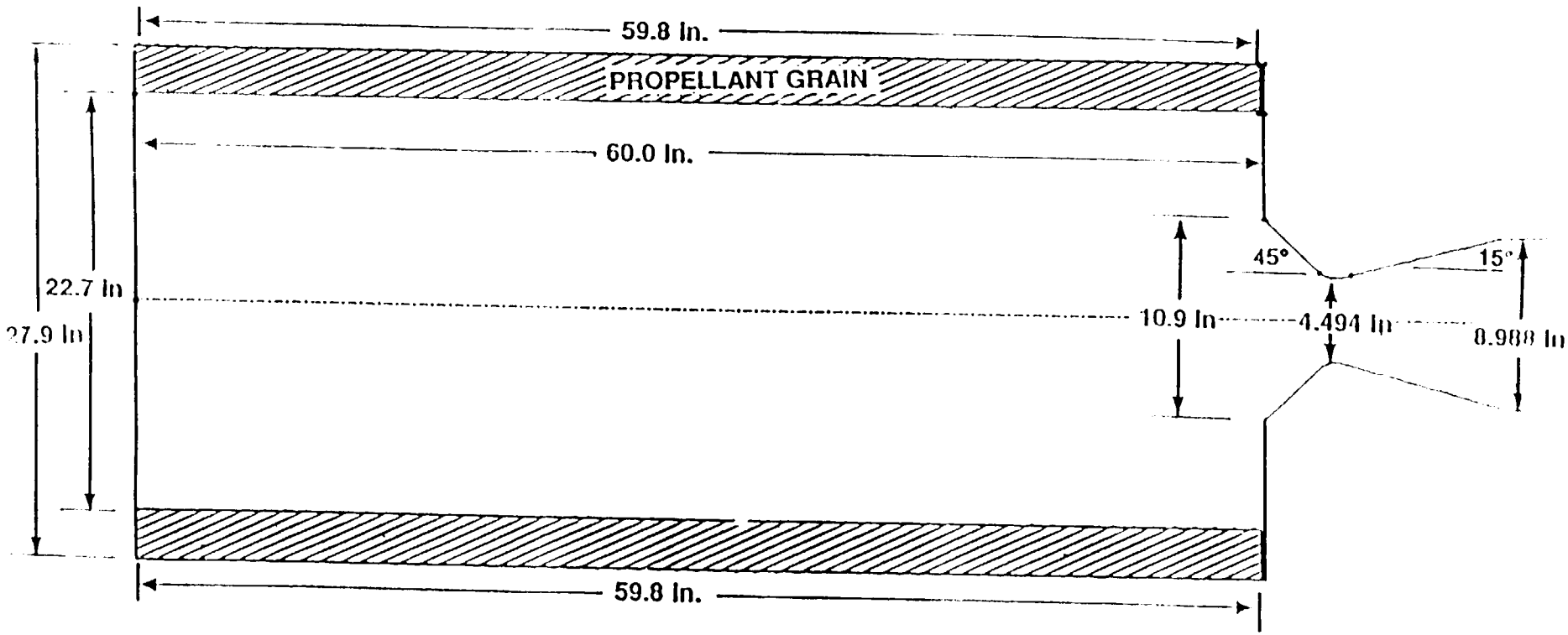

Figure 1A. Super BATES Motor Initial Geometry

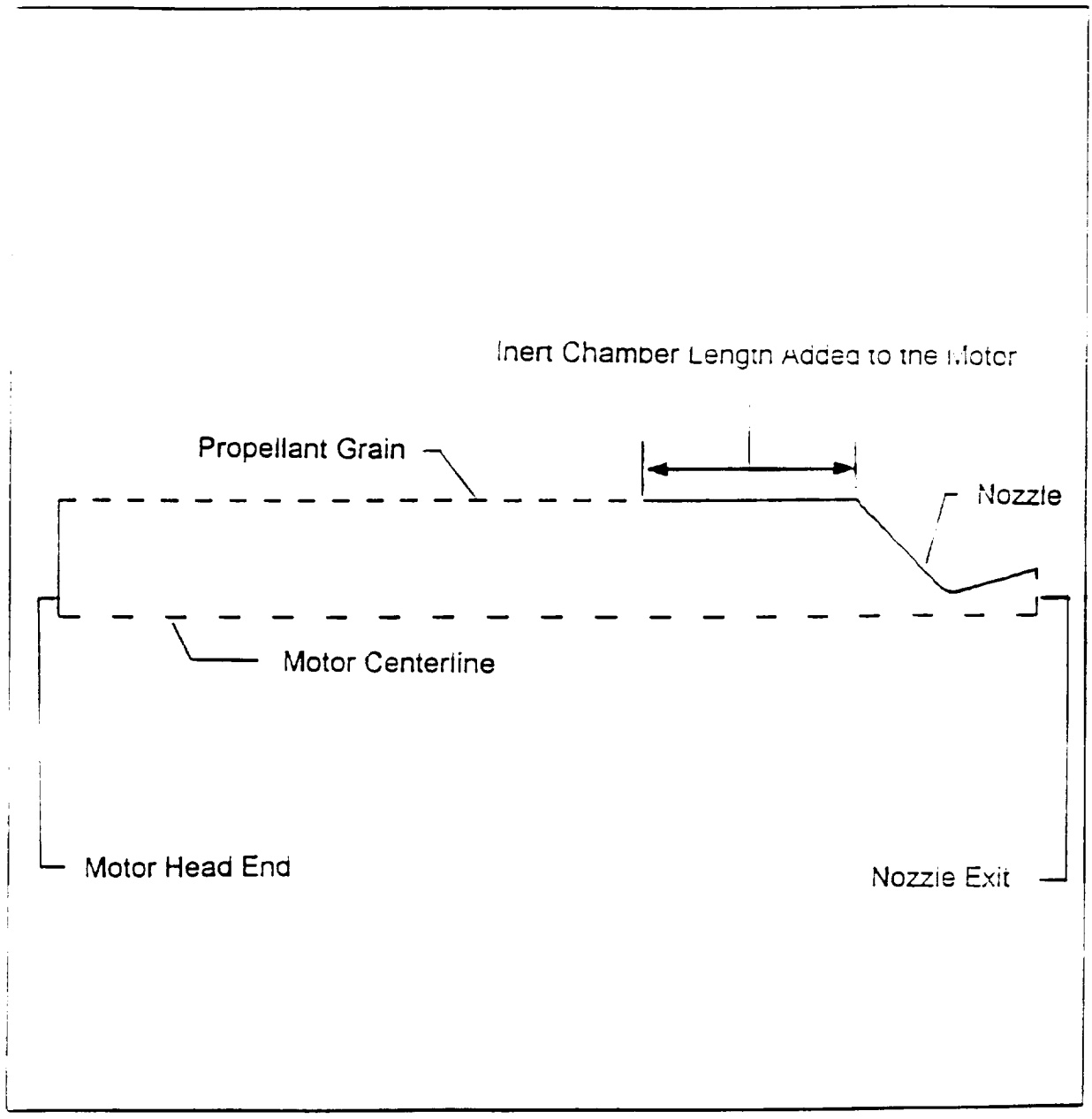

Figure 2A. Super BATES Internal Motor Geometry Used for Computations

4.9 Three Dimensional Polysulfide Bump Analysis

A three dimensional flow analysis was performed on two one inch hemispherical bumps on a flat plate to simulate the polysulfide bumps in the pre-flight RSRM nozzle in order to determine the effects of the bumps on the local nozzle flow environment.

A Cartesian coordinate system was used to solve for the three dimensional flow field. The coordinate system is illustrated in Figure 1A. The z-axis is in the direction of the main axial flow associated with the nozzle. The x-z plane at an x=0 represents the nozzle surface. The y-axis represents the height above the nozzle surface and the x-axis is in the cross stream direction across the width direction separating the bumps. The hemispherical bumps are not shown in the figure but the y-z plane at y=0 bisects one of the bumps and shows the outline of the bump at the right symmetry boundary.

Two separate problems were run. The only difference in the two problems was the separation between the bumps. A four inch and a two inch separation between the bumps was analyzed. The bumps were simulated as hemispheres on a flat plate with a height of one inch. A supersonic boundary condition was used at the problem inlet where temperature, pressure and velocity were all specified. This corresponds to the x-z plane at x=0 shown in Figure 1A. The correct conditions for this boundary were determined from a previously run two dimensional nozzle solution at a point just upstream of joint 4. An outlet boundary condition was used at the outlet boundary (the downstream x-z plane) and a pressure drop consistent with the two dimensional nozzle solution was used to drive the flow. A 30 psi pressure drop was used in this problem. A symmetry boundary was used as the top boundary and the bottom boundary was the solid surface of the nozzle with wall functions employed. A symmetry boundary was also used for the side boundary conditions (y-z planes in Figure 1A). The combustion flame temperature was used as the thermal boundary condition for the energy equation. Table 4.9.1 shows the basic thermochemistry properties used in this analysis. The computational grid used was 50x35x69 or 120750 computational cells.

Table 4.9.1 Thermochemistry Properties Used in All CFD Analyses

Motor Property	
Viscosity	6.189×10^{-5} lbm/sec-ft
Molecular Weight	28.373
Specific Heat Ratio	1.1366
Flame Temperature	6098 °R

Since this is a three dimensional problem and the flow domain can only be plotted in two dimensions, several different two dimensional planes will be presented to illustrate the overall flow field. Figure 2A shows a cut through one of the bumps in a y-z plane at constant x. The figure shows a Mach number of greater than one as red. The plot shows that the bumps create a shock in front of the bumps and disturbs the flow field both upstream and downstream of the bumps. The bumps cause the boundary layer to thicken significantly. Not shown in this figure is the fact that the disturbance does wane downstream of the bump and the boundary layer thickness begins to decrease at a distance of about 7 inches downstream of the bumps. Figure 3A shows a plot of the flow field at the centerline between the two bumps. The boundary layer is definitely thickened but the flow is not as disturbed as seen in Figure 2A. Looking at an x-y plane from in front of the bumps and far upstream of the shock caused by the bumps, Figure 4A shows the undisturbed flow field. Figure 44A shows the flow field disturbance between the bumps and Figure 6A shows the disturbance of the flow several inches downstream of the bumps. Figure 7A shows the disturbance of the flow between the bumps in an x-z plane near the surface of the nozzle. Figure 8A shows the velocity vector field at this same location. There is a recirculation region created in front of the bumps and behind the bumps as shown in Figure 9A with definable flow separation points in front of and behind the bump. Figure 9A shows a y-z plane cut through one of the bumps similar to the Mach number plot shown in Figure 2A. As the figures show, the flow far above the bumps is not greatly disturbed by the presence of the bumps.

Plots for the solution with a bump separation of two inches will not be shown because they are very similar to the plots already shown. The same conclusions can be drawn as previously stated with the difference in the results showing slightly more interaction between the bumps near the nozzle surface. This is expected since the bumps are closer together.

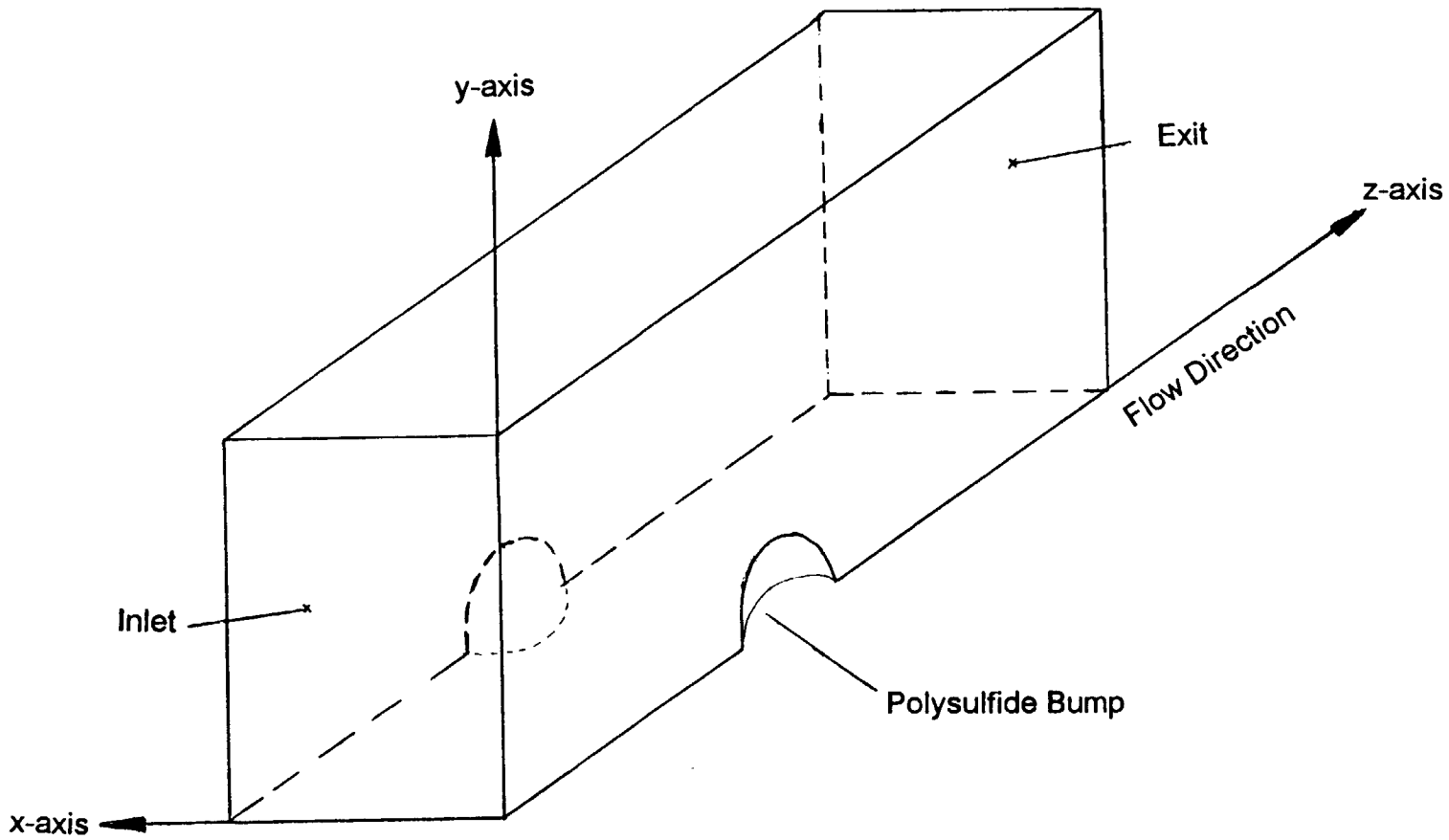

Figure 1A. Three Dimensional Polysulfide Bump Coordinate System

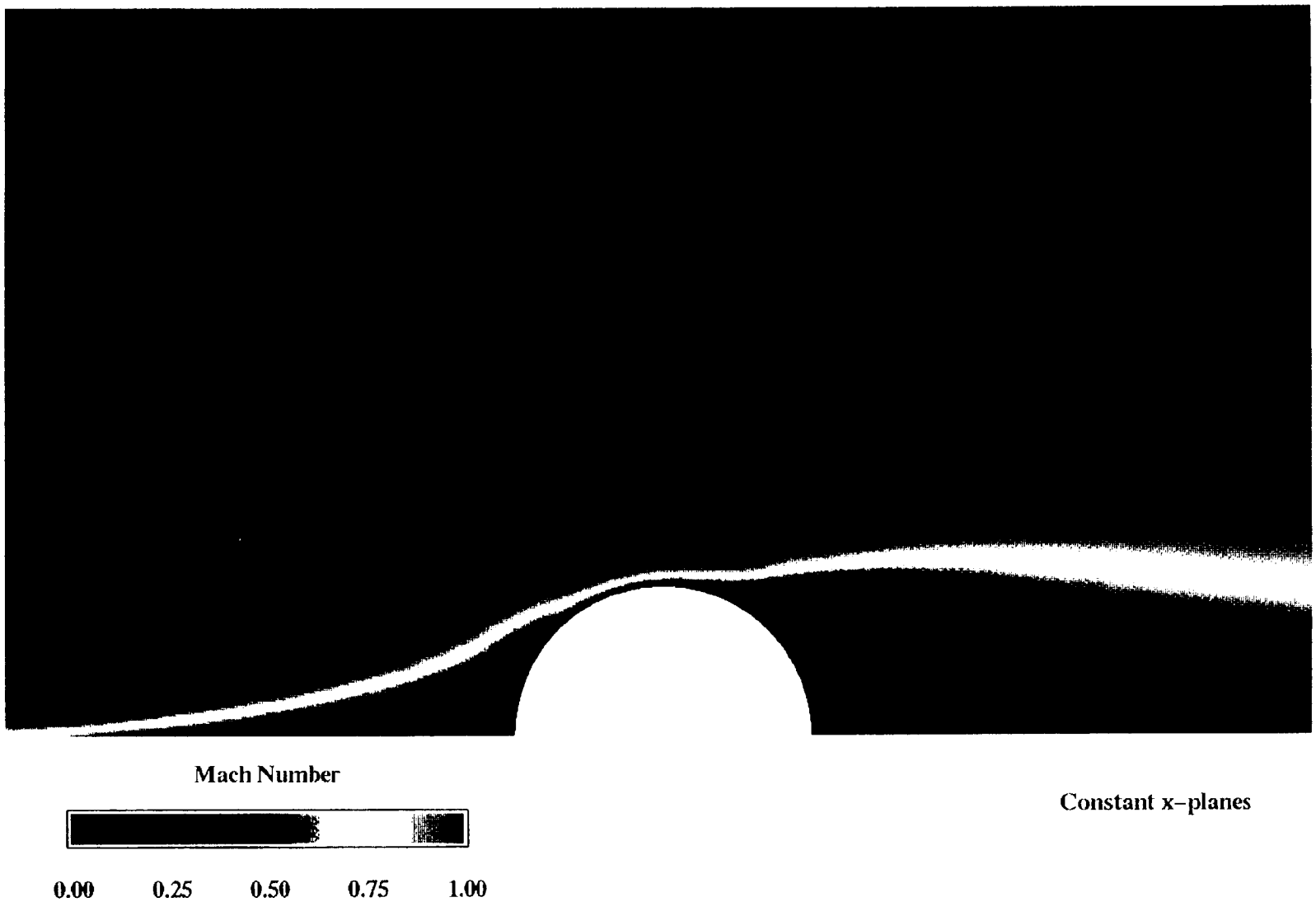

Figure 2A. Polysulfide Bump Mach Numbers, y-z Plane Through Bump

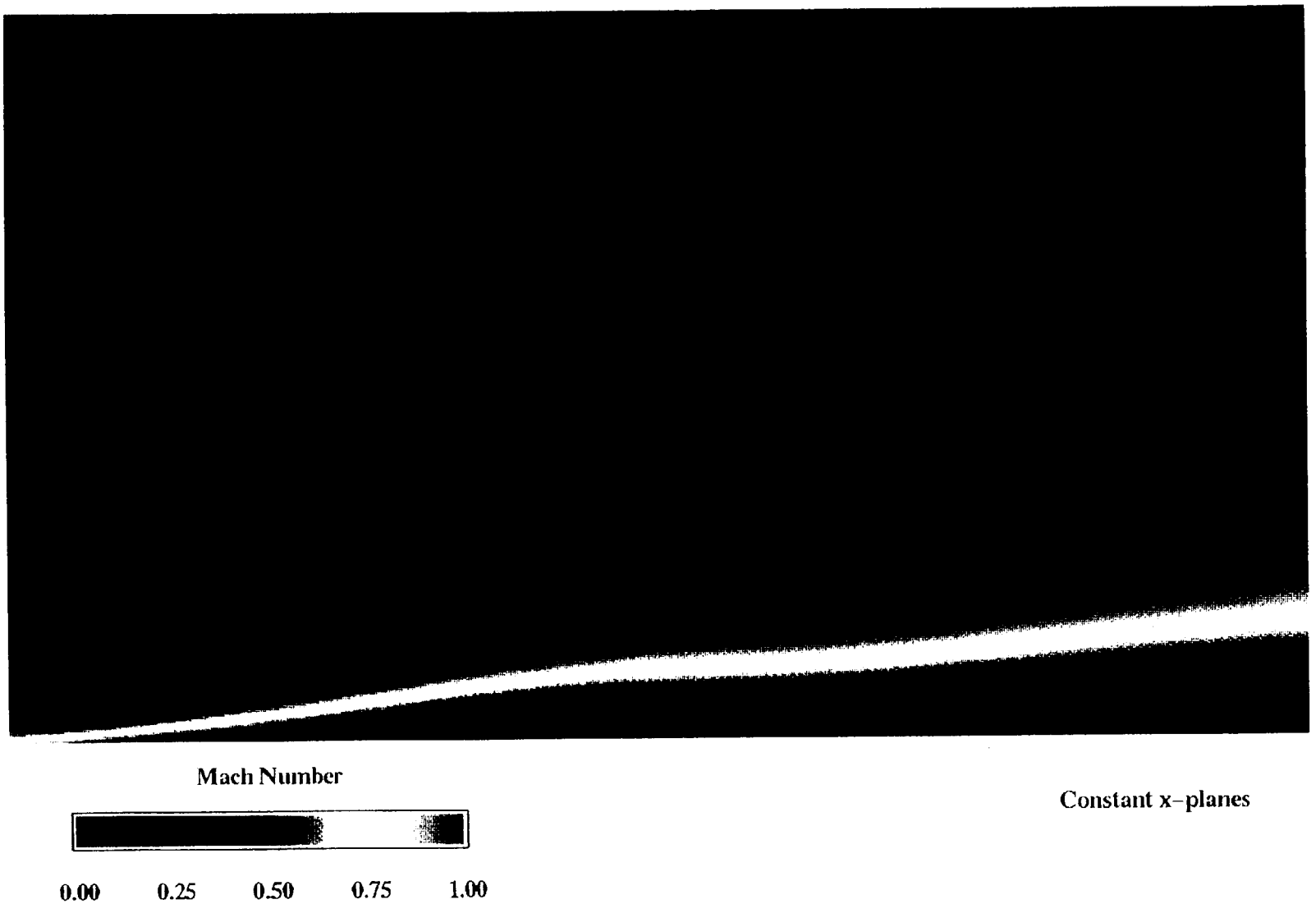

Figure 3A. Polysulfide Bump Mach Numbers, y-z Plane Through Centerline

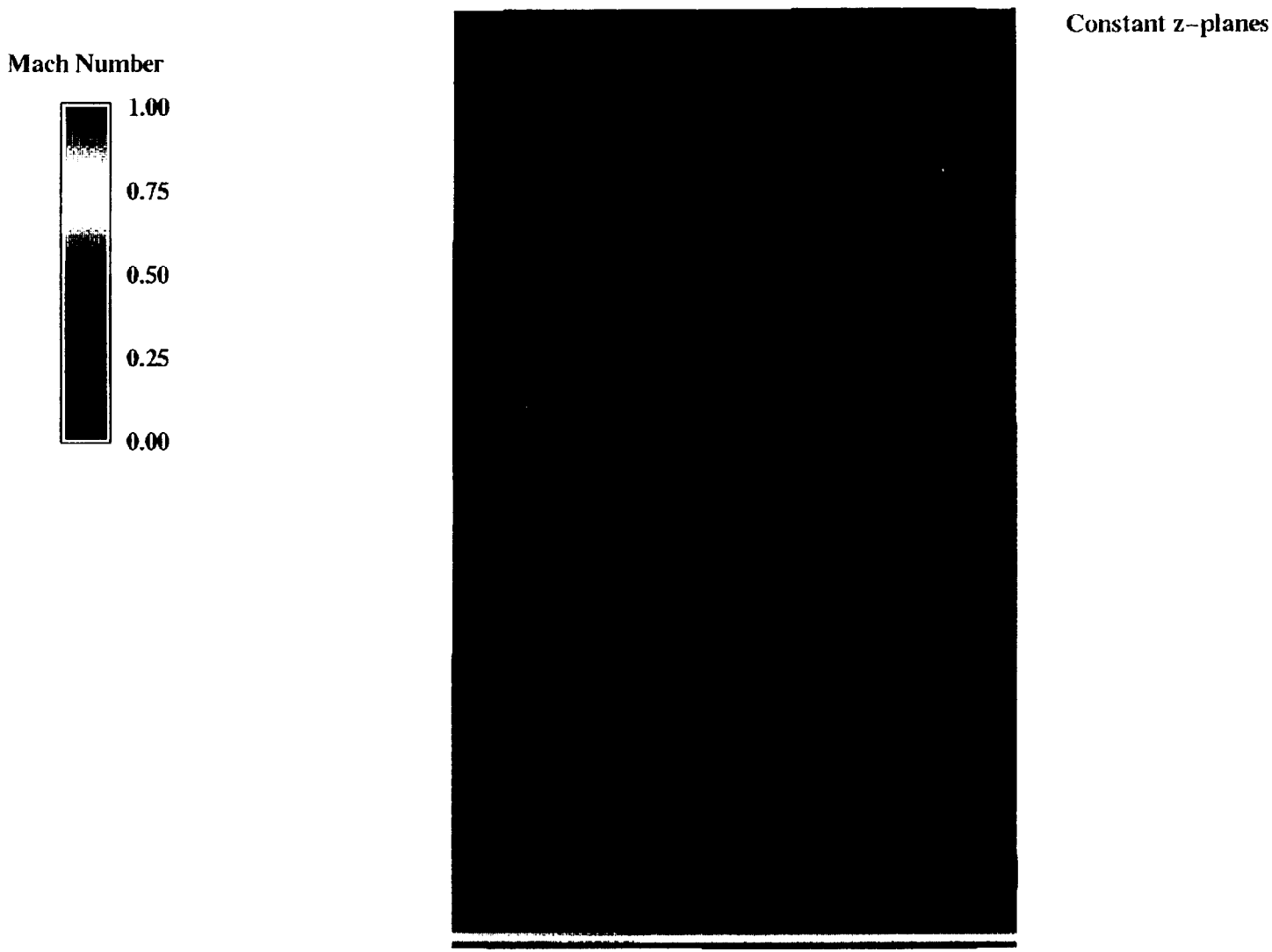

Figure 4A. Polysulfide Bump Mach Numbers, x-y Plane Upstream of Bump

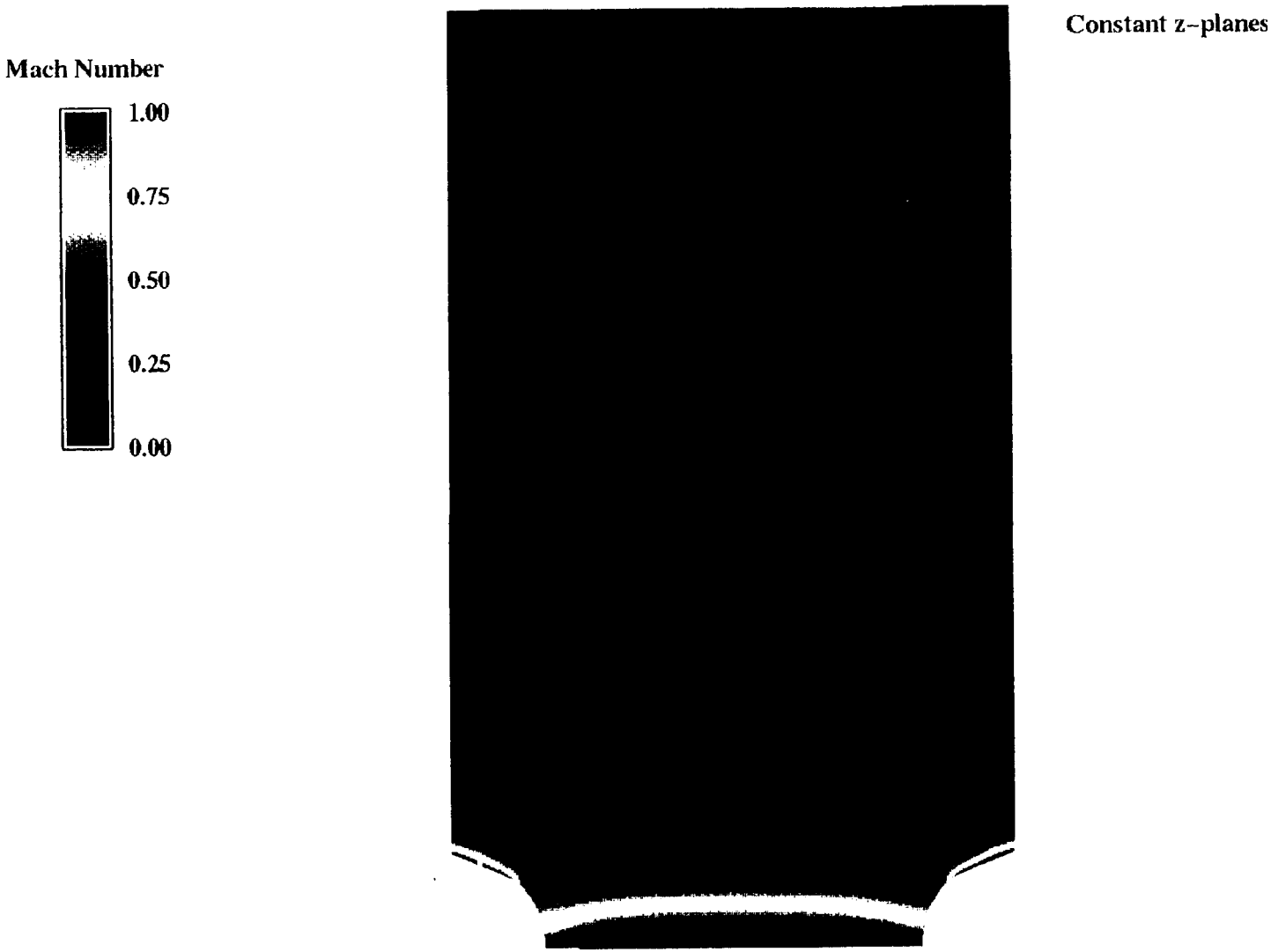

Figure 5A. Polysulfide Bump Mach Numbers, x-y Plane Through Bump

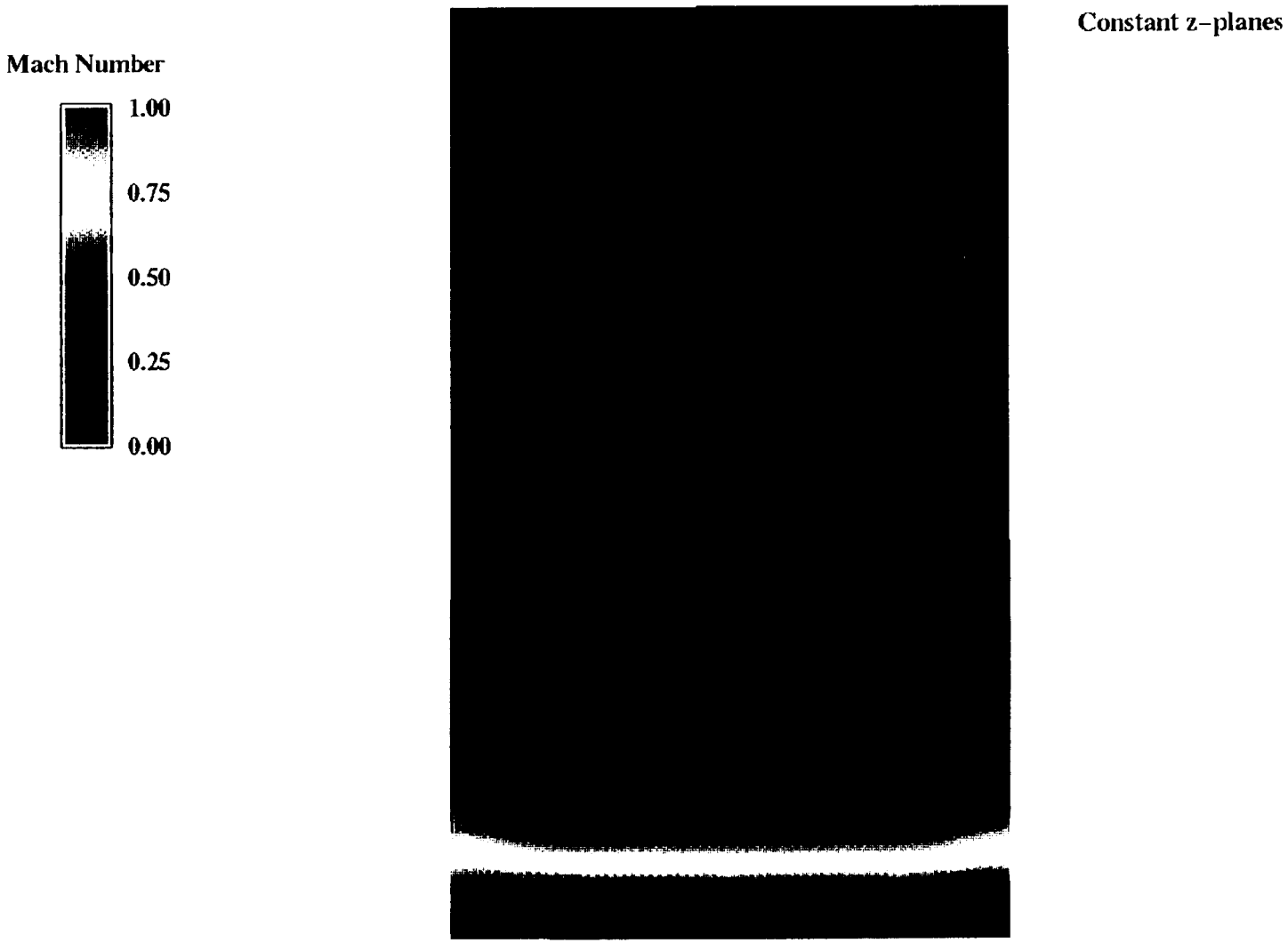

Figure 6A. Polysulfide Bump Mach Numbers, x-y Plane Downstream of Bump

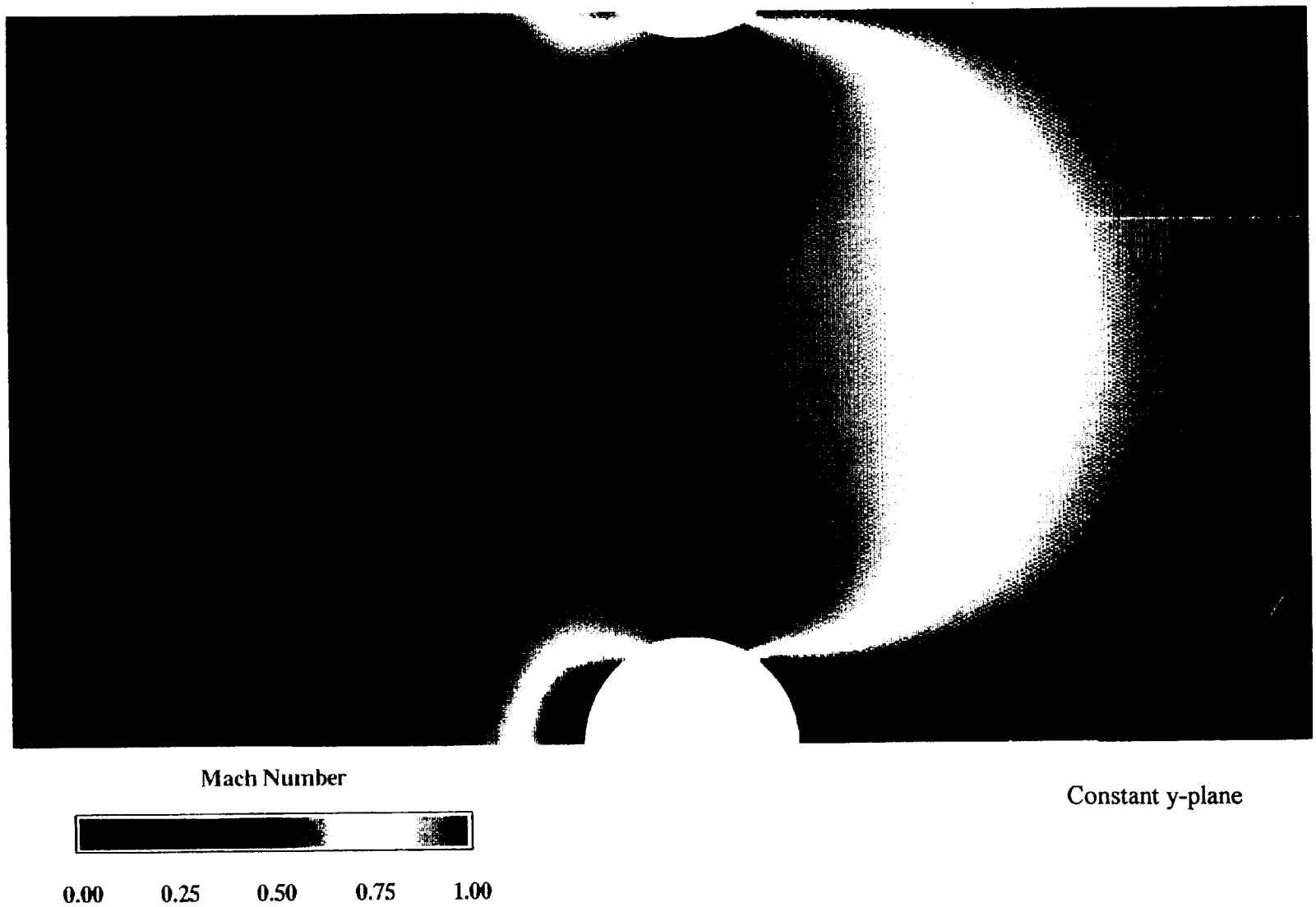

Figure 7A. Polysulfide Bump Mach Numbers, x-z Plane Through Bump

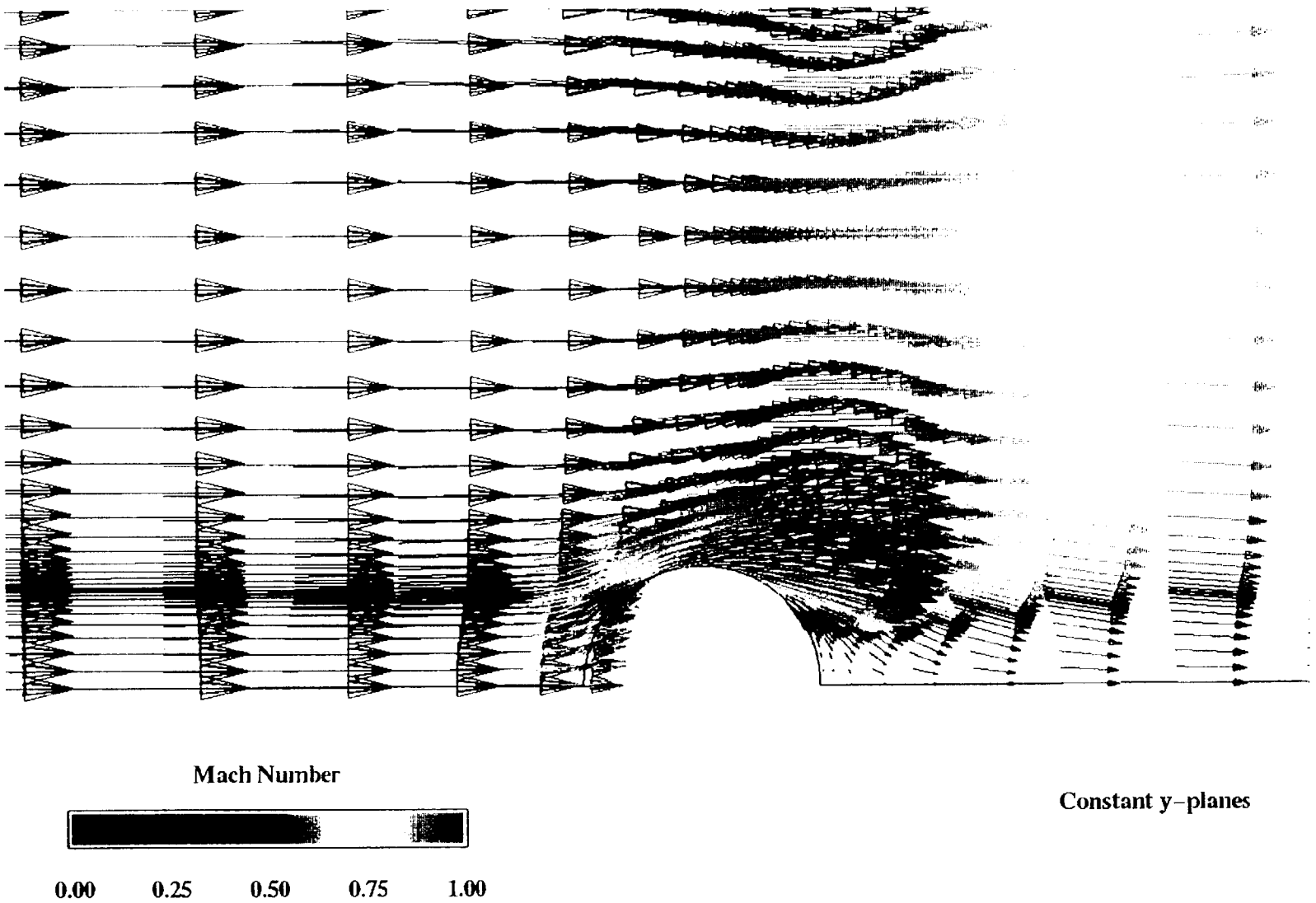

Figure 8A. Polysulfide Bump Velocity Field, x-z Plane Through Bump

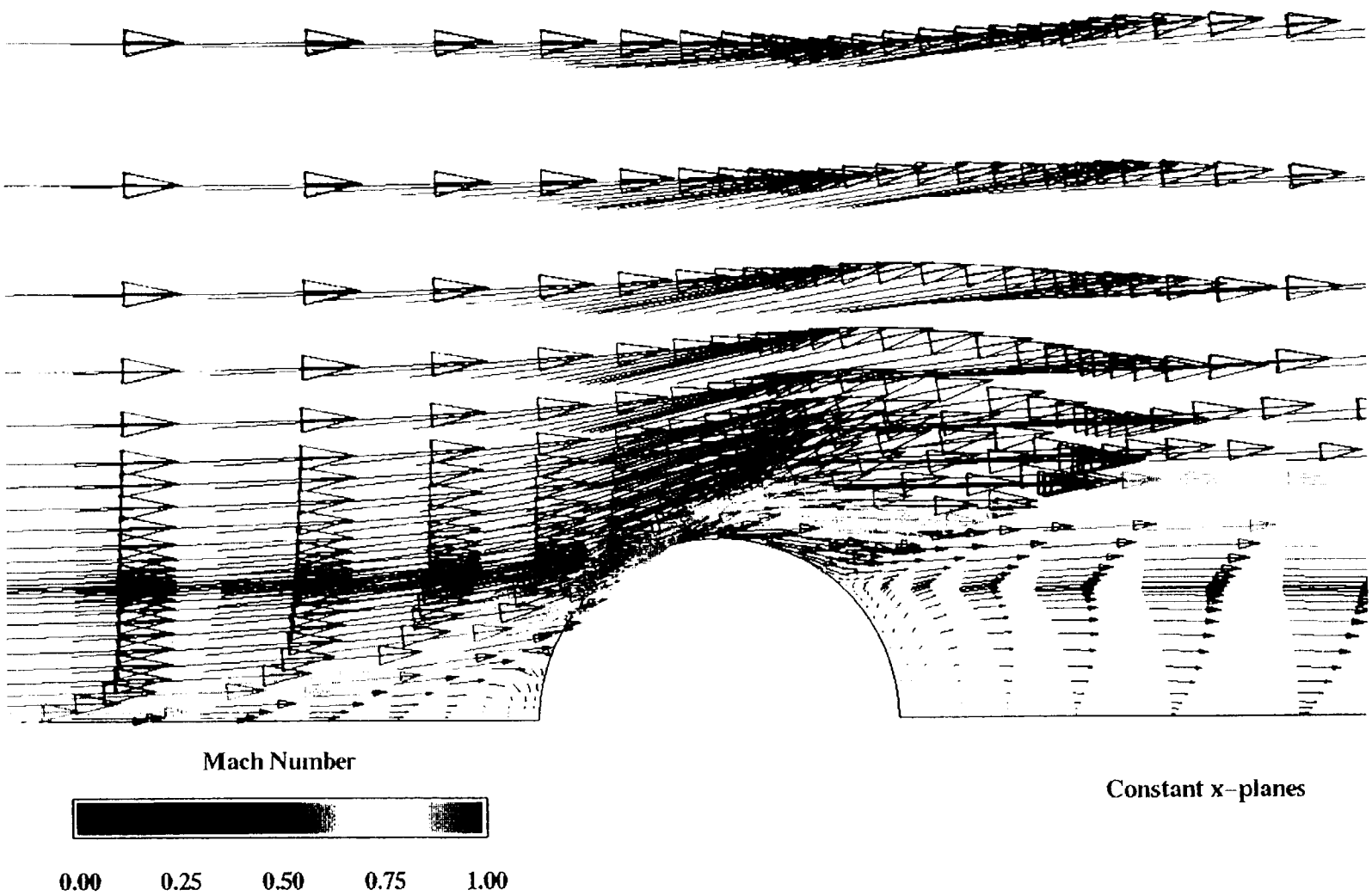

Figure 9A. Polysulfide Bump Velocity Field, y-z Plane Through Bump